Fracture Modeling in Elastomeric Materials: Relating the Macroscopic Response to Microscopic Processes

by

Shawn Ryan Lavoie

A thesis submitted in partial fulfillment of the requirements for the degree of

Doctor of Philosophy

Department of Mechanical Engineering
University of Alberta

Abstract

Inelastic material behavior is known to be able to enhance the fracture toughness of elastomers. However, how to optimally exploit this toughening mechanism is still being investigated. In this thesis a series of continuum models are developed to describe such inelastic behaviors, with the goal of gaining greater understanding of the fracture process which can then be exploited to produce tougher elastomers. This is accomplished by relating the mechanical response of the macroscopic elastomer to the extension and rupture of the microscopic polymer chains which comprise the material.

The peeling of a viscoelastic double cantilever beams by rupturing a layer of polymer chains along the plane of fracture was first investigated. The fracture energy consists of two components: the adhesive fracture energy arising from interfacial bond rupture, and viscous dissipation within the bulk material. Faster crack propagation requires larger adhesive fracture energy whereas the rate-dependence of bulk viscous dissipation is non-monotonic. The coupling between bulk and adhesive behavior was found to be weak in this problem because the strain in the beam and the adhesive stress on the interface are perpendicular.

Motivated by experimental observation of chain rupture in a large area surrounding crack tips, kinetic modeling of polymer chain scission was incorporated into the constitutive model of the bulk elastomer. When the material is assumed to contain a distribution of chains with different lengths the model produces two important results during uniaxial loading. First, the polydispersity causes the maximum stress to decrease because chains with different lengths attain their maximum force and rupture at different deformations. Second, progressive damage occurs in the material, which results in hysteresis between first loading and unloading under cyclic condition. This

elastomeric damage model was subsequently applied to establish a constitutive relation for multinetwork elastomers. These materials are synthesized by swelling a primary elastomeric network with filler network(s), a process which prestretches the chains of the network formed in the previous step(s). The effect of such a process is captured by basing the strain energy of the material on the combined effect of swelling and subsequent deformation of the completed multinetwork elastomers. The model provides a good match to experimental data on uniaxial extension, including cyclic loading, for a variety of prestretches.

The relationship between the force applied on a chain and its extension plays an important role in the mechanical properties of elastomers. Classical models for the chain force-extension relationship are too stiff at large extension due to the lack of consideration of bond deformation on the polymer chains backbone. A new model was developed to correct this, which is accomplished by considering free energy contributions from not only the configurational entropy, but also bond stretching and bond angle distortion. The model was also extended to include the consideration of active polymer chains containing mechanophores or molecules which have reactions that are triggered by mechanical force.

Preface

Chapter 2 of this thesis has been published as Lavoie, S.R., Long, R., Tang, T, "Rate Dependent Fracture of a Double Cantilever beam with Combined Bulk and Interfacial Dissipation" *Int. J. Solid Struct.*, **2015**,75-76, 277-286. Chapter 3 of this thesis has been published as Lavoie, S.R., Long, R., Tang, T., "An Adhesive Zone Model for Polymeric Interfaces" *Int. J. Fract.*, **2016**, 197, 169-183. Chapter 4 of this thesis has been published as Lavoie, S.R., Long, R., Tang, T., "A rate-dependent damage model for elastomers at large strain" *Extreme Mechanics Letters*, **2016,** 8, 114-124. For all the three articles, I was responsible for the formulation and numerical solution of governing equations, as well as manuscript composition. T. Tang and R. Long were involved in concept formation, assisted in a supervisory role and contributed manuscript edits.

Research conducted in Chapter 5 of this thesis forms part of an international research collaboration, led by Dr. Rong Long at the University of Colorado Boulder, with Dr. Tian Tang being the lead collaborator at the University of Alberta. Experiment data on multinetwork elastomers was provided by Drs. Pierre Millereau and Costantino Creton from ESPIC Paris, and the model for this material was developed by myself, with the assistance of Drs. Rong long and Tian Tang.

Acknowledgements

Shawn Lavoie acknowledges financial support from the Natural Science and Engineering Research Council (NSERC), Canada Foundation for Innovation and Alberta Innovates Technology Futures.

Table of Contents

List of Tables

List of Figures

List of Symbols

Provided at the end of each chapter. Note that some symbols are reused and may have different meanings in separate chapters.

Chapter 1. Introduction

Elastomers are frequently utilized in polymeric industry as well as in biomaterials. To predict the load bearing capacity of these materials numerous models have been developed to study the fracture of elastomeric materials. Greater insight into the toughness of the material obtained from fracture modeling can allow for improved design of components made from these materials. The goal of this research is to predict the macroscopic response of elastomeric materials by considering microscopic processes within the materials. This will be accomplished through theoretical modeling and comparison of the model predictions with experimental data.

One of these microscopic processes is the rate dependent scission (rupture) of chains within a network of cross-linked polymer chains. In a previous model, a microscopic description of an interface was presented [1-3] where the chains bridging the interface rupture according to certain kinetics. The bulk material in this model, however, was assumed to be elastic. This is a significant shortcoming since recent experimental works have been able to map the rupture of polymer chains [4] in a large area surrounding crack tips and this large damage causes the fracture toughness of the material to significantly exceed that of the interface. It is therefore important to develop models that account for both interfacial chain rupture [1-3] and damage in the bulk material [5]. This thesis contains a sequence of works in this direction. Chapters 2 to 6 each is a standalone publication (published or to be submitted) which contains its own introduction, nomenclature and conclusion. A compiled list of references is also provided at the end of the thesis. Supporting Information for each chapter is provided in the appendices.

The project began with simple cases where a fundamental understanding of the essential physics behind coupled bulk and interfacial dissipation can be gained. First, a kinetic interfacial model [1-3] was introduced into a simple double cantilever beam (DCB) with a linear viscoelastic bulk dissipation mechanism [6, 7]. Chapter 2 is a paper published in the International Journal of Solids and Structures [6] where the rate dependent coupling between bulk viscoelastic relaxation and interfacial bond rupture is investigated for DCB peeling. Chapter 3 is a paper published in the International Journal of Fracture [7], where an extension of the model presented in Chapter 2 is conducted to incorporate a more realistic polymer chain force-extension relationship and allow for the possibility of interface healing.

Next, more complicated geometries were investigated. Motivated by recent experimental data which mapped the rupture of polymer chains [4] in a larger area surrounding a crack tip, it

became apparent that the assumption of scission only occurring along an infinitesimally thin fracture interface was untrue for many tough elastomers. Therefore, the underlying physics of the kinetic interfacial model [1-3, 6, 7] was extended to create a framework for implementing material damage due to scission into the bulk [5]. The modeling results were able to capture some interesting experimental observations, which is presented in Chapter 4 and was published in Extreme Mechanics Letters.

To validate the effectiveness of the framework presented in Chapter 4, the model was extended to Multinetwork Elastomers (MNE), a new class of material where filler elastomer(s) are introduced into an existing elastomer to prestretch the chains of the original material [4]. These prestretched chains, because they occupy only a small percentage of the MNE volume, can dissipate energy over a large region before the MNE fails, enhancing the fracture toughness. This model is presented in Chapter 5 and will be submitted for publication soon. The development of such model which accurately describes the mechanical response of MNEs allows for rapid systematic study to optimize controllable parameters in the materials design, such as prestretch and original network volume fraction, to maximize fracture toughness. During the development of this MNE model it was found that existing models for polymer chain elasticity [9], which are based on configuration entropy, were inadequate for reproducing the behavior of the highly stretched chains near rupture. Thus a model which accounts for not only configuration entropy but the deformation of bonds on the backbone of a polymer chain was developed this model is presented in Chapter 6 and will be submitted for publication soon.

Chapter 2. Rate Dependent Fracture of a Double Cantilever beam with Combined Bulk and Interfacial Dissipation[1]

Abstract

The energy required to fracture viscoelastic media is known to depend on the rate of crack propagation. In this work, crack propagation, driven by applied moments, in an idealized model of a viscoelastic double cantilever beam (DCB) is studied. Rate dependency is taken into account through a standard linear solid viscoelastic model for the bulk material, and an adhesive zone model describing bond rupture kinetics for the polymer chains which bridge the interface. Attractive van der Waals (vdW) forces are also taken into account within the adhesive zone. The apparent energy release rate consists of two parts: the energy to overcome adhesion on the interface as well as viscous dissipation in the bulk. The adhesive energy in rupturing polymer chains increases as crack propagation speed increases. Relaxation of the bulk material causes viscous dissipation as stored strain energy is lost. For a beam of fixed length this dissipation was found to be negligible at high and low rates of crack propagation. Between these two limits there is a critical crack propagation speed where viscous dissipation is maximized.

[1] A version of this chapter has been published. Reprinted with permission from Lavoie, S. R.; Long, R. Tang, T. "Rate dependent fracture of a double cantilever beam with combined bulk and interfacial dissipation" Int. J. Solids. Struc. (2015) 75-76: 277-286. https://doi.org/10.1016/j.ijsolstr.2015.08.020

2.1. Introduction

The failure of polymeric materials is a phenomenon frequently encountered in a wide range of technological applications. Many of these materials display viscoelastic properties upon mechanical loading. However, the fracture mechanics of viscoelastic materials has yet to be fully understood [8]. Numerous experimental studies have found that the energy required to fracture polymeric materials depends on the rate of fracture [2, 3, 8, 10]. The work needed to propagate a crack at constant speed is often found to increase as the speed is increased [1, 8]. A similar phenomenon has also been observed for viscoelastic adhesives. Gent and Schultz found that the energy needed to peel viscoelastic rubbery adhesives was strongly dependent on the rate of peeling [11, 12] had similar findings. The adhesive failure of amorphous rubber adhered to a rigid substrate was studied by Andrews and Kinloch [13] who found that the energy required to detach the rubber consisted of two components: the intrinsic failure energy and the energy dissipated viscoelastically. Their results when reduced to a reference temperature using the Williams-Landel-Ferry (WLF) equation [14] yielded a single master curve, reminiscent of the time-temperature superposition for the relaxation modulus of viscoelastic materials. It is generally accepted that the energy supplied to propagate a crack at a constant speed must be sufficient to overcome energy dissipation in the bulk polymer [8, 15, 16] as well as the adhesive or cohesive energy on the crack interface [1¸2, 3, 15], henceforth referred to as the fracture energy.

Several theoretical efforts have been made to quantify viscous dissipation in the bulk material. Xu et al. [15] and Hui et al. [17] studied the peeling of a viscoelastic double cantilever beam (DCB) as well as an infinite viscoelastic solid with small scale yielding. In both cases the viscoelastic material was modelled as a standard linear solid [15, 17]. Chen et al [18] and Gao and Su [19] studied peeling of viscoelastic Bernouli-Euler beams using linear viscoelastic models which use the Boltzmann superposition integral. More sophisticated models which consider microstructural changes brought about by scission and reforming of polymer networks have been proposed [20, 21]. These models can provide a more accurate description of viscoelastic polymers, especially under finite deformation, but would also add significant complexity to the problem.

There have also been works seeking to model interfacial phenomena for crack propagation in polymeric materials. Xu et al. [15] and Hui et al [17] used a simple Dugdale-Barenblatt cohesive zone model with a constant cohesive stress, and a Newtonian fluid model with a cut-off stress to

describe the cohesive interaction in their works. Lake and Thomas studied the failure of vulcanized rubber and concluded that the fracture energy was amplified by the number of monomer units on the chains bridging the crack [10]. However, the Lake-Thomas theory did not explain why the fracture energy is rate dependent, and Chaudhury [2] proposed that this rate dependency is related to chemical kinetic processes at the interface. To quantify the kinetics of such interfacial processes, Chaudhury [2] introduced a kinetic equation, with the Lake and Thomas amplification factor incorporated, to study the dissociation of bonds bridging two interfaces as they were separated. This rate equation was later applied to a crack with an idealized wedge-shaped opening profile (3), and further to more realistic crack opening profiles [1]. This approach differs from traditional rate-independent models where the criterion for interface separation is based on a critical energy release rate or cohesive stress. An overview of the historical application of chemical kinetics to interfacial problems and further justification for the use of kinetic equations in fracture problems was given by Chaudhury [2].

The works cited above all made excellent contributions to advancing the field. However, in his review of several experiments, Gent [8] concluded that rate dependency of the apparent energy release rate should result from a combined effect of both interfacial and bulk properties. The conclusion that the interfacial model must also be rate dependent was reached by Rahulkumar et al. [22] after attempting to match finite element results to experimental data for peel tests. Among the prior theoretical works several have considered basic bulk viscoelastic models [15, 17], however the adhesive zone models used in these works were too simplistic. On the other hand, none of the prior works that captured rupture kinetics of the polymer chains bridging a crack have considered bulk viscoelastic behavior [1, 2, 3]. The goal of this work is to develop a simple model which takes into account both bulk viscoelasticity and rate dependent rupture of polymer chains across the interface. We will accomplish this by considering steady state crack propagation in a simple viscoelastic DCB geometry which was used by [15]. The crack will be reinforced by an adhesive zone with polymer chains which undergo rate dependent breakage following the kinetics previously presented in the literature [1, 2, 3].

The structure of the paper is as follows. The mathematical formulation of our model is presented in Section 2.2. The numerical methods used to solve the equations are described in

Section 2.3. Numerical results are presented and discussed in Section 2.4. Conclusions are given in Section 2.5.

2.2. Formulation

The problem studied in this work is the rate dependent fracture of a viscoelastic material, represented by a DCB as shown in Figure 3.4a). Here the applied moments M_∞ cause a crack to propagate in a steady state at speed V, and separates the DCB into two identical beams. The rightmost point in the fully bonded portion (no separation) of the DCB is referred to as the adhesive zone tip. An adhesive zone is introduced to the right of the adhesive zone tip, within this zone stresses from both van der Waals (vdW) attractions and the stretch of polymer chains resist the separation of the two beams (see Figure 3.4a)). As one moves away from the adhesive zone tip (to the right) eventually stretched chains will rupture, which will reduce the density of chains bridging the crack tip and cause the adhesive stress to decrease. A suitable criterion will be specified later to define the crack tip as the leftmost point where these stresses vanish. The region between the adhesive zone tip and the crack tip is the adhesive zone. X-Y is a fixed coordinate system and x-y is a coordinate system which is attached to the adhesive zone tip and translates at constant speed V with the crack. The crack opening δ depends on position x. Because the two beams are assumed to be identical, the system is symmetrical about line o_1-o_2 which is the crack interface. Our goal is to calculate the energy required to propagate the crack at a given speed V. This energy consists of work required to overcome attractions in the adhesive zone, and energy dissipated by viscoelastic processes in the bulk material.

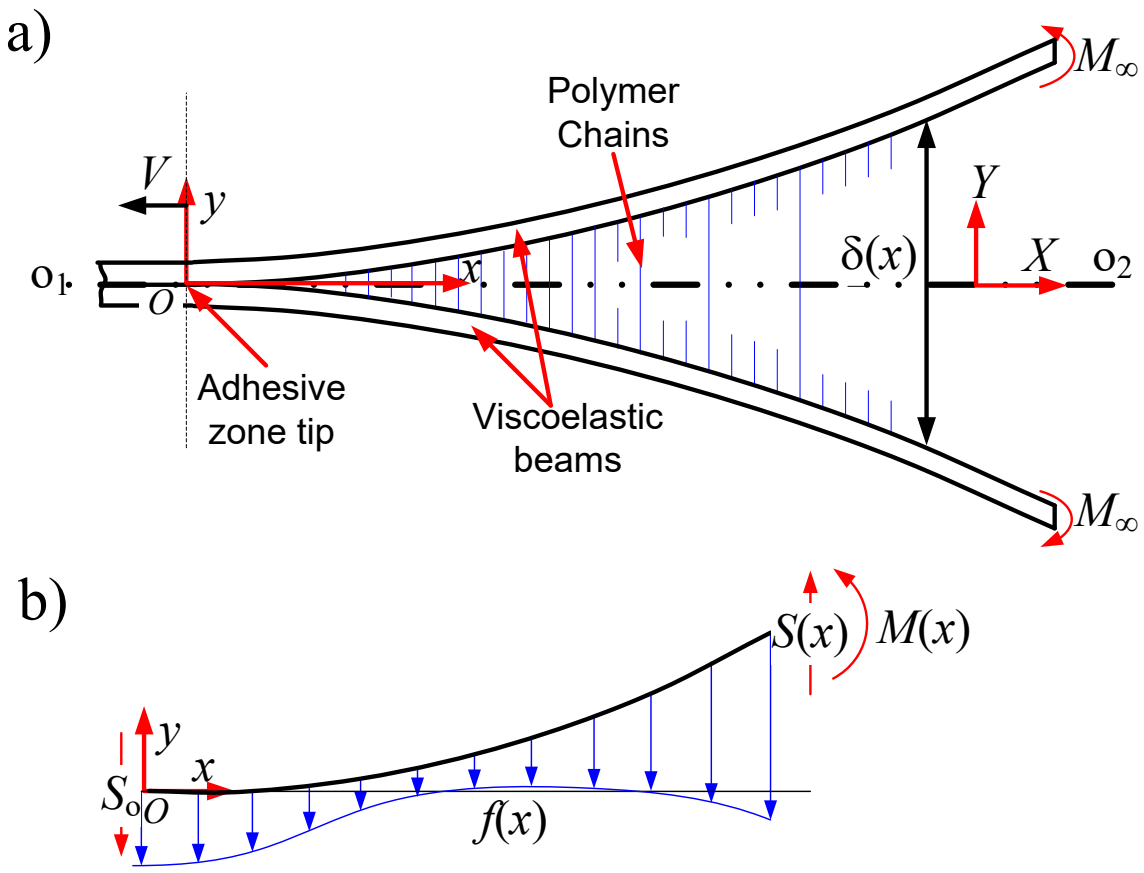

Figure 2.1: a) Schematic of the viscoelastic DCB studied in this work. The representative polymer chains shown in this figure are not meant to indicate the chains are disabled at some positions and enables at others. The density of chains is smaller for larger x. The crack-tip is the point where the bond density first becomes zero. b) free body diagram of a section of the upper beam within the adhesive zone.

2.2.1. *Viscoelastic Beam*

Consider the free-body diagram of a section of the upper beam shown in Figure 3.4b). The beam is shown in a deflected state and is acted upon by a distributed adhesive stress *f*. *f* consists of contributions from polymer chains which bridge the crack interface and vdW attractions. An imaginary cut is made in the beam at *x* to reveal the two internal loads acting on the beam: a shear

force S, and a bending moment M. At point O there is a reaction shear force S_o. Xu et al. [15] formulated a differential equation for the deflection of a viscoelastic DCB:

$$M - \tau_o V S = \frac{E_\infty I}{2}\frac{d^2\delta}{dx^2} + \frac{\tau_o V E_o I}{2}\frac{d^3\delta}{dx^3}, \quad (2.1)$$

where I is the moment of inertia of the beams' cross section. The derivatives in the equation are with respect to x instead of time t because under steady state condition, the transformation $d/dt = Vd/dx$ can be introduced using the translating coordinate system x-y fixed to the adhesive zone tip. Eq. (2.1) is based on a standard linear viscoelastic solid model, which for a uniaxial stress state reduces to the following stress-strain relation $\sigma + \tau_o\dot{\sigma} = E_\infty\varepsilon + \tau_o E_o\dot{\varepsilon}$, where E_o is the instantaneous or unrelaxed modulus, E_∞ is the infinite time or relaxed modulus, τ_o is the bulk relaxation time, σ is stress, ε is strain and the overhead dot ($\dot{\sigma}, \dot{\varepsilon}$) indicates differentiation with respect to time [15].

2.2.2. *Rate Dependent Chain Rupture*

The two beams are bridged by polymer chains. Kinetic equations can be written to model the rupture of bonds on the polymer chains; rupture of any one bond on a chain's backbone prevents it from bridging the crack. When a tensile force (F) is applied to a chemical bond it decreases the activation energy of bond dissociation [2], and hence increases the probability of bond rupture. The number of chains bridging the two surfaces can be obtained from the solution of an equation governing the kinetics of bond rupture [2]

$$-V\frac{d\Sigma_b}{dx} = \frac{n}{\tau_-}\Sigma_b e^{F\lambda/k_BT}, \quad (2.2)$$

$$\Sigma_b(0) = \Sigma_o \quad (2.3)$$

In Eq. (2.2), Σ_b is the number of chains that cross a unit area of the interface, n is the number of bonds per polymer chain, λ is the bond activation length, F is the tensile force acting on each chain, k_B is the Boltzman constant, T is the absolute temperature and τ_- is the characteristic time of bond dissociation which depends on the activation energy for bond dissociation [2]. In particular,

$\tau_{-} = h_P e^{E_a / k_B T} / k_B T$, where h_P is Plank's constant; larger vibration energy of molecules at higher temperature allows more rapid passage over the activation energy (E_a) barrier and leads to faster dissociation. The right hand side of Eq. (2.2) is the rate of chain dissociation. Theoretically, there can also be a term responsible for chain association, but it is typically assumed to be considerably smaller than the chain dissociation rate and has been neglected [2]. Eq. (2.2) is accompanied by a boundary condition Eq. (2.3) which states that at x = 0, where the crack opening is zero and the chains are not stretched, no chains are broken. Σ_o is the chain density for perfectly bonded interface. The original kinetic equation [2] is expressed in term of time derivative of Σ_b, which has been converted to a derivative with respect to position by using a steady-state assumption and a coordinate transformation ($d/dt = Vd/dx$) from the fixed X-Y system to the translating x-y system with velocity V (see Figure 3.4a)). The tensile force acting on each chain, F, can be related to the extension of the polymer chains bridging the crack interface. Although the force-extension relationship is usually not linear [3], we will adopt an assumption from the literature where the chains are assumed to be linear springs [1, 2]), i.e., $F = k_s \delta$, where k_s is the average spring stiffness defined from $U = \int_0^{L_c} k_s \delta d\delta = k_s L_c^2 / 2$. Here U is the work required to stretch the chain from its unstressed configuration to its contour length L_c. Defining the average spring stiffness in this way ensures that the work U to stretch the linear chain is equal to that for its nonlinear counterpart.

The distributed load acting on the beams,

$$f = \Sigma_b F + \frac{W_{vdW}}{\delta_c} e^{-\delta/\delta_c}, \qquad (2.4)$$

is made up of two components: the adhesive stress from polymer chains $\Sigma_b F$ (the force acting on each chain, F, times the density of chains Σ_b), and the attractive vdW stress $W_{vdW} e^{-\delta/\delta_c} / \delta_c$ where δ_c is a characteristic decay length and W_{vdW} is the work of adhesion due to vdW attractions. The inclusion of the vdW component of the adhesive stress was shown to be necessary in order to have a well-defined adhesive zone tip [1]. This exponential function for vdW attractions is an approximation which has been chosen for mathematical convenience. It is well-known that dispersion forces decay much slower than the exponential function [1]. However, provided that the vdW region is much smaller than the chain bridging region, it is expected, and demonstrated

later in this work, that fracture problems are insensitive to the form of the vdW interaction potential as long as it produces the same work of adhesion [1].

2.2.3. *Non-dimensionalized Boundary Value Problem*

The viscoelastic beam model introduced in section 2.2.1 and the rate-dependent interface model described in section 2.2.2 are combined to study the steady-state crack propagation in the DCB. The interface and beam models are coupled through the stretch of interfacial polymer chains and the resulting forces acting on the beams. Balance of the distributed load f on the interface with the internal shear forces S and moment M, shown in Figure 3.4b) [23], leads to a system of ordinary differential equations (ODEs) and boundary conditions (BCs). Through the formulation 16 parameters have been identified which define the rate of crack propagation, geometry and properties of the bulk and interfacial models: V, n, τ_-, λ, k_B, T, Σ_o, τ_o, E_o, E_∞, I, L_c, U, W_{vdW}, δ_c, and D. All of these parameters have been introduced in previous sections except the last one which is the out-of-plane depth of the beam. To reduce the number of parameters and simplify the ensuing discussion we introduce the following non-dimensional parameters.

$$\Sigma_b^* = \frac{\Sigma_b}{\Sigma_o}, \quad x^* = x\left(\frac{2k_BT\Sigma_oD}{E_oIL_c^2}\right)^{1/4}, \quad \delta^* = \frac{\delta}{L_c}, \quad F^* = \frac{FL_c}{k_BT}, \quad f^* = \frac{fL_c}{k_BT\Sigma_oD},$$

$$S^* = \frac{SL_c}{k_BT\Sigma_oD}\left(\frac{2k_BT\Sigma_oD}{E_oIL_c^2}\right)^{1/4}, \qquad M^* = M\left(\frac{2}{k_BT\Sigma_oDE_oI}\right)^{1/2},$$

$$V^* = \tau_oV\left(\frac{2k_BT\Sigma_oD}{E_oIL_c^2}\right)^{1/4}, \; U^* = \frac{U}{k_BT}, \; \gamma_E = \frac{E_\infty}{E_o}, \; \gamma_\tau = n\frac{\tau_o}{\tau_-}, \; \gamma_L = \frac{\lambda}{L_c}, \; \delta_c^* = \frac{\delta_c}{L_c},$$

$$W_{vdW}^* = \frac{W_{vdW}}{k_BT\Sigma_o}, \; G^* = \frac{G}{k_BT\Sigma_o}, \; G_{ad}^* = \frac{G_{ad}}{k_BT\Sigma_o}, \; G_{vis}^* = \frac{G_{vis}}{k_BT\Sigma_o}. \qquad (2.5)$$

The physical meanings of the variables from Eq. (2.5) are summarized in Table 2.1.

After nondimensionalization using Eq. (2.5), the bond dissociation equation, Eq. (2.2)-(2.3), becomes

$\frac{d\Sigma_b^*}{dx^*} = -\frac{\gamma_\tau}{V^*}\Sigma_b^* e^{F^*\gamma_L}$,	(2.6)
$\Sigma_b^*(0) = 1$,	(2.7)

and the polymer chain force-stretch relationship, becomes $F^* = 2U^*\delta^*$. Similarly, introduction of the parameters in Eq. (2.5) into the beam equation gives

$M^* - V^* S^* = \gamma_E \frac{d^2\delta^*}{dx^{*2}} + V^* \frac{d^3\delta^*}{dx^{*3}}$.	(2.8)

The balance of the shear force with the distributed load leads to

$\frac{dS^*}{dx^*} = f^* = \Sigma_b^* F^* + \frac{W_{vdW}^*}{\delta_c^*} e^{-\delta^*/\delta_c^*}$,	(2.9)

and the bending moment is related to the shear force by

$\frac{dM^*}{dx^*} = -S^*$.	(2.10)

Eq. (2.8)-(2.10) contain two first order ODEs and one third order ODE, and should be accompanied by five BCs. Firstly, on the left of the adhesive zone at $x = 0$, the crack opening is identically zero therefore the slope and deflection at the adhesive zone tip will be zero or

$\delta^*(0) = 0$, $\frac{d\delta^*}{dx^*}(0) = 0$.	(2.11)

Secondly, the steady-state assumption implies that the beams experience a sudden loading at the adhesive zone tip. As a result the material at the adhesive zone tip can be treated as elastic with the unrelaxed or instantaneous modulus. Using the *j*-integral [25, 26, 27, 28] both the moment and curvature at the adhesive zone tip are found to be zero,

$M^*(0) = 0$, $\frac{d^2\delta^*}{dx^{*2}}(0) = 0$.	(2.12)

In Appendix 1.1 we present an alternative approach where the vdW attractions are not explicitly included in f^* but are accounted for at the adhesive zone tip by using nonzero curvature and moment conditions obtained from the *j*-integral. This approach represents the limit as the vdW decay length δ_c approaches zero. Physically it is less realistic but results in a simpler model. It is

also explained in Appendix 1.1 that if all sources of adhesive attraction are considered explicitly in the adhesive stress f^* then the moment and curvature at the adhesive zone tip must be zero.

Table 2.1: Description of Non-dimensional Parameters

Category	Parameter	Description of Non-dimensional Parameter
Position-Dependent Variables	x^*	position
	Σ_b^*	bond density
	δ^*	crack opening
	F^*	force on a single polymer chain
	f^*	distributed load on the interface
	S^*	shear force
	M^*	bending moment
Governing Parameters	V^*	crack propagation speed
	U^*	energy of a polymer chain when stretched to its full contour length
	γ_E	ratio of relaxed to unrelaxed Young's modulus in the standard linear solid viscoelastic model
	γ_τ	ratio of relaxation times of bulk and chain dissociation
	γ_L	ratio of activation length to contour length
	δ_c^*	vdW decay length
	W_{vdW}^*	vdW work of adhesion
Fracture Energies (Desired Output)	G^*	fracture energy
	G_{ad}^*	adhesive fracture energy; describing interfacial dissipation
	G_{vis}^*	viscous fracture energy; describing bulk dissipation

BCs far from the adhesive zone tip require more discussion. It is expected that, as the crack opening increases from the adhesive zone tip, the chains will undergo greater stretch and hence faster dissociation as indicated by Eq. (2.6); eventually the low bond density will cause f^* on the interface to be negligible. On the other hand, the decrease in force is continuous and f^* will approach but never actually reach zero. To resolve the dilemma of not having a clearly defined crack tip, we introduce the adhesive zone length L^*. Ideally this length would be defined so that $f^*(x^* = L^*)$ reduces below some tolerance; however, f^* can have a local minimum (data not shown), as the decay of the vdW portion can be stronger than the increase of the chain portion (stretching) for small openings. This local minimum makes such a criteria undesirable; therefore the following criteria was implemented

$\Sigma_b^*(L^*) \le \varepsilon_b^*$ and $\delta^*(L^*) \ge \delta_{cr,vdW}^*$.	(2.13)

Here the first condition ensures that at L^* the bond density and hence the adhesive stress from polymer chains has decreased below a desired tolerance. The second condition ensures that at L^* the crack has opened sufficiently far such that the work done by the vdW attractions is sufficiently close to the vdW work of adhesion. The critical vdW opening, $\delta_{cr,vdW}^*$, is a constant which depends on δ_c^*. If, for example, we require the work done by vdW attractions to be least 99% of W_{vdW}^* then $\delta_{cr,vdW}^* = 4.605\delta_c^*$. In Appendix 1.2 we explore a number of different criteria for determining L^* and found that the value of L^* can change considerably depending on what criteria is used. However, the fracture energies were found to be insensitive to the criteria. In light of the definition of L^* above, the traction outside of the adhesive zone is negligible. Therefore, from Eq. (2.9) the shear force must be constant and since only a moment, M_∞^*, is applied at the far field, the constant must be zero, i.e.

$S^*(L^*) = 0$.	(2.14)

Similarly, from Eq. (2.10), outside of the adhesive zone the moment must be constant and equal to the far field value, M_∞^*; therefore the necessary moment for crack propagation at a given speed V^* can be evaluated from $M_\infty^* = M^*\left(L^*\right)$.

2.2.4. *Fracture Energies*

Eq. (2.6) - (2.14) constitute a boundary value problem that can be solved to compute the crack opening profile and adhesive zone length; however, a few additional steps are required to extract the energy release rate. The apparent energy release rate for crack growth, G^*, can be obtained from the work done by the applied moment to advance a unit area of the crack, after subtracting a strain energy correction due to the translating coordinate system (see Appendix 1.3)

$$G^*(x^*) = \frac{M_\infty^*}{2}\frac{d^2\delta^*}{dx^{*2}}. \tag{2.15}$$

Eq. (2.15) is valid outside of the adhesive zone ($x^* > L^*$) where $S^* = 0$ and $M^* = M_\infty^*$, however G^* still depends on position because viscoelastic dissipation still occurs in the bulk material outside of the adhesive zone. The simple loading condition outside of the adhesive zone allows for an explicit expression for $d^2\delta^*/dx^{*2}$ to be derived from Eq. (2.8)

$$\frac{d^2\delta^*}{dx^{*2}} = \left(\left.\frac{d^2\delta^*}{dx^{*2}}\right|_{L^*} - \left.\frac{d^2\delta^*}{dx^{*2}}\right|_{\infty} \right) e^{-\frac{\gamma_E}{V^*}\left(x^* - L^*\right)} + \left.\frac{d^2\delta^*}{dx^{*2}}\right|_{\infty}. \tag{2.16}$$

Here $d^2\delta^*/dx^{*2}(L^*)$ is known from the solution within the adhesive zone. At infinity the beams are fully relaxed; therefore, $d^2\delta^*/dx^{*2}(\infty)$ can be evaluated by assuming the beam were elastic with the infinite time modulus

$$\left.\frac{d^2\delta^*}{dx^{*2}}\right|_{\infty} = \frac{M_\infty^*}{\gamma_E}. \tag{2.17}$$

Together with (2.16) and (2.17), the energy release rate can be evaluated from (2.15) at any given position x^* outside the adhesive zone.

The energy release rate as calculated above can also be expressed as

$$G^* = G_{ad}^* + G_{vis}^* \tag{2.18}$$

where G_{ad}^* is the work per unit area done by tractions within the adhesive zone, and G_{vis}^* is the viscous dissipation in the beam per unit area of crack advancement. G_{ad}^* can be calculated using the definition of work for a non-constant force

$$G_{ad}^{*}=\int_{0}^{\infty} f^{*}d\delta^{*} \approx \int_{0}^{\delta^{*}\left(L^{*}\right)} \Sigma_{b}^{*}F^{*}d\delta^{*}+W_{vdW}^{*}, \quad (2.19)$$

where we have separated the contributions to G_{ad}^{*} into components from polymer chains and vdW attractions. Since the traction is negligible outside of the adhesive zone the integration does not need to extend to δ greater than the crack opening displacement (COD), $\delta^{*}\left(L^{*}\right)$. The viscous dissipation G_{vis}^{*} is obtained from Eq. (2.18) with G^{*} evaluated from Eq. (2.15) and G_{ad}^{*} evaluated from Eq. (2.19). Note that the energy of both beams' has been taken into account in the above equations.

2.3. Numerical Methods

To solve Eq. (2.6) and (2.8)-(2.10) a shooting method is used. First the value of $S^{*}(0)$ is guessed, which converts the boundary value problem into an initial value problem with initial conditions Eq. (2.7), (2.11) and (2.12). A solution for $\{\Sigma_{b}^{*}(x^{*}), S^{*}(x^{*}), M^{*}(x^{*}), \delta^{*}(x^{*}), d\delta^{*}/dx^{*}$ and $d^{2}\delta^{*}/dx^{*2}\}$ is found by integrating Eq. (2.6) and (2.8)-(2.10) using a 4th order Runge-Kutta method with adaptive step size control [24]. $f^{*}(x^{*})$ is calculated from Eq. (2.9) and the adhesive zone length L^{*} is determined from Eq. (2.13). After L^{*} is determined, the shear force at L^{*} is checked to satisfy Eq. (2.14). If it is not satisfied within some small tolerance, a new guess for $S^{*}(0)$ is made and the procedure repeats until Eq. (2.14) is satisfied.

The adhesive zone length can be sensitive to the criteria used in its definition (Eq. (2.13)), which was confirmed in Appendix 1.2 using results obtained from several different criteria. However G_{ad}^{*} was found to be the same for all criteria. This insensitivity allows us to present below the results obtained from a single criterion. The nontrivial results and discussion on L^{*} are given only in Appendix 1.4 so as not to distract from the main objectives of this work.

In addition, because bulk viscous dissipation within the beam can continue beyond the adhesive zone, the two energy release rates G_{vis}^{*} and G^{*} depend on the position x^{*} where they are evaluated and G_{vis}^{*} can greatly exceed the adhesive fracture energy if the beam length approaches infinity. Practically, it is more realistic to consider DCBs of finite length for evaluating these energies. We used several fixed beam lengths to compute the fracture energies, all of which are

larger than the adhesive zone length. In section 2.4 below we present representative results with a fixed beam length at $x^* = 1$ which is of the same order of magnitude as the largest adhesive zone length obtained with different combination of parameters used in this work. Other cases, including $x^* = \infty$, have been presented in Appendix 1.5.

2.4. Results and Discussion

Even in the normalized form there are still seven parameters which govern the rate dependent fracture: V^*, γ_τ, γ_E, γ_L, U^*, W^*_{vdW} and δ_c^*. Among these, V^* and γ_τ can be identified as the most essential parameters since V^* is the normalized crack propagation speed while γ_τ captures the ratio of the relaxation times of the two sources of dissipation (bulk vs. interfacial). Therefore we vary V^* and γ_τ over many orders of magnitude (10^{-10} to 10^{10} for V^* and 10^{-5} to 10^3 for γ_τ), based on reported values of physical parameters [1, 2, 3]. The remaining parameters are fixed at physically reasonable values. For γ_E, we will consider both an elastic case $\gamma_E = 1$, and a representative viscoelastic case where $\gamma_E = 0.01$ [15]. The activation length λ has been reported as 0.1 nm [29] for some biopolymers, and for $n = 150$ the contour length L_c has been reported to be 45 nm [2, 3], thus a representative value of $\gamma_L = 0.02222$ will be used. A representative value of $U^* = 2850$ was found by numerically integrating experimental data from the work of Ghatak et al. [3] to find U, and assuming standard ambient temperature and pressure (SATP) so that $T = 298$ K. Choosing a work of adhesion from dispersion forces of about $W_{vdW} = 50$ mJ/m^2 from Tang et al. [30], and a bond density $\Sigma_o = 2.5\text{x}10^{18}$ from Ghatak et al. [3] gives, at SATP, $W_{vdW}^* = 5$. The vdW decay length is obtained from W^*_{vdW} and by assuming a vdW stress of about 2MPa so that $\delta_c^* = 0.02$. A sensitivity study for several values of δ_c^* is presented in Appendix 1.6.

With the above parameters, below we first study the rate-dependent fracture of an elastic DCB where bulk dissipation is absent (Section 2.4.1). This section is intended to elucidate the rate-dependent interfacial behavior before introducing the complexity of bulk viscoelastic behavior. In Section 2.4.2 we introduce bulk viscoelasticity in order to see the combined bulk and interfacial dissipation.

2.4.1. *Elastic DCB*

Consider the case of an elastic DCB, which can be obtained by setting $\gamma_E = 1$. This simplification removes viscous dissipation from the bulk. Therefore rate dependency will only come from interfacial bond dissociation. Studying this case will allow us to directly address the interfacial rate dependence so that later when we introduce bulk viscoelasticity it will be easier to identify the contributions from each rate-dependent process. Returning to Eq. (2.6) it is clear that the two parameters V^* and γ_τ can be grouped into a single parameter V^*/γ_τ. Also for the elastic DCB Eq. (2.8) can be replaced with $M^* = d^2\delta^*/dx^{*2}$; hence V^* and γ_τ do not appear individually in the formulation. Therefore, we will obtain results by varying V^*/γ_τ over a large range of values.

First consider Figure. 2.2a) where the COD, $\delta^*(L^*)$, is shown on the *y*-axis and V^*/γ_τ is shown on the *x*-axis. At low V^*/γ_τ the crack opening is constant and there is no rate dependence. At high speed the COD appears to grow logarithmically. To understand these results, we note that when V^*/γ_τ is small the dissociation reaction, governed by Eq. (2.6), proceeds rapidly. Since the bonds dissociate so quickly the chains bridging the interface are not significantly stretched before the chain density becomes negligible. Hence, for small V^*/γ_τ the adhesive stress primarily comes from vdW attractions, represented by the last term in Eq. (2.9), which only depends on the crack opening and not on the rate of fracture. This is why there is no rate dependence at low speed as observed in Figure. 2.2a), and the constant COD value at small V^*/γ_τ corresponds to the critical vdW opening $\delta^*_{cr,vdW} = 4.605\delta_c^* = 0.092$ for the parameters used here. At a critical V^*/γ_τ(≈ 0.03 in Figure. 2.2a)), the COD starts to exhibit rate dependent behavior. This transition occurs because the dissociation reaction in Eq. (2.6) slows down when V^*/γ_τ increases so that when the COD reaches the critical vdW opening there is still a considerable number of chains bridging the interface. As a result, the location of the crack tip is now determined by the kinetics of bond rupture for the polymer chains. Further increases in V^*/γ_τ result in even greater chain stretch, and therefore crack opening, before dissociation. This phenomenon causes the rate dependency seen in Figure. 2.2a). It should be noted that until now we have only discussed how V^*/γ_τ in Eq. (2.6)

affects bond dissociation; however it is important to understand that bond dissociation is coupled to the beams deflection through the exponential term in Eq. (2.6). While an increase in V^*/γ_τ slows down bond dissociation and allows for increased chain stretch, this stretch increases the tensile force on each chain and each bond therein, leading to an increase in the rate of bond dissociation. This feedback limits the increase of the COD to be logarithmic, as seen in Figure. 2.2a).

Having noted that COD increases with V^*/γ_τ and greater COD implies that the chains have more stored energy, it is now of interest to consider the energy required to propagate a crack. For an elastic beam there is no bulk viscous dissipation so the only energy component is G_{ad}^* which is shown in Figure. 2.2b) as a function of V^*/γ_τ; the embedded figure contains the same G_{ad}^* only plotted against the COD data from Figure. 2.2a). As established during the discussion of Figure. 2.2a), for slow crack propagation the fracture is governed by the vdW attractions. The crack tip is located where the COD reaches the critical vdW opening, and within the adhesive zone the adhesive stress due to chain stretching is negligibly small. Hence, G_{ad}^* is equal to W_{vdW}^* at low speed, as shown in Figure. 2.2b). As V^*/γ_τ is increased the rate of bond dissociation decreases and allows the chains, on average, to reach a greater stretch and store more energy before dissociating. Since all of the energy stored in the chains is lost when the bonds dissociate, the larger V^*/γ_τ causes G_{ad}^* to increase; physically this means that a greater moment M_∞^* will be needed to propagate the crack. Although the energy dissipated by chains continuously increases as V^*/γ_τ is increased, G_{ad}^* remains approximately constant at W_{vdW}^* for $V^*/\gamma_\tau < 0.02$, which indicates that this energy needed to dissociate chain bonds remains negligible for a large range of slow crack propagation speeds.

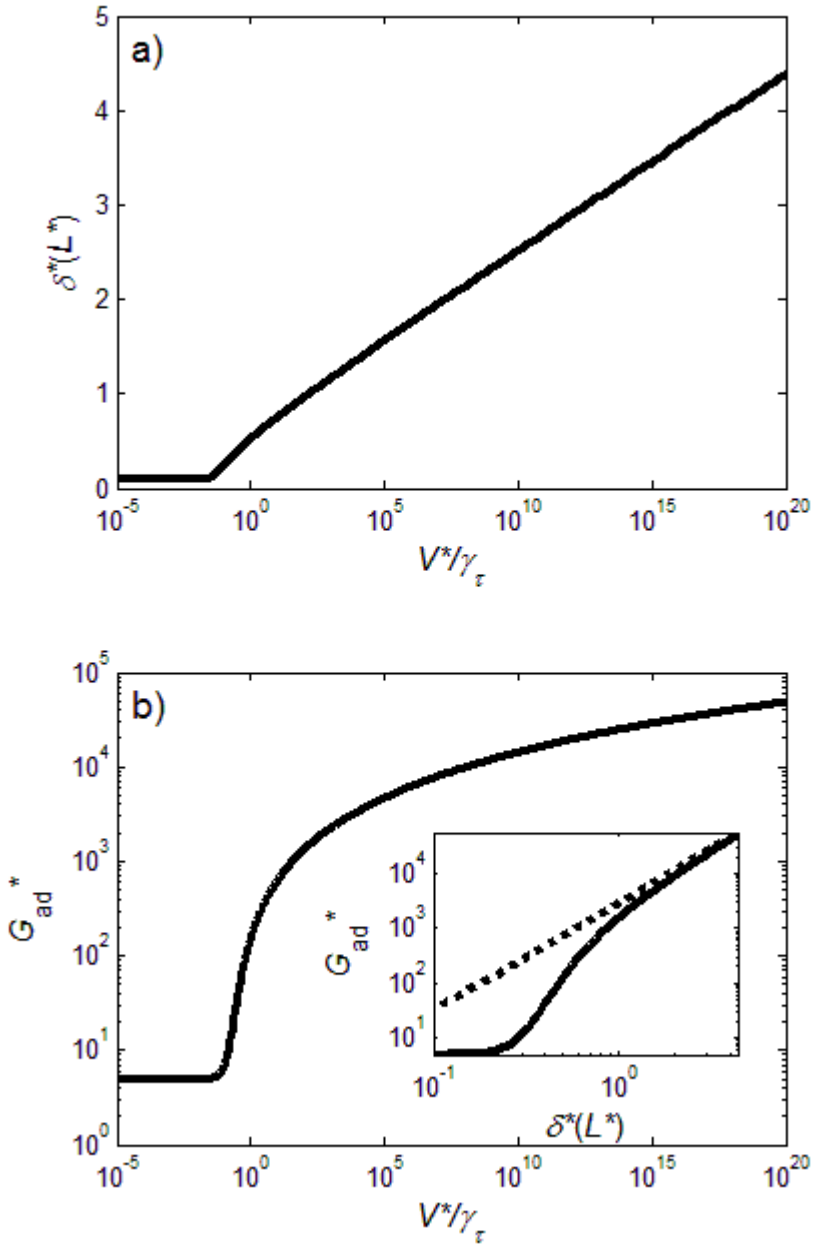

Figure. 2.2: Plots for a) crack opening displacement, $\delta^*(L^*)$, and b) adhesive fracture energy, G_{ad}^*, obtained by varying V^*/γ_τ while holding the other governing parameters fixed at $U^* = 2850$, $\gamma_E = 1$, $\gamma_L = 0.0022222$, $\delta_c^* = 0.02$ and $W_{vdW}^* = 5$. The embedded figure in b) plots G_{ad}^* against the $\delta^*(L^*)$ result from a) and the dotted line represents the analytical result based on a "reverse-step" distribution for the bond density.

It is of interest to study in detail how V^*/γ_τ impacts the bond density and adhesive stress within the adhesive zone, which is shown in Figure 2.3. In Figure 2.3a), the bond density is shown in the *y*-axis and position relative to the adhesive zone tip is shown on the *x*-axis. Four curves are shown each for a different value of V^*/γ_τ. In all cases, the bond density starts at 1 and decreases with position. For the lowest V^*/γ_τ value (0.01), the bond density decays exponentially. As V^*/γ_τ is increased the distribution increasingly resembles a reverse step where all of the bonds remain unbroken until the edge of the adhesive zone where all bonds break at once. To best understand this behavior it should be discussed in conjunction with Figure 2.3b) where the crack opening is plotted as a function of the position. In all cases the crack opening starts at zero and increases with position. Furthermore, at the same x^*/L^*, the magnitude of δ^* increases as V^*/γ_τ is increased. Consider the case of V^*/γ_τ = 0.01. The crack opening in Figure 2.3b) is very small throughout the adhesive zone. As a result the exponential term in Eq. (2.6) is negligible, so the bond density is expected to decay exponentially which is confirmed in Figure 2.3a). Extending this idea, for any V^*/γ_τ, at the beginning of the adhesive zone the crack opening is small; thus initially the exponential term in Eq. (2.6) can be neglected. In a semilog plot, such as Figure 2.3a), the initial slope of the bond density curves should be $-\gamma_\tau/V^*$, and hence higher values of V^*/γ_τ have an initial slope closer to zero. Further from the adhesive zone tip where higher openings are reached, the chain stretch decreases the activation energy and accelerates the bond dissociation process. This acceleration is more significant for larger V^*/γ_τ. These two features, i.e., near zero initial slope and accelerated bond dissociation at higher openings, result in the bond density distribution approaching a reverse step distribution as V^*/γ_τ becomes large. In the extreme case of $V^*/\gamma_\tau \to \infty$, an exact reverse step distribution is expected, and the same distribution exists for the so-called "rate independent" fracture [1], which was elucidated by considering the limit as the absolute temperature goes to zero. A consequence of the bond density distribution within the adhesive zone resembling a reverse step is that the adhesive stress, f^*, when plotted against the opening $\delta^*\left(x^*\right)$, will increasingly resemble a saw tooth as V^*/γ_τ becomes large. The adhesive stress vs. crack opening for different V^*/γ_τ can be seen in Figure 2.3c). At δ^* = 0 the stress

contributed by the chains is zero and the stress from vdW attractions is maximum. As the opening increases the vdW attractions decay, and each polymer chain is stretched so that the force F^* acting on it increases. The chain stress is $\Sigma_b^* F^*$, while the chain force F^* always increases with crack opening, the chain density Σ_b^* always decreases. This causes the adhesive stress to first increase with δ^* but eventually drop due to the rupture of polymer chain bonds.

Based on the above observations, an interesting result for G_{ad}^* can be obtained for the extreme case of $V^*/\gamma_\tau \to \infty$. In this limit, the bond density distribution is a reverse step function. Because the polymer chains remain intact within the adhesive zone, the distance over which the vdW stress is non-negligible is expected to be considerably smaller than the size of the adhesive zone. Therefore, as shown in Appendix 1.7, using the reverse step distribution for Σ_b^* and assuming $\delta_c^* = 0$ give a linear saw tooth distribution for the adhesive stress: $f^*(\delta^*) = 2U^*\delta^*$ up to $\delta^*(L^*)$. G_{ad}^* can then be derived in a closed form: $\left(G_{ad}^*\right)_{RS} = U^*\left[\delta^*\left(L^*\right)\right]^2 + W_{vdW}^*$ where $\left(G_{ad}^*\right)_{RS}$ is the adhesive fracture energy based on the reverse step bond density distribution. $\left(G_{ad}^*\right)_{RS}$ is plotted (dotted line) against the COD $\delta^*\left(L^*\right)$ in the embedded figure in Figure. 2.2b). Clearly the results of G_{ad}^* converge to $\left(G_{ad}^*\right)_{RS}$ when V^*/γ_τ and hence $\delta^*\left(L^*\right)$ is large. The COD $\delta^*\left(L^*\right)$ in Figure. 2.2a) shows logarithmic dependence on V^*/γ_τ at high speed, which can be written as $\delta^*\left(L^*\right) = \alpha \ln\left(\beta V^*/\gamma_\tau\right)$, α and β being constants. Introducing this results into $\left(G_{ad}^*\right)_{RS}$ gives the following expression

$$\left(G_{ad}^*\right)_{RS} = U^*\left[\alpha \ln\left(\beta V^*/\gamma_\tau\right)\right]^2 + W_{vdW}^*, \qquad (2.20)$$

which is in agreement with the high speed dependency of G on V, $G \sim \left[\ln(V)\right]^2$, previously reported in the literature [2, 3, 1] for fracture in elastic medium with rate-dependent interfacial process.

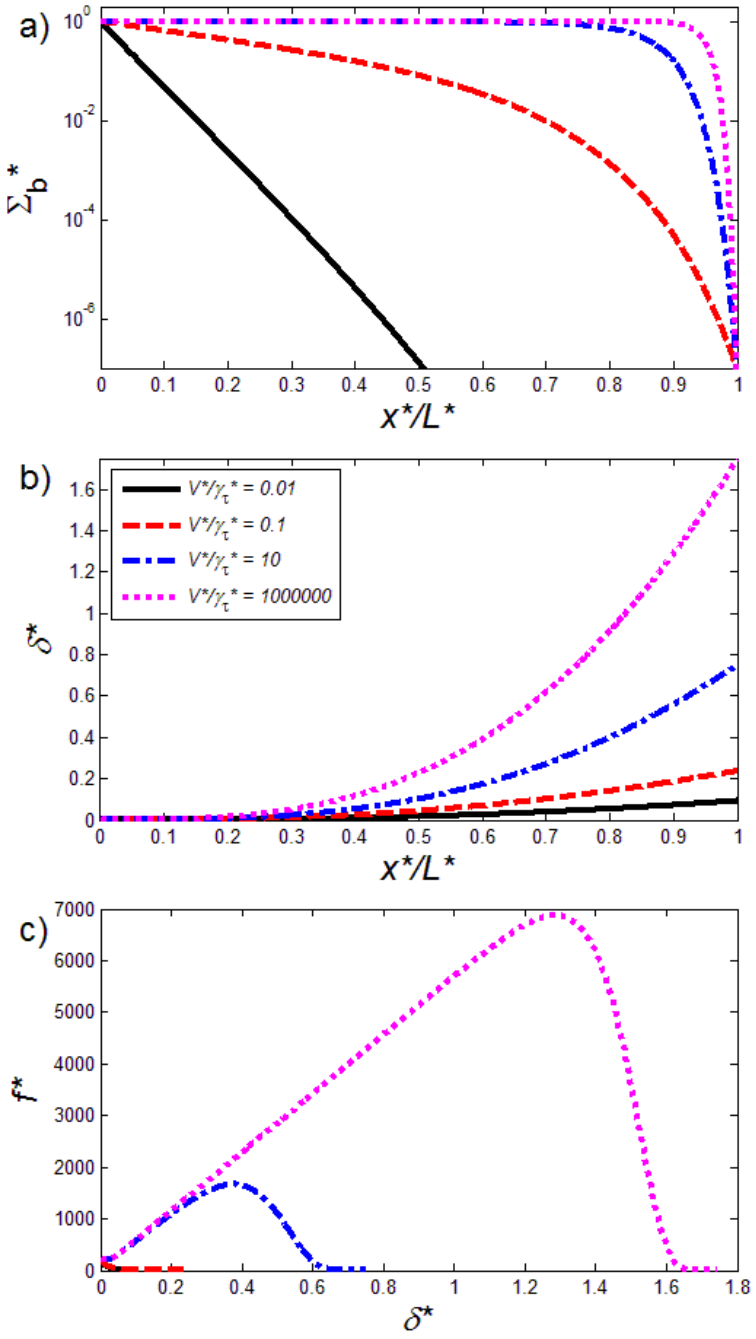

Figure 2.3: Plots for a) bond density Σ_b^*, b) crack opening δ^* and c) adhesive stress f^*. In each figure each curve represents a different value of V^*/γ_τ. Note that horizontal axis in b) and c) are x^*/L^*, where the adhesive zone length L^* for different curves would be different. Results were obtained while holding the following governing parameters fixed: $U^* = 2850$, $\gamma_E = 1$, $\gamma_L = 0.0022222$, $W_{vdW}^* = 5$ and $\delta_c = 0.02$.

2.4.2. *Viscoelastic DCB*

Now we consider results where bulk viscoelasticity is included by setting $\gamma_E = 0.01$. V^* is varied over a wide range of values and this process is repeated for five different values of γ_τ. As a complement to Figure. 2.2a) we first plot the COD against V^*/γ_τ in Figure 2.4. According to the normalization, Eq. (2.5), V^*/γ_τ is independent of the bulk relaxation time τ_o. The result is remarkably similar in behavior to Figure. 2.2a), only this time there are different lines corresponding to different values of γ_τ, the ratio of bulk relaxation time over the characteristic time for chain dissociation. With this choice of x-axes, the curves for different γ_τ nearly collapse which suggests that γ_τ primarily functions as a speed shift in Eq. (2.6). Only minor differences can be observed for a limited range of V^*/γ_τ. This region has been enlarged in the embedded figure. The interfacial kinetics is coupled to beam deformation through the adhesive tractions from the polymer chains, yet compared with the elastic beam, Figure. 2.2a), and over several orders of magnitude of γ_τ we observe only small differences. These differences are due to relaxation of the beams' effective modulus, and will be discussed later. Distributions of bond density and adhesive stress for a representative viscoelastic beam are shown in Appendix 1.8.

Although the influence of bulk viscoelasticity on COD appears to be minimal, when we consider the work needed to propagate the crack, G^*, bulk viscoelasticity is much more important. For a viscoelastic beam, there is dissipation within the beam which can increase for longer beams as mentioned previously. Here we have chosen to evaluate G^* at $x^* = 1$, which corresponds to a DCB with a fixed length that is larger than, but on the same order of magnitude as, the adhesive zone length L^*. In Figure 2.5a) the results for $G^*(1)$ are plotted against V^*/γ_τ. In the embedded figure the same $G^*(1)$ data is plotted against V^*. As in Figure 2.4 each curve represents a different value of γ_τ. The main graph bears some resemblance to Figure. 2.2b) but now the behavior is non-monotonic with each curve peaking at a different value of V^*/γ_τ. As Figure 2.5a) is not trivial to understand, we decompose G^* according to Eq. (2.18) and discuss the two components: G_{ad}^*, shown in Figure 2.5b), and G_{vis}^*, shown in Figure 2.5c).

Starting with Figure 2.5b), where G_{ad}^* is plotted on the y-axis and V^*/γ_τ is shown on the x-axis. In the embedded figure the same G_{ad}^* data is plotted against V^*. Unlike G^*, outside of the adhesive zone there will be no further contributions to G_{ad}^* so the result of G_{ad}^* is independent of

the chosen beam length. First by comparing Figure 2.5a) and Figure 2.5b) the contribution from G_{ad}^* is significant. In addition, very much like the COD, not only does the behavior of G_{ad}^* closely resemble what was seen for the elastic case (Figure. 2.2b)), but all the curves corresponding to different γ_τ nearly collapse onto a master curve with only slight differences observed for a limited range of V^*/γ_τ. This implies that changing γ_τ primarily acts like an effective speed shift in the bond dissociation equation, Eq. (2.6). γ_τ does not appear in the beam equation, Eq. (2.8), and the fact that the speed is not shifted by γ_τ in the beam equation suggests that bulk viscoelasticity seems to have only a second-order impact on bond dissociation and the adhesive portion of the fracture energy. We will return to these second order effects, seen in Figure 2.4 and Figure 2.5b), after we examine the viscous portion of G^*.

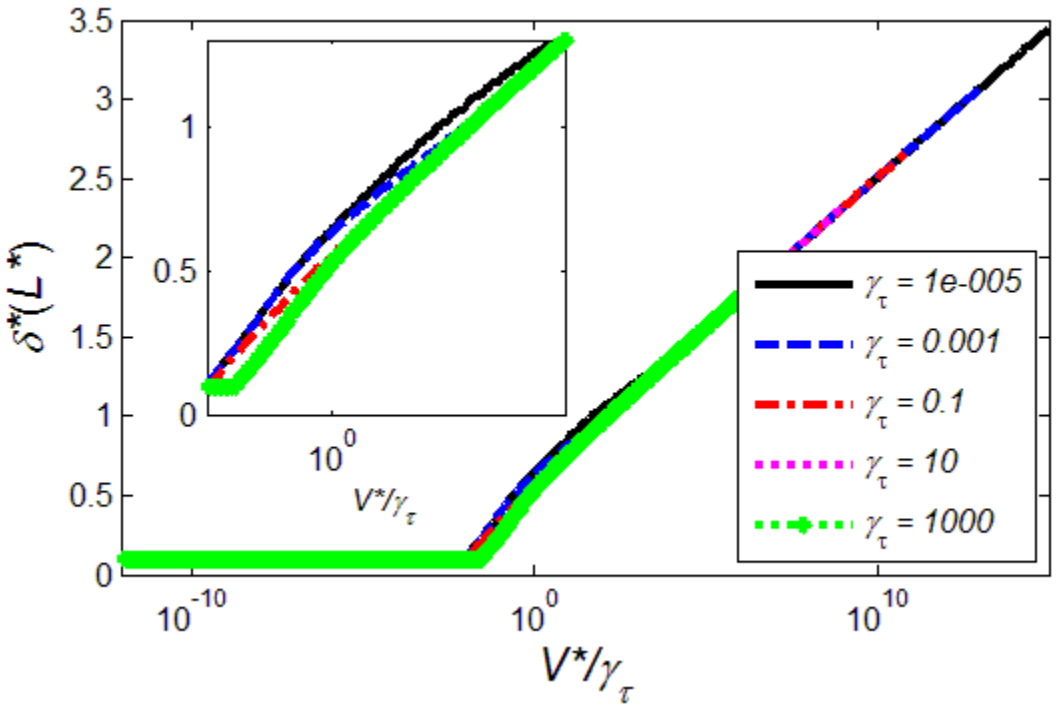

Figure 2.4: Crack opening displacement, $\delta^*(L^*)$, plotted against V^*/γ_τ. This plot was obtained by varying V^* while keeping γ_τ fixed at the five values shown in the legend. The other governing parameters were held fixed at $U^* = 2850$, $\gamma_E = 1$, $\gamma_L = 0.0022222$, and $W_{vdW}^* = 5$. The embedded figure is zoomed in on the region around $V^*/\gamma_\tau = 1$ to better show details.

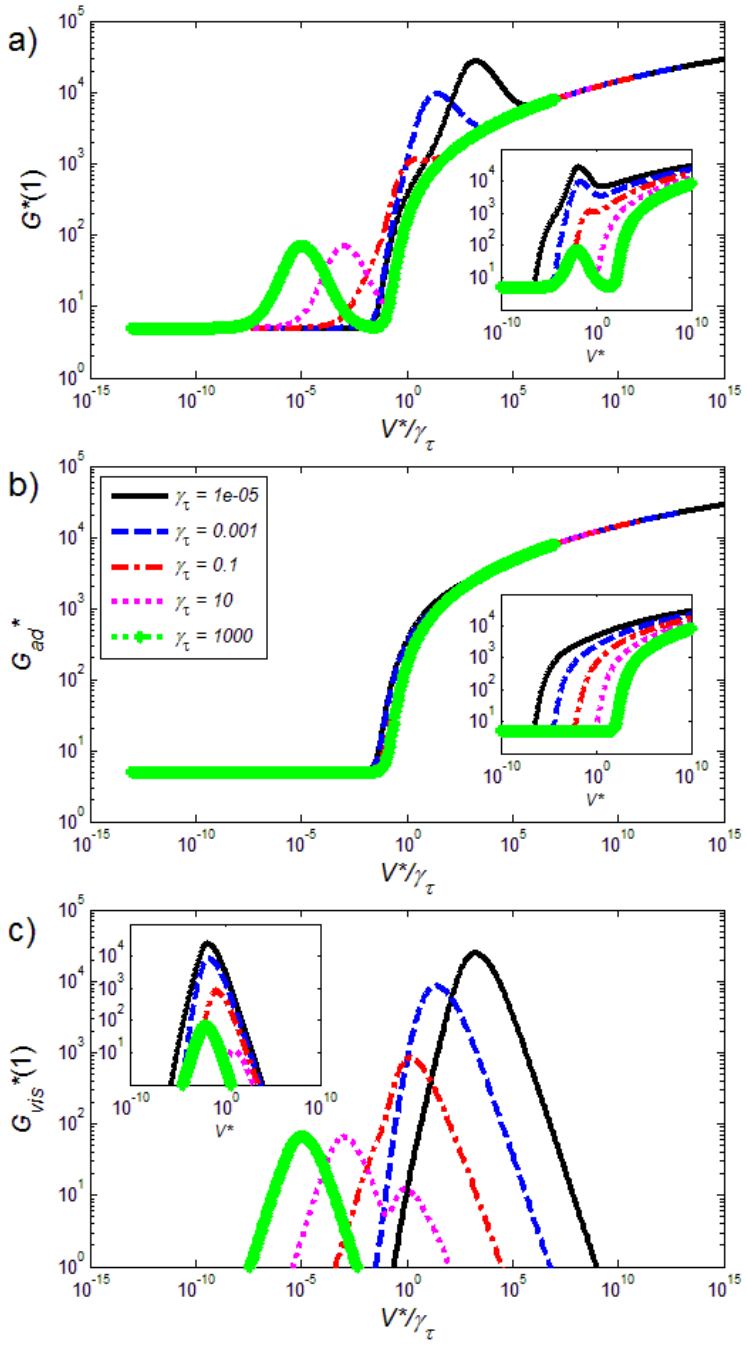

Figure 2.5: Plots for a) total fracture energy $G^*(1)$*, b) adhesive fracture energy* G_{ad}^* *and c) viscous dissipation* $G_{vis}^*(1)$*, plotted against* V^*/γ_τ*. These plots were obtained by varying* V^* *while keeping* γ_τ *fixed at the five values shown in the legend. The other governing parameters were held fixed at* $U^* = 2850$, $\gamma_E = 1$, $\gamma_L = 0.0022222$, *and* $W_{vdW}^* = 5$. *Embedded figures shows the same data plotted against normalized crack propagation speed* V^*.

Consider the portion of G^* from bulk viscous dissipation shown in Figure 2.5c). Here $G_{vis}^*(1)$ is shown on the *y*-axis, V^*/γ_τ is shown on the *x*-axis and each curve represents a different value of γ_τ. G_{vis}^* comes from the beam viscoelasticity, which is governed by Eq. (2.8) where γ_τ does not appear. Hence γ_τ does not directly impact the results of G_{vis}^*, and the normalized crack speed V^* would be a more suitable choice for the *x*-axis as shown in the inset of Figure 2.5c). The behavior of $G_{vis}^*(1)$ is as follows. It approaches zero for both small and large V^*. Between these two limits there is a maximum, with the lowest values of γ_τ achieving the highest peak. These peaks are higher since V^*/γ_τ is larger and so is the associated crack opening (Figure 2.4) which results is greater deformation and hence dissipation. Comparing Figure 2.5c) and Figure 2.5a), it is clear that the peaks in Figure 2.5a) are caused by viscous dissipation.

To understand the viscous dissipation we make an analogy to an elastic beam and define a local effective modulus E^* so that $M^*(x^*) = E^*(x^*)d^2\delta^*/dx^{*2}$. Like G^* and G_{vis}^* the effective modulus varies with position so to compare with $G^*(1)$ we have plotted $E^*(1)$ on the *y*-axis and V^* on the *x*-axis in Figure 2.6a). The behavior is simple: at low V^*, $E^*(1) = \gamma_E$, and as V^* is increased there is a transition to another plateau at high V^* where $E^*(1) = 1$. Physically this transition means that when the crack propagates slowly there is sufficient time for the beam to fully relax and the modulus decays to the infinite time value. When the crack propagates rapidly, within the fixed length under consideration, the beam has not yet had sufficient time to relax at all so the effective modulus is still the zero time modulus. Between these two extremes there is a viscoelastic transition. Comparing Figure 2.6a) and Figure 2.5c) it is clear that this transition occurs over the same speed range as the nonzero G_{vis}^*. To explain the behavior observed in Figure 2.5c), consider that as the beams deflect to open the crack they acquire strain energy from the work done by applied moments. However as the effective modulus of the beams relaxes, the strain energy stored in the beams is reduced even with a fixed deflection. This difference in strain energy is lost as viscous dissipation. At low speed negligible energy is lost because the beams relax to the infinite time modulus before there is any deflection or stored strain energy. Conversely at high crack propagation speed the beams deflect and have stored strain energy, however here the beams have not yet relaxed so viscous dissipation is again negligible. A consequence of this is that at high speed within the adhesive zone the beam is essentially elastic. Therefore, at very large V^*/γ_τ, G_{ad}^*

and $G^*(1)$ approach $\left(G^*_{ad}\right)_{RS}$ which was discussed earlier for the elastic beam and shown in the inset of Figure. 2.2b).

Interestingly, for $\gamma_\tau = 10$ two peaks in $G_{vis}^*(1)$ can be seen in Figure 2.5c). The first peak can be attributed to the transition of E^* as discussed above. The second peak appears as V^* exceeds the critical value where the COD begins to increase above $\delta^*_{cr,vdW}$ (Figure 2.4). The increased COD and beam deformation causes higher dissipation before eventually the unrelaxed limit shown in Figure 2.6 is reached. This second increase in dissipation also results in the asymmetry visible for $\gamma_\tau = 0.1$ and 0.001 in Figure 2.6c).

One interesting observation made from Figure 2.6 is that there is little difference between the $E^*(1)$ curves for different values of γ_τ. Pending a thorough explanation for this, we will use the E^* data in Figure 2.6 to discuss the slight deviations between the curves for different γ_τ seen in Figure 2.4 and Figure 2.5b). In Eq. (2.6) changing γ_τ is equivalent to a speed shift, however γ_τ does not appear in the beam equation (Eq. (2.8)). If we consider the actual speed V^* rather than the shifted speed V^*/γ_τ, as in the embedded figure in Figure 2.5b), at the same V^*/γ_τ we observe that curves for smaller γ_τ would be translated to lower speed. Since at lower V^* the effective modulus of the beam is smaller which lowers its flexural rigidity, the beam provides less resistance to crack opening. As a result, at the same V^*/γ_τ, for smaller γ_τ and hence smaller V^* the effective modulus is lower and therefore, the crack opening is slightly larger, as seen in Figure 2.4. Since the chains have been stretched slightly more G_{ad}^* is also slightly larger as seen in the embedded figure of Figure 2.5b). In Appendix 1.9 we discuss the relaxation of E^* outside of the adhesive zone and the length of the dissipative zone relative to the adhesive zone.

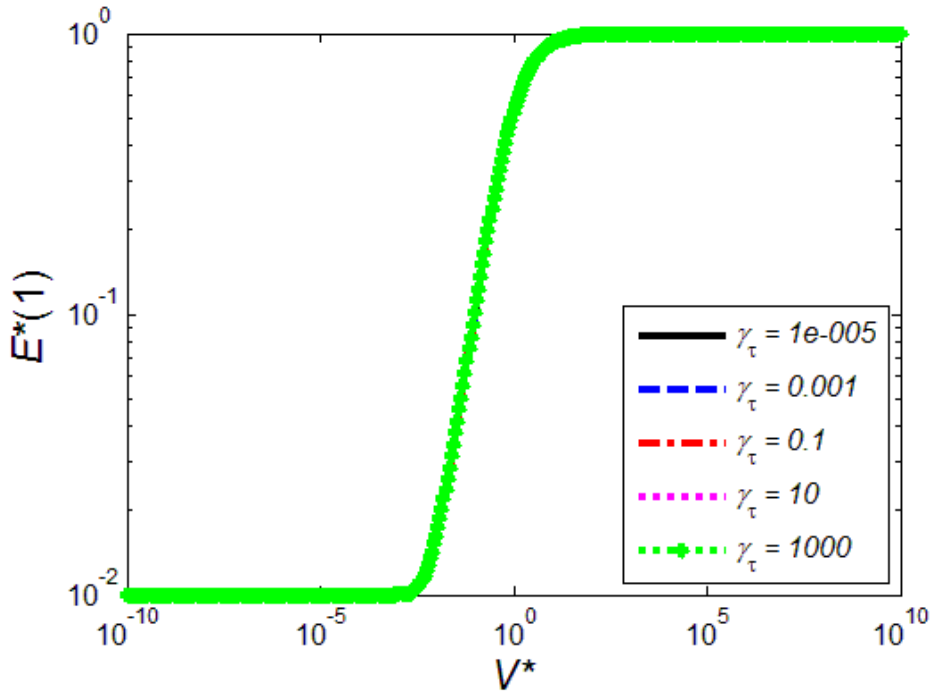

Figure 2.6: Effective Young's modulus, $E^*(1)$*, plotted against* V^**. These plots were obtained by varying* V^* *while keeping* γ_τ *fixed at the five values shown in the legend. The other governing parameters were held fixed at* $U^* = 2850$, $\gamma_E = 1$, $\gamma_L = 0.0022222$, *and* $W^*_{vdW} = 5$.

So far we have qualitatively explained the results of our model and have taken several steps, either through literature comparison (see Appendix 1.10) or by examining limits, to verify that a correct numerical solution to the governing equations has been obtained. Qualitatively our results match several other works in the literature. For example for a viscoelastic beam of fixed length it has been reported that G_{vis} is zero at high and low speed and has a critical speed where it is maximum [15], much like what was observed in Figure 2.6b). It has been experimentally observed that G increases with crack propagation speed [8], and G_{ad} displays this same character (Figure 2.5b)). However, introducing coupled bulk and interfacial rate-dependence allows the model to explain or predict behavior not previously possible. For example, Figure 12 of [3] reported the rate dependency of fracture energy of silicone elastomers against an acrylic pressure-sensitive adhesive from rolling contact experiments. The fracture energy was shown to be significantly enhanced by introducing small amounts of H-bonding groups to increase the

interfacial relaxation time without substantially increasing the surface energy. In addition, the fracture energy changed from nearly rate-independent to strongly rate-dependent upon the addition of H-bonding groups on the interface. In terms of our model the addition of H-bonding groups would be described by an increase in τ-, which in turn leads to a decrease in γ_τ. Consulting the inset of Fig. 5c) where the bulk viscous dissipation is plotted against the crack speed, as γ_τ decreases from 10 to 0.001, the peak $G_{vis}^*(1)$ value increases from approximately 60 to 8000; on a linear scale the former would appear rather rate insensitive in comparison to the latter case. This observation is qualitatively similar to the experimental observation of [3]. Because our model has two characteristic time scales (one for bulk relaxation, and another for bond dissociation), an effective speed shift in G_{ad} can be created by varying the ratio of these two relaxation times. Furthermore, the coupling of bulk and interfacial rate dependence resulted in complex non-monotonic behaviors of G for finite sized beams (Figure 2.5a)). This behavior has the potential to offer much more flexibility in designing adhesive of a desired strength.

Often in viscoelastic fracture experiments the fracture energy G is expressed in the following form [3, 8, 11, 13, 15, 22]

$$G = W_o\left(1 + f(V)\right), \tag{2.21}$$

where W_o is the thermodynamic work of adhesion for separating the two surfaces under equilibrium conditions [3] (also referred to as the intrinsic strength [13], and $f(V)$ represents the increase in fracture energy for finite rates of crack propagation. The function $f(V)$ has been described as the energy dissipated in the material at the propagating crack tip [13], the enhancement in strength when the adhesive is imperfectly elastic [11], or the energy expended in irreversible processes [8]. However it is not fully understood which physical processes this function represents [8]. It has been shown that the function depends not only on the micromechanical properties of the interface and viscoelastic properties of the bulk material but also on the specimen dimensions [15]. In addition it has been proposed that the micromechanical properties of the interface must also be rate dependent [22], as is the case in the model presented in this work where interface kinetics are considered. To connect the results of our model to Eq. (2.21), we note that in our model as V approaches zero $W_o = W_{vdW}$. It then follows that $f(V) = \left(G - W_{vdW}\right)/W_{vdW}$ which can be obtained by vertically shifting and scaling Figure 2.5a).

The fact that $W_o = W_{vdW}$ as $V \rightarrow 0$ implies that to separate the two beams under equilibrium condition, one only needs to overcome the vdW attractions, while no energy is needed to break the polymer chains.

To explain this seemingly unrealistic result consider Eq. (2.6) where it can be seen that even if the force F^* on each chain is zero, the bond dissociation rate will be non-zero (i.e., the chain will break) unless the speed is very high. This implies that given enough time all bonds in the material would dissociate under zero load, which may be unphysical. This deficiency is directly due to the interfacial model we adopted in Eq. (2.6) which has been used in the literature several times [1, 2 3]. Rate equations have been written with the addition of a bond association term [2; 3], however this term was assumed to be negligible. While it is true that bond association quickly becomes negligible as the crack opens, at low speed very small crack openings were observed and bond reforming can play an important role. Taking this into account can increase the bond density and G_{ad}^* at low speed.

To address another limitation of the present work, recall that the normalized crack opening was defined as $\delta^* = \delta / L_c$ where L_c is the contour length of the polymer chain. Given this definition physically within the adhesive zone we should have $0 \le \delta^* \le 1$. However, the COD was observed to be near 4.5 at high speed in Figure. 2.2a) and Figure 2.4. In other words, the model allows the crack to open too far at high speeds and this will over-predict G_{ad}^* in these cases. The source of this deficiency is likely the linearized force-extension relationship of the polymer chain as proposed in the literature [2, 3]. The notion of a nonlinear chain model has been explored [1, 3]. Tensile experiments on polymer chains show a force extension curve which is very flat for most of the extension but increases rapidly before the chain is fully stretched and fails [3]. Taking into account this behavior should have two important effects on the model presented. First, the chain forces F^* at extensions near $\delta^* = 1$ would be much higher and through Eq. (2.6) would cause the chains to break before $\delta^* = 1$. Secondly, at low extensions the force acting on the chain would be much less, which combined with bond reforming would prevent the chain density from going to zero at small crack openings when the crack propagation speed is small.

Finally, it was observed that changing γ_τ over several orders of magnitude only created small changes in the effective modulus. A possible reason is the bulk viscoelastic beam model we have

adopted. For a viscoelastic beam there is only one stress component and it is in the axial direction which is perpendicular to the direction of the extension of polymer chains. That is, there is no viscoelastic relaxation of the material in the direction of chain extension. Therefore, we expect that implementing higher dimensional continuum viscoelastic models could lead to stronger coupling between the bulk and interfacial rate processes and is a subject of future research.

2.5. Conclusion

In this work, the rate dependent fracture of a viscoelastic double cantilever beam (DCB) is studied. Two sources of rate dependence were considered. The beam itself was assumed to be a standard linear solid and an interfacial adhesion model describing the kinetics of breaking polymer chains was used. Within the adhesive zone, van der Waals (vdW) attractions were also considered. Seven nondimensional parameters governing the fracture of the DCB were identified, among which the impact of the V^* (normalized crack propagation speed) and γ_τ (ratio of bulk relaxation time to bond dissociation relaxation time) on the energy required to propagate the crack were discussed in detail. The apparent energy release rate G^* is made up of two components: the energy needed to overcome adhesion (G_{ad}^*), and viscous dissipation within the bulk material (G_{vis}^*). G_{ad}^* increases with crack propagation speed, whereas G_{vis}^* is negligible for both small and large crack propagation speeds and has a maximum value at an intermediate V^*. The net result from the two dissipation mechanisms is that G^* varies non-monotonically with the crack propagation speed. A closed-form scaling relation between G^* and V^* was derived for very fast crack propagation. The relaxation time ratio γ_τ was shown to primarily function as a speed shift in affecting G_{ad}^*.

2.6. Nomenclature

Note Non-dimensional parameters are summarized in Table 2.1

δ	Crack opening
δ_c	is a characteristic decay length
D	Depth of beam
ε	is strain
E	Young's Modulus
E_o	the instantaneous or unrelaxed modulus
E_∞	is the infinite time or relaxed modulus
E_a	activation energy
f	Distributed adhesive stress
$f(V)$	increase in fracture energy for finite rates of crack propagation
F	is the tensile force acting on each chain
G	Fracture energy
h_p	is Plank's constant
I	Area moment of inertia
k_B	is the Boltzmann constant
k_s	is the average spring stiffness
λ	is the bond activation length
L_c.	contour length
M	Bending Moment
n	is the number of bonds per polymer chain
σ	stress
S	Shear force
Σ_b	is the number of chains that cross a unit area of the interface
Σ_o	is the chain density for perfectly bonded interface
τ_o	is the bulk relaxation time
τ-	is the characteristic time of bond dissociation
t	time
T	is the absolute temperature
U	is the work required to stretch the chain from its unstressed configuration to its contour length
V	Crack propagation speed
W_{vdW}	is the work of adhesion due to vdW attractions
W_o	is the thermodynamic work of adhesion for separating the two surfaces under equilibrium conditions
x, y	Coordinates translating with crack tip
X, Y	Fixed Coordinates

Chapter 3. An Adhesive Zone Model for Polymeric Interfaces[2]

Abstract

In this work we develop an adhesive zone model for polymeric interfaces, which describes the kinetics of dissociation and association of polymer chains bridging the interface. Compared with previous works on interfacial bond rupture, our adhesive zone model includes two novel features: possibility of bond reforming and a highly nonlinear force-extension relationship for the polymer chain motivated by previous experimental measurements. The absence of these two features was demonstrated in an earlier work to cause unphysical crack propagation under zero load as well as overextension of the chains beyond their full contour length. Using the rate dependent crack propagation in a double cantilever beam, which may be elastic or viscoelastic, as an example, the new adhesive zone model is shown to correct the unphysical results obtained earlier. Specifically, it leads to a significantly increased adhesive fracture energy, i.e., the energy per unit area required to rupture the chains on the interface, for slow crack propagation, owing to the ability to achieve a dynamic equilibrium of bond dissociation and association. Furthermore, the nonlinear chain model predicts a near-catastrophic decrease in chain density as the finite extensibility limit is approached. This results in an adhesive fracture energy which is orders of magnitude smaller than that predicted by the linear chain model for fast crack propagation. Although the adhesive zone model has only been applied to a double cantilever beam in this work, it is a generic model for polymeric interface, and can be implemented in finite element models to simulate fracture in bulk polymers in general.

[2] A version of this chapter has been published. Reprinted with permission from Lavoie, S. R.; Long, R. Tang, T. "An adhesive zone model for polymeric interfaces" Int J Fract (2016) 197: 169. https://doi.org/10.1007/s10704-016-0073-2 Copyright 2016 Springer

3.1. Introduction

The fracture of polymeric materials typically exhibits rate-dependent characteristics [16], which, at the molecular level, involves reorientation of macromolecules as well as the stretching and scission of bonds or crosslinks on polymer chains [2]. These molecular processes can lead to significant rate-dependence of the macroscopic fracture behavior which is not yet fully understood [8]. For example, previous experiments suggest that the energy needed to fracture polymeric materials depends on the rate of mechanical loading and can be correlated to the speed of crack propagation [2, 3, 8, 10]: the fracture energy increases with crack propagation speed [1, 8]. Experiments on rubber adhesives lead to the conclusion that the apparent fracture energy consists of the intrinsic fracture energy (thermodynamic work of adhesion for equilibrium separation of two surfaces)[11, 13] and additional energy dissipation which can be further divided into dissipation components in the bulk material [8, 15, 16] and in rupturing bonds which bridge the crack interface [1, 2, 3, 15].

Bulk dissipation in viscoelastic materials has been considered in several theoretical works. The standard linear solid model has been applied to analyze the debonding of a double cantilever beam (DCB) [15] and fracture of an infinite viscoelastic solid [17]. Newer models can account for additional rate dependent microscopic mechanisms such as scission and reforming of polymer networks [20, 21]. The bulk dissipation is found to be proportional to the thermodynamic work of adhesion [3]. Although such an approach is useful in decoupling bulk and interfacial processes, it was proposed by Rahulkumar *et al* [22] that a rate dependent interfacial model was needed to match computational and experimental results for the peeling of polybutadiene elastomer sheets.

Several approaches have been taken to develop a model which captures the interfacial rate dependence in viscoelastic fracture mechanics. For example, an adhesive zone model was implemented based upon a Newtonian fluid in which the crack opens when the normal traction on the interface exceeds a cut-off value [15, 17]. Chaudhury [2] proposed a different approach where a rate equation was written to describe the dissociation kinetics of bonds bridging an interface following the theoretical framework proposed by Bell [31]. This framework was originally developed for kinetic association and dissociation of ligands and receptors in cell adhesion and the concept of mechanochemistry (i.e., mechanical activation of covalent bonds) [32] was introduced to capture the effect of mechanical forces on the chemical kinetics. The interfacial rate equation proposed by Chaudhury [2] has been applied to cases with different crack opening profiles,

including a wedge-like linear profile [3], more realistic profiles based on linear elasticity [1], and crack profiles determined from elastic or viscoelastic beams [6]. It must be noted that the general form of the rate equation proposed by Chaudhury [2] also included a term for bond association between two polymer chain fragments, however this term was neglected to create a special case of the kinetic model; similarly in all previous adhesive zone models bond reforming has been neglected [1, 3, 6].

At first glance, the neglect of bond reforming is reasonable, as the rate of reforming polymer fragments quickly diminishes as the stress on the interface increases. However, when the rate equation without bond reforming was applied to the fracture of a standard linear solid (viscoelastic) DCB [6], it was found that complete bond dissociation can occur, if given enough time, without a tensile force applied on the polymer chains. As a result, in the limit of very slow crack propagation, the polymer chains would rupture even under zero stress and hence the intrinsic failure energy of the material would only be due to van der Waals (vdW) attractions, in contradiction to previous observations [13]. We believe this unphysical result is exactly due to the lack of bond reforming in the rate equation, which becomes comparably important to bond dissociation at low crack propagation speed. Therefore, a step towards being able to more accurately describe the fracture of polymeric media requires an adhesive zone model which can predict dynamic association and dissociation of bonds for polymer chains under a tensile load. The practical applications of such a model would extend beyond fracture mechanics, and bears the potential to be used for self-healing materials [33]. As will be described in this paper, when two separate surfaces are placed in contact, the model could predict an increase in bond density towards an equilibrium value along the interface—effectively joining the materials.

Another important issue to be addressed in this work is the force-extension relationship of the polymer chains bridging the interface. Such a relationship is necessary in order to couple the rate equation of the chains to the crack profile. In the past, for the sake of mathematical convenience, the force on a chain has been assumed to be linearly proportional to the chain extension. A direct consequence of the linear model is that for high crack propagation speeds the crack opening displacement predicted could significantly exceed the contour length of the chain bridging the fracture plane [6], which is unphysical. To overcome this deficiency, we propose that the chains can stiffen significantly near its full extension, which is described by a highly nonlinear force-extension relationship.

This paper proceeds as follows. An adhesive zone model incorporating bond dissociation and nonlinear chain behavior is presented in section 3.2. We demonstrate the application of this adhesive zone model for elastic and viscoelastic DCB geometry in section 3.3. Conclusions are given in section 3.4.

3.2. The Adhesive Zone Model

3.2.1. *Rate Equation*

Classical stress or energy based fracture criteria cannot explain why the fracture energy is rate dependent and this phenomenon has typically been attributed to bulk viscoelasticity [13, 11]. On the other hand, subsequent studies showed that chemical kinetic processes at the interface may also play a role [2, 3, 1]. Reaction rate theory has been used to model the breaking of bonds in cellular adhesion [31], and in dynamic rupture of individual polymer chains [29]. Our starting point will be the rate equation for bond rupture proposed by Chaudhury [2]

$$-\frac{d\Sigma_b}{dt} = \frac{n}{\tau_-} e^{F\lambda/k_BT}\Sigma_b - \frac{1}{\tau_+} e^{-E_c/k_BT}\left(\Sigma_o - \Sigma_b\right). \quad (3.1)$$

where Σ_b and Σ_o - Σ_b are the number of polymer chains in the bonded and unbonded states per unit area of the interface, respectively. Σ_o is the total number of chains per unit area on the interface. τ_- and τ_+ are the characteristic times of bond dissociation and association respectively. F is the tensile force applied to a bond, E_c is the elastic spring energy required to stretch two relaxed (unstressed) polymer chain fragments on opposite sides of the interface so that they make contact, n is the average number of bonds per polymer chain, λ is the activation length of the bond (0.1-3nm for some biopolymers [2]), k_B is the Boltzmann constant, and T is temperature in Kelvin. The two terms on the right hand side are respectively the rates of dissociation and association. The rate of dissociation is multiplied by the Lake and Thomas [10] amplification factor, n, which appears because all bonds on the chain are stretched however only one bond needs to dissociate for the chain to be ruptured. The rate of dissociation of a single bond is proportional to $e^{F\lambda/k_BT}/\tau_-$, i.e. it is accelerated when a tensile force acts on the bond. τ_- is given by [2] $\tau_- = h_P e^{E_a/k_BT}/k_BT$ where h_P is the Planck's constant, and E_a is the activation energy of bond dissociation. By combining the above expressions it can be seen that the factor $F\lambda$ effectively causes a decrease in the

activation energy for bond dissociation and hence an increase in the dissociation rate. It should be noted that kinetic model presented above is based on the transition state theory of Eyring [3]; however, it has been shown that the tensile force F can alter λ [29]. There are more advanced models which consider dissociation as a diffusion process [3, 34, 35] and can overcome this shortcoming. However, these models are more complex and involve many parameters whose values yet need to be obtained from experiments, so the authors will defer their use for future research.

The rate of association term is proportional to $e^{-E_c/k_BT}/\tau_+$. Because contact is required before association, E_c effectively increases the activation energy of association. Under zero load and at zero surface separation, the number of intact chains crossing a unit area, Σ_{b0}, can be obtained by considering equilibrium where $d\Sigma_b/dt$, F and E_c all vanish, which gives the following expression

$$\Sigma_{b0} = \Sigma_o/(1+n\tau_+/\tau_-). \quad (3.2)$$

Σ_{b0} will be hereafter referred to as "the initial bond density", i.e., bond density before any surface separation. It is an effective measure of the relative magnitude of bond association and dissociation rates: high initial bond density corresponds to relatively large bond association rate and/or small bond dissociation rate.

Past works on rate dependent fracture using Eq. (3.1) have typically neglected the bond reforming term [1, 2, 3, 6]. This is based on the assumption that as mechanical stress is applied and the interface separates, the rate of association quickly becomes negligible in comparison to the rate of dissociation. However, the primary problem which stems from this simplifying assumption is that for the case of equilibrium, or infinitely slow, crack propagation the polymer chains provide no resistance. In the rate dependent fracture of viscoelastic materials the fracture energy G is often expressed by the following relationship [3, 8, 11, 13, 15]

$$G = W_o(1+\phi(V)) \quad (3.3)$$

where W_o is the equilibrium fracture energy or "intrinsic strength" of the material and $\phi(V)$ represents the rate dependent increase in fracture energy due to dissipative processes. Without the consideration of bond reforming, Eq. (3.1) reduces to $-d(\ln\Sigma_b)/dt = ne^{F\lambda/k_BT}/\tau_- = (nk_BT/h_P)e^{(F\lambda-E_a)/k_BT}$, which suggests that even under zero force (F

= 0), Σ_b will decrease leading to spontaneous rupture of all the polymer chains crossing an interface (if given enough time). In other words, when the crack propagation is infinitely slow (V approaches 0), without reforming the polymer chains do not contribute to the intrinsic strength W_o, which is unphysical.

3.2.2. *Nonlinear force-extension relationship*

The force applied to each bond, F, and the energy required to stretch two polymer fragments to contact, E_c, can be obtained from the force-extension relationship for the polymer chains. In the literature, the force-extension relationship was often assumed to be linear [2] so that the chains behave as linear springs [1, 2, 3] $F = k_s\delta$. However, experiments on single polymer chains [3] have shown that the force-extension relationship is highly nonlinear. For low extension the chain elongation corresponds primarily to uncoiling of the polymer chain, and elasticity of the chain originates from change in the configurational entropy. However, once the chain length approaches the contour length (L_c), which represents the length of the polymer chain when fully extended, additional extension requires bonds on the polymer chain to be stretched, resulting in much higher stiffness. Obviously a linear spring model is not able to capture such stiffening behavior, and the choice of a linear model was purely for the ease of mathematical analysis. To extract the "effective stiffness", k_s, of the linear chain model, the usual approaches include obtaining the value as a fitting parameter to match experimental fracture energy vs crack propagation speed data [2], or matching $\int_0^{L_c} F(\delta)d\delta$ to U, which is the work done on the chain in stretching it to its contour length [1] and can be determined from experiments. A direct result of this approach is that the effective stiffness of the linear spring is an overestimate at small stretch and an underestimate at large stretch. Therefore, a very small interfacial separation will cause the effective activation energy for bond dissociation to significantly decrease and that for bond association to significantly increase. Consequently, bond association quickly becomes negligible for a linear polymer chain model. Conversely for large interfacial separation, the lack of stiffening can lead to unrealistic chain extensions larger than the full contour length.

To provide a more accurate description of the force-extension relationship, we start with experimental work which has shown that a persistence chain model [3] provides an excellent representation of the nonlinear force-extension relationship for individual polymer chains up to a fractional extension of 90%:

$$F(\delta) = \frac{k_B T}{P}\left[\frac{1}{4}\left(1-\frac{\delta}{L_c}\right)^{-2} - \frac{1}{4} + \frac{\delta}{L_c}\right], \quad \frac{\delta}{L_c} \le 0.9 \qquad (3.4a)$$

,

where δ is the extension of the chain, usually taken to be the interfacial separation between the two surfaces. P is the persistence length, which is related to the contour length by $L_c = nA \approx 2nP$ with $A \approx 2P$ [36] being the Kuhn length of the polymer. The persistence chain model is only valid for δ less than 90% of the contour length. For $\delta / L_c > 0.9$ we will approximate the force-extension relationship as a quadratic function of δ / L_c. The quadratic function is the simplest function that allows us to satisfy three conditions we deemed necessary. The first two are continuity of force and "stiffness", $k = dF / d\delta$, at $\delta / L_c = 0.9$. A previous work [1] using a linear function beyond 90% extension did not match the stiffness at $\delta / L_c = 0.9$ and resulted in an unphysical kink in the force-extension curve. For the third condition we match the energy of the chain when stretched to its contour length to U as defined earlier. The quadratic function that satisfies these 3 conditions was found to be:

$$F(\delta) = 3000\left(\frac{U}{L_c} - 7.5\frac{k_B T}{P}\right)\left(\frac{\delta}{L_c} - 0.9\right)^2 + 501\frac{k_B T}{P}\left(\frac{\delta}{L_c} - 0.9\right) + 25.65\frac{k_B T}{P}, \quad \frac{\delta}{L_c} > 0.9 \qquad (3.4b)$$

.

An example of the nonlinear force-extension relationship, given by Eq. (3.4) and presented in a normalized form, is shown in Figure 3.1. The experimental data by Ghatak et al. [3] for extensions above 90% are also presented in Figure 3.1, which shows good agreement; Eq. (3.4a) is known to be a good fit for experimental data [3] so to prevent cluttering of Figure 3.1 experimental data from its range of applicability is not shown. To understand the magnitude of the change in the chain stiffness, consider the chain stiffness at zero extension, $k_o = dF / d\delta(0) = 3k_B T / 2PL_c$ and compare it with the chain stiffness at $\delta / L_c = 0.9$, $k(0.9L_c) = 501k_B T / PL_c = 334k_o$. Up to 90% extension, the stiffness has increased by a factor of 334 and will continue to increase, more rapidly, as δ / L_c exceeds 0.9.

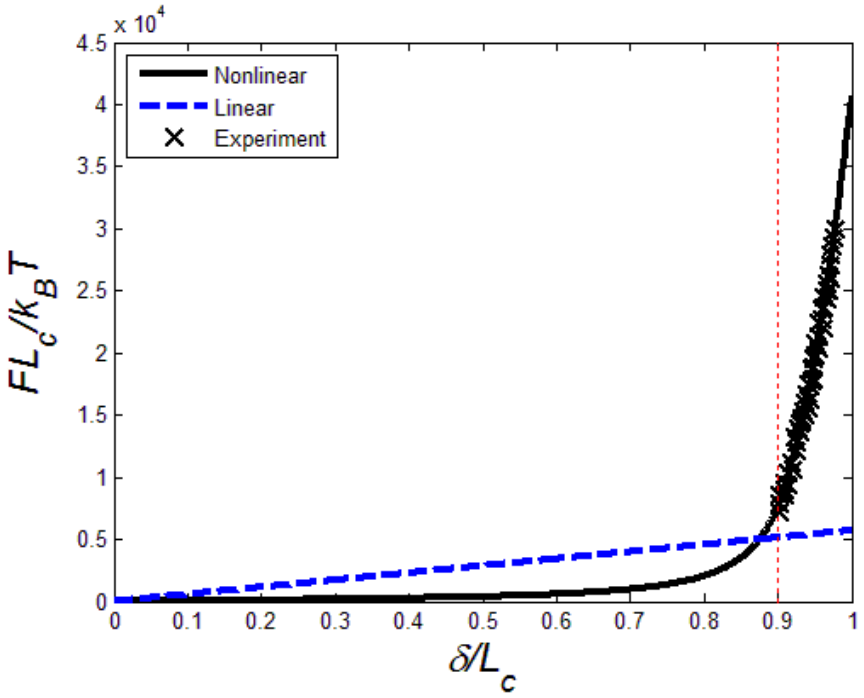

Figure 3.1: Normalized polymer chain tensile force $F^* = FL_c/k_BT$ plotted against normalized extension $\delta^* = \delta/L_c$, for linear and nonlinear chain models. Experimental data was taken from Ghatak et al. [3] where $n = 150$. $U^* = U/k_BT$ is determined to be 2850 by using data from Ghatak et al. [3]

The elastic energy required to stretch two polymer chain fragments from their relaxed state to form contact, E_c, can be determined from

$$E_c(\delta) = \int_0^{\delta} F(\mu)d\mu, \qquad (3.5)$$

using the force-extension relationship given in Eq. (3.4) or the linear counterpart. To understand this equation, firstly we note that the relaxed state corresponds to extension of zero, whereas the state at which bond reforming occurs corresponds to extension of δ. Secondly, although this equation appears to be written for the extension of a single chain, the same result can be obtained if the extensions of two separate chain segments are considered. In that case, the separation δ should be divided and assigned to the two chain segments in proportional to their contour lengths, and the force F would be same for the two chains.

With the rate equation and force-extension relationship described in sections 3.2.1 and 3.2.2, the adhesive zone model is furnished and can be applied to study surface separation and crack propagation.

3.2.3. *Application to equilibrium surface separation*

Consider two surfaces that are initially bonded and then separated in a very slow (quasi-static) manner so that at each interfacial separation δ they can be considered as in equilibrium. We now apply the adhesive zone model introduced above to the interface and study this separation process. Inclusion of bond reforming in Eq. (3.1) allows for the chain density to approach a dynamic equilibrium value $\Sigma_{be}(\delta)$ at each interfacial separation (= chain extension) δ, when the rates of bond association and dissociation are in balance; i.e. $d\Sigma_b / dt = 0$ in Eq. (3.1). As the chain extension increases the tensile force applied to each bond increases the rate of dissociation and decreases that of association. Therefore, as the chain extension is increased the equilibrium density, shown in Figure 3.2a) in the normalized form, decreases from the initial value Σ_{b0}^{*} at zero opening and after a certain point becomes negligible.

Shown in Figure 3.2a) are results using both the nonlinear chain model (bold) and linear chain model (thin lines) with constant stiffness determined from the approach discussed in section 3.2.2. The behavior is qualitatively similar but quantitatively different. For the nonlinear chain model the equilibrium density becomes negligible when the fractional extension of the chain, δ^{*}, exceeds ~0.16. Whereas for the linear chain model, the density becomes negligible at a much lower δ^{*} (~0.05). For these small extensions the linear chain model has a much higher stiffness which results in significantly higher chain tension (Figure 3.1). This causes the shift in activation energies (decrease in effective activation energy for bond dissociation and increase in effective activation energy for bond association) to be more dramatic for the linear chain model which leads to a more rapid decrease in the equilibrium chain density as the chain extension increases.

The adhesive stress from the chains can be calculated from $\sigma_{ch} = \Sigma_b F$, namely the product of the chain density and the tensile force in each chain, for the case of equilibrium separation this stress is plotted against separation in Figure 3.2b). Here we see that stress is zero at zero separation (since the chains are unstretched) however as the separation increases the stress increases, reaches a maximum and then decreases to zero. The decrease is caused by the rupture of chains shown in Figure 3.2a). For the range of extensions shown in Figure 3.2b) the linear chain model has a larger

spring stiffness (slope of Figure 3.1), which results in a faster increase in stress as well as a larger peak stress.

A second source of adhesive stress is from the vdW attractions. Numerous forms have been used in the literature to model vdW interactions, however, for fracture of polymeric interfaces the vdW interactions are considered to have a much smaller zone of action than the polymer chains. Under such a situation, the detailed form of the vdW interaction has been shown to be unimportant as long as the maximum stress and the work of adhesion are similar [1]. Therefore, a simple form for the vdW component of the adhesive stress will be used: $\sigma_c e^{-\delta/\delta_c}$ where δ_c is a characteristic decay length, and σ_c is the maximum vdW stress. Note that the vdW attractions are rate independent and depend only on the surface separation δ. Combining the two components gives the following expression for the total adhesive stress

$\sigma_{ad} = \Sigma_b F \ + \sigma_c e^{-\delta/\delta_c}$.	(3.6)

The maximum vdW stress σ_c can be replaced by $\sigma_c = W_{vdW} / \delta_c$ by recognizing that the vdW work of adhesion follows from $W_{vdW} = \int_0^\infty \sigma_c e^{-\delta/\delta_c} d\delta = \sigma_c \delta_c$.

Now consider the process of separating the two surfaces slowly from $\delta = 0$ to $\delta \to \infty$ where they no longer interact. Energy is required for this process to break the polymer chains on the interface and overcome vdW attractions between the two surfaces. The intrinsic strength of the interface can be calculated from

$W_o = \int_0^\infty \Sigma_{be} F d\delta + W_{vdW}$,	(3.7)

where $\int_0^\infty \Sigma_{be} F d\delta$ would be the area under curves in Figure 3.2b). In other words, the existence of equilibrium bond density allows for the polymer chains to contribute to the intrinsic strength and enhance the fracture energy for slow surface separation. The intrinsic strength, in normalized form, is shown in Figure 3.2c) as a function of the normalized initial chain density Σ_{b0}^*. Here we see that increasing Σ_{b0}^*, which corresponds to faster bond association and/or slower bond dissociation, results in higher intrinsic strength. In addition, the nonlinear chain model gives larger intrinsic strength than that of the linear chain model. However, the difference is small since that

the higher stiffness of linear chain model at small surface separation compensates for its lower chain density.

While we have applied the adhesive zone model to equilibrium surface separation, the same can be done to model the joining of two surfaces in self-healing materials. In surface separation problems, initially the interface has zero opening and the bond density is given by Eq. (3.2). Whereas for interface healing, the two surfaces are brought into contact with zero initial bond density. Over time the bond density will increase according to the kinetics of Eq. (3.1), and ultimately reach the zero separation equilibrium value (Eq. (3.2)) if left long enough. Applying conditions such as heat can alter the activation energies for bond association and dissociation which may result in faster healing kinetics; for example decreasing the activation energy for association will decrease the association time constant, τ_+, and from Eq. (3.1) result in a faster rate of increase in bond density.

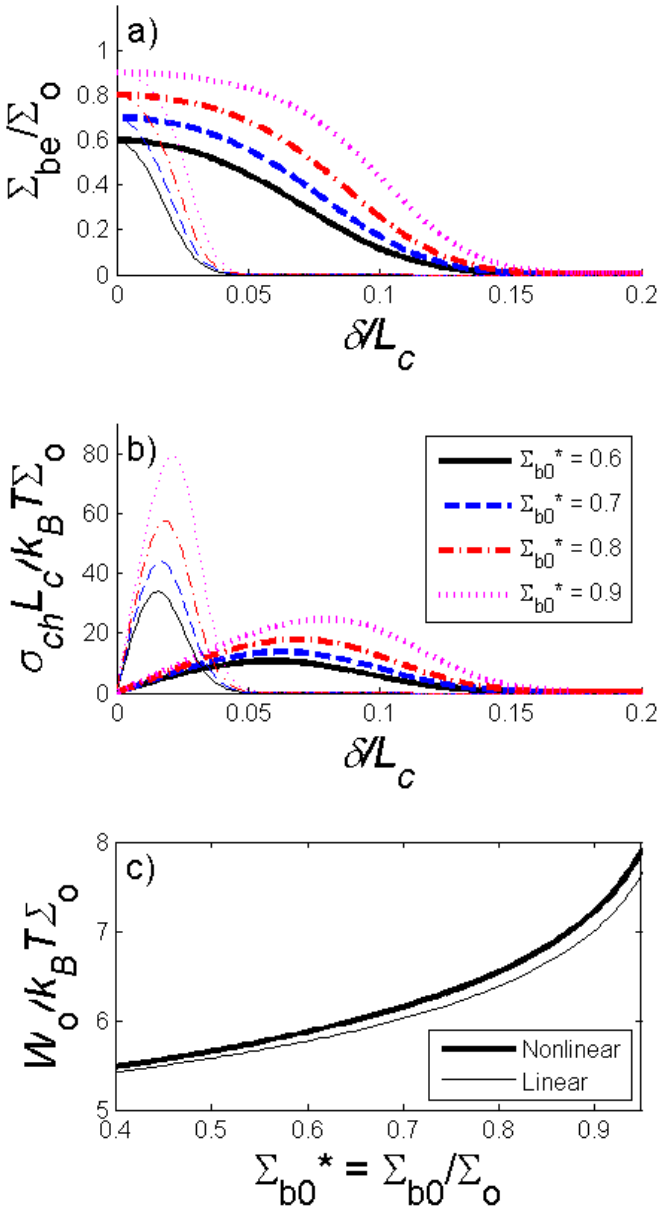

Figure 3.2: a) Normalized polymer chain density under equilibrium, $\Sigma_{be}^* = \Sigma_{be}/\Sigma_o$, plotted against $\delta^* = \delta/L_c$, for different initial bonded density, Σ_{b0}^*. b) Normalized equilibrium adhesive stress from polymer chains, $\sigma_{ch}^* = \sigma_{ch} L_c/k_BT\Sigma_o$, plotted against $\delta^* = \delta/L_c$, for different initial bonded density, $\Sigma_{b0}^* = \Sigma_{b0}/\Sigma_o$. The thick curves represent results from the nonlinear chain model and the thin lines represent results from the linear chain model. c) Normalized intrinsic strength $W_o^* = W_o/k_BT\Sigma_o$ plotted against initial bonded density $\Sigma_{b0}^* = \Sigma_{b0}/\Sigma_o$. These plots were generated by varying extension δ^* while holding the other governing parameters fixed at $U^* = U/k_BT = 2850$, $\gamma_L = \lambda/L_c = 2.222 \times 10^{-3}$, $n = 150$ (for nonlinear models), and $W_{vdW}^* = W_{vdW}/k_BT\Sigma_o = 5$ [6]

3.2.4. *Application to dynamic surface separation*

When the adhesive zone model is applied to very slow surface separation as in section 3.2.3, there is sufficient time to reach equilibrium for each separation δ. However, for fast surface separation the system falls out of equilibrium and the kinetic term $d\Sigma_b / dt$ in Eq. (3.1), describing the change in chain density, will have an important impact. The decrease in chain density is accelerated by the activation energy shift ($F\lambda / k_B T$ in Eq. (3.1)). In addition, unlike equilibrium, for fast separation bond association will be negligible due to the large activation energy needed to stretch and rejoin two ruptured chain segments. Figure. 3.3a) shows the chain density plotted against separation for several values of surface separation speed, v. Compared with equilibrium surface separation, where the chain density drops rapidly from its initial value with increasing opening and becomes negligible before the fractional extension reaches 20% (see Figure 3.2a)). Under the opposite limit of rapid crack growth the chain density will remain close to constant for some openings (e.g., beyond 80% extension when $v^* = vL_c/\tau_- = 100$) and then catastrophically decrease once a certain opening is reached (Figure. 3.3a)) [6]. The bonds are able to survive to larger chain extension at higher speed because at a given chain extension the bond dissociation reaction proceeds at a certain rate. For faster separation a given extension will be reached in less time which will allow for fewer bonds to dissociate.

The impact of the survival of chains to larger separations on the adhesive stress can be seen in Figure. 3.3b). Unlike Figure 3.2b) the stresses in Figure. 3.3b) contain contributions from both the chains and vdW attractions. The vdW attractions decay with separation and result in the initial decrease in adhesive stress observed at small extension Figure. 3.3b). Recall that under equilibrium separation the continuous decrease in chain density combined with the increase in polymer chain tension with separation created a non-monotonic adhesive stress from the polymer chains (Figure 3.2b)). At low speed the rate dependent adhesive stress due to chains approaches the equilibrium result. As the speed of separation increases more polymer chains will survive to larger extensions and hence the adhesive stress at the same extension becomes larger. As pointed out above, in the high speed limit the chain density remains close to constant and then catastrophically decreases. Therefore, before the catastrophic decrease occurs, the adhesive stress distribution would resemble the polymer chain force-extension relationship shown in Figure 3.1. This is followed by a sharp decrease in the adhesive stress due to the loss of bridging chains. With

increasing separation speed, the plateau region in Figure. 3.3a) extends to larger δ^*, and as a result, the location of the peak adhesive stress in Figure. 3.3b) shifts to the right. The overall increased magnitude of adhesive stress and the larger range of δ^* for which the adhesive stress is non-zero will lead to larger energy dissipated on the interface when it is separated at higher speed.

The adhesive fracture energy, G_{ad}, is calculated by determining the work done by the adhesive stress, σ_{ad}, or

$$G_{ad} = \int_0^\infty \sigma_{ad} d\delta = \int_0^\infty \Sigma_b F d\delta + W_{vdW}. \quad (3.8)$$

Eq. (3.8) differs from the intrinsic strength Eq. (3.7) in that the bond density Σ_b depends on the rate of separation rather than being Σ_{be}, the value at infinitely slow separation. G_{ad} therefore is rate dependent and can be much larger than the intrinsic strength. Numerically, it is impossible to integrate the adhesive stress to infinity, so a cut-off value is usually introduced for δ^* beyond which the adhesive stress is negligible.

Figure. 3.3 also shows the comparison between the linear and nonlinear chain models. Similar to equilibrium surface separation, the two models give different results for fast separation. Since F increases rapidly at openings near L_c for the nonlinear chain model (Figure 3.1), so does the rate of chain rupture as chain extensions approach the contour length, and at higher separation speeds the peak stress will occur at a normalized separation which approaches 1 (for example vL_c/τ = 10 and 100 in Figure. 3.3b)). Whereas for the linear chain model the stiffness does not increase and increasing vL_c/τ always creates a significant increase in the interface separation where the peak stress occurs.

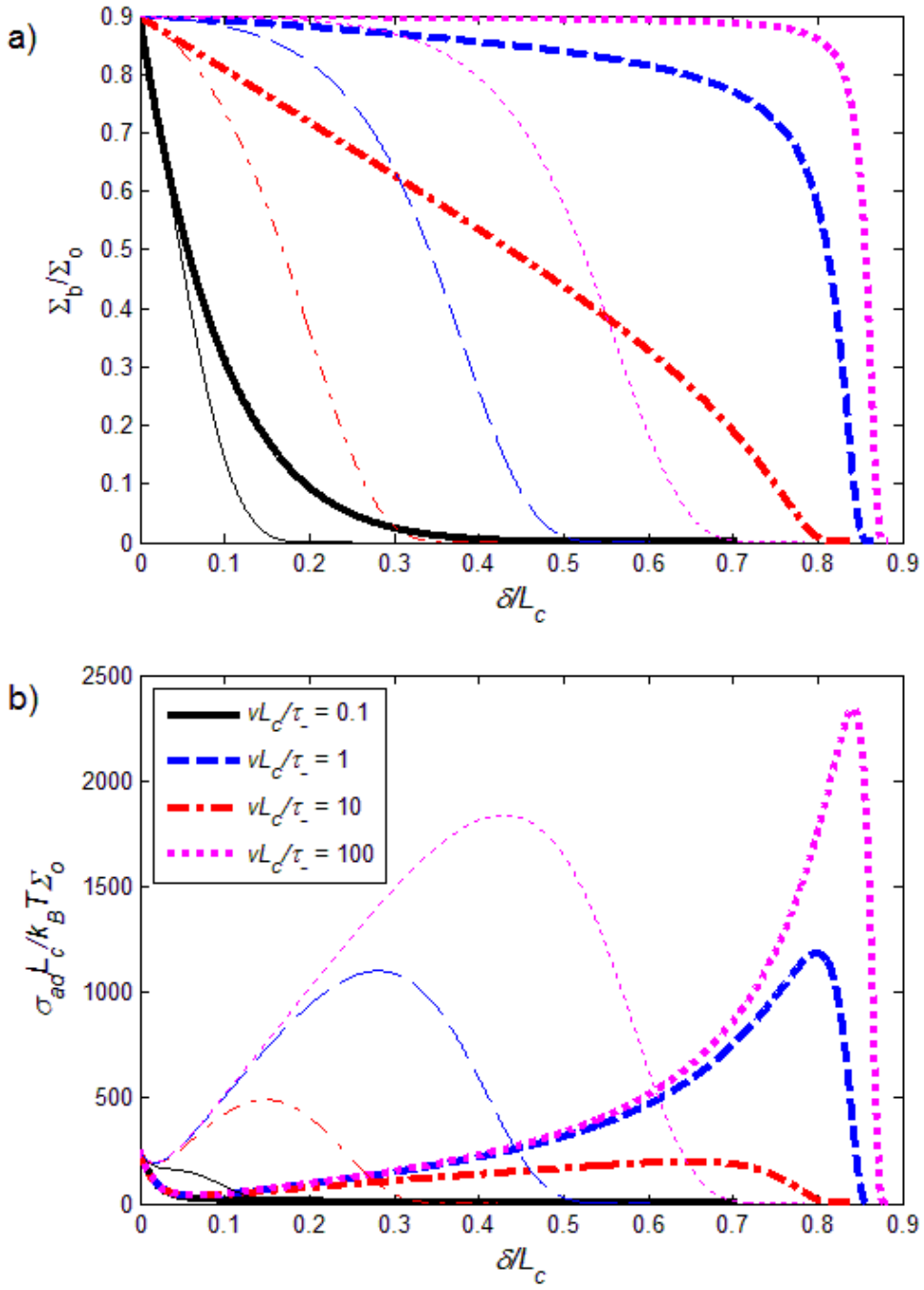

Figure. 3.3: a) Normalized polymer chain density Σ_b/Σ_o plotted against normalized extension $\delta^* = \delta/L_c$ and b) Normalized adhesive stress $\sigma_{ad}L_c/k_BT\Sigma_o$ plotted against normalized extension $\delta^* = \delta/L_c$, for different normalized separation speeds vL_c/τ_-. These plots were generated, using the adhesive zone model with bond reforming, by varying extension δ/L_c while holding the other governing parameters fixed at $\Sigma_{b0}^* = \Sigma_{b0}/\Sigma_o = 0.9$, $U^* = U/k_BT = 2850$, $\gamma_L = \lambda/L_c = 2.222 \times 10^{-3}$, $n = 150$, $\delta_c/L_c = 0.02$ and $W_{vdW}^* = W_{vdW}/k_BT\Sigma_o = 5$. Thick lines are for nonlinear chain model and thin lines are for linear chain model

3.3. Example: Double Cantilever Beam

To demonstrate the use of the adhesive zone model in fracture, we consider the steady-state propagation of a crack at a constant speed V which splits a material into the DCB shown in Figure 3.4. The crack propagation is driven by moments M_∞ applied on the two identical beams, which may be elastic or viscoelastic, each with moment of inertia I and depth D into the page. Their separation is resisted by tension in the stretched polymer chains and van der Waals (vdW) attractions, described by the adhesive zone model presented in section 2. The same physical problem was studied in an earlier work [6], but without the consideration of bond reforming or a nonlinear force-extension relationship for the chains. Therefore, comparison to the previous results will allow us to address the advantages of the new adhesive zone model and how it will impact the fracture behavior.

The adhesive zone begins at the adhesive zone tip (point O) and extends till the crack tip where the magnitude of the tractions decrease below a prescribed tolerance. The so-determined effective adhesive zone length will be denoted by L. The work needed to propagate the crack must be sufficient to overcome these adhesive tractions and in the case of a viscoelastic beam bulk dissipation as well. Analysis will be conducted within a translating coordinate system (x-y) at the adhesive zone tip, which moves at speed V relative to a fixed coordinate system (X-Y). Taking advantage of the steady-state assumption, the vertical distance δ between the beams depends only on position x, and the transformation, $\partial / \partial t = V \partial / \partial x$, within the translating coordinate system can be applied. The problem possesses symmetry about the crack interface (line o_1-o_2) so that the analysis only needs to be done on one of the beams.

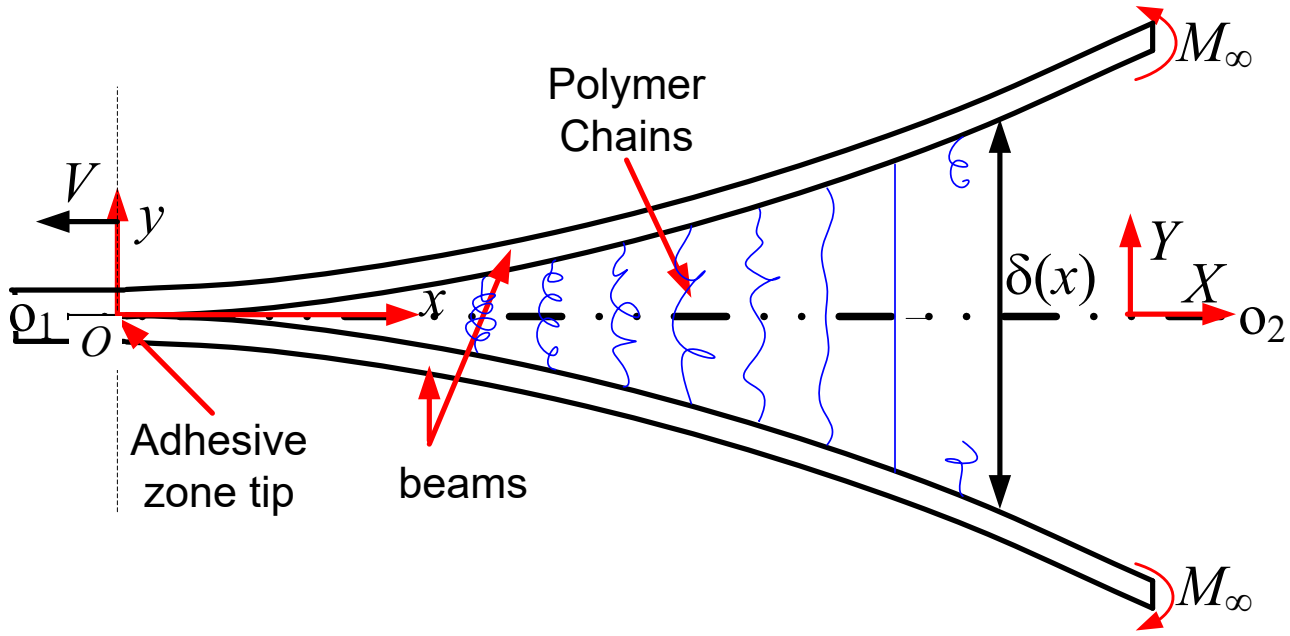

Figure 3.4: Schematic of the DCB debonding problem

The beams are modeled as either linearly elastic or viscoelastic; in the latter case a standard linear solid model is adopted where the Young's modulus decays from an instantaneous value of E_o to a long term value of E_∞ according to a relaxation time τ_o. The linearly elastic beams can be regarded as a special case of viscoelastic beams with $E_o = E_\infty$. For viscoelastic beams with the adhesive zone model described in section 3.2 there are 18 independent governing parameters. In Appendix 2.1, nondimensional variables and governing equations are presented. The associated non-dimensionalized boundary conditions to complete the boundary value problem are given in Appendix 2.2. This nondimensionalization reduced the number of governing parameters from 18 to the following 9:

$$V^* = \tau_o V\left(\frac{2k_B T\Sigma_o D}{E_o I L_c^2}\right)^{1/4},\ \gamma_E = \frac{E_\infty}{E_o},\ \gamma_\tau = n\frac{\tau_o}{\tau_-},\ \gamma_L = \frac{\lambda}{L_c},\ U^* = \frac{U}{k_B T},\ n,\ \Sigma_{b0}^* = \frac{\Sigma_{b0}}{\Sigma_o},$$
$$\delta_c^* = \frac{\delta_c}{L_c},\ W_{vdW}^* = \frac{W_{vdW}}{k_B T\Sigma_o}. \qquad (3.9)$$

The physical interpretations of the parameters shown in Eq. (3.9) are respectively: normalized crack propagation speed, ratio of long term to instantaneous modulus for the viscoelastic beam,

ratio of bulk relaxation time to interfacial bond dissociation time, ratio of bond activation length to contour length of a polymer chain, normalized rupture energy of a polymer chain, number of Kuhn lengths per polymer chain, normalized equilibrium areal density of load bearing polymer chains at zero crack opening (capturing association kinetics, see Eq. (5)), normalized vdW decay length, and normalized vdW work of adhesion. In addition there are several nondimensional quantities that will be calculated from the analysis

$$L^* = L\left(\frac{2k_BT\Sigma_oD}{E_oIL_c^2}\right)^{1/4},\ \delta^* = \frac{\delta}{L_c},\ G^* = \frac{G}{k_BT\Sigma_o},\ G_{ad}^* = \frac{G_{ad}}{k_BT\Sigma_o},\ G_{vis}^* = \frac{G_{vis}}{k_BT\Sigma_o}, \quad (3.10)$$

which are respectively the normalized adhesive zone length, normalized chain extension (separation between beams), normalized fracture energy, normalized adhesive portion of fracture energy, and normalized bulk viscous dissipation portion of fracture energy. The energy required to propagate a unit crack area, G^* after normalization, in a viscoelastic material consists of two contributions: the energy needed to overcome adhesive attractions on the interface, G_{ad}^*, and the viscous energy dissipation within the bulk material, G_{vis}^*, or

$$G^* = G_{ad}^* + G_{vis}^*. \quad (3.11)$$

G^* can be directly determined from the results of the analysis using $G^*(x^*) = 0.5M^*d^2\delta^*/dx^{*2}$ [6]. G_{ad}^* is evaluated from Eq. (3.8) and the bulk dissipation, G_{vis}^*, is obtained indirectly by subtracting G_{ad}^* from G^* according to Eq. (3.11). The numerical procedure used to solve the boundary value problem is described in Appendix 2.3.

The discussion below is divided into two main sections. In Section 3.1 we apply the adhesive zone model to an elastic DCB and, by comparison to models without bond reforming and nonlinear chain elasticity [6], the effect of these two features is evaluated. In Section 3.2 we apply the adhesive zone model to a viscoelastic beam in order to investigate the coupling between interfacial and bulk rate dependent behaviors.

3.3.1. *Elastic Beam*

3.3.1.1. *Effect of Bond Reforming and Nonlinear Chain Model*

To address the effect of bond reforming and nonlinear force-extension relationship in the new adhesive zone model, we first consider elastic beams where bulk viscous dissipation is absent. For comparison we have solved four cases where: (i) the linear chain model is used without bond

reforming, studied previously [6] (ii) the nonlinear chain model is used without bond reforming (iii) the linear chain model is used with bond reforming and (iv) the complete adhesive model with both the nonlinear chain model and bond reforming. Figure 3.5 shows the results obtained from the four models, generated by varying V^*/γ_τ, which is independent of bulk relaxation time, over a wide range while keeping the other governing parameters fixed. The crack opening displacement (COD), $\delta^*(L^*)$, and adhesive fracture energy, $G_{ad}{}^*$, are plotted against V^*/γ_τ in Figure 3.5a) and Figure 3.5b) respectively. The COD represents the distance between the two beams at the edge of the adhesive zone which indicates the maximum polymer chain extension reached within the adhesive zone.

In the COD results, Figure 3.5a), starting from small V^*/γ_τ we see that all the curves are horizontal which indicates rate independence. As V^*/γ_τ is increased there is a rapid increase in $\delta^*(L^*)$. Afterwards, the slope of COD versus V^*/γ_τ becomes smaller. Having observed the general rate dependent characteristics of the COD, we can now discuss how bond reforming and a nonlinear force-extension relationship impact the results. For small V^*/γ_τ the rate independence of COD indicates that the tractions in the adhesive zone primarily consists of vdW interactions (in absence of bond reforming), and the additional tension in the chains under equilibrium (if reforming is considered). Except for the case with both nonlinear chain and bond reforming, which has a low-speed plateau value of 0.27, the other three cases all have a smaller plateau COD value of 0.092. If the chains were completely removed from the adhesive zone model leaving only the vdW attraction, the adhesive stress would become negligible at a COD value of 0.092. This is easy to understand for cases (i) and (ii) as without bond reforming, at small V^*/γ_τ the contribution from chains is negligible. The difference between cases (iii) and (iv), both having bond reforming and hence chains in dynamic equilibrium for small V^*/γ_τ, can be explained using Figure 3.2a). With the linear chain model the equilibrium chain density becomes negligible when $\delta^* \approx 0.05$, less than the COD if only the vdW attractions were present (0.092). That is, the adhesive zone is still governed by vdW when the chains are linear, even if bond reforming is included. While for the nonlinear chain model the equilibrium chain density is still significant at 0.092 which means that when the vdW attraction becomes negligible, there is still considerable traction on the interface coming from the chains. In other words, the length of the adhesive zone is determined by the

chains, which results in the larger COD at small V^*/γ_τ observed for case (iv) alone in Figure 3.5a).

Clearly, bond reforming and then nonlinear chain model both affect the fracture behavior at small propagation speed. However, it is important to note that bond reforming kinetics are only important for small V^*/γ_τ. At larger V^*/γ_τ, the CODs are much larger as seen in Figure 3.5a); consequently the energy to activate bond association becomes so large that the rate of chain reforming is negligible over most of the adhesive zone. This is why the curves with and without bond reforming are indistinguishable at large V^*/γ_τ, if the same polymer chain force-extension relationship is used. There is, however, considerable difference between the models using linear and nonlinear chain models. To explain, we note that in addition to negligible association, an increase in crack propagation speed relative to the relaxation time for bond dissociation results in insufficient time for the chain density to decrease to the equilibrium value. Therefore, for faster crack propagation the adhesive zone is dominated by the kinetics of chain rupture, which allows the chains to stretch farther before rupturing as compared to the equilibrium state discussed in Section 3.2.3. These greater levels of stretch create a feedback effect by increasing the tensile force on each chain which accelerates the rate of rupture (Eq. (3.1)). It is due to this feedback that we see a significant difference between results from linear and nonlinear chain models at large V^*/γ_τ. As shown in Figure 3.1 the tensile force for the nonlinear polymer chain is much larger than that of the linear polymer chain for large chain extensions. In the adhesive zone model this feature results in catastrophic rupture of polymer chains when the fractional extension approaches one (fully extended chains), which is why the COD in Figure 3.5a) levels to one, that is, the limiting COD value where the chain extension is equal to its contour length, at large V^*/γ_τ. For the linear chain model the stiffness does not increase and the crack opening can reach unphysical levels above the value of one (Figure 3.5a)).

Now consider the adhesive fracture energy results shown in Figure 3.5b). For this figure the beams are elastic so G_{ad}^* represents the total fracture energy. Qualitatively the G_{ad}^* results bear many similarities to that of the COD. Starting from small V^*/γ_τ the curves are almost horizontal, indicating rate independence. Larger V^*/γ_τ results in a rapid increase in G_{ad}^* and the slope decreases with subsequent increases in V^*/γ_τ. Physically, the same process previously described

when discussing the COD can also be used to understand the results for adhesive fracture energy. First consider small V^*/γ_τ, where the scenario of intrinsic strength presented in Figure 3.2c) is applicable. With reforming the polymer chains contribute to the intrinsic strength and the fracture energy is higher. For example the adhesive fracture energy for the nonlinear chain model is G_{ad}^* = 7.21 with bond reforming and for both chain models $G_{ad}^* = W_{vdW}^* = 5$ without bond reforming. Comparing the fracture energies for linear and nonlinear chain models with reforming at small V^*/γ_τ we see a slight increase in G_{ad}^* from 6.95 to 7.21 when the nonlinear chain model is introduced. The increase is much smaller in comparison to the increase in COD as seen in Figure 3.5a). This is because although the crack opening is much smaller for the linear chain model, it is partly compensated by the chains having higher stiffness. At large V^*/γ_τ bond reforming is negligible and therefore similar to Figure. 3.3a), the adhesive fracture energy is only affected by the chain model. The nonlinear chain model causes a catastrophic decrease in chain density when the fractional extension of polymer chains approaches the contour length, which leads to significantly smaller adhesive fracture energy (Figure 3.5b)).

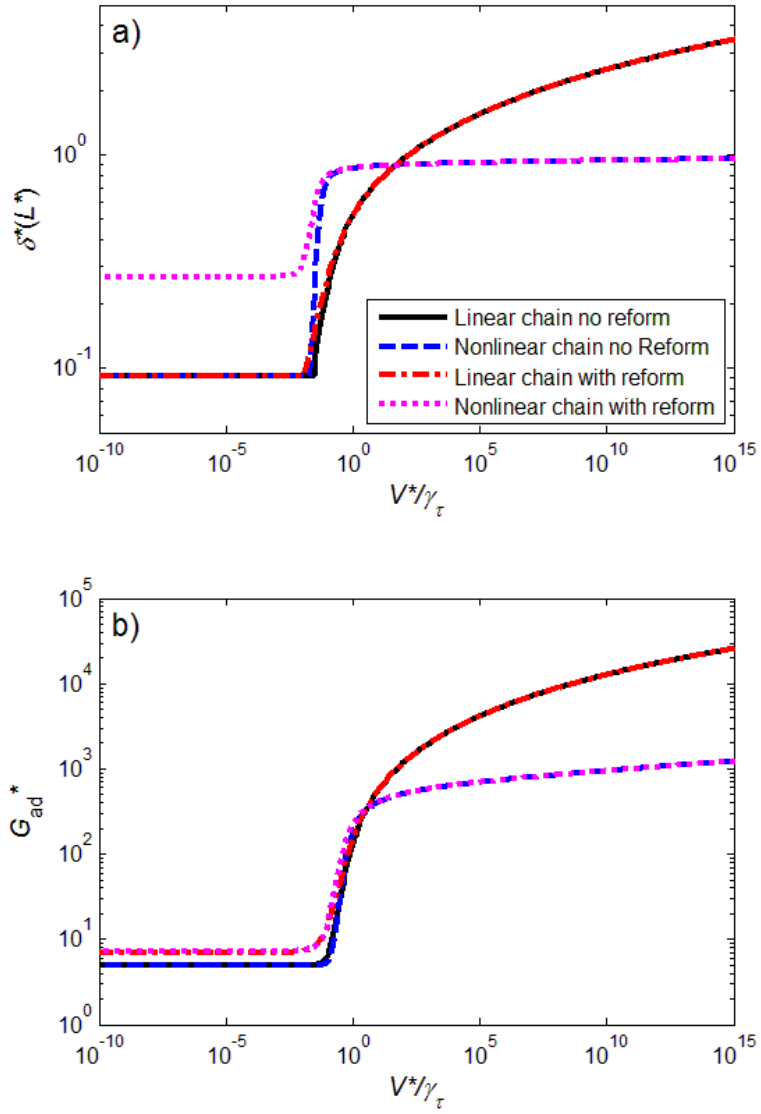

Figure 3.5: Plots for a) crack opening displacement, $\delta^*(L^*)$, and b) adhesive fracture energy, G_{ad}^*, obtained by varying V^*/γ_τ while holding the other governing parameters fixed at $U^* = 2850$, $\gamma_E = 1$, $\gamma_L = 2.222 \times 10^{-3}$, $\Sigma_{b0}^* = 0.9$ (for reforming models), $n = 150$ (for nonlinear models), $\delta_c^* = 0.02$ and $W_{vdW}^* = 5$. Each curve in these figures represents a different use of bond reforming/no reforming and linear/nonlinear chain models as indicated in the legend

3.3.1.2. *Effect of Initial Bond Density*

The initial bond density, Σ_{b0}^*, is an effective measure of the characteristic bond association time τ_+: high initial bond density means that the bond association rate is large relative to the bond dissociation rate (Eq. (3.2)). Similar to what was done in Section 3.3.1.1 we have plotted COD

and adhesive fracture energy against V^*/γ_τ in Figure 3.6. However, in Figure 3.6 all results are for the nonlinear chain model with bond reforming and each curve represents a different value of Σ_{b0}^*. The COD is shown in Figure 3.6a). It was established in Section 3.3.1.1 that at large V^*/γ_τ bond reforming is negligible. Therefore, it is not surprising that at large V^*/γ_τ the COD for all Σ_{b0}^* are coincident. However, at low V^*/γ_τ higher initial bond densities result in higher COD. In the limit of low V^*/γ_τ the polymer chains exist in dynamic equilibrium, and the equilibrium bond density is shown in Figure 3.2a). Clearly for higher initial bond densities, the enhanced association reaction rate allows for a larger bond density at all crack openings. Therefore, a larger crack opening is achieved before the load on the crack becomes negligible.

Although Σ_{b0}^* was varied to represent changes in the rate of bond association relative to dissociation, changing this value also affects the initial density of load bearing chains before the crack opens. Therefore, since there are more bonded chains which need to be ruptured, it is expected that larger Σ_{b0}^* will result in larger G_{ad}^*. Furthermore, to glean insight into how the kinetics change when the initial bond density is changed, the average amount of work done to rupture one chain would be of interest; this information can be obtained from a plot of $\left(G_{ad}^* - W_{vdW}^*\right)/\Sigma_{b0}^*$ vs. V^*/γ_τ which is shown in Figure 3.6b). For large V^*/γ_τ bond association is negligible so again all curves are coincident. The low speed limit is more interesting and we can see that not only does larger Σ_{b0}^* increase G_{ad}^*, relative to the initial chain density more work is done in rupturing one chain. To explain, after rupturing and dissipating their stored energy, for larger Σ_{b0}^*, chains are more likely to associate and form new chains and bridge the crack. These new chains must be ruptured again in order for the crack to propagate, leading to a higher value of average adhesive fracture energy per chain.

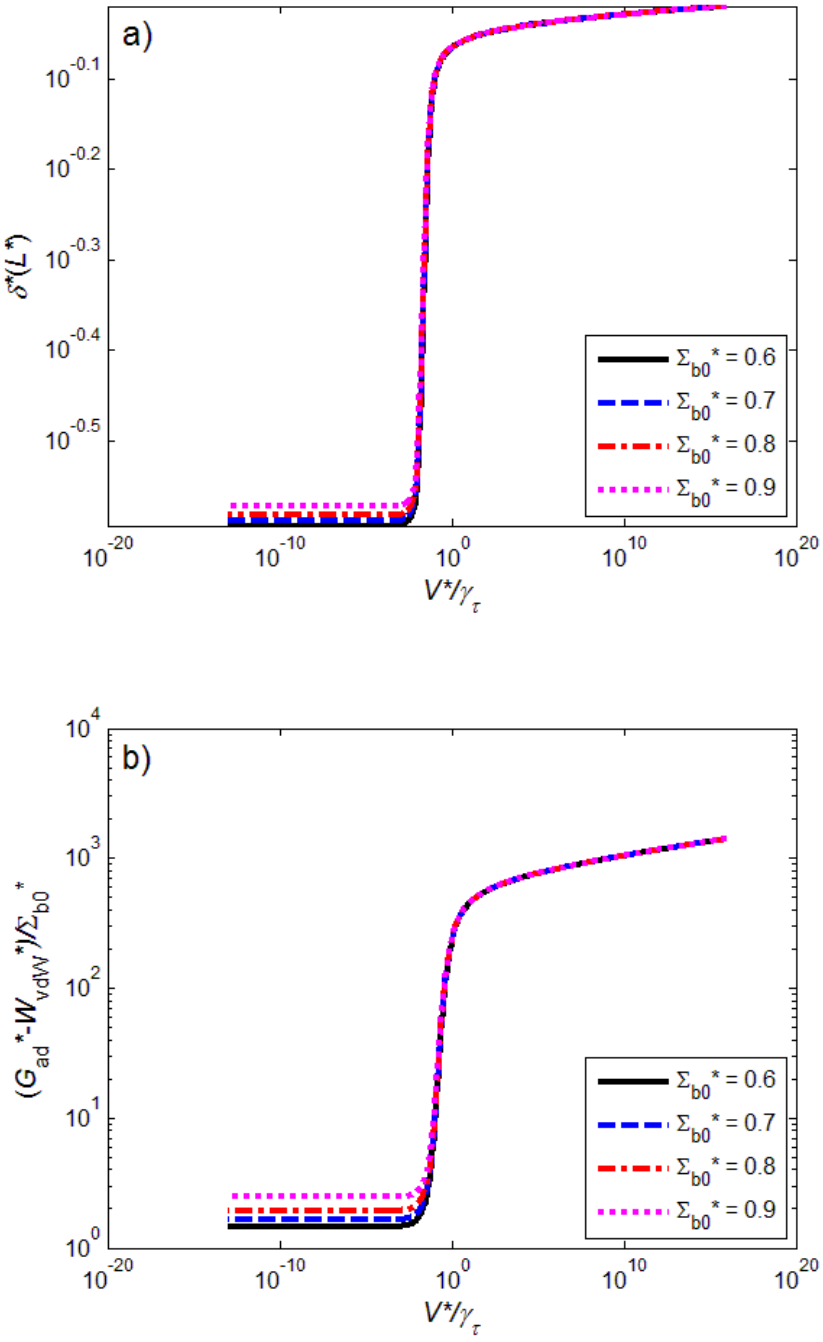

Figure 3.6: Plots for a) crack opening displacement, $\delta^*(L^*)$, and b) portion of adhesive fracture energy due to polymer chains normalized by initial bond density, $(G_{ad}^* - W_{vdW}^*)/\Sigma_{b0}^*$, obtained by varying V^*/γ_τ while holding the other governing parameters fixed at $U^* = 2850$, $\gamma_E = 1$, $\gamma_L = 2.222 \times 10^{-3}$, $n = 150$, $\delta_c^* = 0.02$ and $W_{vdW}^* = 5$. Each curve in these figures represents a different initial bond density Σ_{b0}^* as indicated in the legend

3.3.2. *Viscoelastic Beam*

When a viscoelastic beam model is used, the applied mechanical work needs to overcome the adhesive tractions as well as bulk viscoelastic dissipation. The amount of viscoelastic dissipation will depend on the length of the beam which we consider; long beams will tend to have more dissipation [6 supporting material]. For the following analysis we consider a beam with a fixed normalized length, $L^* = L\left(2k_BT\Sigma_oD/E_oIL_c^2\right)^{1/4} = 1$. Both bond reforming and nonlinear force-extension relationship are considered in the calculations. The apparent energy release rate $G^*(1)$, including both sources, is plotted in Figure 3.7a), the adhesive portion G_{ad}^* in Figure 3.7b) and the bulk dissipation $G_{vis}^*(1)$ in Figure 3.7c). The qualitative features of these results are very similar to the results for a linear chain model without bond reforming [6] so we will first briefly describe them without in depth discussion. In these figures each curve represents a different value of γ_τ, the ratio of bulk relaxation time to the relaxation time for bond dissociation on the interface. In Figure 3.7a) and b) the *x*-axis is V^*/γ_τ and each figure contains an inset where the axis has been changed to V^*. The change in axis from V^* to V^*/γ_τ represents a horizontal shift caused by different values of γ_τ; decreasing γ_τ effectively slows chain dissociation which results in larger chain stretch before dissociation and therefore greater G_{ad}^* and $G^*(1)$. When shown on V^*/γ_τ axes G_{ad}^* in the viscoelastic case looks strikingly similar to G_{ad}^* for the elastic case shown in Figure 3.6b). This means the interfacial rate-dependence, at least in the DCB model, does not depend strongly on bulk viscoelastic effects. The contribution of G_{ad}^* to $G^*(1)$ is apparent in comparing Figure 3.7a) and Figure 3.7b): $G^*(1)$ is equal to the intrinsic strength at small V^*/γ_τ, followed by a rapid increase as V^*/γ_τ is increased, and finally a slower rate of increase at large V^*/γ_τ. However, each curve in Figure 3.7a) also has a local maximum which is due to the second contribution to $G^*(1)$, namely $G_{vis}^*(1)$, plotted against V^* in Figure 3.7c). At both low and high V^* the value of $G_{vis}^*(1)$ approaches zero asymptotically and between these two extremes there is a maximum. The value of this maximum depends on γ_τ with the smallest values of γ_τ achieving the largest $G_{vis}^*(1)$ peak.

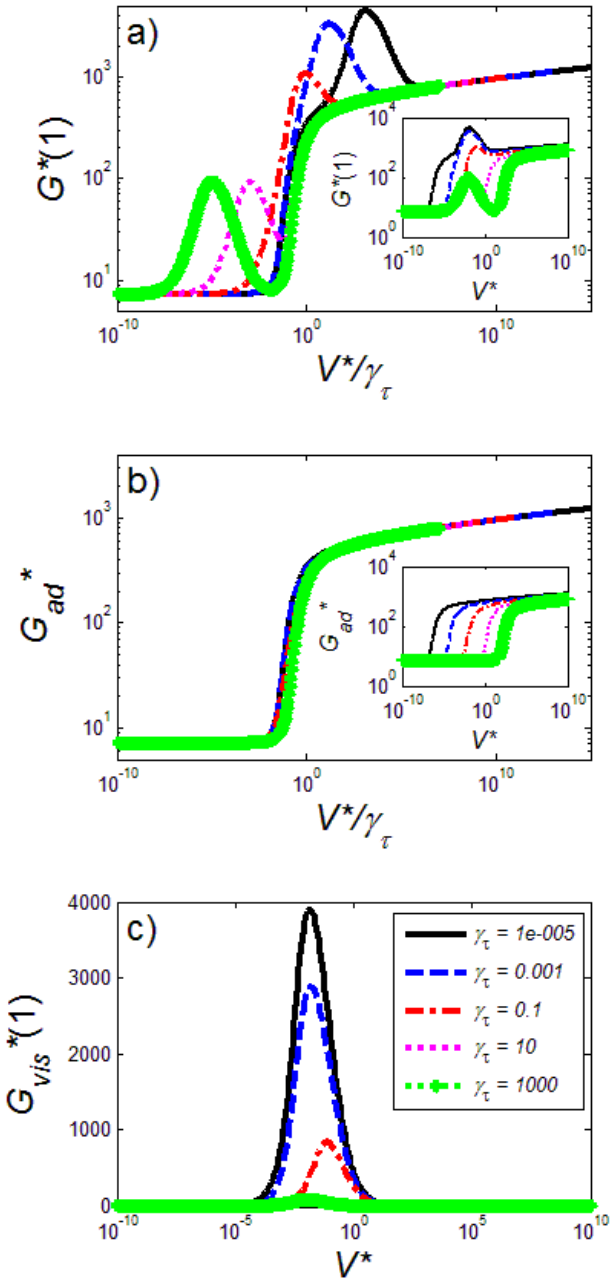

Figure 3.7 Plots for a) fracture energy, $G^*(1)$, b) adhesive fracture energy, G_{ad}^*, and c) viscous dissipation, $G_{vis}^*(1)$, plotted against V^* and/or V^*/γ_τ. These plots were obtained by varying V^* while keeping γ_τ fixed at the five values shown in the legend. The other governing parameters were held fixed at $U^* = 2850$, $\gamma_E = 0.01$, $\gamma_L = 2.222 \times 10^{-3}$, $n = 150$, $\Sigma_{b0}^* = 0.9$, $\delta_c^* = 0.02$ and $W_{vdW}^* = 5$. The figure embedded in b) shows fracture energy, G^*, plotted against normalized crack propagation speed V^*

A detailed explanation as to why $G_{vis}^*(1)$ tends to zero in both limits has been previously presented in Lavoie et al. [6] for the linear chain model without reforming, and is also applicable to this case. Consider that the viscoelastic beam is made of three zones: starting from the adhesive zone tip the glassy (unrelaxed zone), the dissipative (viscoelastic) zone and the rubbery (relaxed) zone [6]. $G_{vis}^*(1)$ is generated within the dissipative zone where the beam relaxes. For small V^* the glassy and dissipative zones are negligibly small which results in negligible $G_{vis}^*(1)$. Increasing V^* causes both the glassy and dissipative zones to expand. Eventually within a finite sized beam the rubbery zone will no longer exist and subsequent increases in V^* will cause the glassy zone to expand and the dissipative zone to shrink. Further increase in V^* can cause the dissipative zone to vanish in the DCB, and $G_{vis}^*(1)$ reduces to zero again. Such non-monotonic bulk dissipation and was also observed for finite sized specimens by Xu *et al*. [15].

Although the above qualitative behavior was also observed with an adhesive zone model that lacks bond reforming and nonlinear force-extension relationship for the polymer chains, quantitatively the peak $G_{vis}^*(1)$ values are substantially lower in the present work. For example with a linear chain model the peak dissipation for $\gamma_\tau = 10^{-5}$ was ≈ 24500 [6] whereas for the nonlinear chain model the peak value is ≈ 4000, six times smaller. Very much like the large difference in G_{ad}^* between the two models, described in Section 3.3.1.1, this difference can be attributed to the fact that at these values of γ_τ the nonlinear chain model leads to significantly smaller crack openings at moderate to large crack propagation speeds where the peaks in $G_{vis}^*(1)$ are located, and the smaller deformation results in smaller viscous dissipation. The impact of bond reforming on $G_{vis}^*(1)$ is small (data not shown) since it is only important for small V^*/γ_τ where $G_{vis}^*(1)$ is insignificant.

The introduction of the bond reforming term in the kinetic equation (Eq. (3.1)) allows for the existence of equilibrium bond density, and the prediction of the intrinsic strength of the material W_o which depends on the properties of the polymer chains. The adhesive zone model can also predict the function $\phi(V)$ in Eq. (3.3). Note that the rate dependence $\phi(V)$ here are caused by physical processes in both the bulk material and on the interface; a plot of $\phi(V)$ is not shown since it would appear nearly identical in shape to Figure 3.7a). By comparing the inset of Figure 3.7b) and Figure 3.7c) it can be seen that the peak bulk dissipation $G_{vis}^*(1)$ is correlated to G_{ad}^*: at a given V^*; larger G_{ad}^* results in larger $G_{vis}^*(1)$. This observation should be compared with that of

Andrews and Kinloch [13] who noted that viscoelastic dissipation was found to be proportional to the intrinsic energy, since stronger interfaces can allow larger bulk deformation before crack propagation and hence larger viscoelastic dissipation. In our case, Figure 3.7, all curves have the same intrinsic strength (Figure 3.2c)), however the adhesive fracture energy is rate-dependent. We find that at a particular rate the viscoelastic dissipation is related to the adhesive energy rather than the intrinsic value at the limit of infinitely slow rate. Such behavior reinforces the hypothesis of Rahulkumar *et al*. [22]: simulations with a rate-independent adhesive zone model failed to generate enough rate dependency to match experimental data, the authors concluded that a rate dependent adhesive zone model was necessary.

3.4. Conclusion

An adhesive zone model which considers association and dissociation of nonlinear polymer chains was developed for understanding rate-dependent fracture of viscoelastic polymeric materials. Since association of bonds between polymer chain fragments is included, this model can also be used for simulations of self-healing materials. This adhesive zone model was implemented in an elastic and viscoelastic double cantilever beam (DCB) to study rate dependent crack propagation. Compared with prior adhesive zone models this version produces several important qualitative differences in the results. The first difference is that the inclusion of bond reforming allows the model to predict dynamic equilibrium and an intrinsic material strength which depends on the polymer chains; this intrinsic strength is the fracture energy for extremely slow crack propagation. The second important difference occurs for high rates of crack propagation, relative to the relaxation time for bond dissociation, where the chains bridging the crack interface achieve stretch levels close to their contour length. In this case, the chain reforming kinetics becomes negligible; however, implementing a nonlinear chain model causes catastrophic dissociation of chain bonds as the contour length of the chain is approached. This feature predicts adhesive fracture energies several orders of magnitude smaller than those from the linear chain model which predicts unphysical crack openings in excess of the contour length. This significant decrease in crack opening also results in a substantial decrease in the amount of bulk dissipation in viscoelastic material.

Considering the difference mentioned above, the rate-dependency of the adhesive fracture energy (from interfacial dissipation) resembles a step-function, with a low-speed plateau followed by a rapid increase and much slower rate of increase at fast crack propagation. The bulk viscous

dissipation has a maximum at an intermediate speed and the peak value is correlated with the magnitude of the adhesive fracture energy.

Although in this article we only applied the adhesive zone model to separation of rigid surfaces and a simple double-cantilever beam (one-dimensional), it can also be applied to cracks in two or three dimensional solids where interfacial tractions can lead to complex multi-axial deformation state in the solid. However, care must be taken in such a situation because loads able to stretch chains along the interface to the point where they rupture rapidly will necessarily result in large deformations within the vicinity of the interface. Such deformation must be captured using finite strain kinematics where it is important to note that the true area of the interface will depend on the bulk deformation which must be taken into account when determining the stress. In addition, the adhesive zone model presented pertains only to normal separation of cracks and therefore is applicable to Mode-I cracks. Extension is needed if Mode-II, Mode-III or mixed mode cracks are to be studied.

3.5. Nomenclature

Note Non-dimensional parameters are summarized in Table A2.1

A	Kuhn length
δ	Crack opening
δ_c	is a characteristic decay length
D	Depth of beam
ε	is strain
E	Young's Modulus
E_o	the instantaneous or unrelaxed modulus
E_∞	is the infinite time or relaxed modulus
E_a	activation energy
E_c	is the elastic spring energy required to stretch two relaxed (unstressed) polymer chain fragments on opposite sides of the interface so that they make contact
f	Distributed adhesive stress
$\phi(V)$	increase in fracture energy for finite rates of crack propagation
F	is the tensile force acting on each chain
G	Fracture energy
G_{ad}	Adhesive Fracture Energy
G_{vis}	Viscous Fracture Energy
h_p	is Plank's constant
I	Area moment of inertia
k_B	is the Boltzmann constant
k_s	is the average spring stiffness
λ	is the bond activation length
L_c.	contour length
M	Bending Moment
n	is the number of bonds per polymer chain
P	Persistence Length
σ	stress
σ_c	Maximum vdW stress
σ_{ad}	Adhesive stress
S	Shear force
Σ_b	is the number of chains that cross a unit area of the interface
Σ_o	is the chain density for perfectly bonded interface
Σ_{b0}	the initial bond density
τ_o	is the bulk relaxation time
τ_-	is the characteristic time of bond dissociation
τ_+	is the characteristic time of bond association
t	time
T	is the absolute temperature

U	is the work required to stretch the chain from its unstressed configuration to its contour length
V	Crack propagation speed
W_{vdW}	is the work of adhesion due to vdW attractions
W_o	is the thermodynamic work of adhesion for separating the two surfaces under equilibrium conditions
x, y	Coordinates translating with crack tip
X, Y	Fixed Coordinates

Chapter 4. A rate-dependent damage model for elastomers at large strain[3]

Abstract

The ability to predict rate and deformation dependent damage in elastomers is important for many applications. To model the rate dependent damage processes we introduce chain scission, predicted using concepts of mechanochemistry, into hyperelastic constitutive models (Arruda-Boyce as an example). The result is a model capable of handling large strain and rate dependent damage. Additionally, polydispersity is incorporated by considering a distribution of chain lengths, which gives the model the capability to predict progressive material damage. To demonstrate the application of the model, uniaxial tensile deformation with constant extension rates is examined. The tensile stress is found to first reach a peak and then decrease due to scission, and faster rates of deformation result in larger peak stress. Under cyclic loading the polydispersity results in progressive material damage which mirrors the Mullins effect at high deformation rates. In addition, the damage model predicts interesting rate-dependent behavior, such as significant hysteresis during unloading and reloading, as the loading rate is decreased. Finally, the model is shown to be capable of fitting experimental data for a variety of materials.

[3] A version of this chapter has been published. Reprinted with permission from Lavoie, S. R.; Long, R. Tang, T. "A rate dependent damage model for elastomers at large strain" Ext. Mech. Let. (2015) September 2016: 114-124: 277-286. https://doi.org/10.1016/j.eml.2016.05.016 Copyright 2016 Elsevier

4.1. Introduction

The ability to predict rate and deformation dependent damage in elastomers is important for many applications. It has been long observed that elastomers exhibit rate dependent fracture behavior which is not yet fully understood [8]. Although, much of this rate dependence can be attributed to viscoelasticity [8], modeling attempts have been unsuccessful in fully capturing this effect by only accounting for viscoelasticity while using rate independent damage models [22]. In addition rate dependence of fracture energy has also been observed in materials which are essentially elastic [37]. Another contributing factor to this rate dependency is the rupture kinetics of the polymer chains [2, 3] or "scission". A rate dependent damage model is important for the development of predictive theories in soft polymer fracture and his process has been modeled using rate equations derived from the concepts of "Mechanochemistry" [32] to predict the rate of rupture of covalent bonds, which bridge an interface, under tensile stress [2, 3]. This theory has previously been implemented in cohesive zone modeling which results in a traction-separation relationship for the interface [1, 2, 3, 6]. However, the nonlinear nature of the relationship between the force applied on a polymer chain and the consequent chain extension [3] can lead to large tractions that exceed the material's shear modulus by orders of magnitude [38], a well-known feature of soft materials [39]. This presents a difficulty for analysis since such high magnitude of stress will generate strains well beyond the range of applicability of linear analysis. This difficultly could be addressed by pairing the cohesive zone model with a hyperelastic model capable of accommodating finite strain and there are many such models [40]. However, more recent experiments where rupture events are mapped using light emitting photophores [4] have shown that scission is not necessarily localized to a fracture plane as is assumed in cohesive zone modeling, but can also occur in the bulk material adjacent to the fracture plane. This observation indicates that it is necessary to consider bulk damage even if the fracture behavior of elastomers is of the primary interest. This is especially relevant for a new class of adaptable polymers with dynamic bonds [41] that can break and reform. Such polymers exhibit rate dependent bulk damage behavior under monotonic loading governed by the molecular kinetics of the dynamic bonds. Theoretical understanding of the mechanical behaviors of adaptable polymers requires models that are capable of connecting the kinetic event of bond breaking to macroscopic mechanics and addressing the potential coupling between mechanical stress and bond breaking kinetics.

There are numerous models in the literature which consider damage of elastomers. A classical family of these models consider the Mullin's effect, see for example Ogden and Roxburgh [42]; these models have damage functions and parameters which depend on the maximum deformation previously experienced by the material and as a result are rate independent. The concept of energy limiters [43] has been used to generate softening hyperelastic models which mimic the mechanical response of elastomers undergoing damage, however, these models cannot generate rate dependence without considering viscoelasticity [43]. Another family of models treats damage as a rate dependent process where the volume fraction of undamaged material evolves temporally instead of being determined by deformation [21, 44, 45]. These models have been utilized to describe elastomers undergoing chain scission as reviewed by Wineman [21]. A model which combines the effects of deformation and chain scission kinetics has also been proposed [46]. In all these damage theories, either rate dependent or independent, the actual stress sustained by the damaged elastomer network is calculated by multiplying the volume fraction of undamaged material and the stress in the undamaged virgin network under the same deformation as the damaged network. This approach provides a link between material damage and the degraded mechanical property, but it does require a damage function with either deformation or time as the controlling variable. Such damage functions are determined empirically in most existing models thus far. Damage models that are directly derived from microscopic physical processes (i.e. chain scission) have not been fully explored, which is the focus of this work.

In this study, we develop a theoretical framework where concepts of mechanochemistry [32] are used to introduce rate dependent damage into elastomer constitutive models. Specifically, we establish a procedure to incorporate rate-dependent scission predicted from mechanochemistry into certain hyperelastic constitutive models by calculating a decrease in the volumetric density of load bearing chains. To demonstrate the procedure we adopt the familiar Arruda-Boyce constitutive model [9], and a simple scission rate equation [2, 3]. In order to illustrate the application of the model, we present and explain the rate-dependent mechanical response produced by this model under uniaxial extension and cyclic uniaxial extension. The model is also shown to have the capability of matching experimental data for a variety of elastomers with different microstructures.

This paper proceeds as follows. Theoretical details of the proposed model are presented in Section 4.2. Application of the model to two examples, uniaxial tension and cyclic uniaxial

loading, are presented in Sections 4.3.1 and 4.3.2, respectively. Applying the model to match experimental data is given in Section 3.3 and Limitations and Future Perspectives are discussed in Section 3.4. Conclusions are given in Section 4.4.

4.2. Theoretical Framework

4.2.1. *Damage Model*

The theory of mechanochemistry [32] has been used to capture the effect of mechanical forces on the rate of dissociation of bonds and hence scission of polymer chains. It has been used to predict the strength of adhesives [1,2,3,6,7] based on a rate equation that calculates the areal density of surviving polymer chains across an interface. This rate-equation is adjusted for volumetric scission of chains as follows

$$-\frac{dN}{dt} = \frac{n_m N}{\tau_-} e^{L_a F / k_B T}, \tag{4.1}$$

where N is the number of surviving chains per unit volume, τ_- and L_a are fixed parameters respectively representing the relaxation time and activation length for bond dissociation, F is the tensile force on a polymer chain, k_B is the Boltzmann constant and T is the absolute temperature. The number of monomers per chain, n_m, appears here since rupture of a single bond on the chain's backbone is sufficient to break the chain – this is known as the Lake-Thomas effect [10]. Without considering the Lake-Thomas effect Eq. (4.1) is similar to the mechanochemistry equations used to predict the activation of mechanophores embedded in viscous rubbery networks [47] and elastomer networks [48]. While these models predict rates of mechanophore activation in a similar way to what we propose for rates of scission, one important difference is that the activation of mechanophores does not alter the mechanical property of the polymer through the introduction of material damage.

Previous works have shown that it may not always be a good assumption that the activation length in Eq. (4.1), L_a, is constant [3, 47]. For example, Silberstein et al. [47] used atomistic simulations to calculate the activation energy values at two different levels of chain force and use a linear function to determine L_a, whereas Ghatak et al. [3] used a more sophisticated rate equation which is based upon Kramers' rather than Eyring's transition state theory. In either approach

additional data must be specified, and for simplicity we will adopt a constant L_a to demonstrate the incorporation of mechanochemistry in the damage model.

Isotropic damage models exist in the literature for deformation induced microstructural changes [20] and scission in elastomers [21] where the undamaged stress of the material is multiplied by the remaining volume fraction *b* of the original material. In this spirit we introduce $b(t) = N(t)/N_o$ as the surviving fraction of chains at time *t*, where N_o is the number of original chains per unit volume in the undamaged material. The variable *b* has a value of 1 in the undamaged material and rate dependent scission processes cause it to decrease. However, rather than directly multiply *b* with the undamaged stress to predict the stress as in Rajagopal and Wineman [20], we will introduce *b* into the strain energy density of the material. Specifically, for any hyperelastic model that is based on a polymer chain force-extension relationship, this relationship can be integrated to obtain the free energy stored in a chain, and multiplying this energy with the number of chains per unit volume gives a strain energy density U_o; there are several examples of this type of model in the literature [9,49]. Clearly, without damage U_o would be proportional to N_o. To introduce damage, we replace N_o by $N(t)$ so that the strain energy density is in the form of $U = bU_o$, where the undamaged strain energy is multiplied by a damage variable. This form is consistent with other models in the literature such as those describing the Mullins effect in elastomers [40, 42].

In constructing the undamaged strain energy density function U_o, it's generally assumed that the polymer chains have a single length [9,49]. However, in reality polymers are polydisperse, i.e. there is a distribution of chain lengths within the material. When considering Eq. (4.1) we can infer that polymer chains will break rapidly when the tensile force on the chains becomes large. If there is only a single chain length, all chains experiencing the same deformation will have the same tensile force and the material can transition from undamaged state to catastrophic failure within a small deformation range. This is inconsistent with experimental observation [4] that scission occurs over a larger range of deformations. Introducing a distribution of chain lengths allows for the model to accommodate this observation since chains of different lengths will experience different tensile forces for the same macroscopic deformation. Polydispersity has been previously combined with the Arruda-Boyce hyperelastic model [48]. However, because chain scission was not considered, singular stresses will occur when the shortest polymer chains reach their critical

extension. By allowing the chains to rupture, polydispersity can be applied over a larger range of deformation. To include polydispersity we introduce a distribution of polymer chain lengths and determine the total strain energy from the sum of the contributions of each chain length:

$$U = \sum_{i=1}^{M} b_i(n_i, t) U_{o,i}(n_i, \underline{\mathbf{B}}(t)) - p(J-1). \quad (4.2)$$

where $b_i(n_i,t) = N_i(n_i,t)/N_o$ are the surviving number of chains of the i^{th} length divided by the initial number of chains in the material, and $U_{o,i}(n_i, \underline{\mathbf{B}}(t))$ are the undamaged strain energy density associated with i^{th} chain length. n_i is a measure of the length of the chain, which depends on the chain model used; for a freely jointed chain it represents the number of Kuhn segments per chain [9]. $\underline{\mathbf{B}} = \underline{\mathbf{F}}\underline{\mathbf{F}}^{\mathbf{T}}$ is the left Cauchy-Green deformation tensor [40], where $\underline{\mathbf{F}}$ is the deformation gradient [64]. M represents the number of possible chain lengths, J is the determinant of the deformation gradient, and p is a Lagrange multiplier to enforce incompressibility. Note that incompressibility is a common assumption for many elastomers since the bulk modulus is often much larger that the shear modulus and hence can sustain finite strains without noticeable volume changes [40]. The total surviving chain fraction is given by $b_t(t) = \sum_{i=1}^{M} b_i(n_i,t)$ such that $b_t(0) = 1$.

The mechanochemistry equation (Eq. (4.1)) can now be rewritten for the chain fraction, b_i, leading to a system of equations for chains of each length

$$-\frac{db_i}{dt} = \frac{n_{m,i} b_i}{\tau_-} e^{L_a F_i / k_B T}. \quad (4.3)$$

where F_i is the force acting on a polymer chain of the i^{th} length, and $n_{m,i}$ is the number of monomers in a chain of the i^{th} length. If we take $M = 1$ (i.e., imposing a single chain length) then Eq. (4.3) reduces to Eq. (4.1) (with $N = b_1(t)N_o = b_t(t)N_o$).

Alternative methods to compute the damage variable b_t are available in literature and it is worth comparing several of them to Eq. (4.3). Wineman and Min [45] and Wineman [21] suggest that, within a range of deformation, scission is independent of deformation and write $b_t(t) = b_o \exp(-t/\tau_o)$. Differentiation with respect to time gives $db_t/dt = -b_t/\tau_o$ which agrees with Eq. (4.3) if $\tau_o = \tau_- e^{L_a F/k_B T}/n_m$, that is, if the deformation is fixed so that the force on

individual polymer chains is constant, e.g. in stress relaxation. This relationship can also approximately agree with Eq. (4.3) if the deformation is such that the fractional extension of polymer chains is small. A typical nonlinear polymer chain force extension relationship is shown in Figure 4.1 (to be discussed later), where for small fractional extension the slope is small and the tensile force changes slowly with extension. When the deformation is in this regime, in Eq. (4.3) $e^{L_a F_i / k_B T} \approx 1$ is approximately constant; hence db_i / dt is nearly independent of deformation, as in the relationship proposed by Wineman and Min [45]. Shaw et al. [44] have shown, from stress relaxation experiments at high temperature, that b_t can be well represented by $b_t(t) = \sum_{l=1}^{l_{\max}} \xi_l \exp(-t/\tau_l)$ where ξ_l are constant coefficients, $\tau_l = h \exp(Q_l / R_g T) / k_B T$ are characteristic times, h is Planck's constant, R_g is the gas constant, and Q_l is an activation energy. In reality most materials have a spectrum of characteristic times, hence the summation in the model of Shaw et al [44]. The characteristic time was further modified by Wineman and Shaw [46], for temperature and shear induced scission in elastomers, to $\tau_l = h \exp((Q_l + Q_\sigma) / R_g T) / k_B T$ where Q_σ represents the potential energy change associated with the application of stress. There are many similarities between this expression and Eq. (4.3), since $\tau_{\_}$ is based on an activation energy [2] similar to Q_l, and $L_a F$ is effectively an activation energy decrease caused by the work of the tensile force acting on bonds, similar to Q_σ. One important difference is the exponential decay, $b_t(t) = \sum_{l=1}^{l_{\max}} \xi_l \exp(-t/\tau_l)$, as suggested by Wineman and Shaw [46]. In Eq. (4.3) if $M = 1$ then $db_t / dt = -b_t / \tau_1$, and if τ_1 is constant this relationship can be integrated to give an exponential decay. However if τ_1 depends on time, as it would for non-constant deformation after the introduction of Q_σ, the integration to determine $b_t(t)$ will not give the suggested exponential decay. Therefore, although altering τ_l using Q_σ as in Wineman and Shaw [46] works well for stress relaxation where Q_σ is a constant, in general there is a stronger physical basis to calculate b_t by numerically integrating rate equations such as Eq. (4.3).

Another difference between our model and that of Wineman and Shaw [46] is that Eq. (4.3) has only a single characteristic time but a number of different lengths. Consider stress relaxation, as in

the experiments of Shaw et al [44], for a polydisperse elastomer. It is not difficult to imagine that polymer chains of different lengths will have different fractional extensions (Eq. (4.9) to be discussed later) and be subjected to different tensile forces (Eq. (4.7) to be discussed later). The physical interpretation of Eq. (4.3) is that the dissociation characteristic time is shifted by the tensile forces acting on each bond. In other words, if we express Eq. (4.3) in the form of $-db_t/dt = n_m b_t/\tau_{dis}$, where τ_{dis} is an effective dissociation characteristic time, then $\tau_{dis} = \tau_- e^{-L_a F/k_B T}$. Therefore in a polydisperse network the distribution in the tensile force F results in a spectrum of effective characteristic times even though the constant τ_- has a single value. Finally, the form suggested by Wineman and Shaw [46] states $Q_\sigma = -\nu \underline{\mathbf{P}} : (\underline{\mathbf{F}} - \underline{\mathbf{I}})$ where ν is the molar volume, and $\underline{\mathbf{P}}$ is the Piola-Kirchhoff stress tensor which differs from $L_a F/k_B T$ in Eq. (4.3). In Eq. (4.3) mechanochemistry theory [32] provides a simple physically motivated form for this term in elastomers.

4.2.2. *Stress and Dissipation*

Consider the balance of power per unit volume

$$\frac{dW}{dt} = \frac{dU}{dt} + \frac{dD_{\text{int}}}{dt}, \tag{4.4}$$

where dW/dt is the rate of work, dU/dt is the rate of change of strain energy and dD_{int}/dt is the rate of internal dissipation. Substituting Eq. (4.2) into Eq. (4.4) expressions for the stress and internal dissipation can be obtained (see details in Appendix 3.1). The stress can be determined from

$$\underline{\boldsymbol{\sigma}} = \sum_{i=1}^{M} 2b_i \frac{\partial U_{o,i}(\underline{\mathbf{B}})}{\partial \underline{\mathbf{B}}} \underline{\mathbf{B}} - p\underline{\mathbf{I}}, \tag{4.5}$$

where $\underline{\boldsymbol{\sigma}}$ is the Cauchy stress tensor. Using Eq. (4.3) the rate of dissipation is given by

$$\frac{dD_{\text{int}}}{dt} = -\sum_{i=1}^{M} \frac{db_i}{dt} U_{o,i}(\underline{\mathbf{B}}) = \sum_{i=1}^{M} \frac{n_{m,i} b_i}{\tau_-} e^{L_a F_i/k_B T} U_{o,i}(\underline{\mathbf{B}}) \geq 0. \tag{4.6}$$

For simple homogenous deformations, such as uniaxial extension described in the following section, $\underline{\mathbf{B}}(t)$ can be easily prescribed. Knowing $\underline{\mathbf{B}}(t)$ and the relationship between the deformations of the chain and the bulk (typically given as part of the constitutive model), Eq. (4.3)

must be solved to obtain $b_i(t)$, finally the stress and dissipation rate can be obtained from Eqs. (4.5) and (4.6). In cases where $\underline{\mathbf{B}}(t)$ is not known a priori (e.g., under load control), Eq. (4.3) is coupled to Eq. (4.5) and the equilibrium equations for stress, which results in a system of coupled partial differential equations to be solved in an initial-boundary value problem.

4.2.3. *Coupling with Arruda-Boyce Constitutive Model*

In the following we discuss how to incorporate the damage model introduced above into constitutive models for isotropic elastomers. While the procedure is applicable for any hyperelastic models based on a polymer chain force-extension relationship, the Arruda-Boyce constitutive model [9] will be used as an example. This model is based upon Langevin chain statistics [9] for which the tensile force on a polymer chain is given by

$$F = \frac{k_B T}{A}\beta, \tag{4.7}$$

where A is the Kuhn length of the polymer chains, β is the inverse Langevin function defined so that $r/L_c = \coth\beta - \beta^{-1}$, $L_c = nA$ is the contour length of the polymer chains, n is the number of Kuhn segments per polymer chain. The force extension relationship is given by Eq. (4.7) and plotted against r/L_c in Figure 4.1. The stiffness of the chain, i.e., slope of the force-extension curve, dramatically increases as the fractional extension approaches unity. Integrating Eq. (4.7) with respect to extension gives the stored energy in a single chain and multiplying by N_o, the number of load bearing polymer chains per unit volume (of undamaged material), gives the strain energy density for the undamaged material [9]

$$U_o\left(\frac{r}{L_c}\right) = N_o k_B T\left[n\left(\frac{r}{L_c}\beta + \ln\left(\frac{\beta}{\sinh\beta}\right)\right) - c\right], \tag{4.8}$$

where c is a constant to ensure that the strain energy is zero at undeformed state. Information is needed to relate the chain extension to the bulk deformation $\underline{\mathbf{B}}$. This is accomplished using the affine network model where the deformation of each chain is assumed to be the same as the macroscopic deformation of the solid [50]. For the freely jointed chain model this assumption gives [9]

$\frac{r}{L_c} = \sqrt{\frac{I_1(\underline{\mathbf{B}})}{3n}}$,	(4.9)

where $I_1(\underline{\mathbf{B}})$ is the first invariant or trace of $\underline{\mathbf{B}}$. When the material is undeformed, $\underline{\mathbf{B}} = \underline{\mathbf{I}}$, where $\underline{\mathbf{I}}$ is the identity tensor, so that $I_1 = 3$, and $(r/L_c)_i = n^{-1/2}$. The constant c in Eq. (4.8) can therefore be obtained as $c_i = n_i\left(n_i^{-1/2}\beta_{o,i} + \ln(\beta_{o,i}/\sinh\beta_{o,i})\right)$ where $\beta_{o,i}$ is implicitly given by the relationship $(r/L_c)_i = n^{-1/2} = \coth\beta_{o,i} - (\beta_{o,i})^{-1}$. In the presence of polydispersity, replacing n with each chain length n_i, Eq. (4.7) provides the force, F_i, for use in Eq. (4.3), and Eq. (4.8) provides the strain energy density for use in Eq. (4.5).

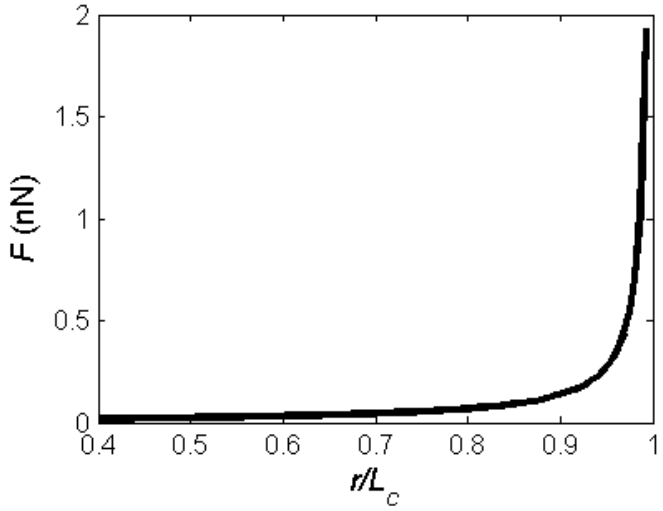

Figure 4.1. Polymer chain force, F, vs fractional extension, r/Lc for the Langevin chain used in the Arruda-Boyce constitutive model (Eq. (4.7)). A = 0.3nm [3], T = 293 K.

4.2.4. *Application to Uniaxial Extension*

The model as presented thus far would be valid for general deformation; however, to demonstrate the model we will focus on a uniaxial deformation state. A schematic of a uniaxial deformation is shown in Figure 4.2a) where λ is the stretch in the form of

$\lambda = 1 + Rt$,	(4.10)

with t being time and R being the rate of stretch.

Details for the determination of stress are given in the Appendix 3.2; here we provide a brief summary of the procedure. Incompressibility requires that $J = \det(\underline{\mathbf{F}}) = \lambda\lambda_t\lambda_t = 1$ which allows for the determination of the unknown transverse stretch λ_t. The stress can be evaluated from Eq. (4.5). In uniaxial extension there is only one non-zero stress component and the Lagrange multiplier *p* is specified to make the other components zero. The tensor notation is therefore removed and the stress given below refers to the stress in the direction of extension. Using Eq. (4.5) we get

$$\sigma = \sum_{i=1}^{M} 2b_i(n_i,t)\frac{\partial U_{o,i}}{\partial I_1}\left[\lambda^2 - \lambda^{-1}\right] = \frac{N_o k_B T}{3}\sum_{i=1}^{M} b_i(n_i,t)\left(\frac{I_1(\underline{\mathbf{B}})}{3n_i}\right)^{-1/2}\beta_i\left[\lambda^2 - \lambda^{-1}\right], \quad (4.11)$$

which is the true or Cauchy stress and can be converted to the nominal or the first Piola-Kirchhoff stress using

$$P = \sigma\lambda^{-1}. \quad (4.12)$$

It is of interest to evaluate the total energy dissipated in stretching a sample till all chains are ruptured. This is accomplished by integrating Eq. (4.4) with respect to time,

$$D_{\text{int}} = W - \Delta U, \quad (4.13)$$

where $\Delta U = U(t) - U(0) = U(t)$ is the change in strain energy per unit volume and $W = \int_1^\lambda \frac{\sigma}{\lambda} d\lambda = \int_1^\lambda P d\lambda$.

Material damage is often demonstrated by using cyclic loading and examining hysteresis in the stress between the initial loading and unloading [42]. The behavior of the damage model will also be demonstrated using a cyclic loading pattern as shown in Figure 4.2b). Here we load and unload the sample at a constant rate i.e. $d\lambda/dt = R$ during loading and $d\lambda/dt = -R$ during unloading. After each cycle the maximum stretch reached is increased.

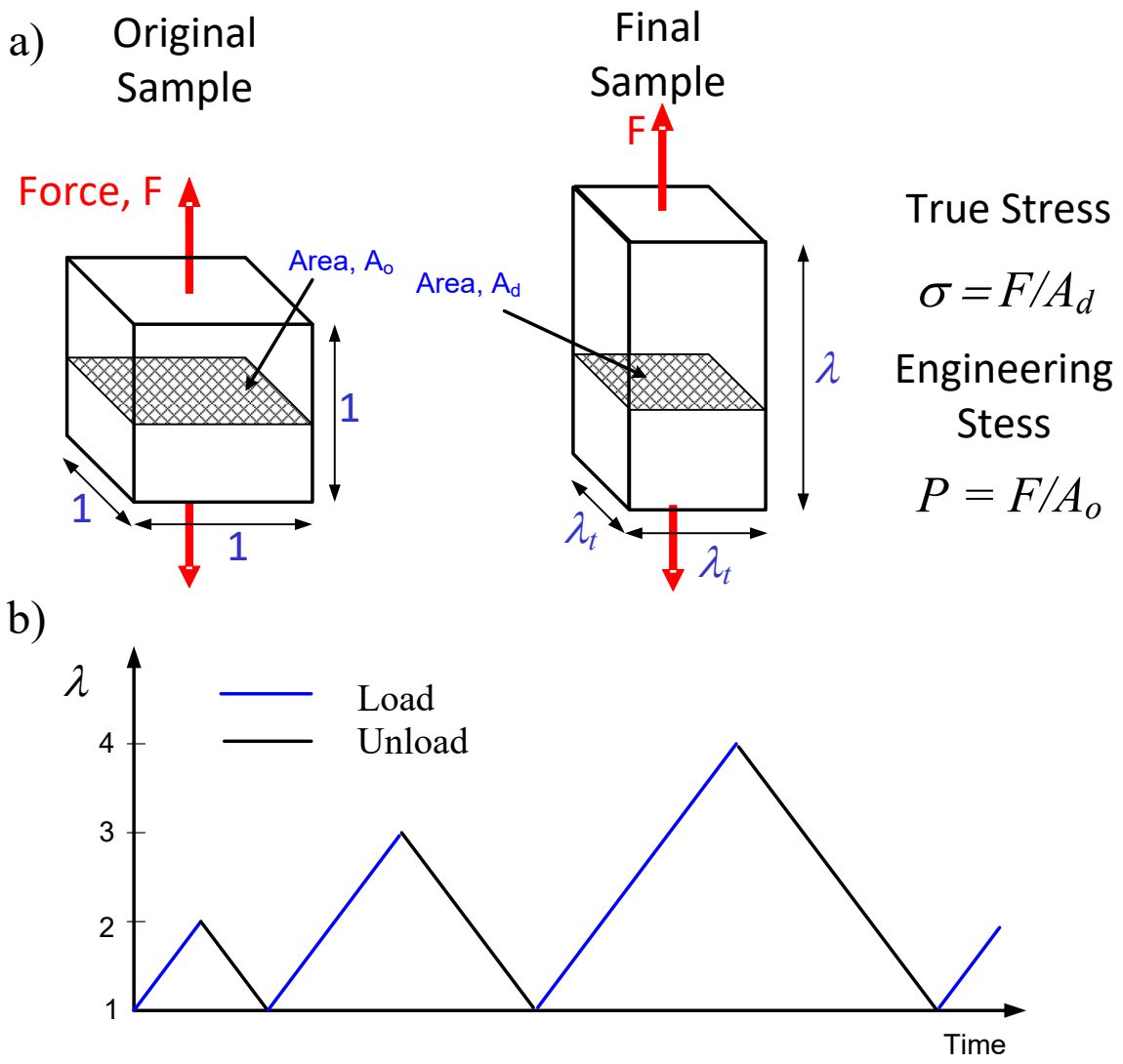

Figure 4.2. a) Schematic of uniaxial deformation where an undeformed sample is stretched axially and unrestrained laterally. b) Example of constant rate cyclic stretching studied in this work; amplitude increases by 1 after each cycle.

To simplify the analysis and discussion we introduce the following non-dimensional parameters

$$\sigma^* = \frac{\sigma}{N_o k_B T}, \quad P^* = \frac{P}{N_o k_B T}, \quad U^* = \frac{U}{N_o k_B T}, \quad W^* = \frac{W}{N_o k_B T}, \quad D_{\text{int}}^* = \frac{D_{\text{int}}}{N_o k_B T},$$
$$F^* = \frac{FA}{k_B T} = \beta, \ \gamma_L = \frac{L_a}{A}, \ R^* = R\tau_-, \ t^* = Rt, \ n_{m,i} = n_R n_i. \tag{4.14}$$

All stresses and energy densities have been normalized with the quantity $N_o k_B T$ which is proportional to the initial shear modulus of the material [40]. The governing parameters for this model are: γ_L, ratio of bond dissociation activation length to Kuhn length; R^*, normalized rate of separation; n_i, number of Kuhn segments for the i^{th} chain length; and n_R, number of monomers per Kuhn length. The stresses σ^* and P^*, surviving chain fraction(s) b_i and the dissipation D_{int}^* are desired outputs. As for the numerical values of the governing parameters used in the next section, n_R has been set equal to 1, L_a has been reported as 0.1nm [29], and A for poly(dimethylsiloxane) is approximately 0.3nm [1] which gives $\gamma_L = 1/3$ and is used in the next section. For different monomer lengths and bond types γ_L could vary and we have performed calculations for other ratios between 0.1 and 0.5 (results not shown). Different values of γ_L give qualitatively similar results with some quantitative differences where larger γ_L enhances the rate of scission. Since physical considerations restrict the range for γ_L to be small (L_a should be on the order of a bond length [2]), its influence is not discussed in this work. Different from γ_L, R^* can vary over many orders of magnitude. In a laboratory setting the rate of stretching R could be on the order of 1/seconds to 1/hours, while in applications elastomeric components could be in service for years and be subjected to slowly changing loads. The characteristic time for bond dissociation can also vary over a large range, for example it was reported as 10^{13} sec [2] for poly(dimethylsiloxane) and high temperature stress relaxation experiments for natural rubber had characteristic times on the order of 10^{-2} sec to 10^{6} sec [44]. Putting these numbers together gives an R^* range of 10^{-10} to 10^{13}. For the sake of demonstration we have chosen a range of R^* from $5\text{x}10^{2}$ to $5\text{x}10^{5}$ which demonstrates both quantitatively and qualitatively the rate dependence of scission. Finally, for the last governing parameter n_i, we have started with a Maxwell-Botzmann distribution [51], $f_{MB}(n)$, with an average chain length of 17.5. Each $b_i(t=0)$ is determined from $b_i(t=0) = f_{MB}(n_i)\Delta n$ (Figure 4.3), where Δn is the width of the numerical bin used to discretize the Maxwell-Boltzmann Distribution. By neglecting (numerically) the tails once the probability dropped below a threshold,

the actual average of the distribution is found to be $n_{avg} = \sum_{i=1}^{m} n_i b_i(t=0) = 17.42$. A relatively short average chain length has been chosen for the distributions to give fast numerical calculations; however once the basic features of the results predicted by the model are understood the extension to predict the results for longer average chain lengths or other distributions should be straightforward. Two cases will be considered: the polydisperse case which uses the distribution of chain lengths (DCL) shown in Figure 4.3, and the case where $M = 1$ and a single chain length (SCL) is chosen to be the average value (17.42) of the distribution in Figure 4.3.

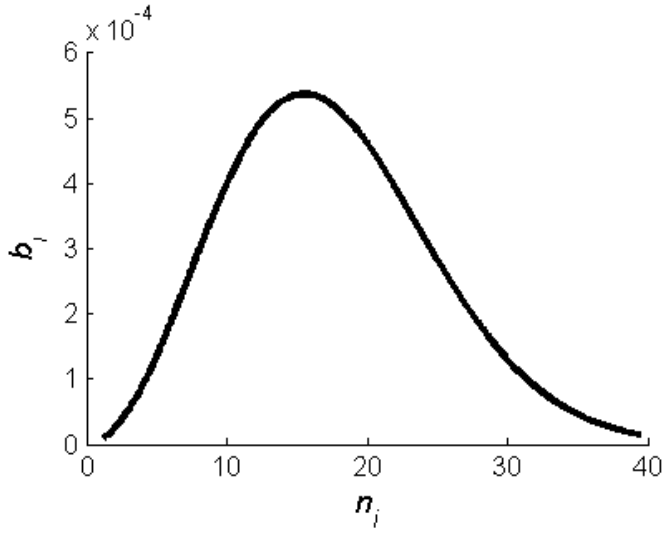

Figure 4.3. Distribution of polymer chain length (b_i) used in this work, based on a Maxwell Boltzmann distribution [51] with average chain length. Tails were neglected once the value was less than a tolerance and average chain length of numerical approximation is $n_{avg} = 17.42$.

Introducing the parameters from Eq. (4.14) into Eqs. (4.3) and (4.11) gives

$$-\frac{db_i}{dt^*} = \frac{n_R n_i b_i}{R^*} e^{\gamma_L \beta_i}, \tag{4.15}$$

and

$$\sigma^* = \lambda P^* = \frac{1}{3}\sum_i b_i(n_i,t)\left(\frac{I_1(\underline{\mathbf{B}})}{3n_i}\right)^{-1/2} \beta_i\left[\lambda^2 - \lambda^{-1}\right]. \tag{4.16}$$

The surviving chain fraction(s), b_i, are calculated by numerically solving Eqs. (4.15) using the 4th order Runge-Kutta method with adaptive step size control [24]. The inverse Langevin function value is obtained using the Newton-Raphson method. Stresses and strain energy can be directly evaluated once b_i and β_i are known at each λ. Dissipation and work can be obtained by integration of the data (non-dimensional versions of Eqs. (4.6) and (S11) in the Appendix 3) using the trapezoid rule.

4.3. Results and Discussion

4.3.1. *Uniaxial Extension*

In Figure 4.4a) the surviving chain fraction, b_t, is plotted against stretch λ, for SCL (black curves) and DCL (blue curves) models. For each model four different rates R^* were used, and the results are represented with different line styles. Initially, the material is unstretched and undamaged, i.e. $\lambda = 1$ and $b_t = 1$. Then the material is stretched with a constant normalized stretch rate R^* until $b_t = 0$; however, the way in which b_t proceeds from 1 to 0 depends on the model and rate of stretching. From Eq. (4.15), slower stretching rates result in more negative initial slope, i.e., the chain fraction will decrease more rapidly with stretch. This is because bond rupture is an irreversible process and slower stretching implies that more time has passed in reaching a given stretch, which allows more bonds to overcome the energy barrier for dissociation leading to more ruptured chains. For SCL as the stretching rate R^* is increased the curves increasingly resemble a reverse step. Here all chains rupture when the stretch reaches a critical value where the chains approach the fully extended state with extremely large chain tension. For DCL there is no longer a single critical chain extension where all chains in the material catastrophically rupture. Rather, shorter chains will reach their critical extension first and rupture at lower stretch. As the stretch continues to increase longer chains will reach their critical extension and rupture. This behavior results in the progressive decrease in surviving chain fractions observed for DCL in Figure 4.4a).

The nominal stress P^* is plotted against the stretch in Figure 4.4b). As in Figure 4.4a) there are curves for both SCL and DCL at four stretching rates. Here we see that at a stretch of unity the stress is zero, further stretching causes the stress to increase and reach a maximum. Finally the stress decreases to zero as all chains are ruptured. At small stretches ($\lambda < 4$) SCL and DCL predict similar stresses. For intermediate stretches ($4 < \lambda < 7$) the DCL stress increases more gradually and reaches a lower peak in comparison to SCL. This is because for a distribution of chain lengths,

at a given stretch, only a small fraction of chains will approach their fully extended state. For larger stretches ($\lambda > 7$), the SCL stress decreases catastrophically, while the decline is gradual for DCL, since the distribution results in more gradual scission of chains seen in Figure 4.4a). If we compare the curves at different stretching rates we can see that faster stretching results in higher peak stresses. To explain, consider the kinetics in Eqs. (4.15). At higher rates R^*, on average a polymer chain will survive to a larger extension before rupture, as seen in Figure 4.4a). This additional extension results in larger polymer chain forces and therefore larger stresses.

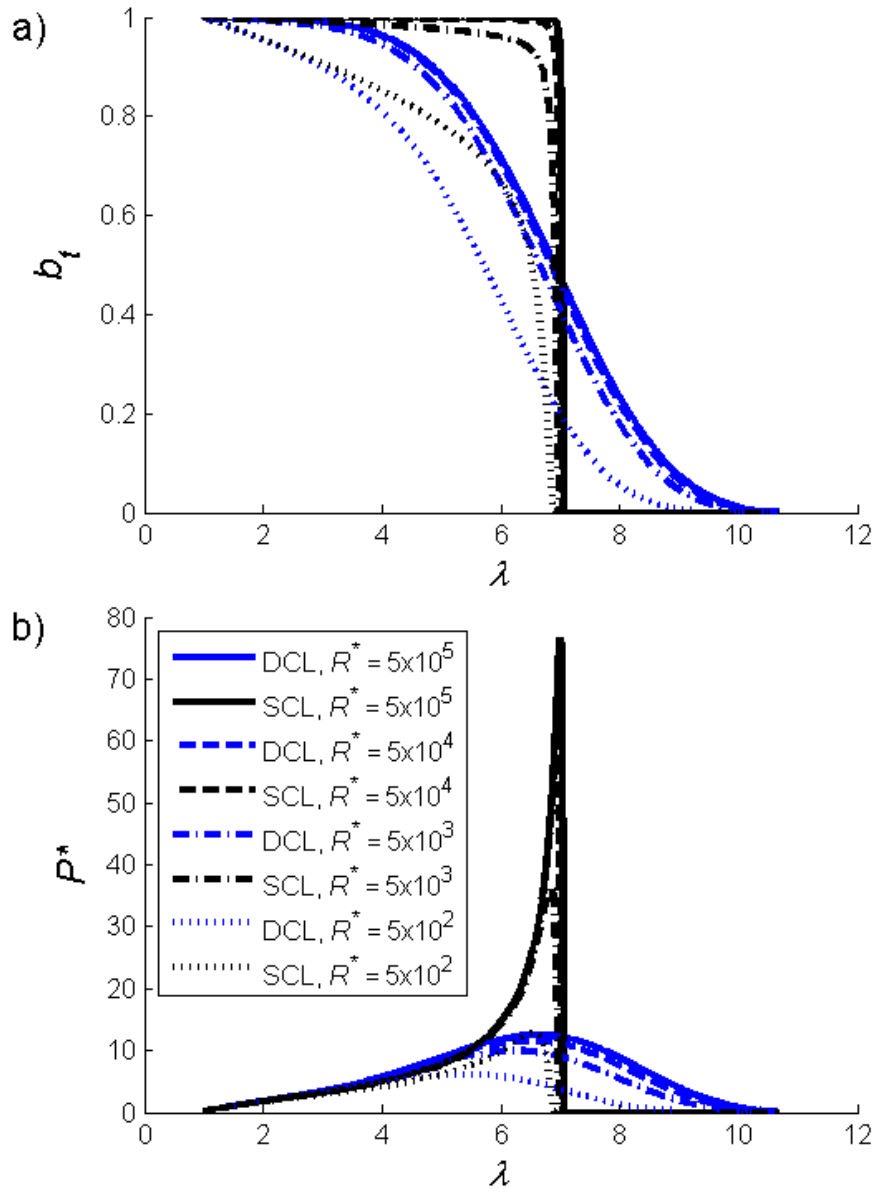

Figure 4.4. Plots for a) surviving chain fraction, b_t, and b) nominal stress, P, obtained by varying the stretch λ while holding $\gamma_L = 1/3$, $n_{avg} = 17.42$ for the SCL model (black) and n_i from Figure 4.3 for the DCL model (blue). Each curve in these figures represents a different use of the SCL/DCL model and four different stretching rates as indicated in the legend.*

In Figure 4.5a) we plot the work, internal dissipation and change in strain energy against the stretch. This data corresponds to $R^* = 5000$ in Figure 4.4. The work W^* represents the area under the stress-stretch curves shown in Figure 4.4b). Both the work and the internal dissipation are monotonically increasing functions. However, the change in strain energy is non-monotonic: it first increases, reaches a peak and decreases afterwards. This behavior is caused by two competing effects: increased deformation which results in higher elastic energy in the chains and decrease in chain density due to scission. At low stretches the work is efficiently transformed into strain energy and dissipation is negligible. At larger stretches the rate of scission, db_i/dt, increases and by Eq. (4.6) the dissipation becomes non-negligible; coinciding with this we can see that the rate of increase in strain energy becomes less than that of the work (this is clearer for DCL). As the stretches further increase, the rate of scission continues to rise, which causes the strain energy to decline. This decline implies that the rate of dissipation can be greater than the rate of work which is evident by comparing slopes of curves in Figure 4.5a). It is interesting to note that when comparing SCL and DCL the work and dissipation both achieve close to the same maximum values. To examine if this is true at other rates, the total dissipation (in rupturing all chains) is shown in Figure 4.5b) for the four stretch rates R^* presented in Figure 4.4. Much like the peak stresses in Figure 4.4b) the total dissipation increases with increasing stretch rate because at faster stretch rates on average the polymer chains will have greater stretch and will release more energy when they rupture. Interestingly, although the stress-stretch curves are drastically different, there is very little difference in dissipation between the SCL and DCL models.

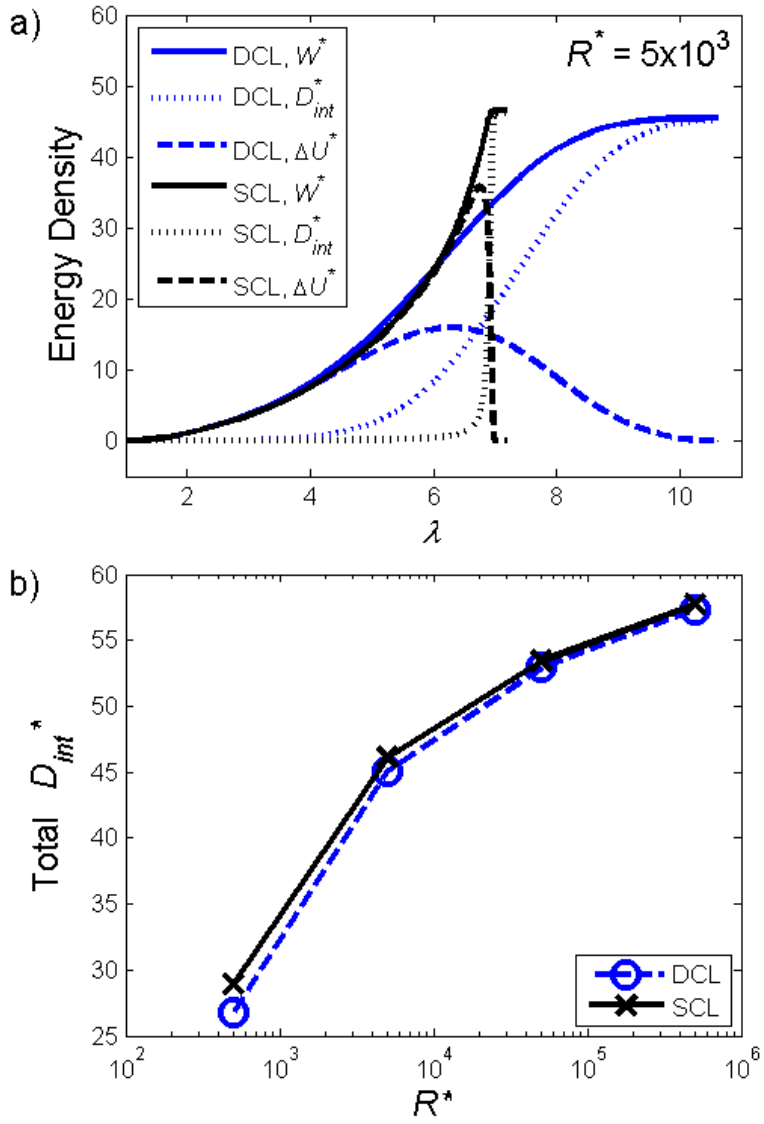

Figure 4.5. a) Plots of the work done on the sample W, energy dissipated D_{int}*, and change in strain energy ΔU* vs. the stretch λ obtained by varying the stretch λ while holding the stretch rate $R^* = 5 \times 10^3$, $\gamma_L = 1/3$, $n_{avg} = 17.42$ in SCL model (black) and n_i from Figure 4.3 for the distribution model (DCL, blue). Each curve in these figures represents a different energy quantity obtained using either SCL or DCL model as indicated in the legend. b) Plots of the total Dissipation (D_{int}*), vs. rate of stretching R^*, in stretching the sample until all chains are ruptured. The two curves represent the two chain models (SCL and DCL) as indicated in the legend.*

4.3.2. *Cyclic Loading*

With the DCL model, shorter chains fail first and progressively longer chains fail with continued stretching. The failure of these chains damages the material so it is of interest to see how the material behaves under cyclic loading. Results for b_t (Figure 4.6a),c),e),g)) and engineering stress (Figure 4.6b),d),f),h)), under cyclic uniaxial loading, are plotted against stretch for the four values of R^* in Figure 4.4. All results are obtained using the DCL model. Loading is shown in blue and unloading is shown in black. Since in some cases the unloading and reloading curves are nearly coincident, it is constructive to consider a typical unloading/reloading cycle for $R^* = 5\text{x}10^5$, A→B→C in Figure 4.6a)-b). At point A the sample has reached the maximum stretch for the current cycle. Damage has occurred due to the loading history, and we can see from Figure 4.6a) that b_t has reduced to 0.6 (i.e. 60% surviving chains). During unloading along the black curve from A to B, negligible additional scission occurs and b_t remains constant (horizontal curve in Figure 4.6a)) till point B, where the sample becomes unstretched and has zero stress. Since from A to B, the material is already damaged ($b_t = 0.6$) and weaker compared with the original undamaged material, there is stress hysteresis in Figure 4.6b) between the black curve (unloading) from A to B and the blue curve representing initial loading to point A. During reloading from B to C up to the point where the stretch at A ($\lambda = 6$) is reached there is negligible additional scission, b_t is still constant and the unloading and reloading stress curves are coincident in Figure 4.6b). On curve B→C once the stretch at A is exceeded ($\lambda > 6$) further damage occurs (decline in b_t in Figure 4.6a)), since now we are exceeding the previous maximum stretch and causing progressively longer chains to rupture due to reaching their critical extension. If we compare Figure 4.6a)-b) with the $R^* = 5\text{x}10^5$ (DCL) data in Figure 4.4a)-b) we can see that the envelopes are nearly identical. For this stretching rate the amount of scission is controlled by the maximum previous stretch in the material; this behavior closely resembles that of the classical Mullins effect [42] in elastomers. For $R^* = 5\text{x}10^4$ the results are shown in Figure 4.6c)-d) and the behavior is qualitatively very similar to that of the faster case. Like Figure 4.4b), the peak stress in the envelope is smaller for slower stretching. There is also a subtle difference between the unloading and reloading curves which is visible as a slightly smaller stress when the reloading reaches the previous maximum stretch (most visible in the stress Figure 4.6d) at $\lambda = 7$ or 8). This difference becomes more pronounced in Figure 4.6e)-f), as the stretch rate is further decreased to $R^* = 5000$. At this relatively slow stretch rate a small amount of scission is evident from A to B in Figure 4.6e); most

of which occurs during the initial phase of the unloading where stretch is highest. Upon reloading from B to C scission also becomes noticeable once the stretch at A is approached, and as a result when we return to the stretch at A ($\lambda = 6$) on the reloading curve the stress is slightly lower (Figure 4.6f)). Finally, at the slowest stretch rate considered here, $R^* = 500$ shown in Figure 4.6g)-h), scission is prevalent along the entire loading history, and significant hysteresis is observed during both unloading and reloading. The peaks stress and the stretch at which all chains rupture (i.e. complete damage) are also significantly decreased.

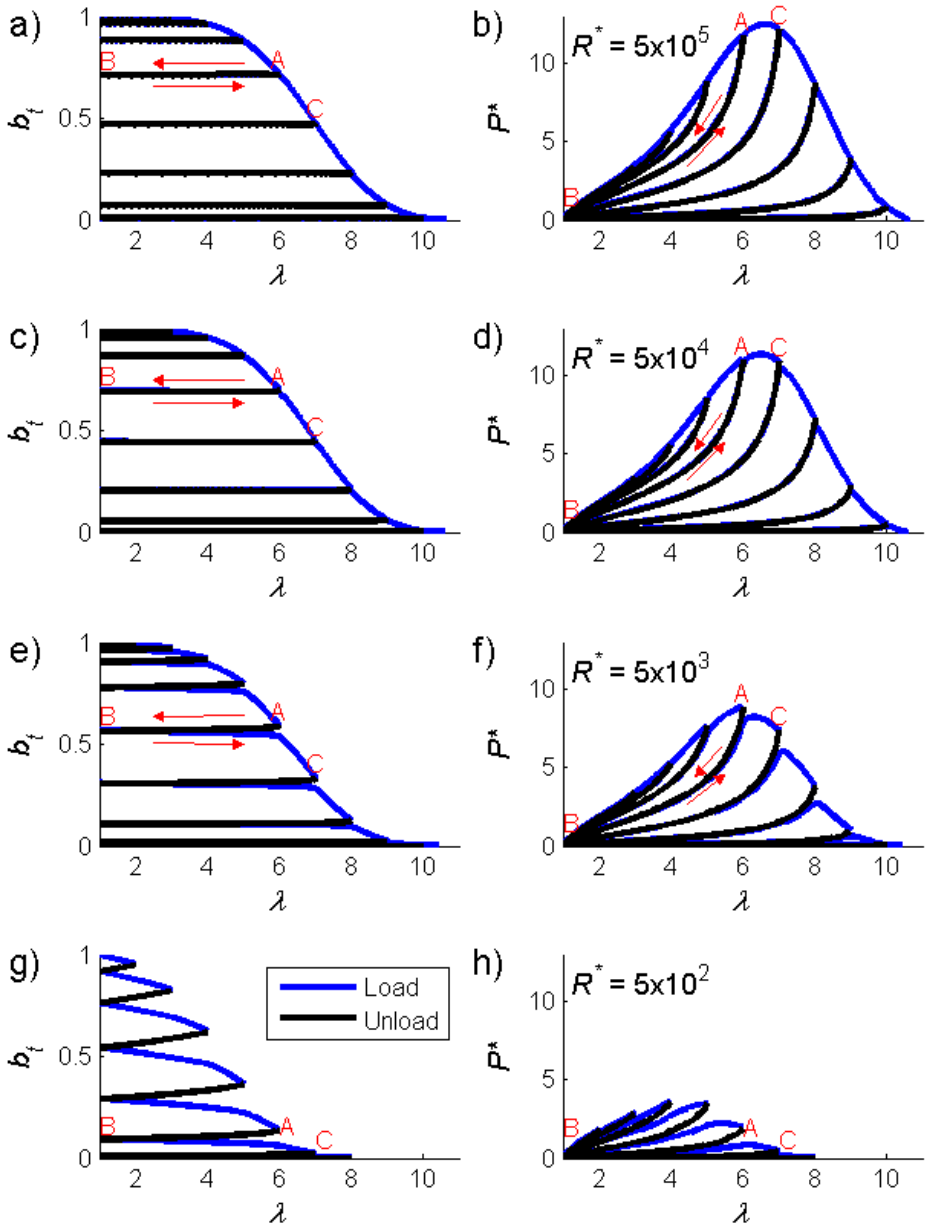

Figure 4.6: a), c), e), g) surviving chain fraction, b_t, and b),d),d),h) nominal stress, P, obtained by varying the stretch λ cyclically while holding $\gamma_L = 1/3$. Loading and unloading curves are indicated in the legend. a),b) are for a stretch rate of $R^* = 5 \times 10^5$. c), d) are for a stretch rate of $R^* = 5 \times 10^4$. e), f) are for a stretch rate of $R^* = 5 \times 10^3$. g),h) are for a stretch rate of $R^* = 5 \times 10^2$.*

4.3.3. *Comparison with Experiments*

In this section we demonstrate how the presented model can be applied to match experimental data for a variety of materials While this model has a strong physical interpretation when applied to unfilled elastomers, its usage should not be limited to this single type of material, and can be extended to other types of elastomers which may have damage mechanisms other than chain scission. In these cases it should be thought of as a phenomenological model which, compared with other phenomenological models that may exist, has the advantage of being able to predict rate dependent damage.

The first comparison we present is for the uniaxial extension test of an abdominal aortic aneurysm [52]. The comparison is given in Figure 4.7 where it can be seen that the theory is able to provide a good fit to the data. The same data were also fitted with an energy limiter model [52], so it is prudent to discuss the key differences between our model and the energy limiter model. The energy limiter approach is a softening hyperelastic model; it generates a stress vs. stretch relationship which mimics that of an elastomer undergoing damage. However, being a softening hyperelastic model there is no dissipation and during unloading the material would exactly follow the loading path backwards. The model presented in the present work has well defined positive dissipation (Eq. (4.6)), which allows for the prediction of the hysteresis between loading and unloading as demonstrated in Figure 4.6. The energy limiter model also has a parameter m which controls the sharpness of the transition to material instability [53]. Small values of m (m = 1) qualitatively resemble the DCL result in Figure 4.4b) while as m is increased the results qualitatively approach the SCL results in Figure 4.4b). The model can phenomenologically capture rate dependent damage if the limiting strain energy were set to be dependent on the deformation rate; however this approach may be challenging to implement for cases with spatially nonuniform deformations or deformation rates that vary over time.

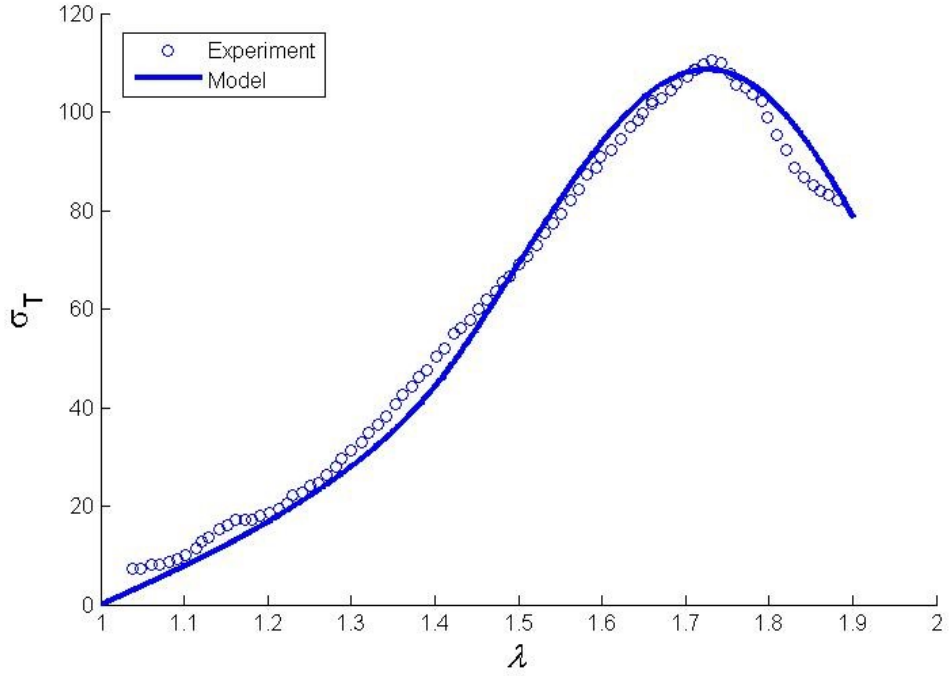

Figure 4.7: True stress (N/cm^2) vs stretch λ showing the comparison between theory and experimental data for the uniaxial extension of an abdominal aortic aneurysm. Experimental data taken from Volokh and Vorp [52]. Fit was obtained by setting $N_o k_B T$ = 11.32 N/cm^2, R^* = 5 x 10^4, γ_L = 1/3, chain length distribution was a shifted Maxwell-Boltzmann distribution (see Appendix 3.4) with average chain length = 1.65 and n_o = 1.2.

Under cyclic loading we have observed that the mechanical response predicted by our model at fast stretching rates is qualitatively similar to that of the Mullins' effect in filled elastomers. It is possible to adjust the parameters in the model to obtain good agreement with cyclic uniaxial extension experimental data where the Mullins' effect is prominent (Figure 4.8). The experimental data has been taken from [54] for GR-S tread vulcanizate. Since the damage in filled elastomers is generally thought to be rate independent and only depend on the previous maximum stretch of the material, we adjust the kinetic parameters to make the rate-dependent model approach the rate independent limit (accomplished by choosing a fast deformation rate R^* = 5 x 10^4).

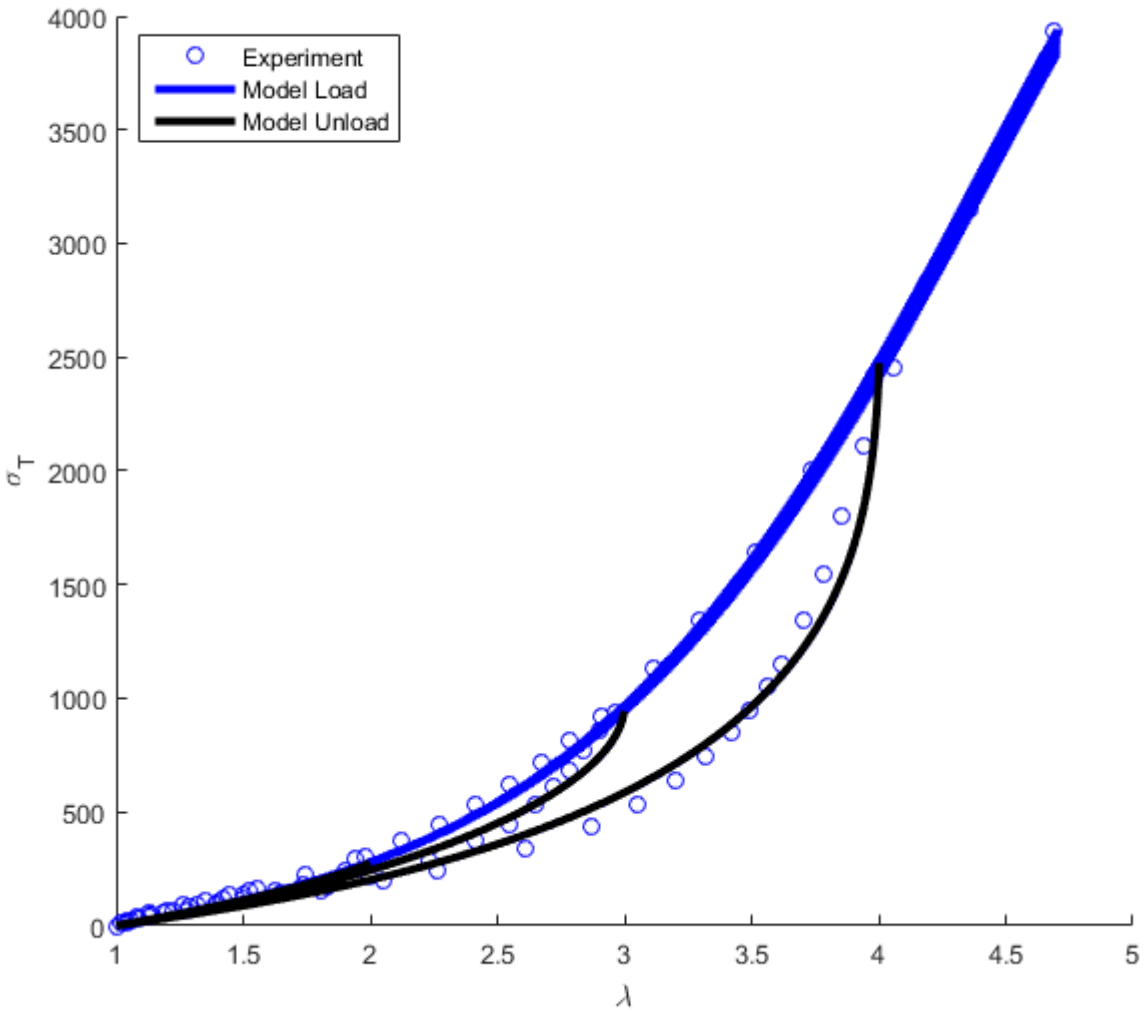

Figure 4.8: True stress (N/cm^2) vs stretch λ showing the comparison between theory and experimental data for cyclic loading of a GR-S tread vulcanizate. Experimental data taken from Mullins and Tobin [54]. Fit was obtained by setting $N_o k_B T$ = 63.77 N/cm^2, R^* = 5 x 10^4, γ_L = 0.04, chain length distribution was a shifted Maxwell-Boltzmann distribution (see Appendix 3.4) with average chain length = 12.2 and n_o = 1.

The third comparison we make is with the cyclic loading of a triple network (TN) elastomer [4]. In the TN elastomer the chains of the first network are prestretched when the second and third networks are added. Due to the nonlinear feature of a polymer chain force extension relationship, the force of a prestretched chain will decrease more rapidly when deformation is decreased. To capture this behavior we alter the deformation gradient used in the evaluation of stress to account

for prestretch; this procedure is described in Appendix 3.3. The second and third networks are neglected in the derivation and the chain length distribution of the first network is tuned to match the experimental data. Similar to what was done for the filled elastomer data we obtain reasonable agreement with the experimental data as shown in Figure 4.9. The primary discrepancy between the model and the experimental data is that the experimental data has noticeably lower stress during the low stretch portion of unloading. This discrepancy could be reduced with a constitutive model that explicitly considers the stress contribution resulting from the second and third networks.

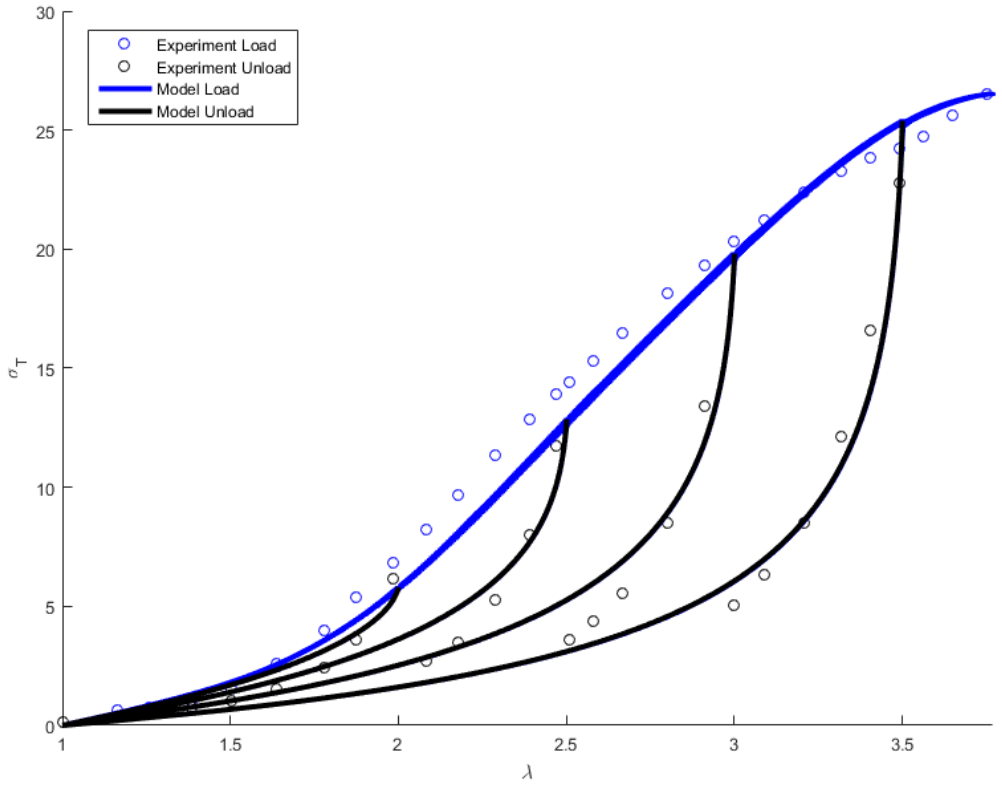

Figure 4.9: True stress (MPa) vs stretch λ showing the comparison between theory and experimental data for the cyclic loading of a TN elastomer. Experimental data taken from Fig 4C of Ducrot et al. [4]. Fit was obtained by setting $N_o k_B T$ = 0.132 MPa, R = 5 x 10^4, γ_L = 0.05, chain length distribution is shown in Figure A3.1 in the Appendix.*

Through the three comparisons above, we have demonstrated that the model can provide good fit to experimental data in absence of rate dependency. However, it should be emphasized that the most novel feature of the model is the capability of predicting rate dependent mechanical behaviors of elastomers. No comparison is made here with experimental data involving rate dependency because in reality the mechanical responses of elastomers have additional sources of rate dependence, such as viscoelasticity. To compare the model with experimental data which also exhibits viscoelasticity, ongoing work will be to couple our model with existing viscoelastic models. In addition, recently there has been an increase in research into the use of dynamic bonds to create structurally dynamic polymers [41]. In this type of material it is very important to have a rate dependent damage model. For example in the transient networks studied by Meng et al [55] a higher peak stress was observed for faster deformation rates; which is in qualitative agreement with the results of our model shown in Figure 4.4b). We will not attempt to match experimental data for this class of materials as these materials also exhibit features such as rearrangement of crosslinks and reforming of physical bonds [55] which is beyond the scope of this work.

4.3.4. *Limitations and Future Considerations*

A damage model was developed to incorporate rate dependent scission into constitutive models for isotropic elastomers undergoing large deformation. While we used the Arruda-Boyce constitutive model [9] as an example, it can be used with any constitutive model which is based upon a polymer chain force extension relationship and a volumetric density of polymer chains. The polymer chain force plays an important role in the rate of scission. Upon reviewing the results it is clear that in many cases the vast majority of polymer chains rupture at large chain extensions (close to being fully extended) where there is a singularity in the force-extension relationship. One limitation is that the tensile force on the chain, which is determined from configurational entropy [9] of a freely jointed (but inextensible) chain, is not entirely accurate when the chain approaches fully extended state. If a force extension relationship which can capture the transition from entropic to enthalpic (stretching of bonds, deformation of bond angles) deformation is used it could quantitatively impact the results and increase the rate-dependency of the dissipation.

Although one of the motivating factors for the development of the model was fracture of elastomers for the examples presented here, to demonstrate the model, we have assumed that the

deformation and all damage remain homogenous throughout the entire process until all chains have been ruptured. In reality this would not be possible as small defects will cause unstable localized damage which would result in premature failure of the sample as observed in the experiments [4, 52]. Our damage model is applicable to general inhomogeneous deformations, and can describe localized damage when implemented in a computational model with defined defect geometry. As such, one area of our ongoing research is to apply the damage model to rate dependent crack initiation and propagation in viscoelastic elastomers. The use of a continuum model with damage will eliminate the need for a cohesive zone model. Allowing for damage in the vicinity of the crack tip should provide physical insight into the processes occurring in this area.

4.4. Conclusion

A model which considers scission in elastomers was developed to study rate-dependent damage under large deformation. The model was demonstrated using uniaxial extension with constant strain rates and cyclic loading for the Arruda-Boyce hyperelastic model. Adding scission allows for the prediction of rate dependent maximum stress, with faster deformations reaching higher maximum stresses. One feature of the model, the consideration of polydispersity (distribution of chain lengths), results in progressive damage during stretching as scission gradually occurs in chains of increasing length. The model has allowed for the prediction of a variety of interesting behaviors under cyclic loading. For fast stretching the damage due to scission is completely controlled by the maximum previous stretch. Negligible scission occurs during unloading a reloading until the previous maximum stretch is exceeded. This behavior closely resembles the ideal Mullins effect in rubbers. As the stretching rate is decreased, the rate dependency of chain rupture causes the amount of scission during unloading and reloading cycles to increase, accompanied by greater hysteresis.

4.5. Nomenclature

Note non-dimensional variables are given in Eq. (4.14)

A	Kuhn length
$b(t)$	Surviving chain fraction
$b_i(n_i,t)$	Surviving chain fraction for chain of length n_i
$\underline{\mathbf{B}} = \underline{\mathbf{F}}\underline{\mathbf{F}}^{\mathbf{T}}$	is the left Cauchy-Green deformation tensor
β	Inverse Langevin Function
D_{int}	Dissipation per unit volume
$\underline{\mathbf{F}}$	is the deformation gradient
F	is the tensile force on a polymer chain
$I_1(\underline{\mathbf{B}})$	1st Invariant of $\underline{\mathbf{B}}$
J	is the determinant of the deformation gradient
k_B	is the Boltzmann constant
L_a	activation length
λ	Stretch
λ_t	Transverse stretch
N	Volumetric Density of load bearing chains
N_o	Initial Volumetric Density of load bearing chains
n_m	The number of monomers per chain
n_i	is a measure of the length of the chain
p	is a Lagrange multiplier to enforce incompressibility
P	Uniaxial extension 1st Piola Kirchoff stress component
r	Polymer chain end to end length
R	Stretch Rate
$\underline{\boldsymbol{\sigma}}$	is the Cauchy stress tensor
σ	Uniaxial extension Cauchy stress component
τ_-	relaxation time for bond dissociation

T	is the absolute temperature
t	time
U	Strain energy density
U_o	Undamaged Strain energy density
W	Work per unit volume

Chapter 5. A continuum model for progressive damage in tough multinetwork elastomers

Abstract

Recently a class of multinetwork elastomers (MNEs) was developed by swelling a primary polymer network with monomers that are subsequently polymerized to form filler networks. Such MNEs were reported to possess remarkable stiffness and fracture toughness while maintaining the ability to sustain large deformation as found in simple elastomers. The enhancement in toughness is attained by prestretching the chains of the primary network through the introduction of one or more filler network(s), thereby promoting energy dissipation through chain scission in the primary network. In this work, a model to capture the mechanical response of MNEs was developed, and validated with experimental data. Prestrech of the polymer chains is incorporated into the model by basing the strain energy of the material on the combined effect of swelling and subsequent deformation of the completed MNE. The primary network is modeled as a polydisperse network of breakable polymer chains with nonlinear chain elasticity, while the filler networks are modeled using the generalized neo-Hookean model. Although the primary network occupies only a small fraction of the material volume, the model shows that it contributes the majority of the stress. Finally, the hysteresis during cyclic loading was found to correlate with the accumulation of damage in the primary network during each cycle.

5.1. Introduction

Elastomers are widely utilized in many industrial and biomedical applications due to their ability to undergo large and reversible deformations. In most of these applications, from traditional industrial applications (e.g. tires) to emerging technologies (e.g. soft robotics and stretchable electronics), elastomeric components are required to sustain certain levels of mechanical loading. Therefore, it is desirable to design elastomers with high fracture toughness to enhance their load carrying capabilities. The first theory describing the intrinsic or threshold fracture of elastomers (in the absence of viscoelastic dissipation) was presented by Lake and Thomas [10], which states that all bonds on a polymer strand between two crosslinks must be stretched to the breaking point before one bond ultimately fails. Thus, the energy to rupture a single polymer strand should scale linearly with the length of the strand l. As a result, the intrinsic fracture energy, estimated by multiplying the energy to rupture a single chain with the areal density of polymer chains across the fracture plane ($\sim l^{-1/2}$), scales with the square root of the average chain length (i.e. $\sim l^{1/2}$). A consequence of this mechanism is that any attempt to increase the stiffness of an elastomer, by increasing the density of crosslinks and thereby decreasing the average chain length, will also make the elastomer more brittle with a decreased intrinsic toughness. This trade-off between stiffness and toughness has been observed in many experimental data [56, 57].

Another route to improve the fracture resistance of materials is to introduce bulk energy dissipation mechanisms, which can lead to the formation of a dissipation zone surrounding a crack [72]. The dissipation zone can prevent the energetic driving force for crack growth, supplied by external loading, from being fully delivered to the crack tip, which enhances the apparent fracture toughness without changing the intrinsic toughness. This is the underlying mechanism for toughness enhancement in filled elastomers [42, 54] where chains can attach and detach from filler particles embedded in the elastomer to dissipate energy, in viscoelastic elastomers[8] where molecular friction provides dissipation, and in interpenetrating networks where dissipation is introduced through the damage of sacrificial networks [58, 59]. The last strategy, i.e. interpenetrating networks, has been implemented in numerous gel systems [58-62], but was only realized in elastomers very recently [4], where a variable fraction of prestretched chains can be built into the elastomer network to control the extent of chain rupture and energy dissipation.

Such interpenetrating multinetwork elastomers (MNEs), as described by Ducrot et al. [4], were created by first forming a crosslinked elastomer, i.e., the "primary" network. This elastomer was then swollen using a solution containing monomers, during which chains of the primary network were stretched. These monomers were then polymerized in place to form a 'filler' network embedded in the primary network. This procedure was repeated to introduce additional filler networks and further stretch the chains in the primary network. To monitor the extent of damage, bond rupture in the primary network around a crack tip was mapped by introducing light emitting photophores into the network. It was hypothesized that the prestretched primary network makes the dominant contribution to stress, while the filler networks mainly serve to prevent large cracks from forming [4]. Validation of this hypothesis, however, is still difficult within the experimental instrumentation. Also, a systematic study of how physical parameters, such as degree of crosslinking and prestretch, impact macroscopic mechanical and fracture behaviors is necessary to optimize the stiffness and toughness of the MNEs, which is challenging with these types of time-consuming experiments. Hence, there is a need to develop quantitative models which can describe the mechanical response of this new class of materials. Such models will allow for an investigation of the relative contributions of each network to the stress. Implementation of such models in finite element analysis will allow for a systematic study of the impact of MNE parameters on the fracture toughness, e.g. how the size of the damage zone around crack tip depends on bulk material properties.

One model has been recently presented for this class of material [63] which is based upon the Mullins effect. In this work, we develop another constitutive model for the MNEs which differs from the previous model in that it considers the physic of polymer chains in the network. Hence all parameters which describe the model have a physical interpretation, which allows for greater insight into how changes to the design of the material will impact the mechanical response. Prestretch of polymer chains is introduced by accounting for the network dilation caused by swelling. Hence each network in the MNE is assigned a unique relaxed state and the respective strain energies are calculated based on different deformations. Because the primary network contains a much higher density of crosslinks and the chains are more severely prestretched than the filler networks, different material models are used to quantify the strain energy contribution from each network. For the primary network the strain energy is based upon a chain elasticity model that couples configurational entropy with deformation of bonds on the backbone of the

polymer chain. On the other hand, the filler networks which contain relatively long and loosely crosslinked chains are modeled using a generalized neo-Hookean model [65]. Progressive damage in the primary network is captured using a kinetic model describing chain rupture, while chain rupture in the filler networks is neglected.

The paper proceeds as follows. The experimental procedures to synthesize MNEs and the subsequent uniaxial tensile testing method are given in Section 5.2. Formulation of the model is presented in Section 5.3 which is divided to present the combined kinematics of swelling and MNE deformation in Section 5.3.1, and the material models in Section 5.3.2. In Section 5.4, the model is applied to uniaxial extension and is compared with experimental data. Conclusions are given in Section 5.5.

5.2. Material and experimental methods

5.2.1. *Reactants*

The monomer ethyl acrylate (EA) and the crosslinker 1,4-butanediol diacrylate (BDA) were purified over a column of activated alumina to remove the inhibitor. The UV initiator, 2-hydroxy-2-methylpropiophenone (HMP) was used as received. Ethyl acetate was used as the solvent. All reagents were purchased from Sigma Aldrich.

5.2.2. *Synthesis*

The synthesis of the MNEs was carried out in a glove box (Mbraun Unilab) under nitrogen atmosphere to avoid side reactions with oxygen in the air. Before introduction into the glove box, every reagent and solvent were bubbled with nitrogen for 45 minutes to remove the dissolved oxygen. The reaction was triggered by UV light (Vilbert Lourmat lamp, model VL-215.L, focused on 365 nm). The UV power was kept low (10 $\mu W/cm^2$) to create slow polymerization.

The preparation of MNEs is carried out in the following waytarting from monomers, a first network (i.e. the primary network) is synthesised, and then multiple steps of swelling and polymerization are conducted to create a multiple network.

5.2.3. *Synthesis of the primary network*

The primary network was prepared from a solution in ethyl acetate consisting of: EA the monomer (50 wt %), BDA the crosslinker (1.45 mol % relative to monomer) and HMP the UV initiator (1 mol % relative to monomer). The solution was cast in a 1 mm thick glass mold and the reaction was initiated by UV for 2 hours. After synthesis, the sample was washed and dried to remove unreacted species and free chains as described in [4, 66]. This single network (SN) is then fully dried under vacuum at 80 °C.

5.2.4. *Preparation of MNEs with a controlled swelling of the primary network*

The synthesis method previously described in [4, 66] has been adapted to obtain a larger range of swelling states of the primary network. The primary network was swollen to equilibrium in a bath composed of monomer and solvent. At equilibrium, a swollen piece of the network was removed from the bath, sealed between PET sheets, and tightened between glass plates. Then a second polymerization, in a similar manner to that of the primary network, was conducted. Then the sample was dried under vacuum at 80 °Cover night to remove the solvent. The resulting material is a double network (DN) elastomer, and its synthesis procedure is schematically depicted in Figure 5.1. This procedure can be then repeated multiple times leading to the creation of a triple network (TN), a quadruple network (QN) and so on, with different volume fractions of each network.

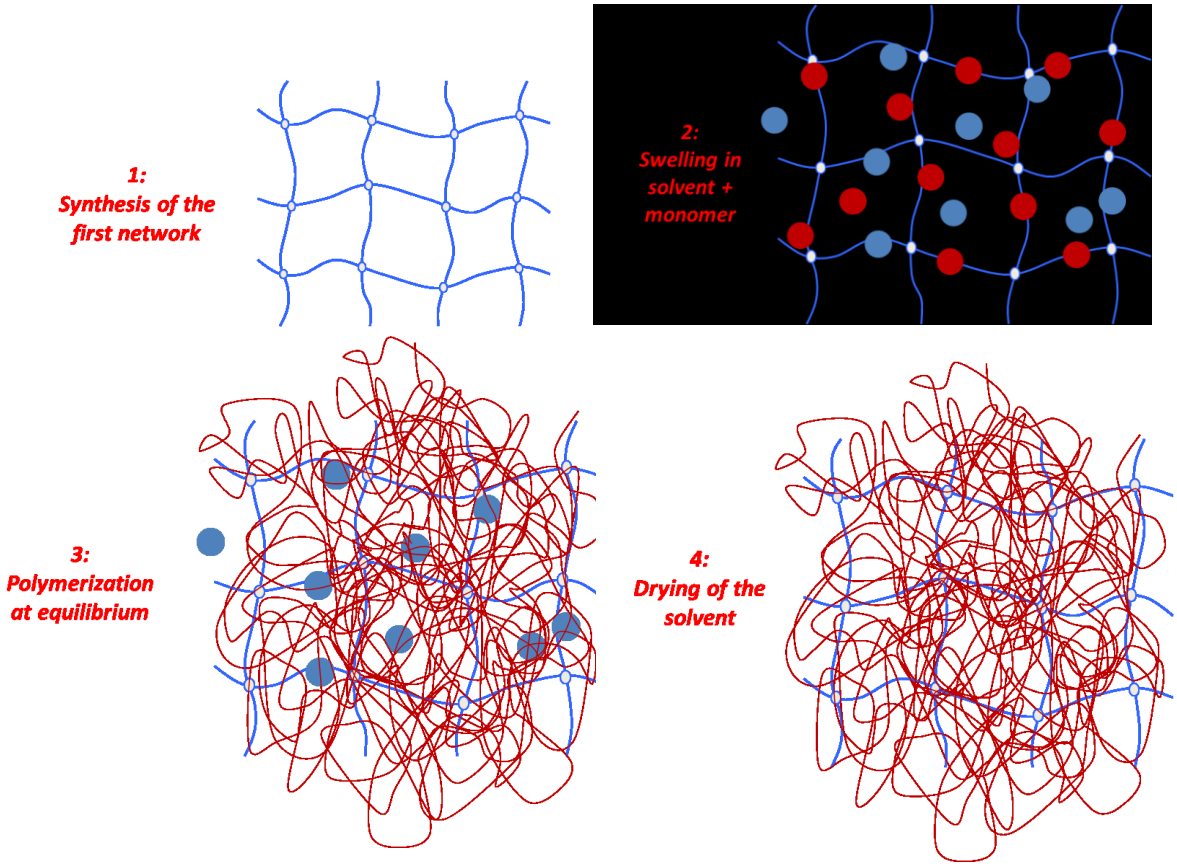

Figure 5.1: Schematics of the synthesis procedure of a double network MNE

5.2.5. *Characterization of the synthesized materials*

To characterize the composition of synthesized MNEs, the mass of a sample is carefully measured after each step. Assuming that (i) all networks have the same density and (ii) the swelling of the networks is isotropic, the prestretch of the primary network λ_0 can be quantified using the measured masses as follows

$$\phi_N^1 = \frac{m_1}{m_N} = \frac{1}{\lambda_0^3}, \tag{5.1}$$

where ϕ_N^1 is the volume fraction of the primary network in an MNE consisting of N networks, m_1 is the mass of the SN sample, and m_N is the mass of the MNE sample.

5.2.6. *Mechanical Tests*

Mechanical tests were performed on a standard tensile Instron machine (model 5565) using a 100 N load cell. A video extensometer gave a local measurement of the stretch $\lambda = L/L_0$ where L_0 is the initial length and L is the corresponding deformed length. The relative uncertainty of the measurements given by the load cell and the video extensometer are respectively 0.1 % in the range of 0 to 100 N and 0.11 % at the full scale of 120 mm. Specimens were cut into a dumbbell shape using a normalized cutter (central part: length 20 mm, cross-section 4 mm and thickness 0.6 – 2.5 mm depending on the sample). Uniaxial tensile tests from small to large strain were performed at a constant 500 $\mu m.s^{-1}$ crosshead velocity and the typical stretch rate on the central part of the sample was around $\dot{\lambda} = 0.04\ s^{-1}$.

5.2.7. *Set of materials*

Mechanical properties of the MNE can be influenced by several factors [4]: (i) number of networks, (ii) type of monomers used in each network, (iii) type of crosslinker, (iv) concentration of crosslinker, and (v) degree of swelling which can be changed by adding a certain amount of solvent to the solution of monomers. In this work, results from our theoretical modeling will be compared with experiments on MNEs in which all networks are comprised of Ethyl Acrylate (EA) but with different crosslinker concentrations and prestretches in the primary network. To be consistent with existing report [67], we use the following notation to denote different MNEs:

EAeX(Y)EA

EA: ethyl acrylate, monomer of the primary network
e: ethyl acetate has been used for the synthesis
X: mol % of crosslinker used for the synthesis of primary network
(Y): **Y**=λ_0, prestretch of the primary network
EA: ethyl acetate, monomer of filler networks.

A summary of the experimental datasets used in this work is given in Table 5.1. A tag is added to each elastomer for a simplified notation as well as to indicate the number of networks. We will be referring to these tags when comparing the modeling results with experiments later. From the base SN elastomer three DN elastomers (DN1-3), with different pre-stretches, are created by controlling the ratio of monomer to solvent during swelling. Three TN elastomers, with different pre-stretches, are synthesised from the DN elastomers; e.g. TN1 is synthesised from DN1. Measurements were also taken for the filler network alone (F), where the crosslinker concentration (0.01 mol%) is 145 times less than that used in forming the primary network. Finally additional DN and TN data were extracted from Ducrot et al [4], DNP and TNP, where the synthesis procedure was similar to that of DN3 and TN3 with the exception that a photophore, chemiluminescent crosslinker bis(adamantly)-1,2-dioxetane bisacrylate, was used in place of BDA.

Table 5.1: Set of MNEs Investigated

Sample name	λ_0	SN wt% $\left(=100\phi_N^1\right)$	Type of network	Number of polymerization steps	Tag
EAe1.45(1)	1	100	SN	1	SN
EAe1.45(1.32)EA	1.32	42.0	DN	2	DN1
EAe1.45(1.51)EA	1.51	29.2	DN	2	DN2
EAe1.45(1.68)EA	1.68	20.5	DN	2	DN3
EAe1.45(2.18)EA	2.18	9.52	TN	3	TN1
EAe1.45(2.41)EA	2.41	7.39	TN	3	TN2
EAe1.45(2.55)EA	2.55	6.06	TN	3	TN3
EAe0.01(1)	1	100	Filler	1	F
EAe1.45(1.48)EA [4]	1.48	30.8	DN	2	DNP
EAe1.45(2.72)EA [4]	2.72	4.97	TN	3	TNP

5.3. Model

5.3.1. *Kinematics*

5.3.1.1. *Swelling*

We number the networks by the order i ($i = 1 \ldots N$) in which they were added to the material, where N is the total number of networks which comprise the material: for a SN $N = 1$, for a DN $N = 2$, and for a TN $N = 3$. Each swelling operation is denoted using the index j which runs from 1 to a maximum value of $N-1$. It is assumed that the swelling is isotropic so that the deformation gradient that maps the network before swelling to its new configuration after swelling is in the form of

$$\underline{\mathbf{\Phi}}_j = \left(J_{sj}\right)^{1/3} \underline{\mathbf{I}} = \lambda_{sj} \underline{\mathbf{I}}, \tag{5.2}$$

where λ_{sj} is the isotropic stretch during the jth swelling, $J_{sj} = \det \underline{\mathbf{\Phi}}_j = \left(\lambda_{sj}\right)^3$ is the volume ratio before and after the jth swelling, and $\underline{\mathbf{I}}$ is the second order identity tensor. The relaxed configuration of each filler network, i.e. the configuration just after this very filler network was polymerized inside the material, will be used as the reference configuration of the filler network from which we measure its deformation. After the jth swelling we obtain a MNE, and if the configuration at this point is set to be the reference configuration of the MNE, the deformation gradient that maps the ith network from its relaxed configuration to the reference configuration of the MNE after the jth swelling is

$$\underline{\mathbf{\Phi}}_j^i = \prod_{k=i}^{j} \underline{\mathbf{\Phi}}_k = \left(\prod_{k=i}^{j} \left(J_{sk}\right)^{1/3} \right) \underline{\mathbf{I}} = \left(\prod_{k=i}^{j} \lambda_{sk} \right) \underline{\mathbf{I}}, \tag{5.3}$$

where Π notation indicates multiplication. For example, consider a TN elastomer just formed ($N = 3$, $j = 2$), the total swelling deformation gradients are given by $\underline{\mathbf{\Phi}}_2^1 = \underline{\mathbf{\Phi}}_2 \underline{\mathbf{\Phi}}_1$ for the primary network, $\underline{\mathbf{\Phi}}_2^2 = \underline{\mathbf{\Phi}}_2$ for the second network, and $\underline{\mathbf{\Phi}}_2^3 = \underline{\mathbf{I}}$ for the third network. Note that the Π notation returns 1 for an empty product, e.g. for a SN elastomer $\underline{\mathbf{\Phi}}_1^1 = \left(\prod_{k=1}^{0} \lambda_{sk} \right) \underline{\mathbf{I}} = \underline{\mathbf{I}}$. Using Eq. (5.3) we can define the ratio between the volume of the ith network after the jth swelling and its volume when it is first introduced:

$$J_{sj}^{i} = \det\left(\underline{\mathbf{\Phi}}_{j}^{i}\right) = \left(\prod_{k=i}^{j} \lambda_{sk}\right)^{3} = \prod_{k=i}^{j} \left(\lambda_{sk}\right)^{3} = \prod_{k=i}^{j} J_{sk} \,. \tag{5.4}$$

In writing the constitutive relationship for this material the contribution from each network will be considered; hence it is necessary to determine the volume fraction of each network that makes up the total MNE volume. The volume fraction that the *i*th network occupies in the material when it is ***first*** introduced ($j = i - 1$) is given by

$$\begin{aligned} \psi^{1} &= 1 \\ \psi^{i} &= 1 - \left(J_{s(i-1)}\right)^{-1} \quad i > 1 \end{aligned} \tag{5.5}$$

which can be explained as follows. After introduction of the *i*th network with the $(i-1)^{\text{th}}$ swelling, the volume of the MNE is increased by a factor of $J_{s(i-1)}$. Assuming all the original material remains intact after swelling, the volume fraction of the original material after this swelling becomes $\left(J_{s(i-1)}\right)^{-1}$. Since the newly introduced filler network occupies the remaining volume, its volume fraction is given by $1 - \left(J_{s(i-1)}\right)^{-1}$. Similarly, subsequent introduction of additional filler networks with the *j*th swelling causes the volume fraction of the existing networks to be divided by a factor of J_{sj}. Therefore, if we extend this idea the volume fraction of the *i*th network when *N* networks are present ($j = N - 1$), denoted by ϕ_{N}^{i}, is obtained by dividing the initial volume fraction ψ^{i} by $J_{s(N-1)}^{i}$

$$\phi_{N}^{i} = \frac{\psi^{i}}{J_{s(N-1)}^{i}}, \tag{5.6}$$

where $J_{s(N-1)}^{i}$ is given by Eq. (5.4). Note that Eq. (5.1) is a special case of Eq. (5.6).

5.3.1.2. *Deformation*

If the MNE, after all swelling operations ($j = N - 1$), is then mechanically deformed, the deformation gradient which maps the reference (i.e. relaxed) configuration of the i^{th} network to the current configuration when *N* networks are present is given by

$$\underline{\mathbf{F}}_{N}^{i} = \underline{\mathbf{F}}\,\underline{\mathbf{\Phi}}_{(N-1)}^{i}, \tag{5.7}$$

where $\underline{\mathbf{F}}$ is the deformation gradient that maps the MNE configuration after all swelling to its deformed configuration. Eq. (5.7) can be understood by considering the example of a TN elastomer for which a schematic of the deformation gradient is shown in Figure 5.2. Four configurations are shown: A when the primary network is formed, B after the primary network has been swollen by a filler network, C after the DN material in configuration B has been swollen by an additional filler network to create a TN, and D after the TN elastomer in configuration C has been mechanically deformed. A is the relaxed configuration for the primary network, B is the relaxed configuration for the second network, and C is the relaxed configuration for the third network. C also represents the reference configuration for the completed TN elastomer relative to which subsequent mechanical deformations are measured.

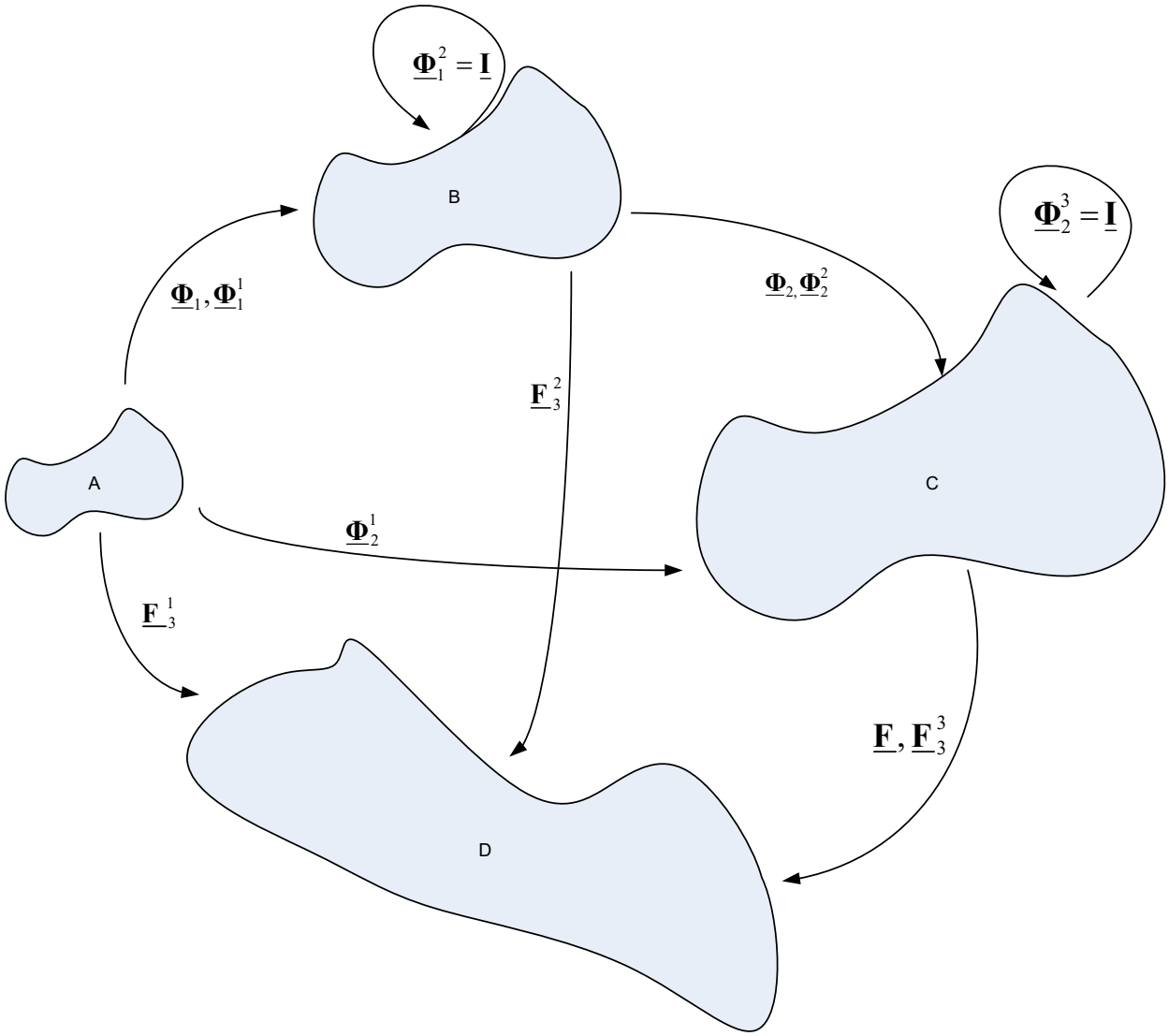

Figure 5.2: Deformation map for a TN elastomer showing reference configurations for the 1st (A), 2nd (B), 3rd (C) networks and the deformed configuration (D). The deformation gradients which relate these configuratiolns are shown schematically.

Spatial forms of constitutive relations are often written in terms of the invariants of the left Cauchy-Green deformation tensor defined as $\underline{\mathbf{B}} = \underline{\mathbf{F}}\underline{\mathbf{F}}^T = \underline{\mathbf{B}}^T$ [68]. Since the swelling pre-deforms

the material we introduce the left Cauchy-Green deformation tensor for each network *i*, denoted by $\underline{\mathbf{B}}_N^i$, which captures both swelling and post-swelling deformation:

$$\underline{\mathbf{B}}_N^i = \underline{\mathbf{F}}_N^i \left(\underline{\mathbf{F}}_N^i\right)^T = \underline{\mathbf{F}}\underline{\boldsymbol{\Phi}}_{(N-1)}^i \left(\underline{\mathbf{F}}\underline{\boldsymbol{\Phi}}_{(N-1)}^i\right)^T = \left(\prod_{k=i}^{N-1} \lambda_{sk}\right)^2 \underline{\mathbf{F}}\underline{\mathbf{F}}^T = \left(J_{s(N-1)}^i\right)^{2/3} \underline{\mathbf{B}}. \tag{5.8}$$

The first, second and third invariants of $\underline{\mathbf{B}}_N^i$ are respectively given by

$$I_1\left(\underline{\mathbf{B}}_N^i\right) = tr\left(\underline{\mathbf{B}}_N^i\right) = \left(J_{s(N-1)}^i\right)^{2/3} tr\left(\underline{\mathbf{B}}\right), \tag{5.9}$$

$$I_2\left(\underline{\mathbf{B}}_N^i\right) = \frac{1}{2}\left[\left(tr\left(\underline{\mathbf{B}}_N^i\right)\right)^2 - tr\left(\left(\underline{\mathbf{B}}_N^i\right)^2\right)\right] = \frac{\left(J_{s(N-1)}^i\right)^{4/3}}{2}\left[\left(tr\left(\underline{\mathbf{B}}\right)\right)^2 - tr\left(\underline{\mathbf{B}}^2\right)\right], \tag{5.10}$$

and

$$I_3\left(\underline{\mathbf{B}}_N^i\right) = \det\left(\underline{\mathbf{B}}_N^i\right) = \left(J_N^i\right)^2. \tag{5.11}$$

where

$$J_N^i = \det\left(\underline{\mathbf{F}}_N^i\right) = \det\left(\underline{\boldsymbol{\Phi}}_{(N-1)}^i\right)\det\left(\underline{\mathbf{F}}\right) = J_{s(N-1)}^i \det\left(\underline{\mathbf{F}}\right). \tag{5.12}$$

In many cases the deformation of the completed MNE can be assumed to be incompressible so that $\det\left(\underline{\mathbf{F}}\right) = 1$. In this case $J_N^i = J_{s(N-1)}^i$.

5.3.2. *Constitutive Model*

The total strain energy per unit volume of the MNE is assumed to be the sum of the contributions from each network ($U_N^i\left(\underline{\mathbf{B}}_N^i\right)$) weighted by its volume fraction (ϕ_N^i), or

$$U_N\left(\underline{\mathbf{B}}\right) = \sum_{i=1}^{N} \phi^i U_N^i\left(\underline{\mathbf{B}}_N^i\right). \tag{5.13}$$

If we assume that the completed MNE is incompressible under further deformation, the Cauchy stress can be computed as follows (see Appendix 4.1)

$$\underline{\boldsymbol{\sigma}}_N = \sum_{i=1}^{N} \underline{\boldsymbol{\sigma}}_N^i = \sum_{i=1}^{N} \phi^i 2 \frac{\partial U_N^i\left(\underline{\mathbf{B}}_N^i\right)}{\partial \underline{\mathbf{B}}_N^i} \underline{\mathbf{B}}_N^i - p\underline{\mathbf{I}}, \tag{5.14}$$

where p is a Lagrange multiplier used to satisfy incompressibility and $\underline{\boldsymbol{\sigma}}_N^i$ represents the contribution to the Cauchy stress from network *i* and is given by

$$\underline{\boldsymbol{\sigma}}_N^i = \phi^i 2 \frac{\partial U_N^i\left(\underline{\mathbf{B}}_N^i\right)}{\partial \underline{\mathbf{B}}_N^i} \underline{\mathbf{B}}_N^i - p^i \underline{\mathbf{I}} \cdot \qquad (5.15)$$

Here $p = \sum_{i=1}^{N} p^i$ and p^i is the contribution to the Lagrange multiplier from network *i*. Note that the determination of p using boundary conditions must be based on $\underline{\boldsymbol{\sigma}}_N$ and not $\underline{\boldsymbol{\sigma}}_N^i$. For the case of uniaxial extension, it is possible to separate p into contributions p^i from each network.

To complete the constitutive relation for the MNE, it is necessary to specify the strain energy density function $U_N^i\left(\underline{\mathbf{B}}_N^i\right)$ for each network. Since the properties of the first (and primary) network usually differ significantly from the filler networks added later, below we propose two different formulations of $U_N^i\left(\underline{\mathbf{B}}_N^i\right)$ for the primary and filler networks.

5.3.2.1. *Primary Network*

The primary network contains a relatively high density of crosslinks. Also, based on experimental measurements with photophores [4] many chains in this network can be ruptured in the bulk material before crack propagation. Therefore, a constitutive model is needed to capture the nonlinear response of polymer chains as they are stretched and ultimately break. In addition, because damage was observed over a range of strains the model must contain a feature which allows the chains to reach critical extensions and break at different times. This has been accomplished in several ways in the literature: polydispersity or a distribution of chain lengths [5] results in shorter chains breaking before longer chains; a distribution of initial end-to-end distance of the chains results in initially more stretched chains breaking before more coiled chains [69]; and different orientations of the chains relative to the principal deformation direction lead to chains aligned with the deformation breaking before unaligned chains [47, 70] . Although in real materials all the previously mentioned effects may be present, we will focus on polydispersity of chain lengths. It should be noted that in this work the distribution of chain lengths is estimated based on experimental measurements of chain rupture in Section 5.4, which effectively captures all effects that contribute to chain breakage at different extensions. Based on the above considerations, for the primary network we propose a strain energy potential in the following form

$$U_N^1 = \mu \int_1^\infty f(N_K)\, b(r_{\max}^*, N_K)\, N_K\, E_{ch}^*(r^*)\, dN_K, \tag{5.16}$$

where, $\mu = \nu\, k_B T$, ν is volumetric density of chains (before any swelling), k_B is the Boltzmann constant, T is the absolute temperature, N_K is the number of Kuhn segments in a polymer chain between crosslinks (i.e. representing the chain length), and $f(N_K)$ is a probability density function which describes the distribution of chain lengths and satisfies $\int_1^\infty f(N_K)\, dN_K = 1$. $r^* = r / N_K A_o$ is the fractional chain extension, where r is the end-to-end distance of the polymer chain and A_o is the Kuhn length of the polymer chain. $b(r_{\max}^*, N_K)$ are a set of damage functions that depend on the chain-length (N_K) and will be described later. $r_{\max}^*$ is the maximum fractional extension a chain has reached in its deformation history, and $E_{ch}^*(r^*) = E_{ch}(r^*)/k_B T$ is the nondimensional chain energy to be discussed next. The integration in Eq. (5.16) accounts for the total contribution of all chain lengths to the strain energy. More details on the derivation of this type of strain energy potential can be found in the following reference [5].

Using the "8-chain" model by Arruda and Boyce [9], the following expression can be written to relate the chain extension r^* to $I_1(\underline{B}_N^1)$

$$r^* = \frac{r}{N_K A_o} = \sqrt{\frac{I_1(\underline{\mathbf{B}}_N^1)}{3N_K}}. \tag{5.17}$$

Introducing a dimensionless chain force as $F_{ch}^*(r^*) = A_o F_{ch}(r^*)/k_B T$, the dimensionless polymer chain energy needed in Eq. (5.16) is calculated from

$$E_{ch}^*(r^*) = \int_{r_o^*}^{r^*} F_{ch}^*(r^*)\, dr^*, \tag{5.18}$$

where $r_o^* = \sqrt{1/N_K}$ is the fractional extension of the chain under load-free condition ($I_1(\underline{\mathbf{B}}_N^1) = 3$). We have chosen to start this integration at r_o^* rather than zero to enforce the zero-strain energy condition at the load-free state where $I_1(\underline{\mathbf{B}}_N^1) = 3$; this choice introduces a constant into the strain energy density and has no impact on the stress predicted by the model.

The kinematic assumption (Eq. (5.17)) implies that the strain energy density depends only on $I_1\left(\underline{\mathbf{B}}_N^1\right)$. One may argue that during swelling there is a large volume change which implies the third invariant $I_3\left(\underline{\mathbf{B}}_N^1\right)$ changes, and for this reason the strain energy can also depend on $I_3\left(\underline{\mathbf{B}}_N^1\right)$. In fact, such a term has often been included in the strain energy function when modeling swelling. For example, Hong et al. include a term $\mu \ln\left(\sqrt{I_3\left(\underline{\mathbf{B}}_N^1\right)}\right)$ for the primary network [75] when modeling a double network hydrogel. On the other hand, this term has been the subject of some controversy in the literature [76] and the discussion remains inconclusive [77]; nevertheless, the effect of such a term is shown to be rather small in most practical cases [77]. Furthermore, in this work we focus on the deformation of a pre-swollen MNE that remains incompressible during post-swelling deformation, in which case $I_3\left(\underline{\mathbf{B}}_N^1\right)$ will be constant, and whether the $I_3\left(\underline{\mathbf{B}}_N^1\right)$ dependency is included in the strain energy density function will not impact our results.

Since U_N^1 depends only on $I_1\left(\underline{\mathbf{B}}_N^1\right)$, we can write

$$\frac{\partial U_N^1\left(I_1\left(\underline{\mathbf{B}}_N^1\right)\right)}{\partial \underline{\mathbf{B}}_N^1} = \frac{dU_N^1\left(I_1\left(\underline{\mathbf{B}}_N^1\right)\right)}{dI_1\left(\underline{\mathbf{B}}_N^1\right)} \frac{\partial I_1\left(\underline{\mathbf{B}}_N^1\right)}{\partial \underline{\mathbf{B}}_N^1} = \frac{dU_N^1\left(I_1\left(\underline{\mathbf{B}}_N^1\right)\right)}{dI_1\left(\underline{\mathbf{B}}_N^1\right)} \underline{\mathbf{I}}$$

Thus, to evaluate the stress in Eq. (5.14) the derivative of the strain energy potential is needed, which can be calculated by

$$\frac{dU_N^1\left(I_1\left(\underline{\mathbf{B}}_N^1\right)\right)}{dI_1\left(\underline{\mathbf{B}}_N^1\right)} = \frac{\mu}{6} \int_1^\infty \frac{f\left(N_K\right) b\left(r_{\max}^*, N_K\right) F_{ch}^*\left(r^*\right)}{r^*} dN_K. \qquad (5.19)$$

There are several models in the literature which can be used to obtain $F_{ch}^*\left(r^*\right)$ or $E_{ch}^*\left(r^*\right)$ [3, 9, 71]; one of the most commonly used models is the Arruda-Boyce model [9]. However, the $F_{ch}^*\left(r^*\right)$ relationship adopted in the Arruda-Boyce model is based on a freely jointed chain model with Langevin statistics, where the chain is inextensible and there is a singularity in chain force when $r^* = 1$. This singular behavior allows only a very small fraction of the chains to experience large forces at any time, which limits the maximum stress that is obtainable. On the contrary, the novel microstructure of the MNE leverages prestretch via swelling to create many chains in the primary network that are subjected to large tensile forces and can rupture during the deformation.

These large tensile forces are sufficient to deform bonds and elongate chains, as discussed in a recent work [73]. Therefore, the Arruda-Boyce or any inextensible model based purely on entropic elasticity will not be suitable for this type of material. Here we use a chain force relationship which we derived that are to be reported in a separate paper [74]

$$F_{ch}^{*} = \frac{1}{2}\left(1 - r^{*}\right)^{-2} - \frac{1}{2} - 2r^{*} \qquad r^{*} < 0.9$$
$$F_{ch}^{*} = \frac{513}{20} + 501\left(r^{*} - 0.9\right) + 26238\left(r^{*} - 0.9\right)^{2} + 68436\left(r^{*} - 0.9\right)^{3} \qquad r^{*} \geq 0.9 \quad . \tag{5.20}$$

This relationship was developed by minimizing the free energy of a polymer chain consisting of configurational entropy and bond deformation energy. Bond deformation is negligible at low extensions and entropic model is used for $r^{*} < 0.9$, while at larger deformations a polynomial function for the chain force is used based on fitting numerical results for PEA [74].

Last, we comment on the damage functions *b*, which represent the fractions of chains that remain intact and are dependent on the number of Kuhn lengths N_K in the chain. *b* equals 1 for undamaged material and decreases as chains are ruptured. The rupture of polymer chains can be modeled using rate dependent nonlinear ordinary differential equations [, 3, 5] where the rate of chain scission depends on the force acting on the bonds in the polymer chain. On the other hand, it was found that [5] if the deformation speed was sufficiently high the damage was nearly rate independent. Extension rates used in the experiment of Ducrot et al fall into this regime and the material exhibited negligible rate dependence [4]. In this work, we focus on this regime and approximate the damage functions by rate-independent functions in the form of $b\left(r_{\max}^{*}, N_K\right)$. These damage functions have been obtained in [74] by numerically solving the rate equations at a given stretch rate in the rate-independent regime, and they are summarized in Appendix 4.2. Since the chain rupture is irreversible, during loading (as $r_{\max}^{*}$ increases) *b* decreases, whereas upon unloading when the chain end-to-end distance r^{*} becomes smaller than $r_{\max}^{*}$, the value of *b* cannot increase.

5.3.2.2. *Filler Networks*

When the filler networks ($i > 1$) are formed the concentration of the crosslinker used is approximately 145 times less than that in the primary network [4]. This results in much longer chain lengths between crosslinks in the filler networks. Since the chains in these networks have

less (or even no) prestretch compared with the chains in the primary network and hence do not experience large fractional extensions, it is plausible to assume that they remain intact (i.e. no rupture) during deformation and their strain stiffening is insignificant. With this consideration, a neo-Hookean material model, which is based on Gaussian freely jointed chains with a linear force extension relationship [77], would seem to be a good choice to represent the filler networks. However, because these networks are so lightly crosslinked, physical entanglements create a strain softening effect at small deformations [4] which cannot be captured by the neo-Hookean model. This softening effect is well described by a molecular model by Rubinstein and Panyukov [78], but it is not straightforward to convert the molecular model into a continuum model for general 3D deformations. Instead, we will use the generalized neo-Hookean constitutive model [65] for the individual filler networks to phenomenologically capture the softening effect:

$$U_N^i\left(I_1\left(\underline{\mathbf{B}}_N^i\right)\right)=\frac{\mu_F}{2n_F}\left\{\left[1+\left(I_1\left(\underline{\mathbf{B}}_N^i\right)-3\right)\right]^{n_F}-1\right\},\ i>1 \qquad (5.21)$$

where μ_F is the shear modulus and n_F is an additional parameter which controls the shape of $U_N^i\left(I_1\left(\underline{\mathbf{B}}_N^i\right)\right)$. Note that a 3rd parameter from the generalized neo-Hookean model [65] was omitted to minimize the number of parameters that are introduced into the MNE model. Like the primary network, the strain energy for each filler network depends only on the first invariant, i.e. $I_1\left(\underline{\mathbf{B}}_N^i\right)$, thus as before to evaluate the stress in Eq. (5.14) the derivative of the strain energy potential is obtained

$$\frac{dU_N^i\left(I_1\left(\underline{\mathbf{B}}_N^i\right)\right)}{dI_1\left(\underline{\mathbf{B}}_N^i\right)}=\frac{\mu_F}{2}\left[1+\left(I_1\left(\underline{\mathbf{B}}_N^i\right)-3\right)\right]^{n_F-1},\ i>1. \qquad (5.22)$$

5.4. Application of the Model

Below we will use the model established above to predict the mechanical response of MNEs under uniaxial loading conditions and compare the results with experimental data. Assuming that the networks contribute independently to the total stress, parameters pertaining to the filler networks will be extracted from available data for these networks alone. Chain length distribution in the primary network will be estimated based on data for DN and TN elastomers with light emitting photophores embedded in the primary network. Finally, comparison will be made to

uniaxial extension and cyclic loading experiments conducted [67] for a variety of MNEs (SN, DN and TN) where the prestretch caused by the first swelling was varied.

Before we proceed, it will be beneficial to specialize the general constitutive model for uniaxial extension. The left Cauchy-Green deformation tensor in this case is given by

$$\underline{\mathbf{B}} = \lambda^2 \underline{\mathbf{e}}_1 \otimes \underline{\mathbf{e}}_1 + \lambda^{-1} \underline{\mathbf{e}}_2 \otimes \underline{\mathbf{e}}_2 + \lambda^{-1} \underline{\mathbf{e}}_3 \otimes \underline{\mathbf{e}}_3 , \tag{5.23}$$

where λ is the stretch of the sample and $\underline{\mathbf{e}}_i$ are orthogonal unit vectors forming the basis of the deformed configuration. Using Eq. (5.8) and the fact that the strain energy potentials depend only on $I_1\left(\underline{\mathbf{B}}_N^i\right)$, Eq.(5.14) can be rewritten as follows

$$\underline{\boldsymbol{\sigma}}_N = 2\left[\sum_{i=1}^{N} \phi^i \left(J^i_{s(N-1)}\right)^{2/3} \frac{dU_N^i\left(I_1\left(\underline{\mathbf{B}}_N^i\right)\right)}{dI_1\left(\underline{\mathbf{B}}_N^i\right)}\right]\underline{\mathbf{B}} - p\underline{\mathbf{I}} \tag{5.24}$$

In uniaxial extension, $\underline{\boldsymbol{\sigma}}_N$ only has one nonzero component which we denote as σ_N. Requiring the other stress components to be zero gives the Lagrange multiplier *p*. Substituting Eq. (5.23) into Eq. (5.24), we can obtain an expression for σ_N

$$\sigma_N = 2\left[\sum_{i=1}^{N} \phi^i \left(J^i_{s(N-1)}\right)^{2/3} \frac{dU_N^i\left(I_1\left(\underline{\mathbf{B}}_N^i\right)\right)}{dI_1\left(\underline{\mathbf{B}}_N^i\right)}\right]\left(\lambda^2 - \lambda^{-1}\right) = \sum_{i=1}^{N} \sigma_N^i \tag{5.25}$$

where the stress contribution from each network is given by

$$\sigma_N^i = \phi^i 2\left(J^i_{s(N-1)}\right)^{2/3} \frac{dU_N^i\left(I_1\left(\underline{\mathbf{B}}_N^i\right)\right)}{dI_1\left(\underline{\mathbf{B}}_N^i\right)}\left(\lambda^2 - \lambda^{-1}\right). \tag{5.26}$$

Note that the stress contribution of each network individually satisfies the uniaxial extension boundary conditions (transverse stress components being zero) as does the total stress of the MNE.

We will extensively compare predictions from the model with experimental data, which without processing, will be the nominal (engineering) stress. For uniaxial extension, the engineering stress can be related to the Cauchy (or true stress) as follows

$$P_N = \frac{\sigma_N}{\lambda}, \tag{5.27}$$

similarly, $P_N^i = \sigma_N^i / \lambda$.

5.4.1. *Extracting Parameters for the Filler Network*

Experiments were conducted on the filler networks alone to determine the parameters μ_F and n_F in Eq. (5.21). The stress for a single filler network alone, P_F, can be evaluated from Eqs. (5.25) and (5.27) by setting $N = 2$, $\phi^1 = 0$, and $\phi^2 = 1$. The experimental data and the best fit are shown in Figure 5.3.

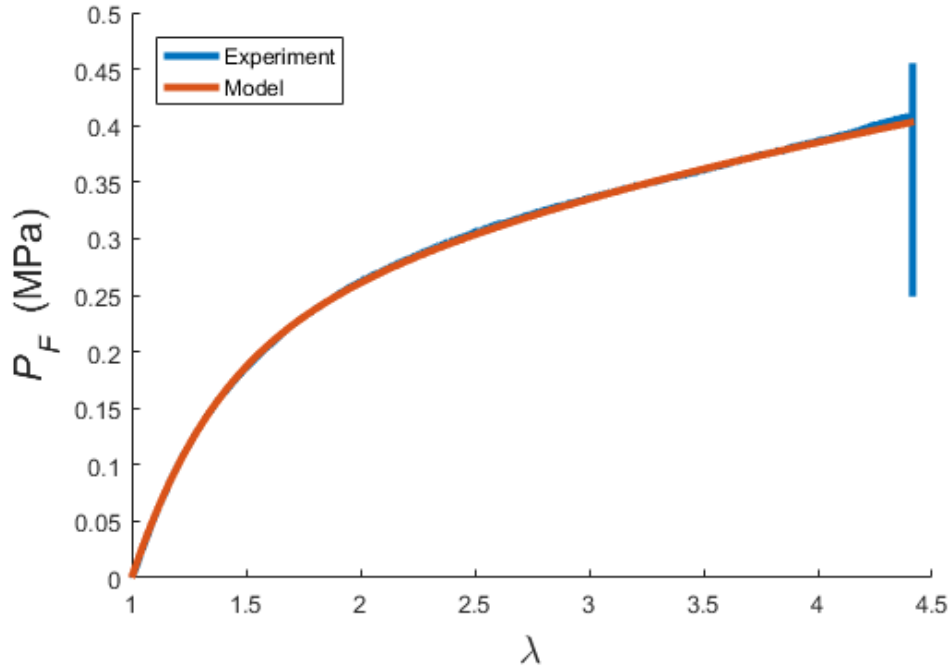

Figure 5.3: Engineering stress plotted against stretch for uniaxial extension of the filler network. The model with parameters $n_F = 0.8325$ *and* $\mu_F = 0.2MPa$ *was found to provide a good fit to the experimental data. The drop in stress at the end of the experimental data occurs because the sample fails.*

5.4.2. *Distribution of Chain Lengths in Primary Network*

Several specialized experiments were conducted for MNEs where photophores were used to crosslink chains in the primary network [4]. These photophores emit light when they rupture, and the recorded light intensity provides a means to estimate the distribution of polymer chain lengths in the primary network. Specifically, when photophores are added to the chains they create weaker

links. If we assume that the rate of chain rupture is proportional to the rate of photophore rupture, the chain length distribution can be correlated to the measured light emission data.

To see this, note that the recorded light intensity was integrated over the sample [4]. Assuming that the elastomer is transparent, so light produced by scission throughout the volume can all be collected, then the light emission intensity can be expressed as

$$LI = -\int_A \alpha_l \nu \int_1^\infty f(N_K) \frac{db\left(r^*_{\max}, N_K\right)}{dt} dN_K D_N dS, \tag{5.28}$$

where α_l is a proportionality constant which relates light intensity to photophore rupture, ν is the volumetric density of chains which is proportional to the density of photophores, t is time, D_N is the thickness of the sample after the $(N-1)^{\text{th}}$ swelling, and S is the area of the sample perpendicular to the thickness direction. Under homogeneous deformation during uniaxial extension, Eq. (5.28) can be rewritten as follows

$$LI = \beta_l \int_1^\infty f\left(N_K\right) \frac{db\left(r^*_{\max}, N_K\right)}{dt} dN_K, \tag{5.29}$$

where $\beta_l = -\alpha_l \nu V_N$ and $V_N = D_N S$ is the constant volume of the sample. To evaluate $db\left(r^*\right)/dt$ consider

$$\frac{db}{dt} = \frac{db}{dr^*_{\max}} \frac{dr^*_{\max}}{dI_1\left(\underline{\mathbf{B}}^1_N\right)} \frac{dI_1\left(\underline{\mathbf{B}}^1_N\right)}{d\lambda} \frac{d\lambda}{dt} = \frac{db}{dr^*_{\max}} \frac{r^*_{\max}}{2I_1\left(\underline{\mathbf{B}}\right)} \left(2\lambda - 2\lambda^{-2}\right) \frac{d\lambda}{dt}, \tag{5.30}$$

where $\dfrac{dr^*_{\max}}{dI_1\left(\underline{\mathbf{B}}^1_N\right)} = \dfrac{r^*_{\max}}{2I_1\left(\underline{\mathbf{B}}^1_N\right)} = \dfrac{r^*_{\max}}{2\left(J^1_{s(N-1)}\right)^{2/3} I_1\left(\underline{\mathbf{B}}\right)}$ and $\dfrac{dI_1\left(\underline{\mathbf{B}}^1_N\right)}{d\lambda} = \left(J^1_{s(N-1)}\right)^{2/3}\left(2\lambda - 2\lambda^{-2}\right)$ are respectively obtained from Eq. (5.17) and Eqs. (5.9) and (5.23), $db / dr^*_{\max}$ is known based on the damage functions presented in Appendix 4.2, and $d\lambda / dt$ is the speed of stretching from the experiment. If r^* does not exceed its previous maximum value, no additional damage will occur and Eq. (5.30) should be taken to be zero.

In general, the rupture of bonds follows certain kinetics and will not occur at the same extension even for chains of the same length. However, the damage will be concentrated near the vicinity of highest extension. This allows us to simplify Eq. (5.30) by approximating

$db\ / dr^*_{\max} = -\delta\left(r^*_{\max} - r^*_{pk}\right)$ where δ is the Dirac delta distribution and r^*_{pk} is the extension at which the peak value of $db\ / dr^*_{\max}$ occurs (see Appendix 4.2). Introducing this approximation and Eq. (5.30) into Eq. (5.29) gives

$LI = -\beta_l \dfrac{\left(\lambda - \lambda^{-2}\right)}{\left(\lambda^2 - 2\lambda^{-1}\right)} \dfrac{d\lambda}{dt} \int_1^\infty f\left(N_K\right)\, \delta\left(r^*_{\max} - r^*_{pk}\right) r^*_{\max}\, dN_K = -\beta_l \dfrac{\left(\lambda - \lambda^{-2}\right)}{\left(\lambda^2 + 2\lambda^{-1}\right)} \dfrac{d\lambda}{dt} f\left(N_K\left(r^*_{pk}\right)\right) r^*_{pk}$, which can be rearranged to solve for $f\left(N_K\left(r^*_{pk}\right)\right)$

$$f\left(N_K\left(r^*_{pk}\right)\right) = \frac{LI(\lambda)}{-\beta_l r^*_{pk} \dfrac{d\lambda}{dt}} \frac{\left(\lambda^2 + 2\lambda^{-1}\right)}{\left(\lambda - \lambda^{-2}\right)}, \qquad (5.31)$$

where $N_K\left(r^*_{pk}\right) = I_1\left(\underline{\mathbf{B}}^1_N\right) / 3r^{*2}_{pk}$. Based on Eq. (31), the experimentally measured light emission data was converted into a chain length distribution, as shown in Figure 4. A probability distribution function in the form of Eq. (5.32) was found to provide a good fit for the chain length distribution measured from light emission data (see Figure 5.4)

$$f\left(N_K\right) = \begin{cases} A_f \left(N_K - N_{\min}\right)^{a_f} \exp\left(-b_f \left(N_K - N_{\min}\right)\right) & N_K \geq N_{\min} \\ 0 & N_K < N_{\min} \end{cases}, \qquad (5.32)$$

where $N_{\min}$ is the minimum number of load bearing Kuhn segments present in the material, a_f and b_f control the shape of the probability function, and A_f is used to ensure the normalization requirement $\int_1^\infty f\left(N_K\right) dN_K = 1$ is satisfied. a_f, b_f, and $N_{\min}$ are the three parameters extracted from the fitting. In Figure 5.4, light emission data are not available for large chain lengths since the material already failed, so the fitting curve is a smooth extrapolation of the measured data.

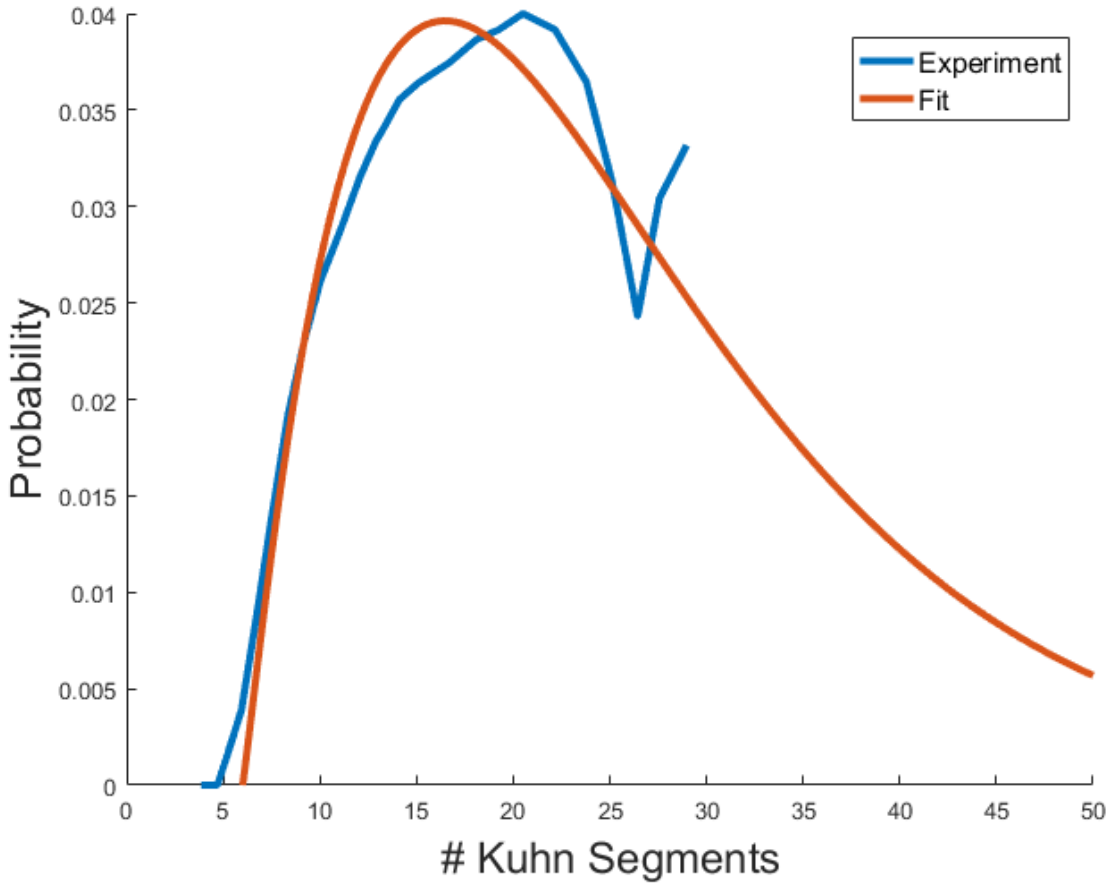

Figure 5.4: Chain length distribution estimated by fitting light emission data. $N_{\min} = 6$, $a_f = 1.1$, $b_f = 0.105$. *Light emission experimental data from Ducrot et al [4] are converted to chain length probability using Eq.(5.31).*

5.4.3. *Uniaxial Extension of MNE*

Model prediction will be compared with two groups of experiments: MNEs with and without photophore. The chain length distribution from Figure 5.4 was applied directly to the MNE with photophore. Whereas for the MNE without photophore, the same form of distribution (Eq. (5.32)) was used but the parameters $N_{\min}$, a_f and b_f were slightly different from those in Figure 5.4. The same tuned distribution was used for all the experiments without photophore, which involved several data sets with different pre-stretches.

5.4.3.1. *With Photophore*

For the experiments on MNEs with photophores [4], i.e., DNP and TNP from Table 5.1, the prestretches of the networks are $\lambda_{s1} = 1.48$ and $\lambda_{s1}\lambda_{s2} = 2.72$, respectively. μ in Eq. (5.16) is related to the volumetric density of chains in the primary network before any swelling, and is a fitting parameter since no SN data was available for MNE with photophores. When used with the chain length distribution in Figure 5.4, it was found that $\mu = 0.264MPa$ and a slightly adjusted value of $\lambda_{s1} = 1.54$ provided the best fit to the experimental data for both DN and TN elastomers while $\lambda_{s1}\lambda_{s2} = 2.72$ was held fixed so that $\lambda_{s2} = 1.77$. The comparisons are shown in Figure 5.5, where the model reproduces all the key features observed in the DN and TN data. For example, the model correctly predicts the small initial slope observed in the stress-stretch curve for both the DN and TN; the slope is small in this region because no chains are sufficiently stretched to create large forces. With further stretching the shortest chains become highly stretched to cause an upturn in the stress, which is observed in both the model and the experimental data. Finally, for the TN with further stretching damage accumulates and causes a second inflection point after which the stress-stretch curve levels off. This phenomenon is not observed in the DN because the material fails before sufficient damage can occur.

It is of interest to calculate the extension of individual chains under the bulk deformation. Because there is a distribution of different chain lengths in the primary network, these chains are subjected to different extensions at the same bulk deformation. The chain extension as a function of the number of Kuhn segments (i.e. chain length) are shown in Figure 5.6, for the chains in the primary network of the SN, DN and TN elastomers. Results are shown for two different bulk stretches: $\lambda = 1$, corresponding to undeformed elastomers, and $\lambda = 2$. Both swelling (from SN to DN and then to TN) and additional bulk deformation (from $\lambda = 1$ to $\lambda = 2$) increase the fractional extension, and their impacts are more significant for chains with shorter length. For the TN with $\lambda = 2$ the large fractional extensions for small N_K have caused material damage. To quantify the damage, we define the following quantity

$$b_N = \int_1^\infty f(N_K)\, b\left(r^*_{\max}, N_K\right) dN_K, \tag{5.33}$$

which represents the fraction of surviving load bearing chains in the primary of an MNE with a total of N networks. The evolution of damage for the TN elastomer is presented in Figure 5.7a). No damage is observed until a sufficient stretch (above 1.5) is reached that causes the shortest chains to break. Afterwards b_3 steadily decreases with additional stretching as more chains are ruptured.

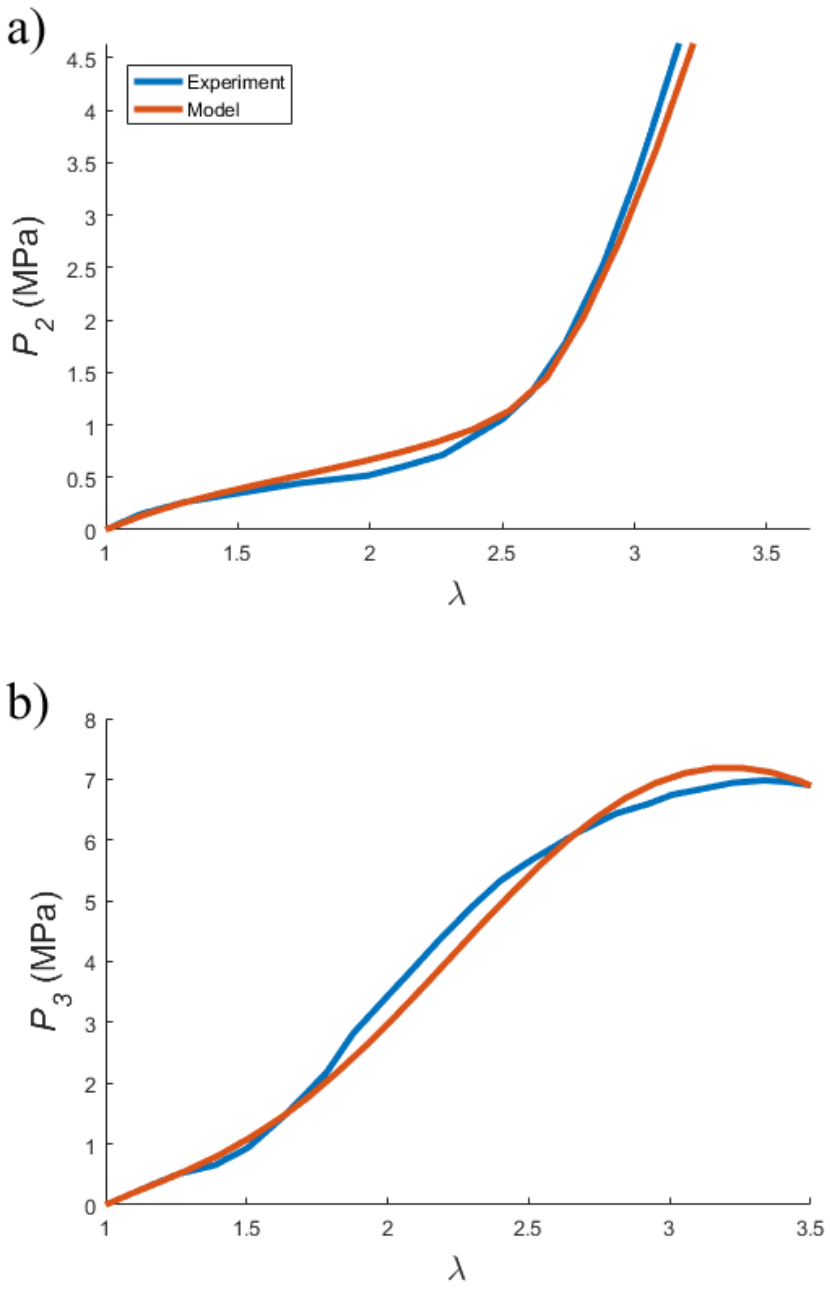

Figure 5.5 Engineering stress plotted against stretch for uniaxial extension of (a) double network elastomer, (b) triple network elastomer. The following prestretches $\lambda_{s1} = 1.54$, $\lambda_{s2} = 1.77$ *and parameter* $\mu = 0.264MPa$ *were found to give good agreement with the experimental data. Experimental data from Ducrot et al [4].*

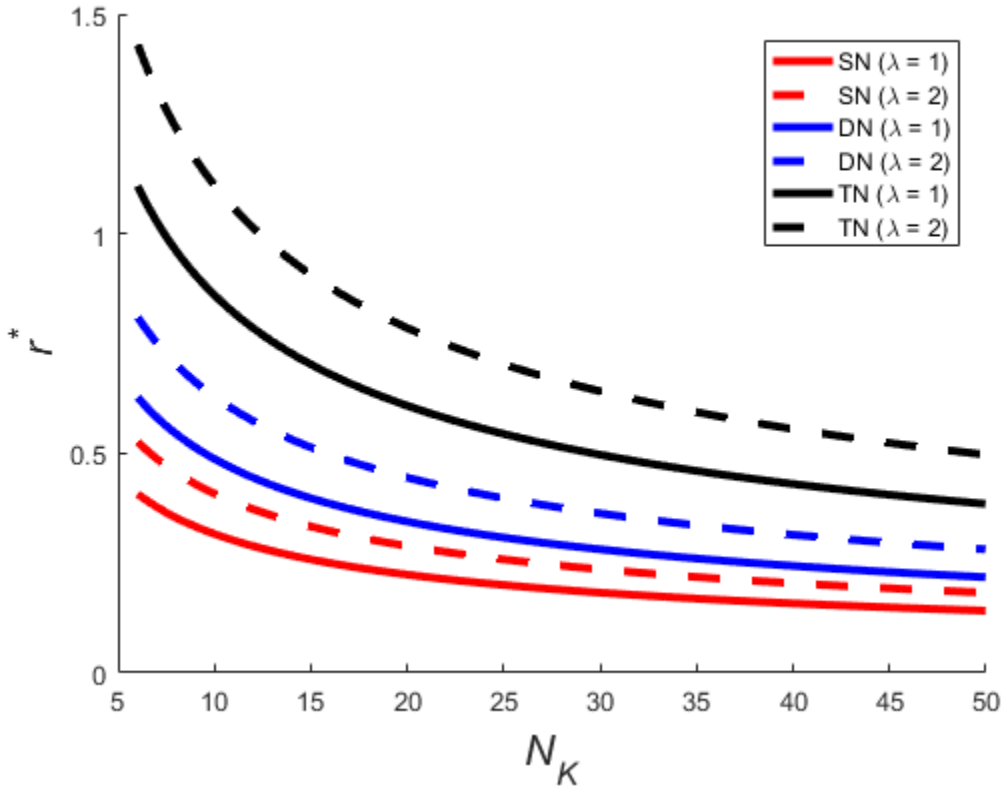

Figure 5.6 Fractional extension plotted against number of Kuhn segments for individual chains in the primary network of SN, DN and TN elastomers.

Using the two prestretches and Eqs. (5.4) to (5.6), the volume fractions of each network can be calculated to be: for the DN elastomer $\phi_2^1 = 0.274$, $\phi_2^2 = 0.726$; for the TN elastomer $\phi_3^1 = 0.05$, $\phi_3^2 = 0.13$, and $\phi_3^3 = 0.82$. The prevailing hypothesis with these materials is that the chains in the primary network (i = 1) control the stress whereas the subsequent filler networks prevent large cracks from forming [4]. To test this hypothesis for the TN elastomer we compared the contribution of each network to the total stress which is presented in Figure 5.7b). In agreement with the hypothesis, the primary network provides most of the stress (P_3^1), while the contributions of the filler networks (P_3^2, P_3^3) are almost negligible although they occupy an estimated 94% of the material volume.

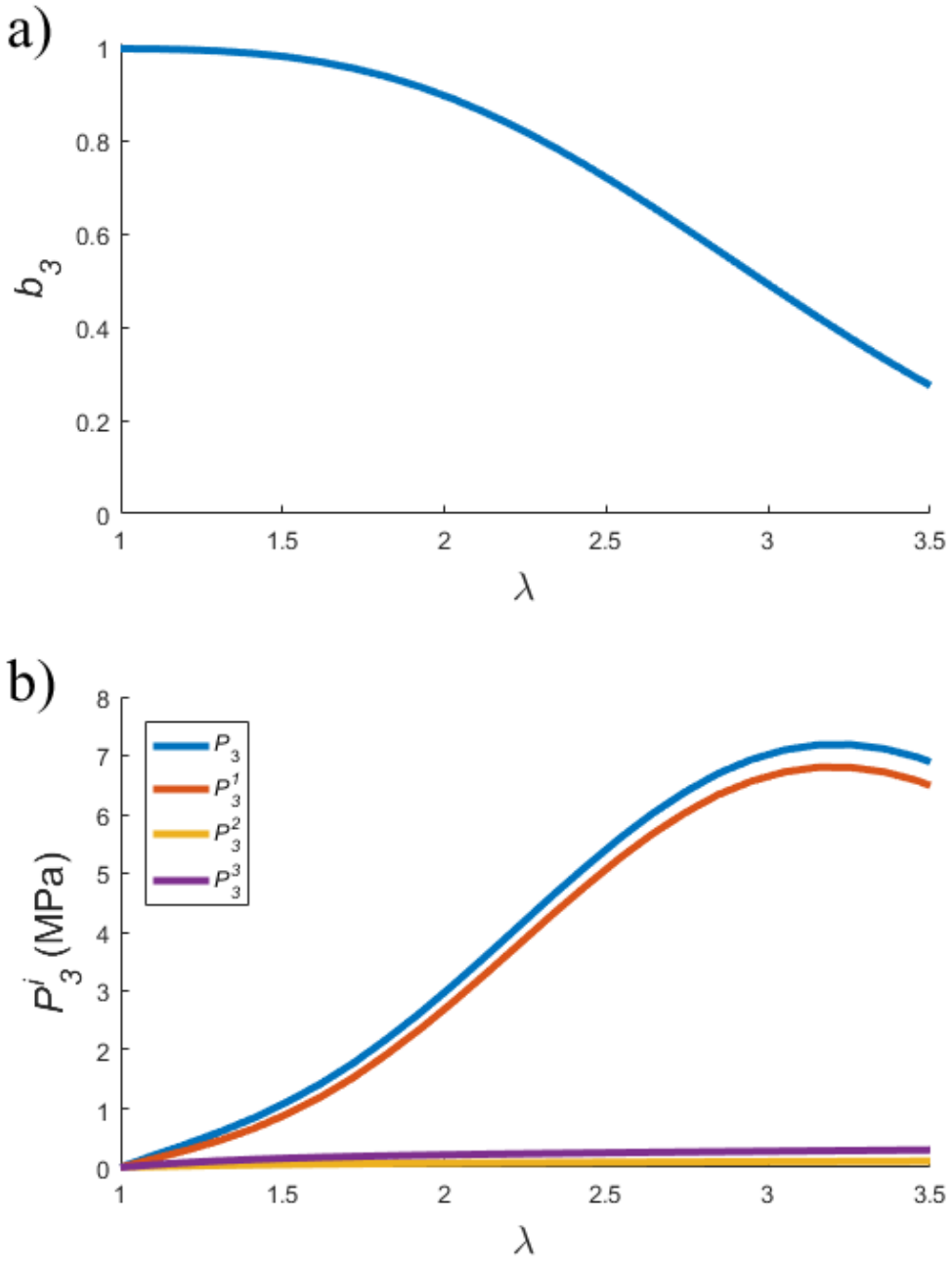

Figure 5.7: (a) The evolution of damage in the primary network of the TN elastomer is shown by plotting the surviving chain fraction (b_3) against stretch. (b) Contribution from each network to the engineering stress of a TN elastomer under uniaxial extension, plotted against stretch.

5.4.3.2. *Without Photophore*

For the MNEs without photophores, we consider three datasets, with different swelling ratios, which were formed from the same original SN. The stress-stretch curve for the SN is shown in Figure 5.8, and matching the initial slope provides $\mu = 0.215MPa$ which will be used for the primary network in all the MNEs. In each case experimental measurements of thickness, percentage of primary network (based on weight), stretch and stress are available. Measurements of sample thickness and weight (Table 5.2) can be used to estimate the prestretch of the networks. Here %SN is the percentage of weight of the primary network obtained by weighing the sample before and after swelling. Since the primary and filler networks are comprised of the same monomers, it is reasonable to assume that all the networks have the same density. This allows the measurement to be directly converted to volume fractions, i.e., % SN = $100\phi_N^1$, which can then be used to determine J_{sj} using Eqs. (5.4) and (5.6). J_{sj} can also be calculated using $J_{sj} = \left(D_{j+1} / D_j\right)^3$, and the values obtained from the two different approaches can be slightly different, see comparison in Table 5.3. For this reason, and due to variations observed in samples with the same crosslink density and swelling (see Appendix 4.4), we allow a small amount of tunability in the chosen values of J_{sj}, tabulated in Table 5.3, to ensure that key features in the mechanical response are properly captured. Finally, other intermediate swelling variables calculated from J_{s1} and J_{s2} are tabulated in Table 5.4.

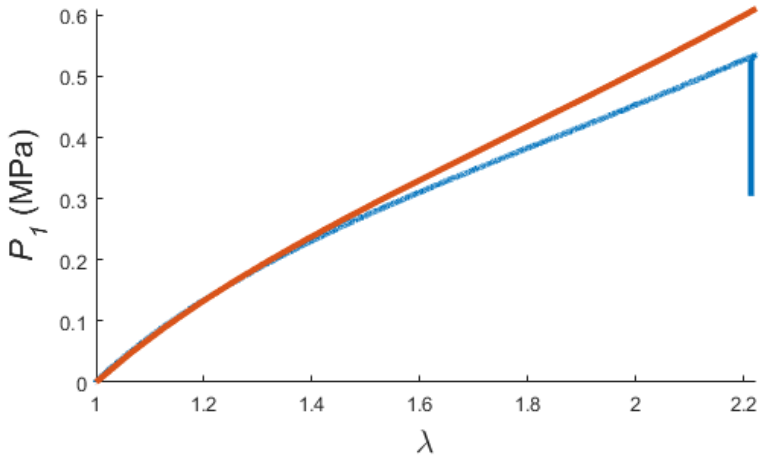

Figure 5.8: Engineering stress plotted against stretch for uniaxial extension of SN elastomer. Experimental data and model fit (with $\mu = 0.215MPa$) are shown.

Table 5.2: Swelling Data for the 3 datasets.

Before Swelling			After 1st Swelling			After 2nd Swelling		
Sample	% SN	D0 (mm)	Sample	%SN	D1 (mm)	Sample	%SN	D2 (mm)
SN	100	0.74	DN1	42	0.97	TN1	9.52	1.6
SN	100	0.74	DN2	29.17	1.13	TN2	7.39	1.79
SN	100	0.74	DN3	20.55	1.27	TN3	6.07	1.84

Table 5.3: Swelling Ratios Estimated by two approaches and the final Chosen values. DN and TN in each dataset share the same J_{s1} values while J_{s2} values are only applicable to TN samples.

Sample	Estimate using *D*i		Estimate Using %SN		Value Used	
	J_{s1}	J_{s2}	J_{s1}	J_{s2}	J_{s1}	J_{s2}
DN1/TN1	2.25	4.49	2.38	4.41	2.41	4.13
DN2/TN2	3.56	3.97	3.43	3.95	3.65	3.33
DN3/TN3	5.05	3.04	4.87	3.39	5.36	2.74

Table 5.4: Calculated Swelling Parameters. DN and TN in each dataset share the same J_{s1}^1 values while J_{s2}^1 and J_{s2}^2 values are only applicable to TN samples. ϕ_2^1 and ϕ_2^2 are volume fractions in DN samples, whereas ϕ_3^1, ϕ_3^2 and ϕ_3^3 are for TN samples.

Sample	J_{s1}^1	J_{s2}^1	J_{s2}^2	ϕ_2^1	ϕ_2^2	ϕ_3^1	ϕ_3^2	ϕ_3^3
DN1/TN1	2.41	9.94	4.13	0.42	0.58	0.10	0.14	0.76
DN2/TN2	3.65	12.17	3.33	0.27	0.73	0.08	0.23	0.70
DN3/TN3	5.36	14.71	2.74	0.19	0.81	0.07	0.29	0.64

When no photophores are incorporated into the polymer network there is no light emission data from which the chain length distribution can be extracted. However, since these MNEs use the same density of crosslinker in the primary network (EAe1.45) the expected distribution will be similar to that of the network with photophores. Using the same form of the distribution (Eq. (5.32)), the values of $N_{\min} = 6.2$, $a_f = 0.6$, and $b_f = 0.18$ are determined based on generating the best fit to the stress-stretch data for all DN and TN elastomers (6 independent samples), which only differ slightly from those in Figure 5.4.

The results of the fitting are shown for the three datasets in Figure 5.9, Figure 5.10, and Figure 5.11 respectively. Each figure shows a comparison between predicted and measured stress-stretch relations for DN and TN elastomers. The model is in reasonable agreement with the experimental data in all cases. A direct comparison between the stresses and damage predicted by our model for the three datasets is presented in Figure 5.12, which illustrates the effect of prestretch on the mechanical response. In Figure 5.12 a) the stresses are presented for three DN elastomers. DN3, which has the largest prestrech (Table 5.2), exhibits an upturn in stress at the smallest stretch. As the prestretch is decreased, the stress upturn occurs at larger stretches. Similar conclusions can be drawn from the TN data in Figure 5.12b). A comparison between the damage evolutions for the three TNs is shown in Figure 5.12c), where damage begins to occur at lower stretches for MNE with larger prestretches.

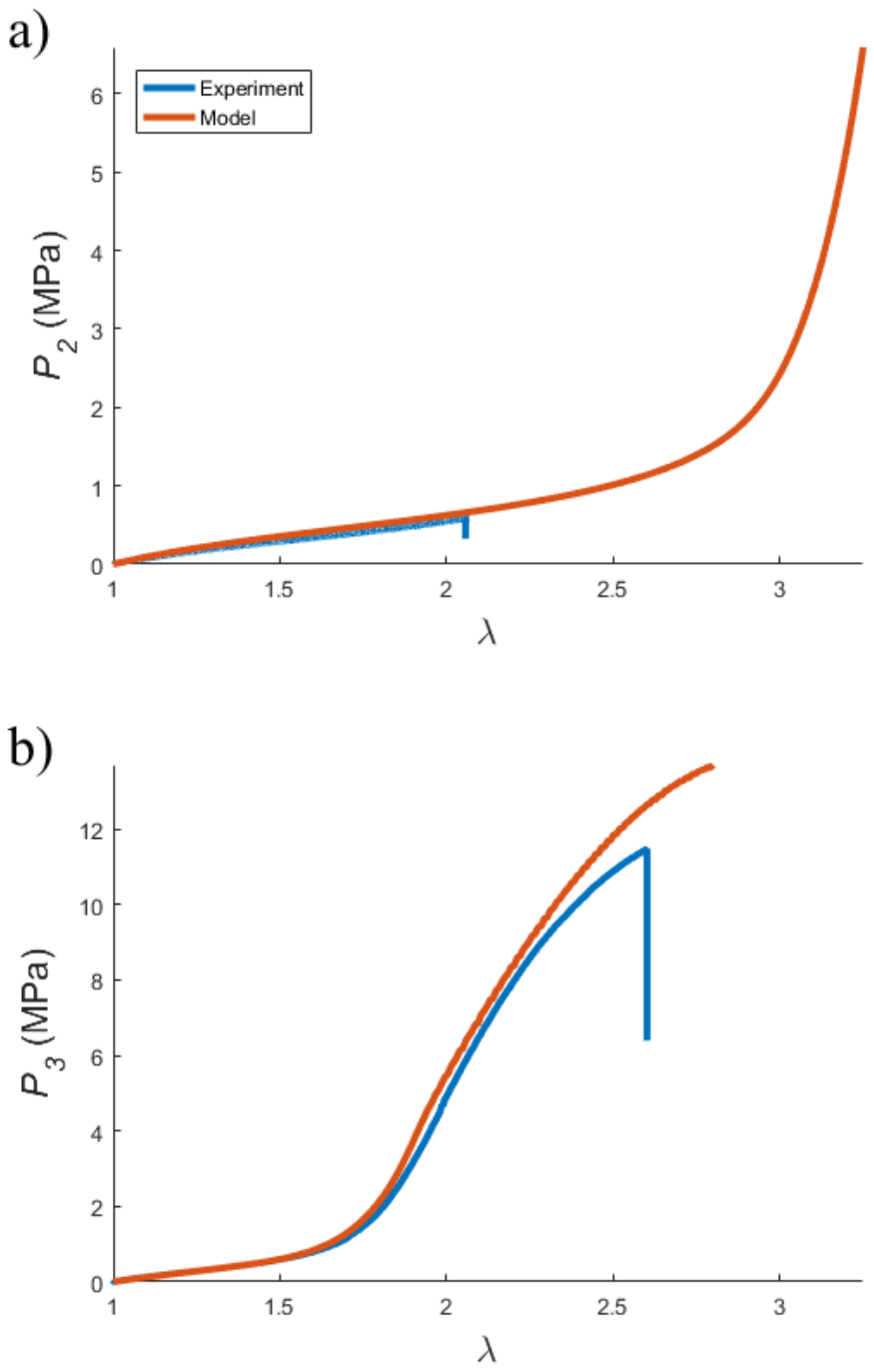

Figure 5.9 Engineering stress plotted against stretch for uniaxial extension of (a) DN elastomer (b) TN elastomer. Experimental data (from dataset DN1/TN1) and model fit are shown.

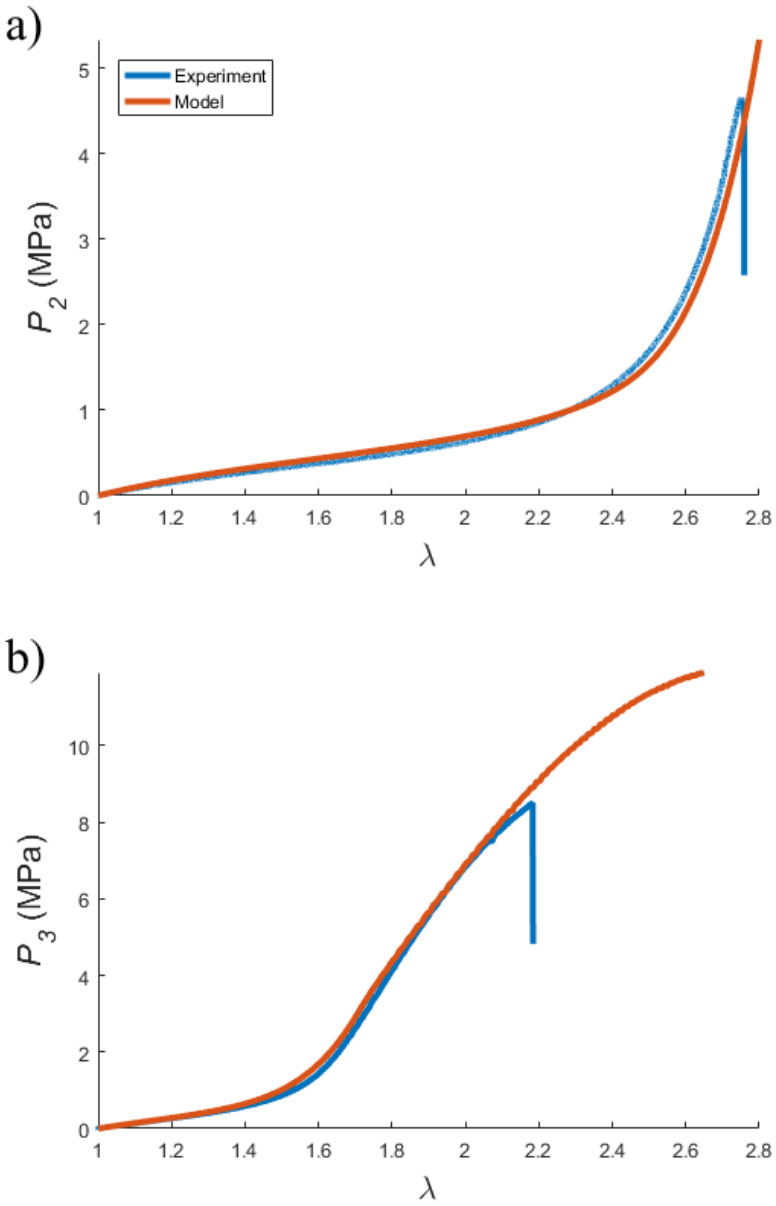

Figure 5.10 Engineering stress plotted against stretch for uniaxial extension of (a) DN elastomer (b) TN elastomer. Experimental data (from the dataset DN2/TN2) and model fit are shown.

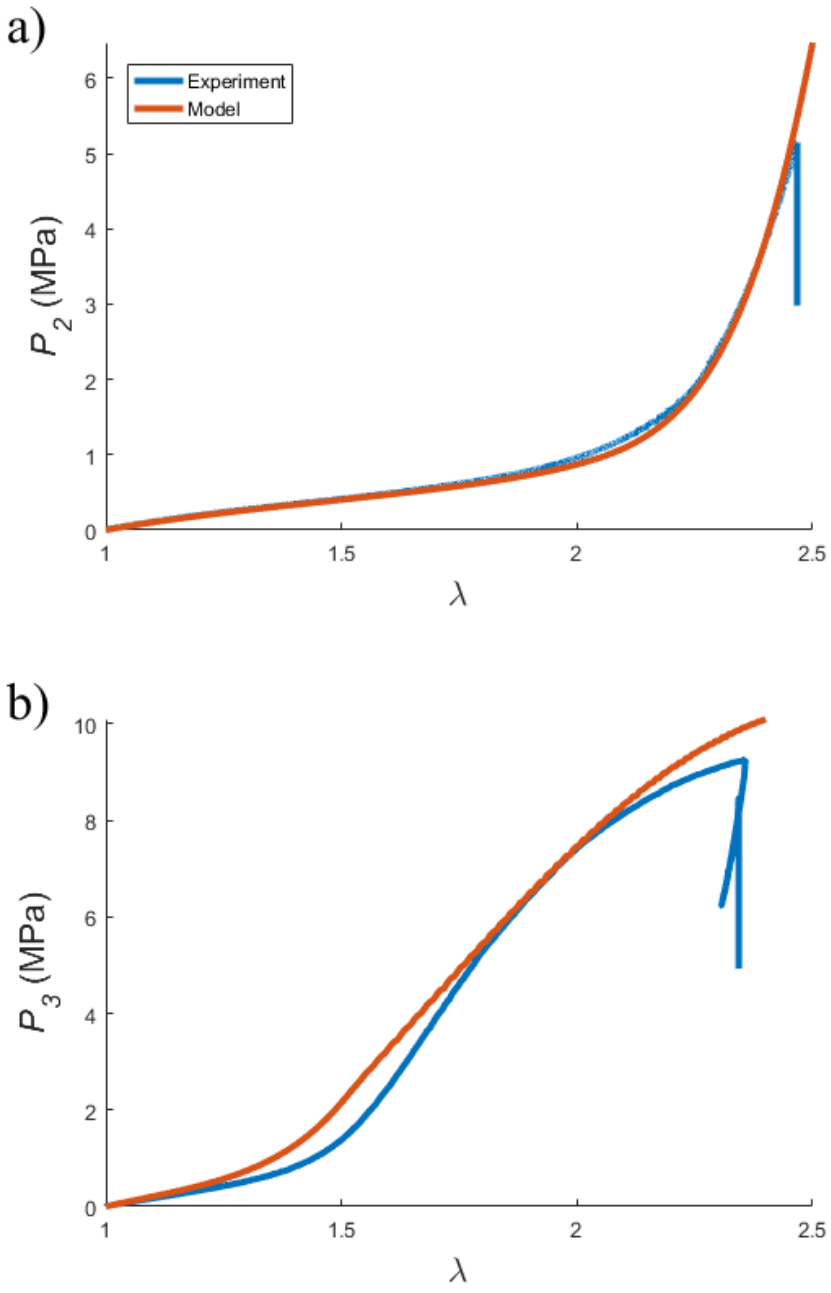

Figure 5.11 Engineering stress plotted against stretch for uniaxial extension of (a) DN elastomer (b) TN elastomer. Experimental data (from dataset dataset DN2/TN3) and model fit are shown.

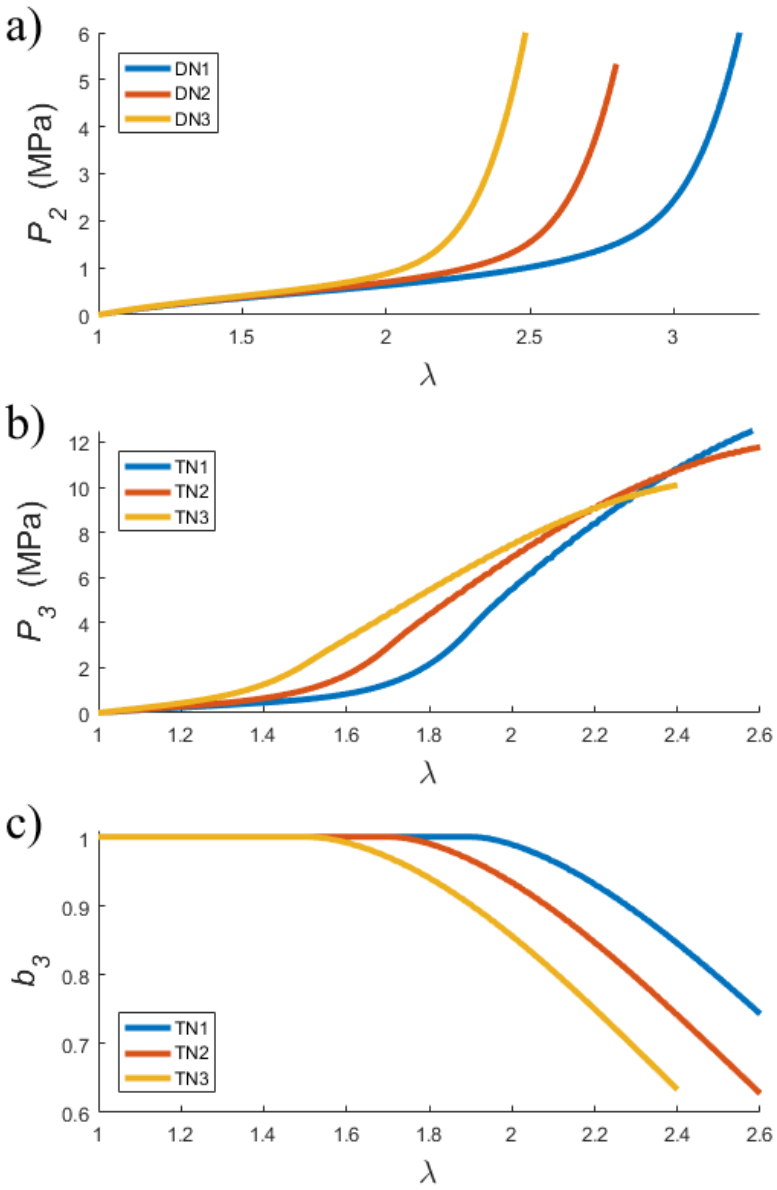

Figure 5.12: Model predictions for (a) engineering stress vs. stretch for DN elastomers; (b) engineering stress vs. stretch for TN elastomers; and (c) the evolution of damage (surviving chain fraction b_3 vs. stretch) for TN elastomers; all under uniaxial extension. Each subfigure contains three curves corresponding to the three different datasets.

5.4.4. *Cyclic Loading of MNE*

The experimental data presented in Ducrot et al [4] for the MNE with photophores was for cyclic loading. It is interesting to apply the model under cyclic uniaxial extension to see how the unloading curves compare with the experimental data; as well studying cyclic loading further elucidates how the evolution of damage impacts the mechanical response of the MNE.

Consider the constant rate cyclic loading pattern shown in Figure 5.13a) where the amplitude of loading is increased after each cycle. In the experiments, three identical cycles were first performed before the amplitude was increased [4]; however, no noticeable change occurred in the 2nd and 3rd cycles so they have been omitted here to simplify the presentation of the numerical results. Engineering stress is plotted against stretch in Figure 5.13b), where loading and unloading curves are shown for both model prediction and experimental data. Similarly, the evolution of the damage variable is shown in Figure 5.13c). It is important to note that the loading envelope in the experiment (blue symbols) correspond to those in Figure 5.5b) and all the fitting parameters in the model remain unchanged from those used to obtain the fit in Figure 5.5b). No additional fitting was performed for the unloading branches.

To understand these results, consider the path A-O_1-A-B-O_2 in Figure 5.13c). Suppose the material has been loaded to reach the stretch at A for the first time. In reaching point A some damage has occurred as can be seen in Figure 5.13c) where $b_3 = 0.72 < 1$ at point A. When the material is then unloaded from A to O_1 it follows the lower "damaged" unloading path (red, A-O) in Figure 5.13b) rather than the higher "undamaged" loading path (blue). From A to O_1 in Figure 5.13c) we follow a horizontal curve because the damage variable depends on the maximum stretch in the history of the deformation (in this case the stretch at point A) instead of the current stretch. During the subsequent reloading O_1-A-B, from O_1-A we retrace the same path as during unloading since the stretch has not exceeded its previous maximum value (at point A) so no additional damage occurs. From A-B stretching the sample further establishes a new maximum stretch, and thus the damage evolves as seen in Figure 5.13c) where the damage variable decreases from 0.72 at point A to 0.49 at point B. This damage results in a decrease in the slope of the stress-stretch curve in Figure 5.13b) at the transition (point A) from reload to additional stretch. Similarly, when we unload after reaching point B we follow the lower unloading path (red, B-O) and again the damage variable remains constant during unload.

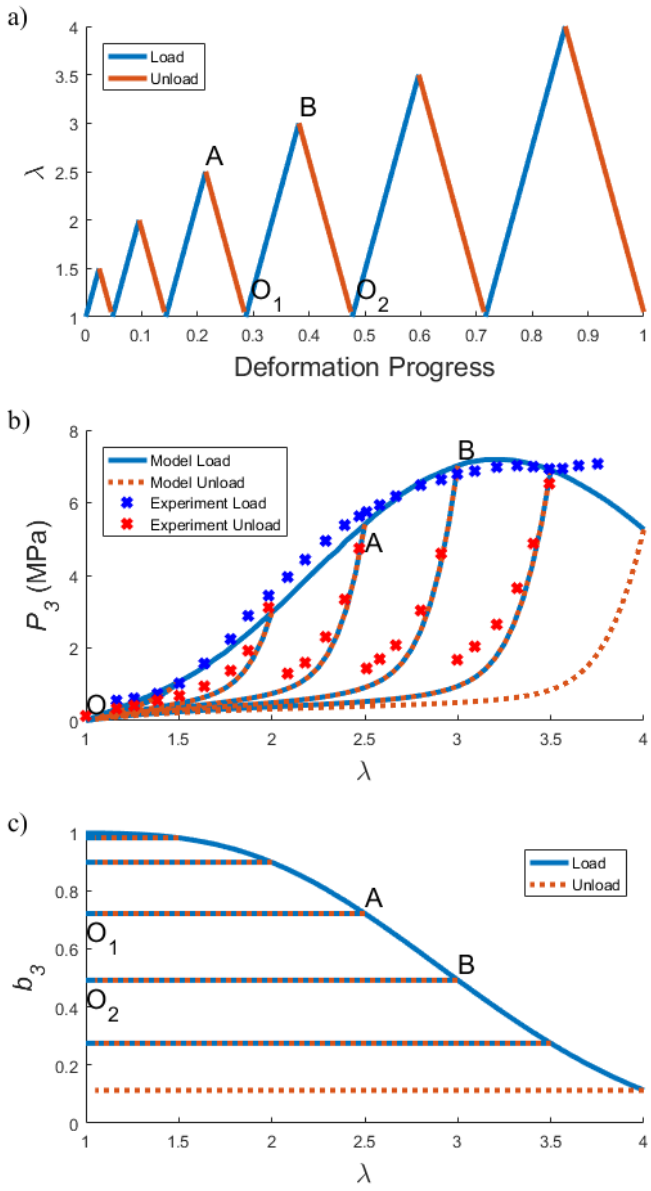

Figure 5.13: (a) Stretch plotted against deformation progress for constant rate cyclic loading where amplitude is increased after each cycle. (b) Engineering stress plotted against stretch for cyclic uniaxial extension of TN elastomer. All parameters in the model are identical to those presented in section 5.4.3.1. Experimental data from Ducrot et al [4]. (c) The evolution of damage is shown by plotting the surviving chain fraction (b_3) against stretch.

The cycle O-A-B-O in Figure 5.13b), included in the path we previously described, forms a hysteresis loop, and the area enclosed in this loop, $D_{\text{int}}^{cyc} = \oint_{cycle} P d\lambda$, has the physical interpretation of energy dissipation. The hysteresis during cyclic uniaxial extension was found to correlate, to some extent, with the size of damage zone in fracture experiments [4], and hence is an important quantity to examine in attempt to increase the fracture toughness of the material. In Ducrot et al. [4] this hysteresis was compared with the cumulative light emitted, whereas in our work, an analogous quantity would be the change in damage variable during a cycle

$$\left|\Delta b_3^{cyc}\right| = -\oint_{cycle}\int_1^{\infty} f(N_K)\dot{b}(r_{\max}^*, N_K)\,dN_K\,dt\,. \tag{5.34}$$

An expression for the rate of energy dissipation in our model $\dot{D}_{\text{int}} = -\phi^1\mu\int_1^{\infty} f(N_K)\dot{b}(r_{\max}^*, N_K)N_K E_{ch}^*(r^*)\,dN_K$ was obtained in the Appendix 4.1, so D_{int}^{cyc} can be determined by either integrating $\dot{D}_{\text{int}}$ over a cycle or by using $D_{\text{int}}^{cyc} = \oint_{cycle} P d\lambda$:

$$D_{\text{int}}^{cyc} = -\phi^1\mu\oint_{cycle}\int_1^{\infty} f(N_K)\dot{b}(r_{\max}^*, N_K)N_K E_{ch}^*(r^*)\,dN_K\,dt = \oint_{cycle} P d\lambda\,. \tag{5.35}$$

The numerical results for $\left|\Delta b_3^{cyc}\right|$ and D_{int}^{cyc} are presented in Figure 5.14, for cycles 2-5 from Figure 5.13. In Ducrot et al [4] the cumulative light was found to vary with the mechanical hysteresis by a power of 0.75, while in Figure 5.14 a power of 0.63 provides a good fit which is in reasonable agreement with experiments.

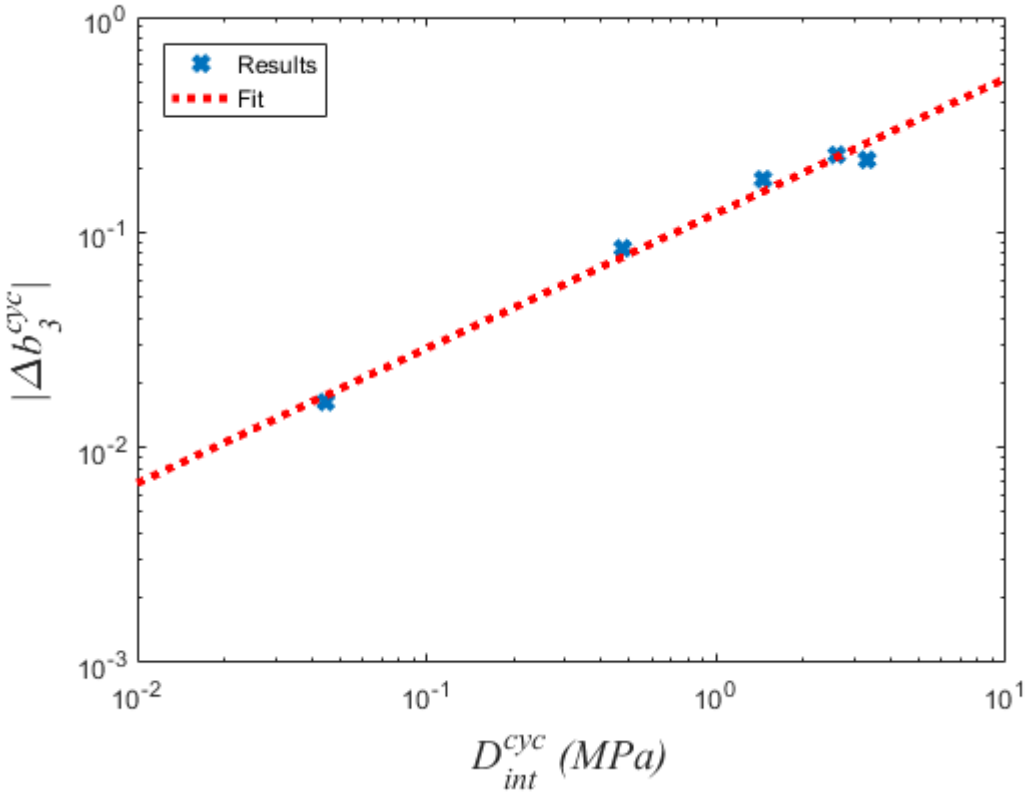

Figure 5.14: Decrease in damage variable per cycle plotted against energy dissipated per cycle. Symbols are from integration of numerical results obtained from the model. Dashed line is a linear fit to the model prediction, on the log-log scale.

5.4.5. *Further Discussion*

While our model predictions have shown good agreement with experiments, there are some discrepancies that warrant further discussion. First, in the uniaxial extension results in Figure 5.9, Figure 5.10, and Figure 5.11 for the TN elastomer, the model seems to overestimate the stress when the sample is about to break. A possible explanation for this is the potential material inhomogeneity not considered in the model. When we apply the model to an idealized uniaxial extension, the deformation is assumed to be perfectly homogenous, which is certainly not valid when the sample fails. Localized damage which grows near a pre-existing defect may also impact the overall stress of the specimen at the stretches leading up to failure. There is evidence to support this hypothesis in the TN light emission data [4]. Specifically, there is a peak in the light emission

after which the intensity decreases with further stretching. In obtaining the chain length distribution from the light emission data (Figure 5.4), a distribution with a single peak was used, because it was assumed that a single damage mechanism occurs within the material. However, the experimental data also showed slightly increased light emission intensity near failure which may indicate the possibility of additional damage mechanisms such as inhomogeneous deformation and localized damage around defects. This over-estimation does not exist in the DN data because the DN elastomers are expected to have lower fracture toughness, evidenced by the experiments of Ducrot et al. [4] where the damage zone in the area surrounding a crack tip [4] is much smaller in the DN elastomers than the TN elastomers. The lower fracture toughness could result in a more brittle failure once damage localizes at a defect; in this case, we do not anticipate a reduction in stress growth near the failure point.

Another discrepancy between the model and the experimental results lies in the unloading curves in Figure 5.13b), where the stress predicted by the model can be noticeably lower than measured stress. To elucidate this point we compute the unstretched Young's modulus (see Appendix 4.1 for definition), i.e., the Young's modulus evaluated at $\lambda = 1$. The ratio between the value at the beginning of cycle i (i>1), $\left(E_o^N\right)_i$, and that before the first cycle $\left(E_o^N\right)_1$ is evaluated and plotted in Figure 5.15 against the maximum stretch λ_{max} reached in that cycle. Here the loss of chains (Figure 5.13c)) translates to a reduction in Young's modulus. A plot similar to Figure 5.15 was presented in the Supporting Material of Ducrot et al [4], for a similar TN elastomer without photophores. In that work, after a maximum stretch of $\lambda_{max} = 2.4$ was reached in the cycle the unstretched Young's modulus decreased by approximately 20%; from Figure 5.15 at $\lambda_{max} = 2.4$ the modulus decreases by approximately 50%. This suggests the possibility that the model over predicts the rupture of chains. There are several potential explanations for the discrepancy. Firstly, one of the assumptions made in the model is that the contribution of each network to the stress is independent. While this may be a reasonable first-order approximation in modeling these materials, due to chain entanglements and a small degree of transfer reactions (e.g., the $(n+1)^{th}$ network reacting chemically with the n networks previously formed), it is likely that damage in the primary network will result in dissipation in the filler networks and these additional dissipation mechanisms may have some impact on the Young's modulus. An evidence of this is the small amount of residual strain observed in the experimental data [4], where after damage the material

did not completely recover its initial configuration. A second possibility could be the existence of critical pathways in the primary network along which the rupture of bonds can result in the relaxation of many chains in the primary network. In this case the damage would not be isotropic and homogenous as is assumed in this model. In fact, stretching pre-deformed samples perpendicular to the direction of initial deformation has yielded some light emissions [79] indicating that damage is not entirely isotropic. A third and related possibility is the coupling between chains in the primary network. There is no direct experimental evidence for this, but in an existing model [80] the rupture of chains was considered to effectively remove crosslinks and increase the length of existing chains in the material. Finally, the specific chain force relationship (Eq. (5.20)) is used for both loading and unloading. During loading the stress is dominated by chains with forces in the bond stretching regime. However, during unloading this is no longer true, and the force on the polymer chain can depend on its bending flexibility [71] which was not considered in Eq. (5.20).

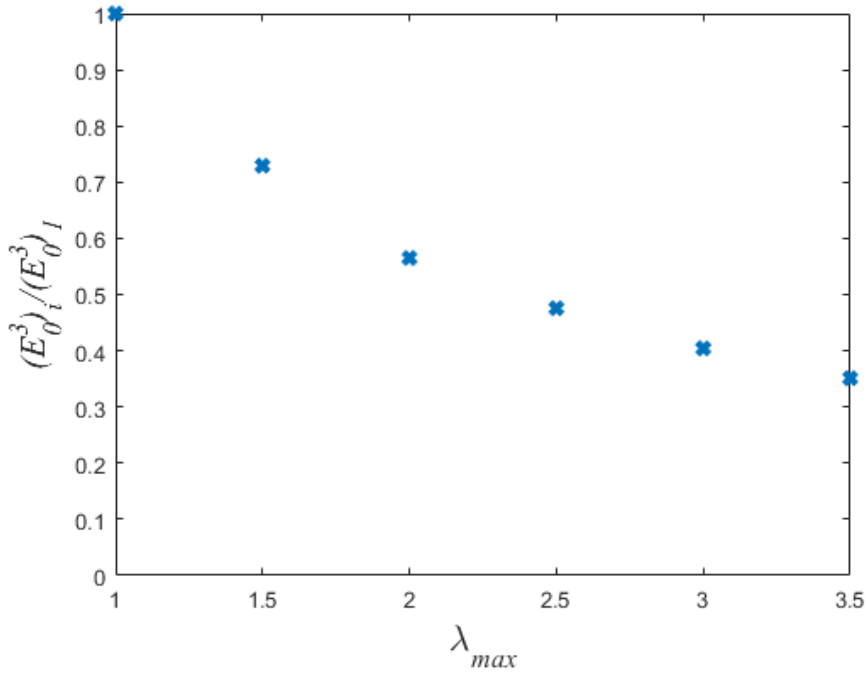

Figure 5.15: Evolution of unstretched Young's modulus at the beginning of cycle i, (i>1) normalized by the unstretched modulus of a fresh sample, as a function of maximum elongation previously achieved by the sample.

Finally, we estimate the force and energy required to cause the rupture of a chain from the cyclic loading data in Figure 5.13. When a bond breaks we define the average force [81], $\langle F_{ch} \rangle = k_B T \int_0^1 F_{ch}^*(r^*) db / A_o$, and the average chain energy $\langle E_{ch} \rangle = k_B T \int_0^1 N_K E_{ch}^*(r^*) db$. For the data in Figure 5.13b) the following values are obtained: $\langle F_{ch} \rangle \sim 1.95nN$ and $\langle E_{ch} \rangle = 1000 - 2000 kJ/mol$ depending on the chain length. The force value is comparable to single chain pulling experiments for polymer chains [82], while the energy requires more discussion. The dissociation energy of the photophore bond was reported to be 150kJ/mol [4], which seems to be one order of magnitude smaller than the $\langle E_{ch} \rangle$ value obtained here. However, it is incorrect to make such a direct comparison, for several reasons explained below. Firstly, the bonds break via a transition state which is altered by the external force [79]. The result of this is that the energy that the bond will be excited to when it breaks can be significantly less than the dissociation energy. Secondly, when a bond on a polymer chain is ruptured the energy of the entire chain is dissipated [10] which includes the deformation of all the bonds. The shortest chains in the model had 6.5 Kuhn segments for PEA we can then equate this to ~78 bonds [74]. Using $\langle E_{ch} \rangle = 1000 kJ/mol$ and if all the bonds in a shortest chain are excited to approximately the same energy this implies ~13 kJ/mol for each bond which is approximately 8.5% of the dissociation energy. Clough et al. [79] have found that typical C-C bonds store 15-18% of the dissociation energy before rupture, which is certainly of the same order of magnitude as was estimated for the dioxetane bond in the photophore.

The model developed in this work provides a method to systematically study how prestretch impacts the mechanical response and damage evolution of a MNE. It is also instrumental to the design of MNE with optimized fracture toughness. Implementing the model into finite element simulations will allow us to explore a wide range of problems involving stress concentration and crack propagation, since this class of material can generate large damage zones [4] locally. It is therefore of interest to systematically investigate how the different prestretches will impact the size of the damage zone around cracks and the overall fracture toughness. In experiments it was observed that when a third swelling operation was performed to generate quadruple network elastomers, necking occurred in the sample and no increase in fracture toughness compared with TN elastomer. Mechanism of this phenomenon is unclear and can be investigated with this model.

However, to predict toughness it will be necessary to extend the model presented to consider failure of the filler networks.

5.5. Conclusion

A continuum model is developed to capture the mechanical response of multinetwork elastomers synthesized by introducing filler network(s) into an existing primary network. The swelling process prestretches the chains of the network formed in the previous step; such prestretch is incorporated into the model by basing the strain energy of each network on the combined deformation caused by swelling and post-swelling deformation of the completed MNE. Because the chains in the heavily crosslinked primary network undergo the greatest amount of prestretch and often break during the deformation, separate material models are used for the primary and filler networks. The primary network is modeled as a polydisperse network of breakable polymer chains with nonlinear chain elasticity, while the filler networks are modeled using the generalized neo-Hookean model. With a few fitting parameters, this model provides a good match to the uniaxial extension, including cyclic loading, experimental data. Although the primary network only occupies a small volume fraction of the MNE, it contributes to the majority of the stress as confirmed by the model. It was found that a larger prestretch of the primary network causes the MNE to exhibit strain stiffening effect at a smaller stretch, and the damage due to chain rupture initiates at lower stretches. Finally, the hysteresis of the stress-stretch curve during cyclic loading is found to correlate to the accumulation of damage during the cycle.

5.6. Nomenclature

S	Area of sample in plane of view	Dimension
A_o	Initial Kuhn length of polymer chain	[L]
α_l	Proportionality constant to relate light intensity to bond rupture	$[M][L][T]^{-2}$
A_f	Parameter in chain length probability density function	-
a_f	Parameter in chain length probability density function	-
b_f	Parameter in chain length probability density function	-
b	Damage evolution function	-
b_N	Surviving chain fraction	-
β_l	Proportionality constant to relate light emission to damage evolution	$[M][L][T]^{-2}$
$\underline{\mathbf{B}}$	Left Cauchy-Green deformation tensor for mechanical deformation of MNE	-
$\underline{\mathbf{B}}_N^i$	Left Cauchy-Green Deformation tensor of multinetwork elastomer with N networks, with respect to the reference configuration of network i. Takes into account both deformation by swelling and mechanically deformation by deformation gradient $\underline{\mathbf{F}}$.	-
$\underline{\mathbf{e}}_k$	Unit vector in k direction	-
E_{ch}^*	Nondimensional Helmholtz free Energy of stretched polymer chain	-
F_{ch}	Tensile force acting on polymer chain	$[M][L][T]^{-2}$
F_{ch}^*	Nondimensional Tensile force acting on polymer chain	-
$\underline{\mathbf{\Phi}}_j$	Deformation gradient for jth swelling operation	-
$\underline{\mathbf{\Phi}}_j^i$	Deformation gradient after j swelling operations with respect to the reference configuration of network i.	-

$\underline{\mathbf{F}}$	Deformation gradient applied to completed MNE by mechanical loading.	-
$\underline{\mathbf{F}}_N^i$	Deformation gradient of MNE with N networks, with respect to the reference configuration of network i. Takes into account both deformation by swelling and mechanically deformation by deformation gradient $\underline{\mathbf{F}}$.	-
f	Probability density function for chain length	-
ΔF_m	Contribution of chain length PDF for bin m.	-
g	Arbitrary function	-
$\underline{\mathbf{I}}$	2nd order Identity tensor	-
$I_1\left(\underline{\mathbf{B}}_N^i\right)$	First invariant of $\underline{\mathbf{B}}_N^i$	-
$I_2\left(\underline{\mathbf{B}}_N^i\right)$	Second invariant of $\underline{\mathbf{B}}_N^i$	-
$I_3\left(\underline{\mathbf{B}}_N^i\right)$	Third invariant of $\underline{\mathbf{B}}_N^i$	-
i	Identifies network	-
j	Identifies swelling operation	-
J_{sj}	Ratio of volume after to volume before jth swelling operation	-
J_{sj}^i	ratio of the volume of the material after j swelling operations to the volume of the material when the ith network was introduced	-
J_N^i	ratio of the volume of the material when network i was introduced to its current volume (with N networks)	-
k_B	Boltzmann constant	$[M][L]^2[T]^{-2}[\theta]^{-1}$
λ	Stretch associated with uniaxial extension	-
λ_{sj}	Isotropic stretch associated with jth swelling operation (ratio of thickness after to before jth swelling operation)	-
λ_o	Isotropic stretch of 1st network due to swelling	
LI	Light emission intensity	$[M][L][T]^{-3}$
M	Number of chain length bins	-
m	Identifies chain length bin	-

m_i	Mass of ith network	[M]
m_N	Mass of multinetwork elastomer with N networks	[M]
n_F	Parameter in constitutive model for filler networks.	-
N	Number of networks	-
N_K	Number of Kuhn length is a polymer chain	-
$N_{\min}$	Minimum number of Kuhn segments in chain length probability density function	-
$\overline{N}_{K,m}$	Average number of Kuhn lengths per chain or bin m	-
$N_{K,m}$	number of Kuhn lengths per chain at start of bin m	-
$N_{K,m+1}$	number of Kuhn lengths per chain at end of bin m	-
p	Lagrange multiplier	$[M][L]^{-1}[T]^{-2}$
p^i	Lagrange multiplier for network i	$[M][L]^{-1}[T]^{-2}$
r	End to end distance of polymer chain	[L]
r^*	Fractional extension of polymer chain	-
$r^*_{\max}$	Maximum achieved fractional extension of a polymer chain during deformation history	-
r^*_{pk}	Fractional extension where peak rate of bond rupture occurs	-
P_N	Nonzero engineering stress component for MNE with N networks, under uniaxial extension	$[M][L]^{-1}[T]^{-2}$
P_N^i	Nonzero engineering stress component for network i for MNE with N networks, under uniaxial extension	$[M][L]^{-1}[T]^{-2}$
ψ^i	Volume fraction that network i occupied in the material when it was first introduced	-
ϕ_N^i	Volume fraction of network i in a multinetwork elastomer with N networks	-
$\underline{\boldsymbol{\sigma}}_N$	Cauchy stress tensor for MNE with N networks	$[M][L]^{-1}[T]^{-2}$
$\underline{\boldsymbol{\sigma}}_N^i$	Cauchy stress tensor for network i in MNE with N networks	$[M][L]^{-1}[T]^{-2}$

σ_N	Nonzero true stress component for MNE with N networks, under uniaxial extension	$[M][L]^{-1}[T]^{-2}$
σ_N^i	Nonzero true stress component for network i for MNE with N networks, under uniaxial extension	$[M][L]^{-1}[T]^{-2}$
D_j	Thickness of sample after j - 1 swelling operations	[L]
t	time	[T]
μ	$\mu = \nu\, k_B T$, parameter in constitutive model for 1st network. Related to shear modulus.	$[M][L]^{-1}[T]^{-2}$
μ_F	Parameter in constitutive model for filler networks. Related to shear modulus	$[M][L]^{-1}[T]^{-2}$
U_N	Strain energy density of multinetwork elastomer with N networks	$[M][L]^{-1}[T]^{-2}$
$U^i\left(\underline{\mathbf{B}}_N^i\right)$	Strain energy density for network i in a multinetwork elastomer with N networks, if the network were to occupy the entire material when introduced.	$[M][L]^{-1}[T]^{-2}$
T	Absolute temperature	$[\theta]$
ν	Volumetric density of load bearing chains in reference configuration of material.	$[L]^{-3}$
ν_m	Volumetric density of load bearing chains in reference configuration of material in bin m.	$[L]^{-3}$
V_j	Volume of sample after j - 1 swelling operations	$[L]^3$

Chapter 6. Modeling Active Breakable Polymer Chains

Abstract

The force-extension relationship of single polymer chains is an essential component underlying the development of macroscopic constitutive models for elastomers. In this work, we present a model that extends the range of accuracy of classical entropic force-extension models by accounting for the energy of bond deformation on the backbone of the polymer chain. Emphasis is placed on reducing the number of fitting parameters, by extensively utilizing molecular parameters tabulated in the literature. In addition, an extension of the model is made to include the effects of mechanophores: molecules which react under the application of a mechanical force. This has given the model the capability of predicting mechanophore reaction as well as chain scission. The model is applied, and compared to experimental data, in a range of scenarios: reproducing the measured PDMS force-extension relationship, calculating the rate dependent fracture energy of PDMS films, and predicting force extensions relationships with a plateau caused by unfolding of mechanophore domains. For the last example it was demonstrated that this type of chain has the potential to be utilized to design elastomers with substantially enhanced strength and toughness.

6.1. Introduction

The force extension relationship for a polymer chain is often utilized in constitutive models for elastomers [5, 9, 71] to capture the nonlinear mechanical behaviors at large deformations. Classically, polymer chain elasticity has been modeled by considering the change in entropy, e.g., the freely jointed chain model [9] or the wormlike chain model [3]. Because these models only consider entropy, they exhibit a limiting extension where the chain force becomes singular, and make unreliable predictions for extension near this singularity. However, for problems where chains are stretched and eventually break, such as fracture, chain force-extension relationships which are accurate in the large extension range are needed. There have been efforts along this direction in the literature. The elastic freely jointed chain model is an extension of the freely jointed chain model which considers the links to be springs [82]. Recently, another model has been presented where the energy is minimized for the chain which consists of entropy and the deformation of bonds [83].

In fracture problems it is also desirable to be able to predict the rupture of chains to predict damage in the vicinity of the cracks. Previously chain rupture has been predicted by using a critical bond deformation energy [83], or by solving rate equations where the rate of scission is enhanced by the tensile force acting on a polymer chain [3, 2, 1]; the latter is able to predict rate dependence of fracture phenomena important in elastomers [1]. Finally there have been strong interests towards the development of active polymer chains containing mechanophores, which could respond to mechanical force by changing color [47,48], emitting light upon rupture [4], or increasing in length [84-88].

In this work, we aim at developing a comprehensive model that considers several aspects on a polymer chains: its entropic elasticity, bond deformation on the backbone, kinetics of bond scission, and activation of mechanophores embedded in the chain. Parameters in the model are largely molecular parameters (e.g. Kuhn length, number of bonds) already available in literature, and additional parameters required for fitting are minimal. The model allows us to generate force-extension relationships that compare very well with experimental data for a large range of extension. It also enables the evaluation of the rate-dependent fracture energy of a polymeric interface, which agrees well with experiments.

Using this model, we also demonstrate how certain types of active polymer chains with mechanophores can be used to enhance the theoretical maximum stress and toughness at the continuum level.

The paper proceeds as follows. The formulation of the model is given in Section 6.2 with the generalization to include mechanophores discussed in Section 6.2.4. Results are presented in Section 6.3 which is divided to present, the force extension relationship for the simple chain in Section 6.3.1, scission of the simple chain in Section 6.3.2, the impact of mechanophores on scission in Section 6.3.3, and the effect of chains that can increase length upon activation in Section 6.3.4. Conclusions are given in in Section 6.4.

6.2. Model

6.2.1. *Chain models based on entropic elasticity*

There are numerous models in the literature [3, 9, 71] which relate the tensile force on a polymer chain to its fractional extension. An implicit assumption in these models is the chain being inextensible in that the contour length, length of the fully extended chain, is a constant. The fractional extension is defined as the ratio between the chain's end-to-end distance and the constant contour length. Since these chains are inextensible the force arises mainly due to the decrease in configurational entropy caused by increasing the end to end distance. For example, in the persistence chain model [3], a chain is idealized as N_K Kuhn segments each with Kuhn length A [50] so that the contour length is given by $L_c = N_K A$. The chain force-extension relationship given by this model is

$$F = \frac{k_B T}{P}\left(\frac{1}{4}\left(1-r^*\right)^{-2} - \frac{1}{4} + r^*\right), \tag{6.1}$$

where F is the tensile force acting on the polymer chain, $P \approx A/2$ [3] is the persistence length, k_B is the Boltzmann constant and T is the absolute temperature. The fractional extension in this equation is

$r^* = \frac{r}{L_c},$	(6.2)

where r is the end to end distance.

The relationship in Eq. (6.1) is in good agreement with experimental data for fractional extension less than 0.9 [3]. Above this extension, Eq. (6.1) predicts that the force increases sharply and approaches infinity as r^* approaches unity (entropic locking extension), which is much higher than that observed in the experiments of single chain extension [3]. In this regime ($r^* > 0.9$), chain force relationships based on entropic elasticity do not work well due to the breakdown of inextensibility assumption. In reality when r^* approaches one the chain will be subjected to forces large enough to significantly deform the bonds on the chain's backbone. Deformation of the bonds will allow the end to end distance, r, to continue increasing beyond L_c. This behavior will cause the force to increase more gradually rather than being singular as in the entropic elasticity model.

6.2.2. *Polymer chain with deformable bonds*

Consider the stretching of a polymer chain, for which a schematic is shown in Figure 6.1. Comparing Figure 6.1a) and c) as the end to end distance increases from its initial value $\sqrt{\langle R_o^2 \rangle}$, there will be less possible configurations the chain can assume which causes a decrease in entropy. Meanwhile if we compare the bonds on the chain backbone shown in Figure 6.1b) and d) the tensile force acting on the chain causes the bonds to stretch from their initial length l_o to l, and the bond angle to decrease from initial value θ_o to θ; both leading to the increase of contour length. If we consider the geometry in Figure 6.1b) the contour length of the chain can also be written in terms of the bond length and angle [50]:

$L_c = N_K A = n_b l \cos\left(\frac{\theta}{2}\right),$	(6.3)

where n_b is the number of bonds on the chain backbone. Assuming that the number of Kuhn segments N_K remains constant, Eq. (6.3) allows us to establish a relationship that determines how the deformation of bonds will impact the Kuhn length and cause it to increase from its initial length A_o ($=\frac{n_b}{N_K} l_0 \cos\left(\frac{\theta_0}{2}\right)$) to the current value of

$A = \frac{L_c}{N_K} = \frac{n_b}{N_K} l \cos\left(\frac{\theta}{2}\right).$	(6.4)

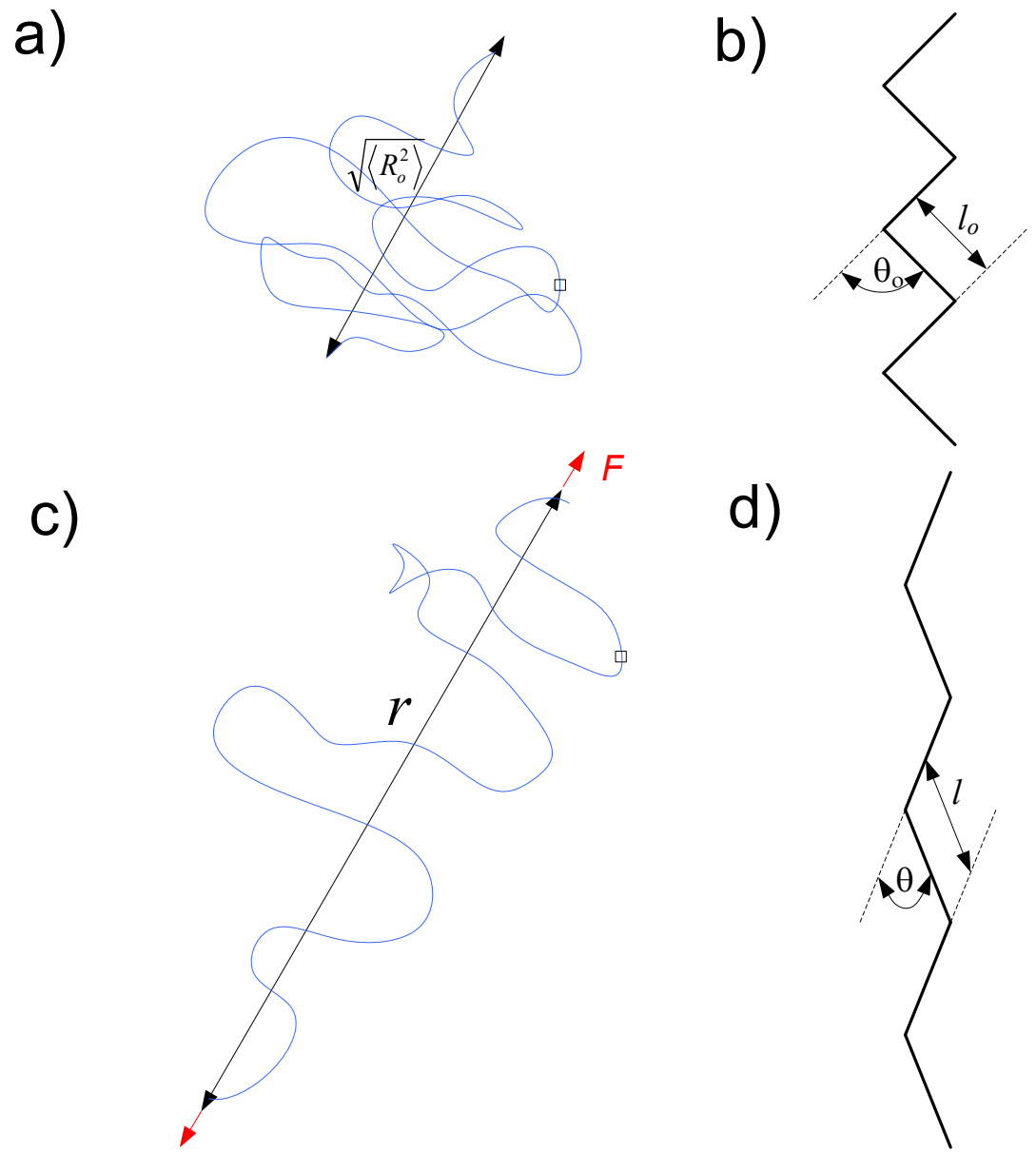

Figure 6.1: a) Polymer chain before stretching b) backbone bonds on polymer chain before stretching c) polymer chain after stretching d) backbone bonds on polymer chain after stretching.

In order to model the deformation of bonds on the chain backbone as the chain is stretched, we assume that the total Helmholtz free energy of the polymer chain, measured relative to a completely relaxed configuration, consists of three components

$$E_{ch} = E_{ent} + n_b\left[E_{str} + E_{ben}\right], \tag{6.5}$$

where, E_{ent} is the change in free energy arising from the decrease in configuration entropy as the chain is straightened, E_{str} is the change in internal energy (per bond) due to bond stretching, and E_{ben} is the change in internal energy (per bond) due to deformation of bond angles.

The first component in Eq. (6.5), E_{ent}, is obtained by integration of Eq. (6.1) as follows

$$E_{ent}\left(r^*\right) = \int F dr = N_K A \int F dr^* = k_B T N_K \left(\frac{1}{2}\left(1-r^*\right)^{-1} - \frac{1}{2}r^* + r^{*2}\right). \tag{6.6}$$

It should be noted that the relationship presented in Eqs. (6.1) and (6.6) is merely one example of entropic chain elasticity, while the methods discussed in this work could be applied to any other relationships. For example in the Appendix we also present relationships based upon Gaussian chains statistics [93] and Langevin chain statistics [9]. Here E_{ent} is written in terms of the fractional extension of the deformed chain i.e. $r^* = r / N_K A < 1$. Later we will show that it is more convenient to define a second fractional extension in terms of the initial Kuhn length, $r_o^* = r / N_K A_o$. The stretching of bonds is assumed to follow a Morse potential [89], with the energy given by

$$E_{str} = D_e\left[\left(1-e^{-\beta_s\left(l-l_o\right)}\right)^2 - 1\right], \tag{6.7}$$

where D_e is the dissociation energy of a bond, $l - l_o$ is the change in length of the bond from its equilibrium value, and β_s is a constant which controls the width of the potential. The Morse potential is used because it has a relatively simple functional form and, unlike a harmonic function, it well captures the energetics of a chemical bond from its equilibrium position to dissociation [89]. The tensile force acting on a bond can be obtained by taking the derivative of the potential as follows.

$$F_{str} = \frac{\partial E_{str}}{\partial l} = 2D_e\beta_s\left[\left(1-e^{-\beta_s\left(l-l_o\right)}\right)\right]e^{-\beta_s\left(l-l_o\right)}. \tag{6.8}$$

For illustration Eq. (6.7) and (6.8), in non-dimensional form, are shown in Figure 6.2. It can be seen that F_{str} has a peak value of $F_{pk} = D_e\beta_s/2$ which occurs at $l_{\max} - l_o = \ln 2/\beta_s$. This peak force corresponds to the maximum force that a bond on the chain can sustain before rupture, although in reality the chain can break much sooner. F_{str}, the tensile force on a bond, should be distinguished from the tensile force acting on the chain, F. The relation between the two quantities will be derived later.

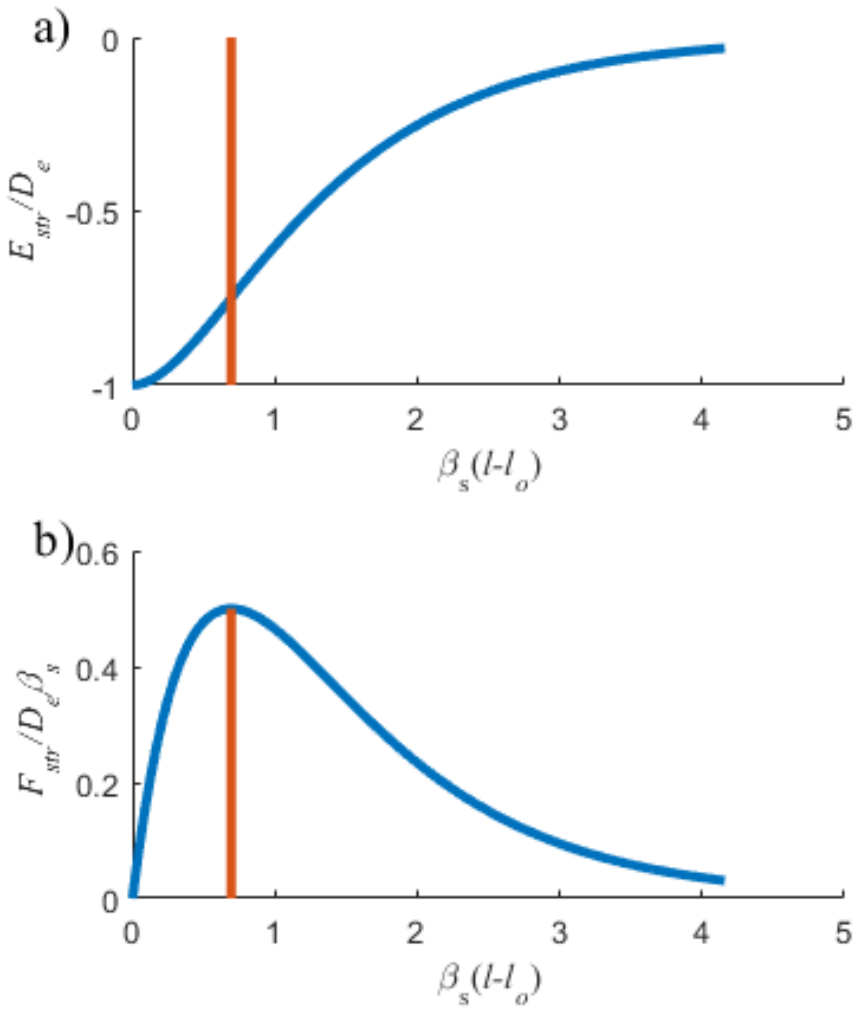

Figure 6.2: a) Morse potential for bond stretching b) Force obtained from the Morse potential. Orange lines mark the location of the peak value for F_{str}, and the corresponding value for E_{str}.

The deformation of a bond angle is assumed to be governed by the following potential [89]

$$E_{ben} = \frac{1}{2} k_\theta (\theta_o - \theta)^2 \left[1 + k_{sexic} (\theta_o - \theta)^4\right], \tag{6.9}$$

where $\theta_o - \theta$ is the change in bond angle from its equilibrium position, and k_θ and k_{sexic} are constants. The bending moment can be obtained from this potential as follows

$$M = \frac{\partial E_{ben}}{\partial \theta} = k_\theta (\theta_o - \theta)\left[1 + 3k_{sexic} (\theta_o - \theta)^4\right]. \tag{6.10}$$

Although the energies in Eq. (6.5) are individually defined by Eqs. (6.6), (6.7), and (6.9), constraints are needed to determine compatible values of r^*, l and θ. Specifically, if the chain's end-to-end distance *r* is fixed, *l* and θ should be such that the Helmholtz free energy is minimized. Since at fixed *r*, $dE_{ch} = \left(\partial E_{ch} / \partial l\right)\big|_{r,\theta} dl + \left(\partial E_{ch} / \partial \theta\right)\big|_{r,l} d\theta$, this condition implies that

$$\left.\frac{\partial E_{ch}}{\partial l}\right|_{r,\theta} = 0 = \frac{dE_{ent}}{dr^*}\left.\frac{\partial r^*}{\partial l}\right|_{r,\theta} + n_b \frac{dE_{str}}{dl} = \frac{dE_{ent}}{dr^*}\frac{\partial}{\partial l}\left(\frac{r}{n_b l \ \cos(\theta/2)}\right) + n_b F_{str}$$

$$= \left(L_c F\right)\left(-\frac{r^*}{L_c} n_b \cos\left(\frac{\theta}{2}\right)\right) + n_b F_{str} = -F n_b r^* \cos\left(\frac{\theta}{2}\right) + n_b F_{str}$$

which leads to

$$F_{str} = F r^* \cos\left(\frac{\theta}{2}\right), \tag{6.11}$$

and

$$\left.\frac{\partial E_{ch}}{\partial \theta}\right|_{r,l} = 0 = \frac{dE_{ent}}{dr^*}\left.\frac{\partial r^*}{\partial \theta}\right|_{r,l} + n_b \frac{dE_{str}}{d\theta} = \frac{dE_{ent}}{dr^*}\frac{\partial}{\partial \theta}\left(\frac{r}{n_b l \ \cos(\theta/2)}\right) + n_b M$$

$$= \left(L_c F\right)\left(\frac{r^*}{2L_c} n_b l \sin\left(\frac{\theta}{2}\right)\right) + n_b M = F\frac{r^*}{2} n_b l \ \sin\frac{\theta}{2} + n_b M$$

which leads to

$$M = -F r^* \frac{l}{2}\sin\left(\frac{\theta}{2}\right) = -F_{str}\frac{l}{2}\tan\left(\frac{\theta}{2}\right). \tag{6.12}$$

Using these two conditions, the tensile force acting on the polymer chain, assuming constant temperature, can now calculated from

$$F = \frac{dE_{ch}}{dr} = \left.\frac{\partial E_{ch}}{\partial r}\right|_{l,\theta} + \left.\frac{\partial E_{ch}}{\partial l}\right|_{r,\theta} \frac{dl}{dr} + \left.\frac{\partial E_{ch}}{\partial \theta}\right|_{r,l} \frac{d\theta}{dr} = \frac{dE_{ent}}{dr} = \frac{dE_{ent}}{dr^*} \frac{1}{N_K A}. \quad (6.13)$$

6.2.3. *Bond and Chain Parameters for Common Polymers*

To use Eqs. (6.7) and (6.9) four constants need to be known. Typical values have been obtained from the literature for C-C and Si-O bonds (Table 6.1), which are common for the backbone bonds in many elastomeric materials.

Table 6.1: Values of constants in bond potential for common elastomer backbone bonds

Bond Type	C-C [89]	Si-O [90]
D_e (J)	6.031×10^{-19}	7×10^{-19}
$\beta_s\,(10^{10}/m)$	2.625	2
k_θ (J/rad^2)	9×10^{-19}	$3.15-12.42\times10^{-19}$
k_{sexic} (rad^{-4})	0.754	0 (potential used did not have k_{sexic})

It is also desirable to obtain the chain parameters l_o, θ_o, A_o, and the number of bonds per Kuhn segments n_b / N_K using existing data. Typical values for the Kuhn length, A_o, and molecular weight of a Kuhn segment, M_K, are summarized in Table 6.2 for a variety of polymers. To determine the ratio n_b / N_K, we express the molecular weight of a chain in two different ways: $M_{ch} = N_K M_K = n_b M_b$, where M_b is the average molecular weight per backbone bond which can be calculated by dividing the molecular weight of the repeat monomer unit M_m by the number of backbone bonds per repeat unit n_m. For example, consider PDMS where the repeat unit structure is $[-Si(CH_3)_2-O-]_n$ and it has a molecular weight of $M_m = 74.17$g/mol. The monomer has three backbone bonds, however two bonds are shared with adjacent monomers so these two bonds are only counted as one towards n_m which gives $n_m = 2$. Therefore, $M_b = M_m / n_m = 37.08$g/mol. Finally, the ratio n_b / N_K, denoted by ξ, can be determined by

$$\xi \equiv \frac{n_b}{N_K} = \frac{M_K n_m}{M_m}. \quad (6.14)$$

To determine the equilibrium bond angle θ_o, consider the mean square end to end distance for a free chain (without external loading applied), which can be expressed in two ways [50]: $\left\langle R_o^2 \right\rangle = N_K A_o^2 = C_\infty n_b l_o^2$, where C_∞ is the long chain asymptotic limit of Flory's characteristic ratio, and its values are available in the literature [50, 91] (Table 6.2). This leads to the following relation: $\left(N_K A_o\right)^2 = N_K C_\infty n_b l_o^2$. According to Eq. (6.3), the contour length of a free chain is $N_K A_o = n_b l_o \cos\left(\theta_o / 2\right)$. Combining the two results we arrive at the following expression

$$\xi = \frac{C_\infty}{\cos^2\left(\frac{\theta_0}{2}\right)}. \qquad (6.15)$$

Since ξ can be obtained from Eq. ((6.14)), this relation allows for the computation of θ_0. Finally, with all other parameters determined, Eq. (6.4) can be applied to a free chain, $A_o = \frac{n_b}{N_K} l_o \cos\left(\frac{\theta_o}{2}\right)$, to calculate the equilibrium bond length. The calculated chain parameters are shown in Table 6.3.

Table 6.2: Tabular data used to define chain parameters for a variety of common polymers.

Polymer	Monomer Structure	C_∞	A_o (Å)	M_K (g/mol)	M_M (g/mol)	n_m	ρ (g/cm^3)
Poly(dimethyl siloxane) (PDMS) [50]	$[-Si(CH_3)_2-O-]_n$	6.8	13	381	74.17	2	0.895
Polypropylene (PP) [50]	$[-CH_2-CH(CH_3)-]_n$	5.9	11	180	42.08	2	0.791
Polyethylene (PE) [50]	$[-CH_2-CH_2-]_n$	7.4	14	150	28.05	2	0.784
Poly(methyl methacrylate) (PMMA) [50]	$[-CH_2-C(CH_3)(COOCH_3)-]_n$	9.0	17	655	100.12	2	1.13
Atactic Polystyrene (PS) [50]	$[-CH_2-CH(C_6H_5)-]_n$	9.5	18	720	104.1	2	0.969
Poly(methyl acrylate) (PMA) [91]	$[-CH_2-CH(COOCH_3)-]_n$	7.91	14.7	494.6	86.09	2	1.22
Poly(ethyl acrylate) (PEA) [91]	$[-CH_2-CH(COOCH_2CH_3)-]_n$	9.76	18.1	710.1	100.1	2	1.13

Table 6.3: Derived Polymer chain parameters.

Polymer	$\frac{n_b}{N_K}$	θ_o (degree)	l_o (Å)
Poly(dimethyl siloxane) (PDMS)	10.27	71.11	1.56
Polypropylene (PP)	8.47	66.85	1.56
Polyethylene (PE)	10.70	67.43	1.57
Poly(methyl methacrylate) (PMMA)	13.08	67.92	1.57
Atactic Polystyrene (PS)	13.83	68.07	1.57
Poly(methyl acrylate) (PMA)	11.49	67.86	1.54
Poly(ethyl acrylate) (PEA)	14.18	67.91	1.54

6.2.4. *Active Chains with Mechanophores*

Recently there have been strong interests into embedding mechanophores, molecules in which mechanical force can trigger a reaction, onto polymer chains to produce active materials capable of emitting light [4], changing color [47, 48], or relieving stress [87]. For example, it was shown that with the addition of certain mechanophores, sufficiently large tensile force caused conversion of monomers on the chains backbone to longer monomers [84-88], which led to a plateau in the chain force-extension relationship. The theory presented above can be modified to describe such systems.

For these polymer chains the backbone structure is more complicated so Eq. (6.5) must be modified to include additional contributions to the chain energy due to mechanophores. If we consider a chain that has n_1 mechanophore units in the unconverted state and n_2 mechanophore units in the converted state, then the chain energy can be written as

$$E = E_{ent} + n_b\left[E_{str} + E_{ben}\right] + n_1 E_1 + n_2 E_2, \tag{6.16}$$

where E_1 and E_2 are the energies of one unit in the unconverted and converted stares respectively. Before any force has been applied $n_2 = 0$. If we denote the lengths of the unconverted and converted units as l_1 and l_2 respectively, where $l_2 > l_1$, the contour length of the chain will be given by

$L_c = N_K A = n_b l \cos\left(\frac{\theta}{2}\right) + n_1 l_1 + n_2 l_2$.	(6.17)

Note that unless $n_1 << n_b$ the tabulated values discussed in the last section cannot be used to determine A_o. Instead the Kuhn length is defined as follows

$A = \frac{L_c}{N_K} = \frac{n_b l \cos\left(\frac{\theta}{2}\right) + n_1 l_1 + n_2 l_2}{N_K}$,	(6.18)

and $A_o = \left[n_b l_0 \cos\left(\theta_0 / 2\right) + n_1 l_1 \right] / N_K$ where no force is applied on the chain and no mechanophores are triggered. The force acting on each mechanophore unit can be obtained by taking the derivative of the potential with respect to the length of the unit:

$F_1 = \frac{dE_1}{dl_1}$,	(6.19)
$F_2 = \frac{dE_2}{dl_2}$.	(6.20)

As before constraints are needed for the compatible values of r^*, l, θ, l_1 and l_2. Specifically, if the chain end-to-end distance *r* is fixed, l, θ, l_1 and l_2 should be such that the free energy is minimized. In particular, Eqs. (6.11) and (6.12) still hold, whereas two more constraints are imposed:

$$\left.\frac{\partial E_{ch}}{\partial l_1}\right|_{r,l,\theta,l_2} = 0 = \frac{dE_{ent}}{dr}\frac{dr}{dr^*}\left.\frac{\partial r^*}{\partial l_1}\right|_{r,l,\theta,l_2} + n_1\frac{dE_1}{dl_1} = FL_c\frac{\partial}{\partial l_1}\left(\frac{r}{n_b l\cos\left(\frac{\theta}{2}\right) + n_1 l_1 + n_2 l_2}\right) + n_1 F_1$$

$$= FL_c\left(-r^*\frac{n_1}{L_c}\right) + n_1 F_1 = -Fn_1 r^* + n_1 F_1$$

similarly

$$\left.\frac{\partial E_{ch}}{\partial l_2}\right|_{r,l_1} = 0 = -Fn_2 r^* + n_2 F_1$$

which leads to

$F_{MP} = F_1 = F_2 = Fr^*,$	(6.21)

where we have denoted the force acting on the mechanophore units to be F_{MP}.

Consider an example where the mechanophores upon external loading undergo a reaction in which their lengths increase by approximately 16% [84]. In this material the entire polymer chain is made of mechanophores, so effectively $n_b = 0$ in Eq. (6.16). E_1 and E_2 in Eq. (6.16) have been represented by quadratic functions [84] and are shown in Figure 6.3a). The forces calculated from Eqs. (6.19) and (6.20) are shown in Figure 6.3b). Here points A ($l_{1o} = 0.948nm$) and B ($l_{2o} = 1.099nm$) mark the lengths for the unconverted and converted mechnophore units, respectively, at which they experience zero force. The dashed line connecting C to D is a hypothetical transition, from the unconverted to the converted states, which occurs at a force of 2nN. According to Eq. (6.21) the force remains constant during this transition.

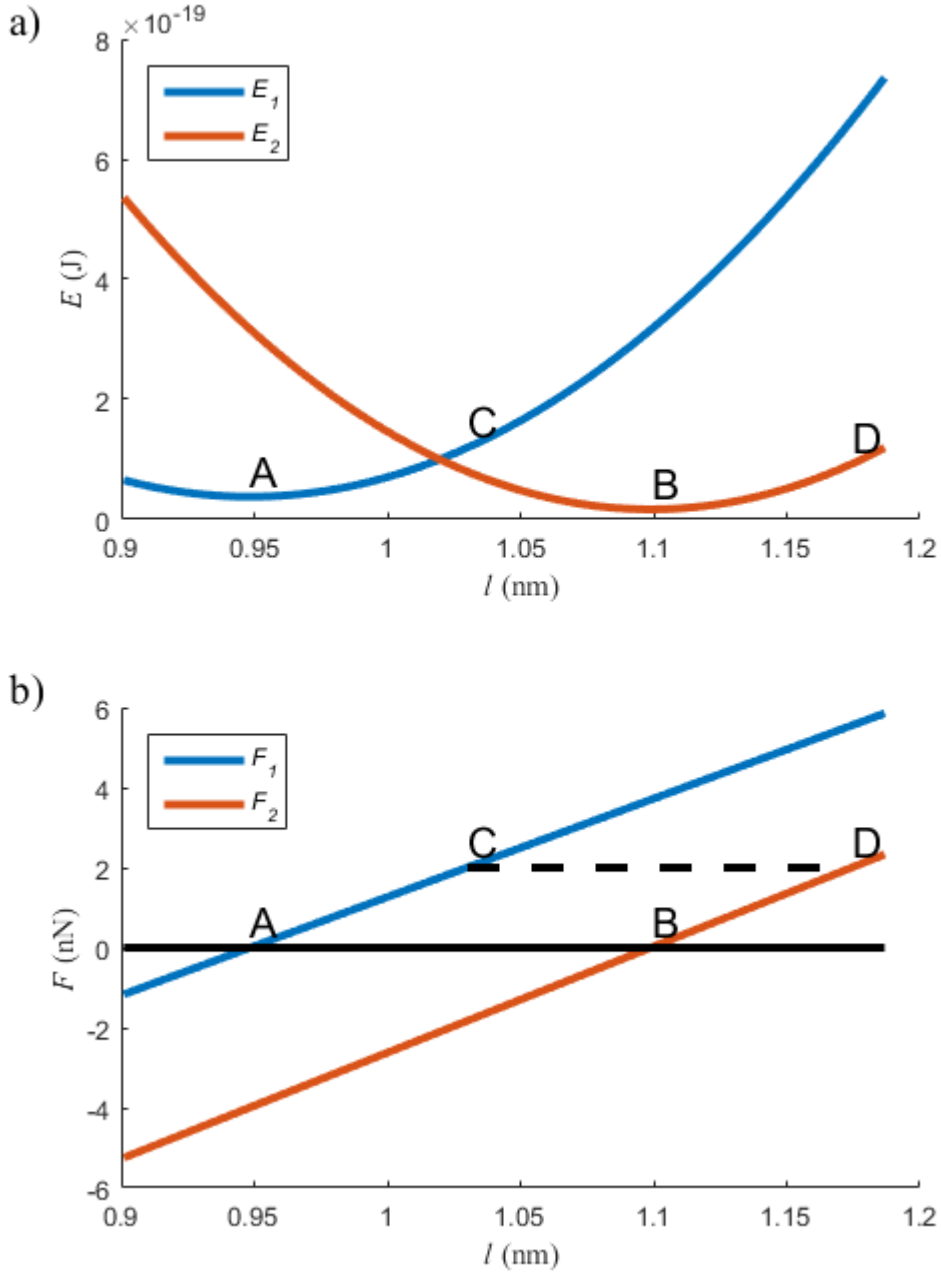

Figure 6.3 a) Energies of unconverted and converted mechanophore units proposed in [84]. E_1 corresponds to cis-syn-CL-gCFC repeating unit $E_1\left[kJ/mol\right]=6678.6-1403.52l_1+73.99l_1^2$ *where* l_1 *is in Angstrom. E2 corresponds to 2-fluro-3-chloro-alkene (Z isomer) repeating unit* $E_2\left[kJ/mol\right]=9652.16-1754.9l_2+79.85l_2^2$ *where* l_2 *is in Angstrom. b) Force vs. length obtained by taking the derivative of E_1 and E_2.*

6.2.5. *Reaction Kinetics*

The bonds on a polymer chain backbone can dissociate, and in some cases can re-associate, with certain reaction rates. Such reactions rates are influenced by the application of external force. For instance, some models propose that the activation energy for bond dissociation is decreased proportionally by the application of an external force with the activation length being a constant controlling the decrease [1¸2, 3,]. A refinement to this model is the cusp model where mechanical force alters the position of the reactants which changes the activation length [81¸85]. In this model, the reaction rate k can be written as [81, 82, 85]

$$k(f) = k_o\left(1-\frac{fx^{\ddagger}}{2\Delta G^{\ddagger}}\right)^{-2}\exp\left(\frac{fx^{\ddagger}}{k_B T}\left(1-\frac{fx^{\ddagger}}{4\Delta G^{\ddagger}}\right)\right), \quad (6.22)$$

where k_o is a constant controlling the reaction rate, $\Delta G^{\ddagger}$ is the activation energy of the transition state, $x^{\ddagger}$ is the activation length of the transition state and f is the mechanical force. Eq. (6.22) predicts a critical force [82] where the reaction rate becomes singular:

$$f_{crit} = \frac{2\Delta G^{\ddagger}}{x^{\ddagger}}. \quad (6.23)$$

The reaction rate equation in Eq. (6.22) can be applied to describe the rupture of regular polymer bonds [81, 82], as well as the transition of mechanophores from shorter to longer lengths [84, 85]. Firstly, if we denote the fraction of surviving regular bonds (i.e., not mechanophore) as b_P then the following expression can be used to predict the scission of these bonds[1, 2, 3, 5]

$$-\frac{db_P}{dt} = n_b b_P k(F_{str}). \quad (6.24)$$

To predict the rate of mechanophore reaction, we denote the unreacted fraction of mechanophores as b_{MP} and write the following expression

$$n_1 = n_0 b_{MP}, \quad (6.25)$$

$$n_2 = n_0(1-b_{MP}), \quad (6.26)$$

where $n_0 = n_1(t=0)$. The mechanophore reaction will be governed by

$$-\frac{db_{MP}}{dt} = n_0\left[b_{MP}k\left(F_{MP}\right) - \left(1-b_{MP}\right)k_R\left(F_{MP}\right)\right], \quad (6.27)$$

where $k_R\left(F_{MP}\right)$ denotes the rate of reverse reaction where the mechanophores transition from long to short lengths. $k\left(F_{str}\right)$, $k\left(F_{MP}\right)$ and $k_R\left(F_{MP}\right)$ will be governed by different constants (k_o, $\Delta G^{\ddagger}$, $x^{\ddagger}$). In addition, $k_R\left(F_{MP}\right)$ would need to have a different functional form than Eq. (6.22) because the reverse reaction is altered by mechanical force differently that the forward reaction [47, 48]. In this work we focus on cases where the forward reaction dominates (i.e., mechanopore elongation upon tensile force) and the reverse reaction is negligible ($k_R\left(F_{MP}\right) \approx 0$) in Eq. (6.27)). There is one more important point to make regarding $k\left(F_{str}\right)$ and $k\left(F_{MP}\right)$. In the literature these reaction rates have typically been predicted by using the polymer chain force F [1, 2, 3, 5, 81, 82, 84, 85]. However, because the model presented in this work provides the force acting on bonds in the polymer chain backbone F_{str} and the force acting on the mechanophore F_{MP} separately, more physical force measures can be used in predicting the reaction rates.

Now consider a polymer chain and denote its surviving chain fraction as b, and the effective force it carries is defined as

$$F_{eff} = bF. \quad (6.28)$$

b can be related to b_P and b_{MP} above. In a simple polymer chain (no mechanophores)

$$b = b_P. \quad (6.29)$$

However, if the chain also contains mechanophores which rupture after reaction, then

$$b = b_{MP}b_P, \quad (6.30)$$

where b_P is predicted by Eq. (6.24) and b_{MP} is predicted by Eq. (6.27) with $k_R = 0$.

There are three special cases involving mechanophores for which the above equations can be simplified. The first case is the bis(adamantyl)-1,2-dioxetane bisacrylate mechanophores used to crosslink elastomers [4]. In this case the reacted state is a dissociated bond, i.e., $E_2 = 0$, $l_2 = \infty$ and they do not need to be considered in Eqs. (6.16) and (6.17). Furthermore, because the

mechanophore is a crosslinker, there is a mechanophore on either end of the chain so $n_1 = 2$. Since $n_1 << n_b$ it is a reasonable approximation to use equations from 6.2.1 to 6.2.3 rather than the more general equations presented on section 6.2.4. Surviving chain fraction for this case is given by by Eq. (6.30). This case is examined in section 6.3.3.

The second case is the activation of a mechanophore which does not produce any change in mechanical properties. This feature can be reproduced by letting $E_1 = E_2$, and $l_1 = l_2$. In this case b_{MP} could indicate quantities such as color change. This case has been previously explored in the literature [47, 48].

The third case is the activation of a mechanophore which increase the contour length of the polymer chain. In particular, in section 6.3.4 we consider the polymer chain constructed entirely of these mechanophores [84] and hence $n_b = 0$. The transition is reported to be permanent [86] so $k_R = 0$.

6.2.6. *Solution Procedure*

The desired output is to find the force-extension relationship (F vs. $r_o^* = r / N_K A_o$), $b_P\left(r_o^*\right)$, and in some cases $b_{MP}\left(r_o^*\right)$. Eqs. (6.24) and (6.27) are solved using a Runge-Kutta method with adaptive step-size control [24] to obtain $b\left(r_o^*\right)$ and $b_{MP}\left(r_o^*\right)$ where r_o^* is increased in each step. During each step it is necessary to solve for several intermediate variables by simultaneously solving multiple equations. For a simple polymer chain (no mechanophores) Eqs. (6.1)-(6.4), (6.8), (6.10)-(6.12) are solved to obtain F, L_c, A, l, θ, F_{st}, M and r^*. If mechanophores are present, then Eqs. (6.1)-(6.2), (6.8), (6.10)-(6.12), (6.17)-(6.21) are solved to obtain F, L_c, A, l, θ, F_{st}, M, r^*, l_1, l_2, and F_{MP}.

While the procedure above is relatively efficient, there are certain applications, such as finite element simulation using a constitutive model based on the present single chain theory, implementation of this numerical procedure at many points in the material would be computationally costly. For this reason, we have also used curve fitting to provide simple yet accurate representations for the solutions to F, b, and db/dt in terms of $r_o^* = r / N_K A_o$ for several polymers. A summary of the fitting procedure and results is given in the Appendix. The variable

r_o^*, the fractional extension with respect to the initial Kuhn length, has been chosen for all fitted function because it can be related to the first invariant of the left Cauchy Green deformation tensor of the bulk material, $I_1(\underline{B})$ [9], which can be computed from a finite element program.

6.3. Results

The results are presented in several sections. For PDMS we compare the predicted chain force and rate dependent damage with experimental measurements in Sections 6.3.1 and 6.3.2 respectively. In Section 6.3.3 we compare the damage of PEA chains that have different lengths, with and without crosslinking mechanophores. Finally in Section 6.3.4 we compare the predicted chain force with experimental data for an active chain made entirely of mechanophore units that increase in length upon activation. It will be demonstrated how this type of chain could lead to improved mechanical properties in polydispearse elastomers. Necessary molecular parameters are taken from Table 6.1 and Table 6.2.

6.3.1. *Simple Chain without bond scission*

To illustrate how chain force and bond deformation change as the fractional extension (r_o^*) is increased, several relevant quantities for a PDMS chain have been plotted in Figure 6.4. In Figure 6.4a) the force acting on the chain F (blue) and the force acting on the bonds F_{str} (red) are plotted. As expected from Eq. (6.11) F is slightly larger than F_{str}. In addition, for this polymer the maximum extension of the entropic model $r_o^* = 1$ is exceeded. The deformation of bond length (blue) and angles (red) as a function of r_o^* are shown in Figure 6.4b). As expected when the force is small the deformation of bonds is negligible indicating the force is determined primarily by entropy. However, once a fractional extension of about $r_o^* = 0.9$ is reached sufficient force is present to cause significant bonds deformation. After this point r^* changes from increasing linearly with r_o^* to asymptotically approaching a value of 1 as shown in Figure 6.4c). This feature prevents the force singularity that occurs at $r_o^* = 1$ in purely entropic models.

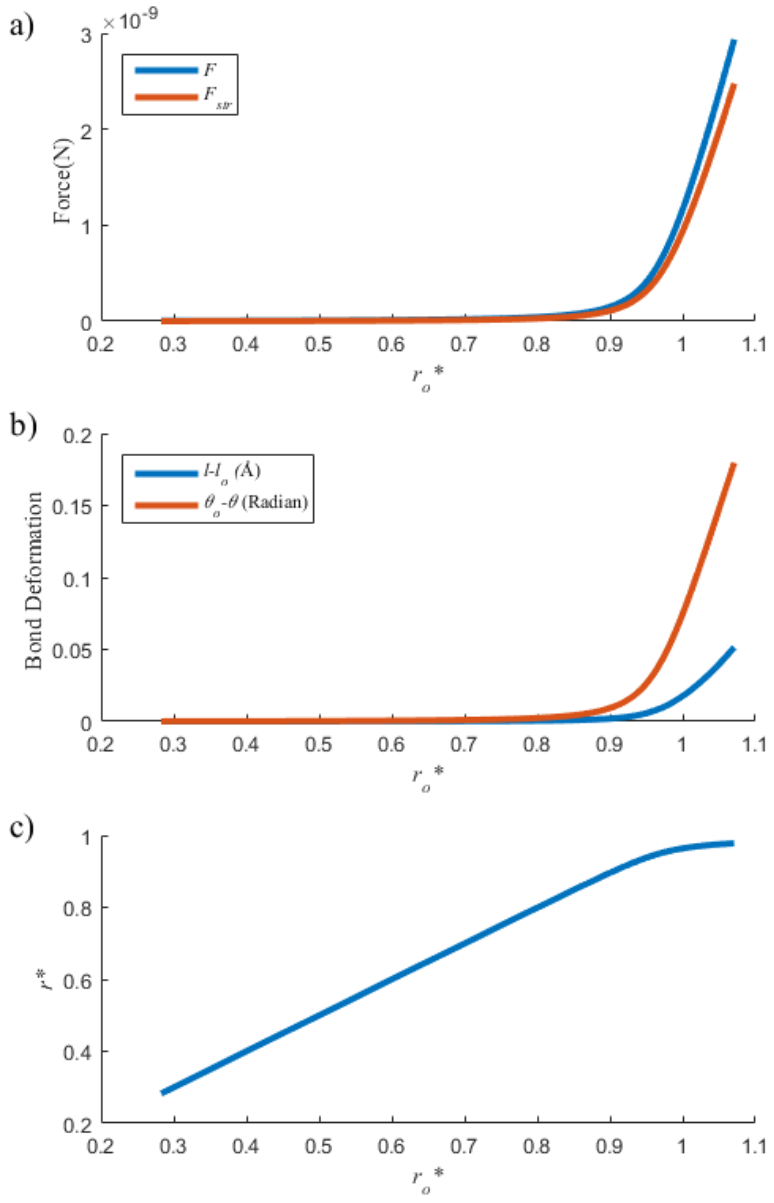

Figure 6.4 a) Comparison of the tensile force acting on the chain with the tensile force acting on the bonds in the chain. b) Bond stretch and bond deformation angle plotted against r_o^*. *c)* r^* *plotted against* r_o^*. *The parameters used in generating these graphs are for PDMS (Table 6.2) and Si-O bond (Table 6.1)*

Without the consideration of damage, the force-extension relationship for PDMS chain is shown in Figure 6.5a) (blue). Also shown in this figure is the relationship based purely on entropic elasticity (yellow) (Eq. (6.1)). Clearly, the deformation of bonds makes the force-extension relationship considerably softer for $r_o^* > 0.9$. In [3], single chain extension data were presented for PDMS, and the entropic chain model was found to be able to fit the data only up to $r_o^* = 0.9$. To see if the model established here performs better in describing the force-extension relationship, the same experimental data are also shown in Figure 6.5a). This data was obtained from atomic force microscopy (AFM) measurements which, in the raw form, is force vs. end to end distance. When attempting to fit the data using the entropic model, two fitting parameters are used: the Kuhn length which impacts the force magnitude predicted (Eq. (6.1)), and the contour length which impacts the fractional extension. The Kuhn length obtained using this method is often much smaller than the tabulated values; for example, 0.3 nm as determined in [3] versus 1.3 nm tabulated in [50]. In our model, the tabulated value for the Kuhn length (1.3 nm for PDMS) is directly used and the only fitting parameter is the contour length. To produce a good fit between our model and experimental data a contour length shorter than that in Ghatak et al [3] is needed, so we have scaled up their reported fractional extensions by a factor of 1.085 in Figure 6.5a).

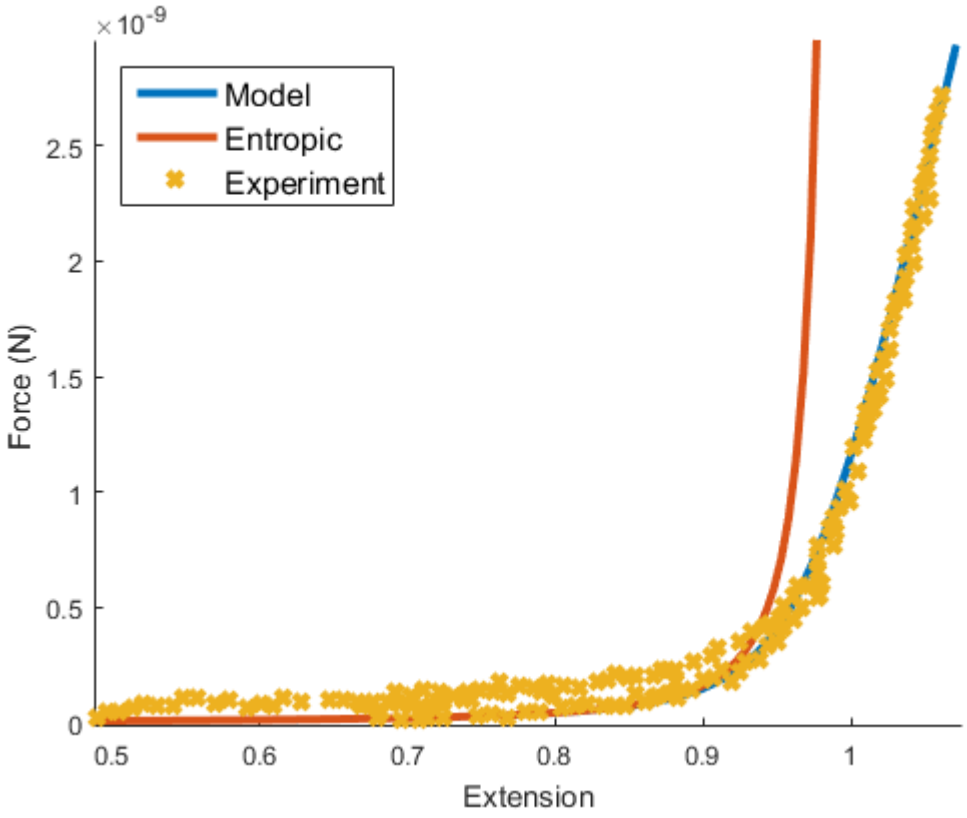

Figure 6.5: Comparison of the force-extension relationship from the entropic elasticity model Eq. (6.1), with the prediction by the model presented in this work and AFM experimental data for a single polymer chain [3]. The parameters used in generating these graphs are for PDMS (Table 6.2) and Si-O bond (Table 6.1)

6.3.2. *Simple Chain with Bond Scission*

To illustrate the scission of PDMS chains and its rate dependence, we calculate the surviving chain fraction b for a number of extension rates (V) presented in Chaudhury et al. [2]. The following parameters were found to provide a good fit to the experimental data in Chaudhury et. al. [2] (to be discussed in conjunction with Figure 6.7): $k_o = 1\times10^{-13}$, $\Delta G^{\ddagger} = 1.125\times10^{-19} J$, and $x^{\ddagger} = 0.09\times10^{-9} m$. Here k_o and $x^{\ddagger}$ are close to the values used in the model of Chaudhury [2] while $\Delta G^{\ddagger}$ is chosen so that the critical force on the polymer chain would be close to the critical value reported in the literature [82]. With these kinetic parameters the surviving chain fraction b and the effective force are shown in Figure 6.6 for four different extension rates. Increasing the extension rate causes the damage to shift to higher fractional extensions (see Figure 6.6a)); and

this translates to an increase in the peak effective force (see Figure 6.6b)). On the other hand, as the extension rate increases the maximum extension approach an asymptotic limit (black dotted line) because the forces on bonds in the chain approach the critical force Eq. (6.23). This is particularly evident in the purple curves in Figure 6.6 which correspond to the highest extension rate.

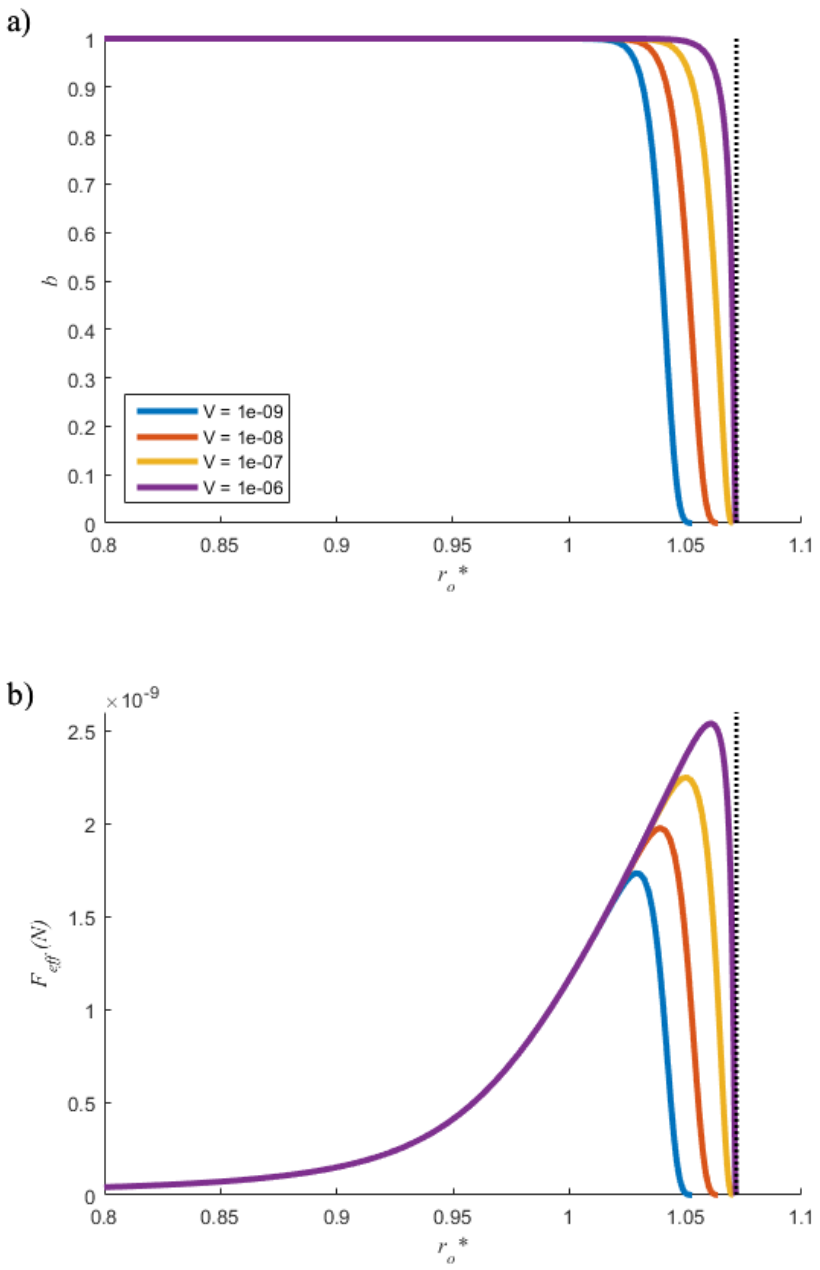

Figure 6.6 a) Surviving chain fraction of polymer chain, b, plotted against fractional extension r_o for 4 different chain extension rates. b) Effective force F_{eff}* = bF* =bFA_o/k_BT plotted against fractional extension r_o* for 4 different chain extension rates. The parameters used in generating these graphs are for PDMS (Table 6.2), Si-O bond (Table 6.1), Temperature T = 298 K,* $k_o = 1\times10^{-13}$, $\Delta G^{\ddagger} = 1.125\times10^{-19} J$, *and* $x^{\ddagger} = 0.09\times10^{-9} m$.

The model also allows us to determine the fracture energy of a PDMS interface (G), which can be computed as follows [1]

$G = \int \Sigma F dr = N_K \Sigma_o k_B T \int b F^* dr_o^*$,	(6.31)

where Σ is the areal density of load bearing polymer chains and Σ_o is the initial areal density of load bearing polymer chains prior to any applied load. This fracture energy was measured as a function of different interface separation speeds (V) in Chaudhury [2], and the experimental data (blue) are compared with predictions made by the model (red) in Figure 6.7. Here the contour length of the chain (L_c = 16.3nm, equivalent to n_b = 129) and $\Sigma_o = 5.28\times10^{18} m^{-2}$ are parameters used to fit the experimental data. The model has reasonably reproduced the experimental data and captured the increased energy needed to rupture polymer chains at higher speed.

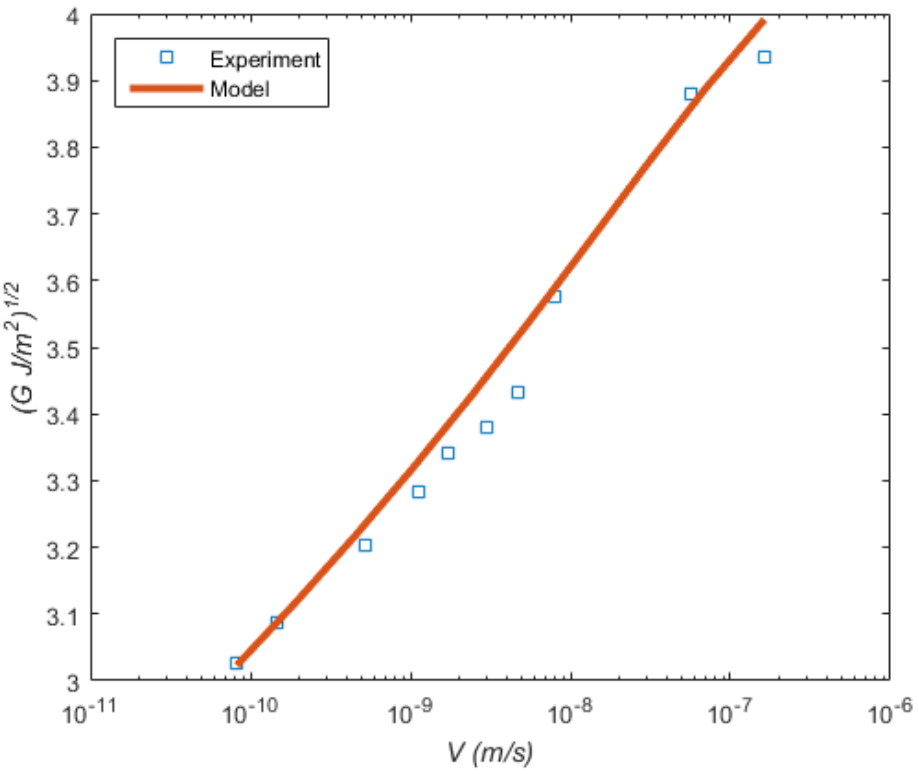

Figure 6.7: Frature energy G plotted agaist interface spearationspeed *V*. Experiemtnal data and model prediction are compared. *The parameters used in generating these graphs are for PDMS (Table 6.2) and Si-O bond (Table 6.1). L_c = 16.3nm and* $\Sigma_o = 5.28\times10^{18} m^{-2}$ *were found to provide a good fit for the experimental data.*

6.3.3. *Effect of Mechanophores on Chain Scission*

Figure 6.8a) shows the surviving chain fraction for 3 PEA chains (containing no mechanophores) of different chain lengths (i.e., different number of Kuhn segments N_K). The corresponding non-dimensional effective force, $F^*_{eff} = F_{eff} A_o / k_B T$, is shown in Figure 6.8b). Here a constant stretch rate of $\dot{\lambda} = 0.0171 s^{-1}$ is applied in all cases, and Eqs. (6.24) and (6.27) can be transformed to eliminate time dependence under the constant rate (see Appendix for details). Longer chains are observed to rupture at shorter extension since there are more bonds and hence more potential failure points. Depending on the chain length, the peak of the effective force is between 2 and 3nN. The maximum extension, at which all bonds break, exceeds the entropic locking extension by 10-12%.

The same calculations are repeated for a polymer chain crosslinked with weaker mechanophore bonds. In this example the mechanophores with dissociation energy of 150kJ/mol, much lower than that of C-C bonds (350 kJ/mol), were used as crosslinker [4]. The surviving chain fraction for 3 different chain lengths (N_K) is shown in Figure 6.9a), and the corresponding effective force is shown in Figure 6.9b). Here because scission is dominated by the rupture of mechanophores the difference between different chain lengths is nearly negligible. Compared with the case without mechanophores (Figure 6.8) the peak force is less, between 1.5 and 2 nN; as well the maximum extension is reduced and only exceeds the entropic locking extension by about 5%.

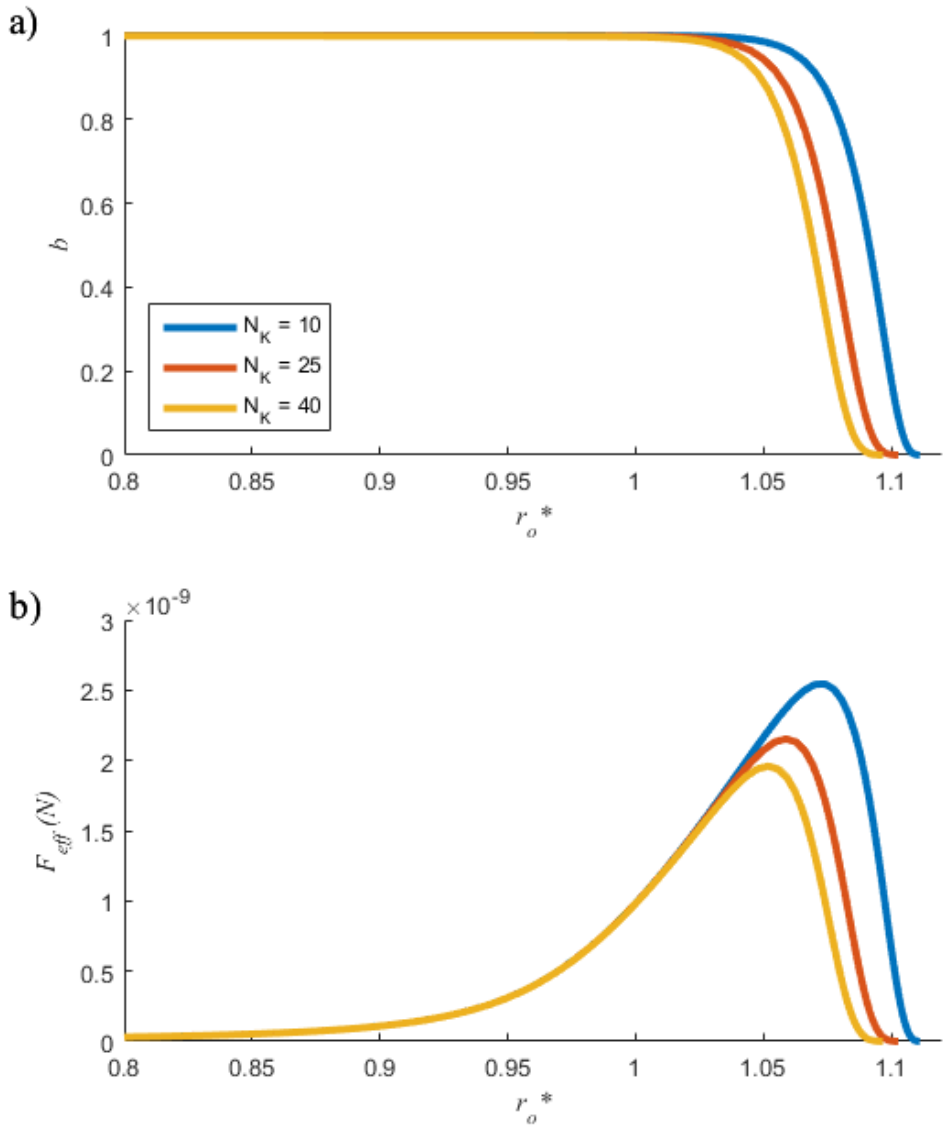

Figure 6.8 *a) Surviving chain fraction, b, plotted against fractional extension r_o* for 3 different chain lengths. b) Effective force F_{eff}* = bF* =bFA_o/k_BT plotted against fractional extension r_o* for 4 different chain lengths. The parameters used in generating these graphs are for PEA (Table 6.2), C-C bond (Table 6.1), Temperature T = 298 K, stretch rate* $\dot{\lambda} = 0.0171 s^{-1}$, $k_o = 5\times10^{-9}$, $\Delta G^{\ddagger} = 40\times10^{-21} J$, *and* $x^{\ddagger} = 0.021\times10^{-9} m$ *these values are based upon the PDMS values in the literature [82] however, these have been calibrated in another model, for which the publication is forthcoming, to match experimental stress magnitudes in multinetwork elastomers .*

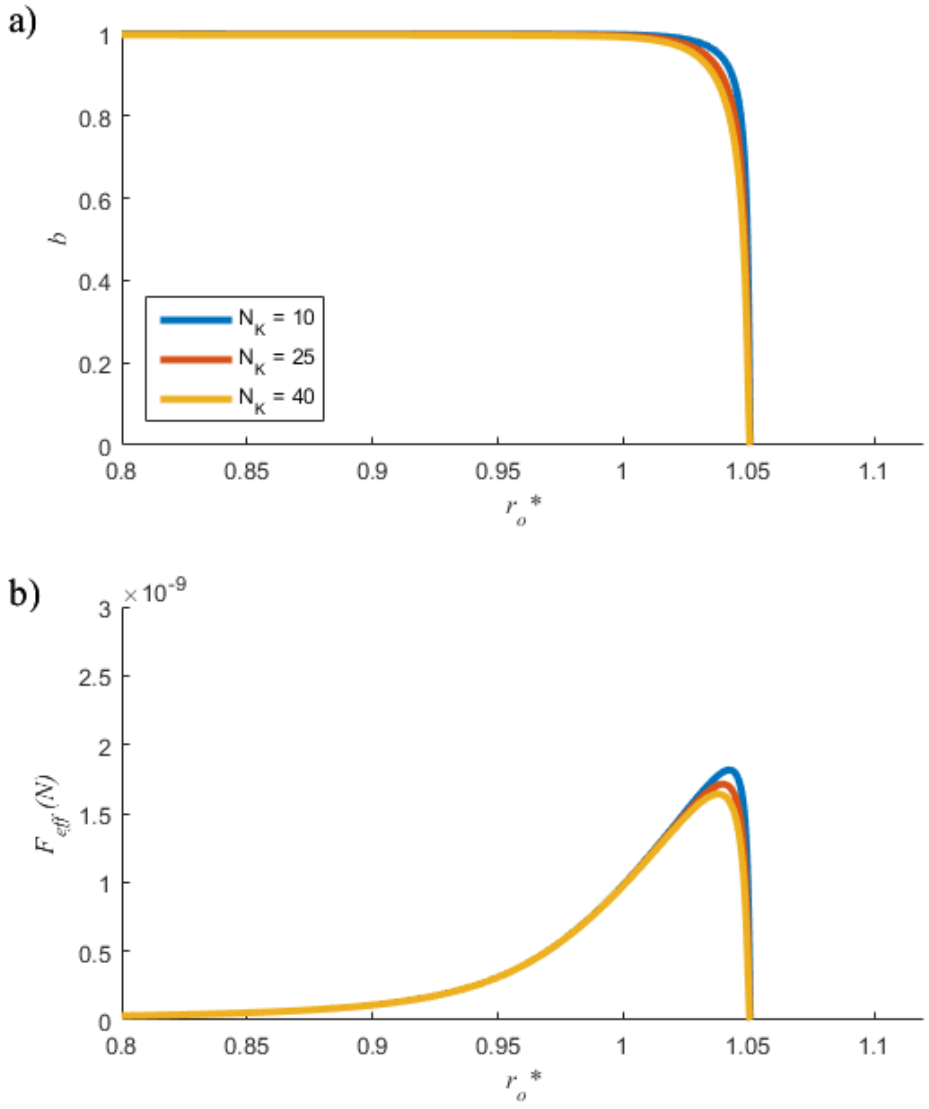

Figure 6.9 With a mechanophore on each end of the chain a) Surviving chain fraction, b, plotted against fractional extension r_o for 4 different chain lengths. b) Effective force F_{eff}* = bF* =bFA_o/k_BT plotted against fractional extension r_o* for 3 different chain lengths. The parameters used in generating these graphs are for PEA (Table 6.2), C-C bond (Table 6.1), Temperature T = 298 K, stretch rate* $\dot{\lambda} = 0.0171 s^{-1}$ $k_o = 5\times10^{-9}$, $\Delta G^{\ddagger} = 40\times10^{-21} J$, *and* $x^{\ddagger} = 0.021\times10^{-9} m$. *For the mechanopohore* $k_o = 2\times10^{-6}$, $\Delta G^{\ddagger} = 20\times10^{-21} J$, *and* $x^{\ddagger} = 0.021\times10^{-9} m$

6.3.4. *Chains composed of mechanophores with elongation reaction*

Finally we examine the situation where a polymer chain is composed entirely of mechanopore units that, upon activation, increase their length. Using the potentials E_1 (syn-CL-gCFC) and E_2 (2-fluro-3-chloro-alkene (Z isomer)) from Wang et al. [84]. , the unreacted fraction b_{MP} and the predicted force are plotted against r_o^* in Figure 6.10. In Figure 6.10a), b_{MP} initially stays at a constant value of 1 until the force, shown in Figure 6.10b), becomes sufficient for the mechanophores to react. Once this occurs b_{MP} drops smoothly to zero as all of the mechanophores react. The reaction of mechanophores increases the contour length of the polymer chain; therefore larger increases in r_o^* are need to increase the force. This creates a region in Figure 6.10b) where the increase of force with r_o^* significantly slows down. Experimental data from Wang et al. [84] is also shown in Figure 6.10b), which can be well fitted by the present model with $\Delta G^{\ddagger} = 32\times10^{-21} J$, $x^{\ddagger} = 0.025 nm$, $k_o = 8\times10^{-5} s^{-1}$, $L_c = 745 nm$, 300nm/s separation velocity [84] this corresponds to $dr_o^*/dt = 0.402$. Also shown for reference in Figure 6.10b) are the force for a purely entropic chain, as well as the forces for a 100% unreacted chain and a 100% reacted chain. The latter two can be calculated from the numerical solution of the reacting chain as follows. Once F_{MP} is known for the reacting chain Eqs. (6.20) and (6.1) are solved for r^* and F where the Kuhn length in Eq. (6.1) is replaced with

$$A_1 = \frac{n_b l \cos\left(\frac{\theta}{2}\right) + n_1 l_1}{N_K}, \tag{6.32}$$

for the 100% unreacted chain and

$$A_2 = \frac{n_b l \cos\left(\frac{\theta}{2}\right) + n_2 l_2}{N_K}, \tag{6.33}$$

for the 100% reacted chain.

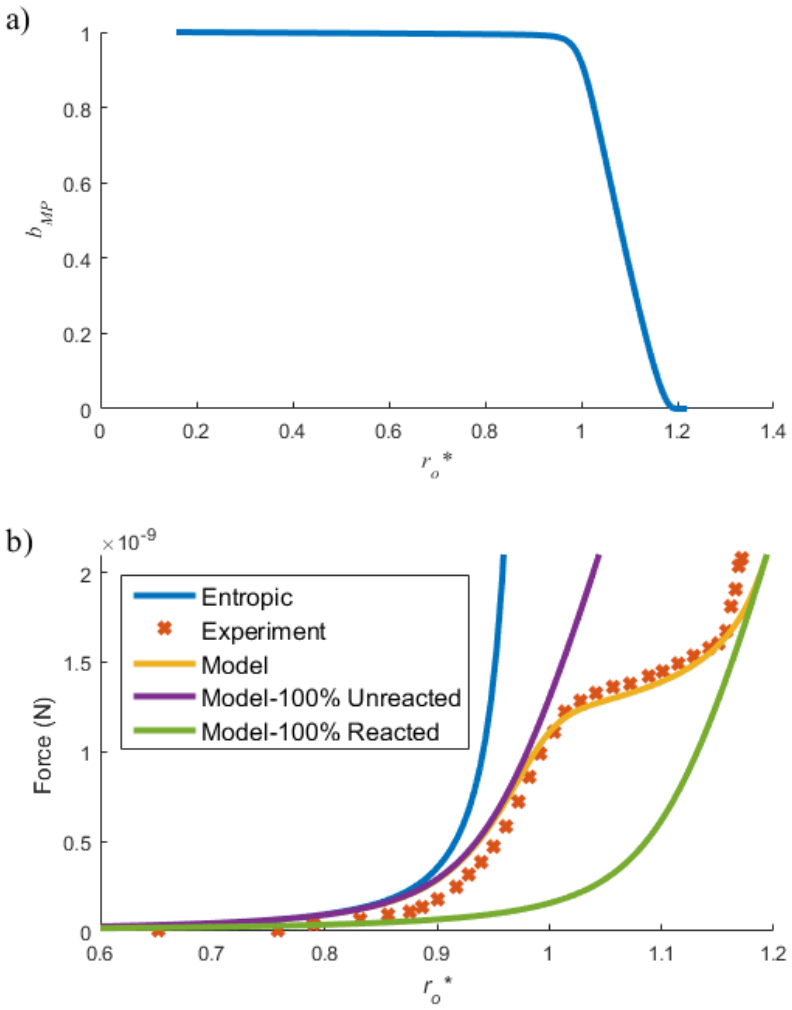

Figure 6.10: a) Unreacted mechanophore fraction vs r_o^*, b) Chain force vs r_o^*. Comparison is made between the force predicted by the model (yellow line) and the experimental data [84] (red x). Also shown is the force predicted by using a purely entropic model (blue), the model if all mechanophorse are unreacted (purple), and the model if all mechanphores are reacted (green). $dr_o^*/dt = 0.402$..

The force extension relationship, with a plateau, shown in Figure 6.10b) has the potential to be used to design elastomers with improved properties such as enhanced fracture toughness and ultimate stress. To illustrate this we will estimate the stress in a material consisting of many chains of different length as was done in Lavoie et al. [5]. For computation efficiency the curves in Figure 6.10b) are fitted with analytical functions and details of the fitting are given in the Appendix. Of interest is to compare how the different force-extension relationships, with the same surviving

chain fraction, Appendix, $b(F)$, will impact the stress this is done for the cases of an entropic chain, a reacting chain with reaction kinetics and a 100% unreacted chain; the resulting effective forces are shown in Figure 6.11. In each case the mean break force [81] defined as

$$\langle F \rangle_b = \frac{k_B T}{A_o} \int_0^1 F^*\left(r_o^*\right) db, \tag{6.34}$$

is the same because $b(F)$ is the same in each case.

The stress in a bulk polymer can be calculated from a chain force-extension relationship by following the procedure from Lavoie et al [5] where the strain energy is given by

$$U = \int_1^\infty w\left(N_K\right) b E_{ch} dN_k . \tag{6.35}$$

Here ν_{ch} is the volumetric density of polymer chains and $w\left(N_K\right)$ is a probability distribution function describing the number of chains which have N_K Kuhn segments. For the case of uniaxial extensions the fractional extension will be given by [9]

$$r_o^* = \sqrt{(\lambda^2 + 2\lambda^{-1})/3N_K} , \tag{6.36}$$

where λ is the stretch, and the stress can be written as [5]

$$\sigma = \mu \int_1^\infty w\left(N_K\right) \frac{b\left(r_o^*, N_K\right) F^*\left(r_o^*\right)}{6 r_o^*} dN_K \left(\lambda^2 - \lambda^{-1}\right). \tag{6.37}$$

where $\mu = \nu_{ch} k_B T$ is the shear modulus when $r_o^* = 0$. The stress, normalized by μ, is plotted in Figure 6.12a) against the stretch. An overall surviving chain fraction which considers the weighted contribution of all chain lengths can be defined as follows [5]

$$b_t = \int_1^\infty w\left(N_K\right) b\left(r_o^*, N_K\right) dN_K , \tag{6.38}$$

and it is plotted in Figure 6.12b). Comparing the three curves in Figure 6.12a) and Figure 6.12b) shows that the reacting mechanophores lead to the largest stress followed by the unreacting mechanophores, while the entropic chain produces the lowest stress. Similarly, chains with higher stress have higher surviving chain fraction in Figure 6.12b). The ability for the chain to prevent failure by increases in length allows more chains, of different lengths, to have higher force at any

given stretch which increases the maximum stress. To quantify this effect we define force efficiency as

$$\eta_F = \frac{\langle F_{eff} \rangle_{N_K}}{\langle F \rangle_b} = \frac{\int_1^\infty w(N_K) b(r_o^*, N_K) F^*(r_o^*) dN_K}{\int_0^1 F^*(r_o^*) db}. \quad (6.39)$$

Where the numerator is the Kuhn average force defined as

$$\langle F_{eff} \rangle_{N_K} = \frac{k_B T}{A_o} \int_1^\infty w(N_K) b(r_o^*, N_K) F^*(r_o^*) dN_K \ . \quad (6.40)$$

The force efficiency is plotted in Figure 6.12c) and correlates well to the stress magnitude due to the similarity in definition. However, what is interesting about the efficiency is the magnitude provides a direct measure of how well the elastomer is able to distribute load between all chains.

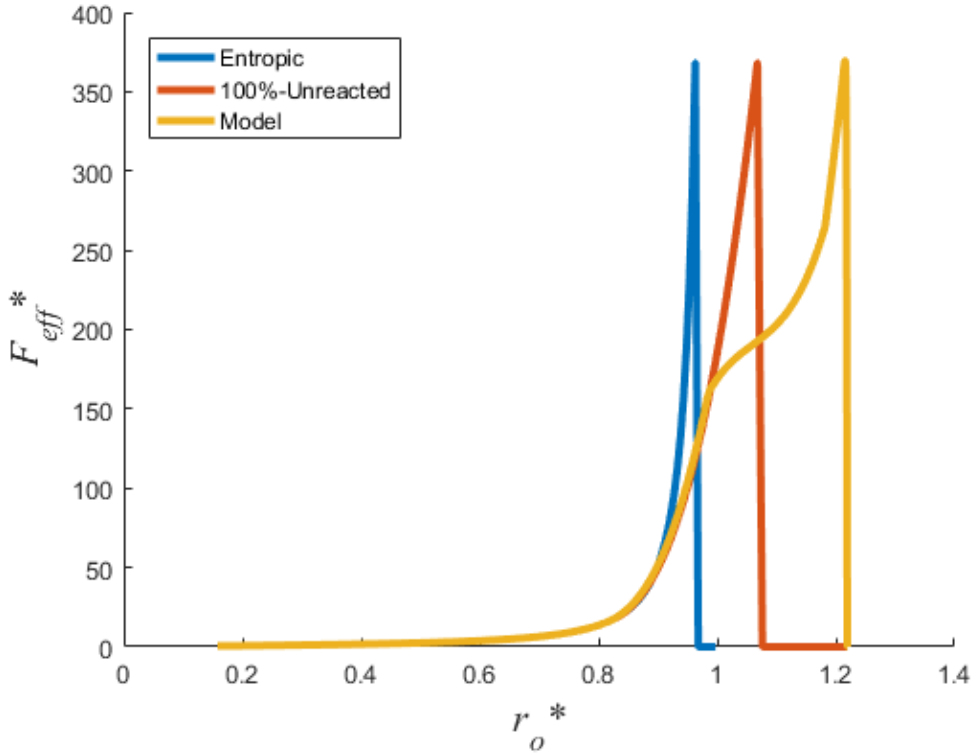

Figure 6.11: Effective force vs r_o^*. The same surviving chain fraction $b(F)$ is applied to each of the three polymer chains (i) a fully entropic chain (ii) a chain where the mechanophore cannot react and (iii) a chain where mechanophore can react.

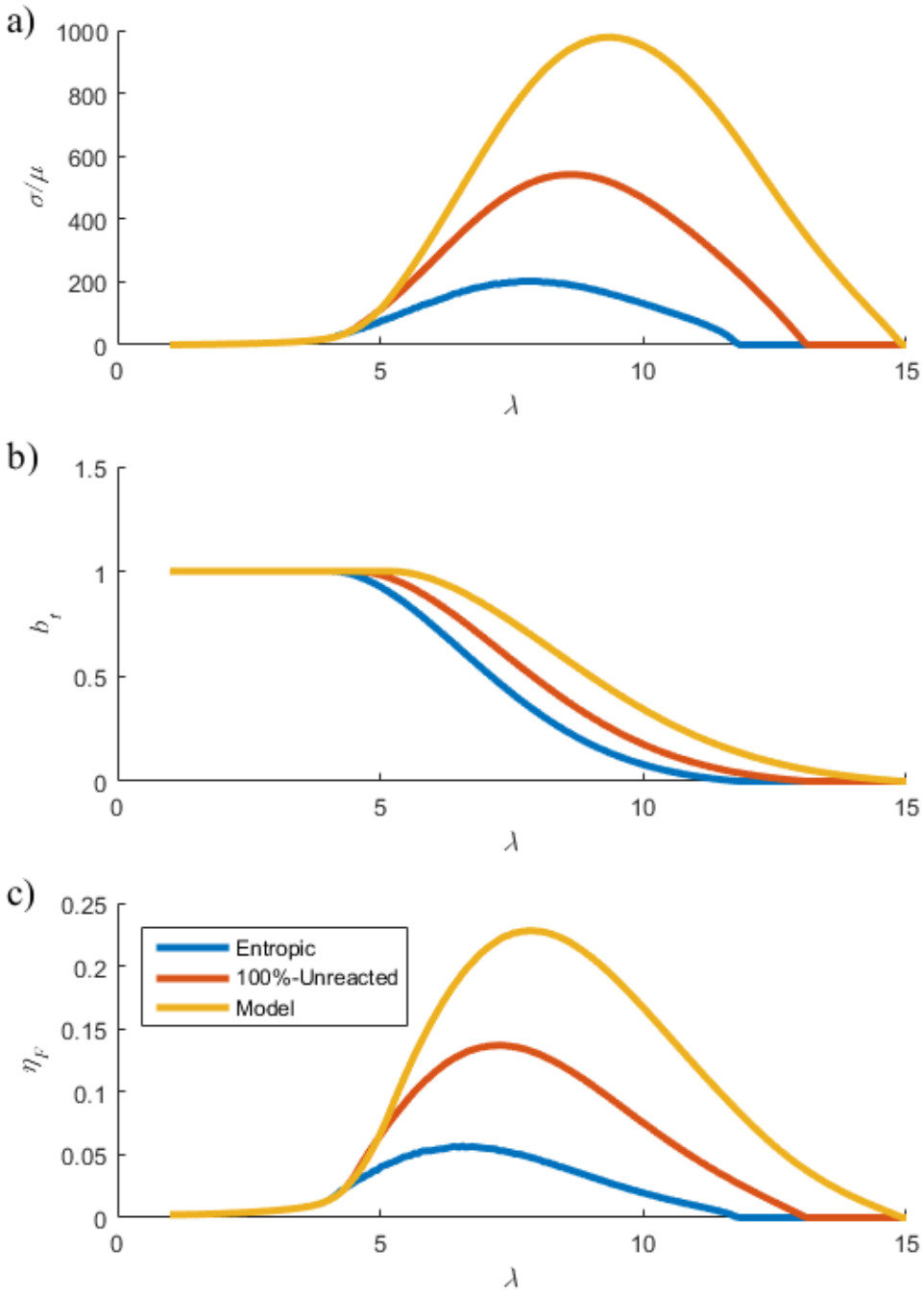

Figure 6.12 a) Nondimensional stress vs stretch b) Surviving chain fraction vs stretch c) Force efficiency vs stretch. In each subfigure three curves are shown each corresponds to a different force relationship from Figure 6.11. The following probability distribution function has been used to describe chain lengths $w(N_K) = 0.0239(N_K - 6.2)^{0.8}\exp(-0.12(N_K - 6.2))$ *[5].*

A few comments are warranted to put Figure 6.12 into perspective. Firstly, Figure 6.12a) suggests that the stress can be three orders of magnitude larger than μ which far exceeds anything that has been observed. For example for the single network elastomers presented in Ducrot et al [4] the true stress at break is of the same order of magnitude as the Young's modulus; whereas data for latex rubber show a true stress at break that is two orders of magnitude greater than μ [92]. The discrepancy in magnitude is most likely due to the fact that real materials contain defects, which lead to stress concentrations, localized damage, and failure much earlier than what is shown in Figure 6.12 a). If a stress concertation is present in experiments, the maximum local stress may be much higher than the maximum measured stress because this large stress only occupies a small fraction of the materials volume. Furthermore, the effect of the nonlinear force-extension relationship often cannot be seen in elastomer experimental data. For example in the single network data presented in Ducrot et al [4], only a small fraction of the material's volume has chains with high force when the sample fails. In these types of brittle elastomers designing the material with special polymer chains is unlikely to yield a significant improvement in properties. However, special manufacturing techniques have been used to dramatically enhance the toughness of brittle elastomers [4]. In particular, in multinetwork elastomers a primary network is prestretched by introducing filler networks. Prestretched chains are able to break in a large fraction of the material while the filler networks prevent large crack from forming [4]. In this type of material it stands to reason that using special polymer chains in the primary network could lead to a significant enhancement to the maximum stress and toughness.

6.4. Conclusion

A model is developed to predict force extension relationships for polymer chains by minimizing the free energy containing contributions from the configurational entropy and the energies for deformation of bonds on the polymer chain's backbone. Parameters in this model are largely molecular parameters available in the literature, and hence the number of parameters needed from fitting experimental data is minimal. Compared with classical entropic chain models the behavior is significantly softer at large extension, owing to the ability of the bonds to deform. The model is subsequently extended to include the consideration of active polymer chains containing mechanophores. It is demonstrated that the cusp model can be used in conjunction with

the chain model to predict rates of chain rupture and mechanophore reaction. In particular the model is able to reproduce the rate dependent fracture energy needed to advance a crack in PDMS, as well as the plateau in force extension relationship caused by mechanophores that increase the contour length of the chain when subjected to sufficient tensile force. By implementing the force extension relationship developed here into a simple constitutive model, it is shown that this type of active chain has the potential to significantly improve the maximum stress and toughness that elastomers can achieve.

6.5. Nomenclature

A_o	Initial Kuhn Length
A	Kuhn length
a_i	Fitting parameters for chain damage
α	Parameter in Maxwell Boltzmann Distribution
b	Surviving chain fraction
$\underline{B}$	left Cauchy green deformation tensor
β_1 , β_2	Fitting parameter in scission equations
β_s	Constant which controls width of Morse potential
C_∞	Asymptotic value of Flory's characteristic ratio
c_i	Fitting parameters for chain force curve fit
d_i	Fitting parameters for activation energy curve fit
D_e	Bond dissociation energy
E	Energy of polymer chain
E_a	Activation energy for bond dissociation
E_{ao}	Activation energy for unstreatched bond
E_{ent}	Entropic component of polymer chain energy
E_{str}	Energy of a single stretched bond on polymer chain backbone
E_{ben}	Energy of a single deformed bond angle on polymer chain backbone
F	Tensile force acting on polymer chain
F^*	Nondimensional polymer chain force
F_{eff}	Effective tensile force with consideration of ruptured polymer chains
F^*_{eff}	Nondimensional effective force
$F_{\max}$	Maximum bond force possible in Morse potential
F_{str}	Tensile force acting on individual bonds in the chain
h_P	Plank's constant

$I_1(\underline{B})$	1st invariant of the left Cauchy green deformation tensor of the bulk material
k_B	Boltzmann Constant
k_θ , k_{sexic}	Bending constants
λ	Uniaxial extension stretch
$\dot{\lambda}$	Uniaxial extension stretch rate
l_o	Initial bond length
l	Bond length
l_a	Activation length of a bond
L_c	Contour length of polymer chain
$l_{\max}$	Bond length required to reach peak of activation energy barrier
M	Bending moment acting on bonds
M_b	Average molecular weight per backbone bond
M_{ch}	Molecular weight of chain
M_K	Molecular weight of Kuhn segment
M_m	Molecular weight of a single monomer (repeat unit)
n_b	Number of backbone bonds on polymer chain
n_m	Number of backbone bonds per repeat monomer unit
n_{mp}	Average number of mechanophores embedded on each polymer chain
N_K	Number of Kuhn segments on polymer chain
P	Persistence length of polymer chain
θ_o	Initial bond angle
θ	Bond angle
ρ	Density of polymer
r	Polymer chain end to end distance
r^*	True Fractional Extension of polymer chain
r_o^*	Fractional extension of polymer chain relative to initial contour length

$r^*_{o,\max}$	Fractional extension where surviving chain fraction becomes negligible
$r^*_{o,peak}$	Fractional extension where peak rate of scission occurs
$\left\langle R_o^2 \right\rangle$	Mean square end to end distance of polymer chain (before stretch)
σ_{eng}	Engineering stress
T	Temperature
t	time
υ_{ch}	Volumetric Density of Polymer Chains

Chapter 7. Conclusion and Future Work

A greater understanding of the fracture process in inelastic elastomers, gained through fracture modelling, can lead to insights that subsequently allow for the design of tough materials which resist crack propagation. With the goal of developing tools to simulate crack initiation and propagation in inelastic elastomers, several models were developed in this thesis to determine the force on a stretched polymer chain, how the chain breaks and how this information can be used to predict the behavior of bulk materials as well as interfacial separation.

The first set of studies were conducted to investigate the peeling of viscoelastic double cantilever beams where an interfacial adhesive model describing the kinetics of breaking polymer chains controlled the separation of the two beams. This problem was solved using both linear and nonlinear polymer chain force-extension relationships. The apparent energy release rate consists of two components: the adhesive fracture energy due to dissipation on the interface, and viscous dissipation within the bulk material. Faster rates of peeling result in larger adhesive fracture energy whereas the rate-dependence of bulk viscous dissipation is non-monotonic. Although the peak magnitude of the viscous dissipation scales with the magnitude of the adhesive fracture energy, varying the ratio of bulk relaxation time and bond rupture time over several orders of magnitude resulted in very small changes in the effective modulus, crack opening displacement, and adhesive fracture energy. The likely explanation for this weak coupling is the fact that the beams' strain is perpendicular to the adhesive stress produced by the interfacial polymer chains.

Recognizing that experimental mapping of bond rupture events in elastomers has shown that chain scission can occur in a large area surrounding a crack, the kinetics of polymer chain breaking was extended from only on the interface to the constitutive model for the bulk material. With such model a cohesive zone is not needed to predict material failure, and higher deformation rate was found to result in larger maximum stresses. Adjusting the model to consider polydispersity, a distribution of chain lengths, decreases the maximum stress because the chains of different lengths attain their maximum force at different time and rupture gradually. This results in the capability of the model to predict progressive damage. An example of this is that the stress-stretch relationship under cyclic loading, with increasing amplitude after each cycle, exhibits hysteresis between loading of undamaged material and unloading of the damage material, which resembles

the Mullin's effect in filled elastomers. This characteristic is important since a strong connection between hysteresis and enhanced fracture toughness has been found in the literature.

The developed elastomer damage model provided an important component to study a new class of tough multinetwork elastomers. These materials are synthesized by swelling a primary elastomeric network with filler network(s), a process which prestretches the chains of the network formed in the previous step(s). Because the chains in the primary network often rupture during deformation, the elastomer damage model is applied to the primary network. The filler networks are subjected to less or negligible damage, and hence are represented by a simpler generalized neo-Hookean model. Pre-stretch of the chains is incorporated into the model by basing the strain energy of the material on the combined effect of swelling and subsequent deformation of the completed multinetwork elastomers. Based on this model, the primary network contributes the majority of the stress, while only occupying a small volume fraction. The model provides a good match to experimental data of multinetwork elastomers under uniaxial extension, including cyclic loading, for a variety of prestretches.

A key element in modeling mechanics of elastomers is the relationship between the force applied on a chain and its extension. Classical models for the chain force-extension relationship are far too stiff at large extension because they do not account for the deformation of bonds on the chains backbone. To overcome this deficiency, a new model was developed by minimizing the free energy containing contributions from the configurational entropy, bond stretch and bond angle deformation. The model was additionally extended to include the consideration of active polymer chains containing mechanophores. Of particular interest is the application of the model to chains that can increase their contour length when subjected to sufficient tensile force. The model well reproduces the experimental observation of a plateau in the chain force extension relationship when the chain length increases. Implementing such force extension relationship into a simple constitutive model, it is shown that this type of active chain has the potential to significantly increase the maximum stress and toughness that elastomers can achieve.

The models presented in Chapters 4 and 5 are being implemented as User Material subroutines within Abaqus, a commercial finite element analysis software package, and will be used to study large deformation crack initiation and propagation. Such analysis should provide new insights into the fracture process for tough inelastic elastomers. Of particular interest are

several questions (i) by what mechanism does stress-stretch hysteresis enhance fracture toughness, (ii) how do the shape of the stress-stretch curve and damage evolution impact the size of the damage zone around a crack rip, (iii) how much does crack tip blunting contribute to the enhancement of fracture toughness, and (iv) are the assumptions made to experimentally estimate fracture energies accurate for inelastic elastomers. Answering these questions will allow for grating insight into the failure of elastomers that will facilitate the design of tougher elastomers.

Bibliography

(1) Hui, C.Y.; Tang, T.; Lin, Y.Y.; Chaudhury, M.K. Failure of Elastomeric Polymers Due to Rate Dependent Bond Rupture. *Langmuir*, 2004, 20, pp 6052–6064

(2) Chaudhury, M.K. Rate-Dependent Fracture at Adhesive Interface. *J. Phys. Chem. B.*, 1999, 103, pp 6562–6566

(3) Ghatak, A.; Vorvolakos, K.; She, H.; Malotky, D.L.; Chaudhury, M.K. Interfacial Rate Processes in Adhesion and Friction. *J. Phys. Chem. B.*, 2000, 104, pp 4018–4030

(4) Ducrot, E., Chen, Y., Butlers, M., Sijbesma, R.P., Creton, C. Toughening Elastomers with Sacrificial Bonds and Watching Them Break. *Science* **2014**, 344, 186-189

(5) Lavoie, S.R.; Long, R.; Tang, T. A rate dependent damage model for elastomers at large strain, Extreme Mech. Lett. 8:115:124 (2016)

(6) Lavoie, S.R, Long, R., Tang, T. Rate Dependent Fracture of a Double Cantilever beam with Combined Bulk and Interfacial Dissipation. *Int. J. Solid Struct.*, **2015**,75-76, 277-286

(7) Lavoie, S.R., Long, R., Tang, T. An Adhesive Zone Model for Polymeric Interfaces, Int. J. Fracture, 2016, 197, 169-183

(8) Gent, A.N, "Adhesion and strength in viscoelastic solids. Is there a relationship between adhesion and bulk properties" *Langmuir*, 12 (1996) 4492–4496

(9) Arruda, E.M, Boyce, M.C. "A Three-Dimensional Constitutive Model For The Large Stretch Behavior of Rubber Elastic Materials." *J. Mech. Phys. Solids.*, 41 (1993) 389-412

(10) Lake, G.J.; Thomas, A.G. "The strength of highly elastic materials" *Proc. R. Soc. Lond. A*, 300 (1967) 108-119

(11) Gent AN, Schultz J (1972) Effect of wetting liquids on the strength of adhesion of viscoelastic material. Adhesion 3: 281–294

(12) Kovalchick, C.; Molinari, A.; Ravichandran, G., ASME J. Appl. Mech. **2014** (81), pp. 041016, 2014.

(13) Andrews EH, Kinloch AJ (1973) Mechanics of adhesive failure I. Proc R Soc Lond A 332*:* 385–399

(14) Williams, M.L.; Landel, R.F; Ferry, J.D, *J. Am. Chem. Soc.*, **1955**, 77 (14), pp 3701–3707

(15) Xu DB, Hui CY, Kramer EJ (1992) Interface fracture and viscoelastic deformation in finite size specimens. J Appl Phys 72(8): 3305–3316

(16) Christiansen RM (2003) Theory of Viscoelasticity 2nd Ed. Dover, New York

(17) Hui CY, Xu DB, Kramer EJ (1992) A fracture model for a weak interface in a viscoelastic material (small scale yielding analysis). J Appl Phys 72 (8): 3294–3304

(18) Chen, H.; Feng, X.; Huang, Y.; Huang, Y. ; Rogers, J. A., *J. Mech. Phys. Solids*, **2013.** 61, pp. 1737-1752

(19), Gao, X.-L.; Su, Y.-Y., *Acta Mech.*, published online, May 2015, DOI 10.1007/s00707-015-1357-8

(20) Rajagopal, K.R.; Wineman, A. A Constitutive Equation for Nonlinear Solids Which Undergo Deformation Induced Microstructural Changes. *Int. J. Plasticity.* **1992**, *8*, 385–395

(21) Wineman, A. On the Mechanics of Elastomers Undergoing Scission and Cross-linking *Int. J. Adv. Eng. Sci. Appl. Math.* **2009**, *1*, 123–131

(22) Rahulkumar, P.; Jagota, A., Bennison, S.J., Saigal, S. Cohesive element modeling of viscoelastic fracture: application to peel testing of polymers, *Int J Solids and Struct*, **2000**, 37, 1873-1897

(23) Hibbeler RC (2005) Mechanics of Materials, SI second ed. Pearson Prentice Hall: Singapore, 589, 607-614

(24) Press, W.H.; Teukolsky, S.A., Vetterling, W.T.; Flannery, B.T. *Numerical Recipes The Art of Scientific Computing 3rd Ed.*; Cambridge University Press: Cambridge, 2007, pp.

(25) Rice, J.R., *J. Appl. Mech.*, **1968**, 35(2), pp 379-386

(26) Glassmaker N, Hui C (2004) Elastica solution for a nanotube formed by self-adhesion of a folded thin film. J of Appl Phys 96: 3429–3434

(27) Anderson, T.L.; *Fracture Mechanics*; CRC Press: Boca Raton, 2005, pp.

(28) Tang T, Glassmaker N (2010) On the inextensible elastica model for the collapse of nanotubes. Math Mech Solids 15: 591–606

(29) Evans, E., Ritchie, K. Dynamic Strength of Molecular Adhesion Bonds. *Biophysical Journal.* **1997**, *72*, 1541–1555

(30) Tang, T.; Jagota, A.; Chaudhury, M.; Hui, C.Y. *J. Adhes*. **2007**, *87*, 671–696

(31) Bell G (1978) Models for the specific adhesion of cells to cells. Science 12: 618-627

(32) Beyer, M.K, Clausen-Schaumann, H. Mechanochemistry: The Mechanical Activation of Covalent Bonds. *Chemical Reviews.* **2005**, *105*, 2921–2948

(33) Wojtecki RJ, Meador MA, Rowan SJ (2011) Using the dynamic bond to access macroscopically responsive structurally dynamic polymers. Nature Materials 10: 14-27

(34) Kramers HA, (1940) Brownian motion in a field of force and the diffusion model of chemical reactions. Physica VII: 284-304

(35) Hanggi, P, Talkner, P, Michal, B, (1990) Reaction-rate theory: fifty years after Kramers. Rev. Mod. Phys. 62: 251-342

(36) She H, Malotky D, Chaudhury MK (1998) Estimation of adhesion hysteresis using rolling contact mechanics. Langmuir 14: 3090-3100

(37) Lefranc, M.; Bouchaud, E. Mode I fracture of a biopolymer gel: Rate-dependent dissipation and large deformations disentangled, *Extreme Mechanics Letters*, **2014**, 1, 97-103

(38) Fakhouri, S., Hutchens, B., Crosby, A. J., Puncture mechanics of soft solids, Soft Matter, 2015, 11 4723-4730

(39) Tang, T., Jagota, A., Chaudhury, M., Hui, C.Y. Thermal Fluctuations Limit the Strength of Compliant Solids. *J. Adhesion* **2006**, 82, 671-696

(40) Holzapfel, G.A., *Nonlinear Solid Mechanics A Continuum Approach for Engineering*; John Wiley and Sons: West Sussex, 2000

(41) Wojtecki, R.J.; Meador, M.A.; Rowan, S.J. "Using the dynamic bond to access macroscopically responsive structurally dynamic polymers," Nature Materials, 10 (2011) 14-27

(42) Ogden, R.W., Roxburgh, D.G, "A pseudo-elastic model for the Mullins effect in filled rubber" *Proc. R. Soc. Lond. A,* 455 (1999) 2861-2877

(43) Volokh, K.Y. "Review of the Energy Limiters Approach to Modeling Failure of Rubber", Rubber Chemistry and Technology 86 (2013) 470-487

(44) Shaw, J.A., Jones, A.S., Wineman, A.S., Chemorheological response of elastomers at elevated temperatures: experiments and simulations. *J Mech Phys. Solids* **2005**, 53, 2758-2793

(45) Wineman, A., Min, J.H, Time Dependent scission and cross-linking in an elastomeric cylinder undergoing circular shear and hear conduction. *Int J. Nonlinear Mech*. **2003**, 38, 969-983

(46) Wineman, A., Shaw, J., Combined deformation- and temperature- induced scission in a rubber cylinder in torsion. *Int J. Nonlinear Mech*. **2007**, 42, 330-335

(47) Silberstein, M.N.; Cremar, L.D.; Beiermann, B.A.; Kramer, S.B., Martinez, T.J., White, S.R., Sottos, N.R. "Modeling mechanophore activation within a viscous rubbery network" *J. Mech. Phys. Solids.* 63 (2014) 141-153

(48) Wang, Q; Gossweiler, G. R.; Craig, S. L.; Zhao, X. "Mechanics of mechanochemically responsive elastomers", JMPS 82 (2015) 320-344

(49) Carrillo, J.M Y., MacKintosh, F.C., Dobrynin, A.V., Nonlinear Elasticity: From Single Chain to Networks and Gels. Macromolecules, 2013, 46 3679-3692

(50) Rubenstein, M., Colby, R.H. Polymer Physics. 2003, Oxford University Press

(51) McQuarrie, D.A., *Statistical Mechanics*; Harper and Row: New York, 1976

(52) Volokh, K.Y.; Vorp, D.A. A model of growth and rupture of abdominal aortic aneurysm, Journal of Biomechanics, 41 (2008), 1015-1021

(53) Volokh, K.Y. "On modeling failure of rubber-like materials", Mechanics Research Communications, 37 (2010) 684-689

(54) Mullins, L.; Tobin, N.R. "Theoretical Model for the Elastic Behavior of Filler-Reinforced Vulcanized Rubbers" *Rubber Chemistry and Technology,* 30 (1957) 555-571.

(55) Meng, F.; Pritchard, R.H.; Terentjev, E. M. “Stress Relaxation, Dynamics, and Plasticity of Transient Polymer Networks,” Macromolecules, 49 (2016) 2843-2852

(56) Creton, C.; Ciccotti, M. “Fracture and adhesion of soft materials: a review” *Rep. Prog. Phys.*, 79 (2016) 57pp

(57) Bhowmick, A. K. “Threshold fracture of elastomers. Journal of Macromolecular Science” *Reviews in macromolecular Chemistry and Physics*, C28 (1988) 339-370.

(58) Gong, J.P.; Katsuyama, Y.; Kurokawa, T.; Osada, Y. “Double-Network Hydrogels with Extremely High Mechanical Strength” *Adv. Mater.*, 15 (2003) 1155-1158

(59) Gong, J.P “Why are double-network hydrogels so tough?” *Soft Matter*., 6 (2010) 2583-2590

(60) Nakajima, T.; Kurokawa, T.; Furukawa, H.; YU, Q. M., Tanaka, Y; Osada, T; Gong, J.P “Super tough gels with a double network structure” *Chinese Journal of Polymer Science*., 27 (2009) 1-9

(61) Yang, C. Y.; Wang, M.X.; Haider, H.; Yang, J. H.; Sun, J.Y, Chen, Y. M.; Zhou, J.; Sou, Z. “Strengthening Alginate/Polyacrylamide Hydrogels using various multivalent cations” *ACS Appl. Mater. Interfaces*, 5 (2013) 10418-10422

(62) Li, J.; Illeperuma, W. R. K.; Sou, Z.; Vlassak, J.J. “Hybrid hydrogels with extremely high stiffness and toughness” *ACS Macro. Lett*., 3 (2014) 520-523

(63) Bacca, M.; Creton, C.; McMeeking, R.M. “A model for the Mullins effect in multinetwork elastomers”, *J. Appl. Mech.*, 84, (2017) 121009.

(64) Gurtin, M.E., *An Introduction to Continuum Mechanics*; Academic Press: New York, 1981

(65) Knowles, J.K, “The finite antiplane shear field near the tip of a crack for a class of incompressible elastic solids” *Int. J. Frac.*, 13 (1977) 611-639

(66) Ducrot, E.; Creton, C. “Characterizing Large Strain Elasticity of Brittle Elastomeric Networks by Embedding Them in a Soft Extensible Matrix” *Adv. Funct. Mater.*, 26 (2016) 2482-2492

(67) Millereau, P. “Large Strain and Fracture of Multiple Network Elastomers”, These de Doctorat De L’Universite Pierre et Marie Curie. 22 May 2017

(68) Holzapfel, G.A., “Nonlinear Solid Mechanics: A Continuum Approach for Engineering” (2000) John Wiley and Sons: West Sussex

(69) Nakajima, T.; Fukuda, Y.; Kurokawa, T.; Sakai, T.; Chung, U.-i.; Gong, J. P. “Synthesis and Fracture Process Analysis of Double Network Hydrogels with a Well-Defined First Network.” *ACS Macro Letters*, 2 (2013) 518-521

(70) Miehe, C.; Goktepe, S.; Lulei, F. “A micro-macro approach to rubber-like materials-Part I: the non-affine micro-sphere model of rubber elasticity” JMPS 63 (2014) 141-153

(71) Dobrynin, A.V., Carrillo, J.M Y., Rubenstein, M., Chains are more flexible under tension, Macromolecules, 2010, 43 9181-9190

(72) Zhang, T., Lin, S., Yuk, H.; Zhao, “X., Predicting fracture energies and crack-tip fields of soft tough materials” *Extreme Mech. Lett*., 4 (2015) 1-8

(73) Mao, Y.; Talamini, B.; Anand, L. “Rupture of polymers by chain scission”, *Extreme Mechanics Letters*, 13 (2017) 17-24.

(74) Lavoie, S.R.; PhD Thesis. University of Alberta January 2018, Chapte 6.

(75) Hong, et al., “A theory of coupled diffusion and large deformation in polymeric gels” *J. Mech. Phys. Solids*, 56 (2008) 1779-1793

(76) James, H. M.; Guth, E. “Statistical Mechanics of Rubber Elasticity” *J. Chem. Phys.*, 21 (1953) 1039-1049

(77) Treloar, L.R.G, “The Physics of Rubber Elasticity” 3rd edition (1975), Clarendon Press, Oxford

(78) Rubinstein, M.; Panyukov, S. "Elasticity of polymer networks." *Macromolecules*, 35 (2002) 6670-6886

(79) Clough, J. M., C. Creton, S. L. Craig and R. P. Sijbesma "Covalent Bond Scission in the Mullins Effect of a Filled Elastomer: Real-Time Visualization with Mechanoluminescence." *Advanced Functional Materials* 26 (2016) 9063-9074.

(80) Zhao, X. "A theory for large deformation and damage of interpenetrating polymer networks." *J. Mech. Phys. Solids* 60 (2012) 319-332.

(81) Dudko, O.L.; Hummer, G.; Szabe, A. "Intrinsic Rates and Activation energies from Single Molecule Pulling Experiments." *PRL* 96 (2006) 108101

(82) Schwaderer, P.; Funk, E.; Achenbach, F.; Wies, J.; Brauchle, C.; Michaelis, J. Single Molecule Measurement of the strength of a Siloxane Bond, Langmuir 24: 1343-1349 (2008)

(83) Mao, Y.; Talamini, T.; Anand, L. "Rupture of Polymers by Chain Scission" Extreme Mechanics Letters 13 (2017) 17-24

(84) Wang, J.; Kouznetsova, T.B.; Craig, S. "Reactivity and Mechanism of a Mechanically Activated anti-Woodward-Hoffmann-DePuy Reaction" *J. Am.Chem. Soc,* 137 (2015) 11554-11557

(85) Wang, J.; Kouznetsova, T.B.; Niu, Z.; Ong, M.T.; Klukovich, H.M.; Rheingold, A.L.; Martinez, T.J.; Craig, S. L. "Inducing and quantifying forbidden reactivity with single molecule polymer mechanochemistry" *Nature Chemistry,* 7 (2015) 323-327

(86) Brown, C.L.; Craig, S. L. "Molecular Engineering of mechanophore activity for stress-responsive polymeric materials" *Chem. Sci.,* 6 (2015) 2158-5165

(87) Wu, D.; Lenhardt, J.M.; Black, A.L.; Akhremitchev, B. B.; Craig, S. L. "Molecular stress relief through a force-induced irreversible extension in polymer contour length" *J. Am.Chem. Soc.,* 132 (2010) 15936-15938

(88) Wang, J.; Kouznetsova, T.B.; Boulatov, R.; Craig, S. L. "Mechanical gating of a mechanochemical reaction cascade" *Nature Communications,* 7 (2016) 13433

(89) Awang, M.; Mohammadpour, M.; Muhammad, I.D. "Finite Element Modeling of Nanotube Structures Linear and Non-linear Models" 2016, Springer, Chapter 2

(90) Stixrude, L.; Bukowinski, M.S.T. Simple Covalent Potential Models of Tetrahedral SiO2 Applications to a-quartz and Coesite at pressure, Phys Chem Minerals (1988) 16:199-206

(91) Mark, J.E. "Physical Properties of Polymers Handbook" 2nd Edition, Springer, 2007, Chapter 25

(92) Treloar, L.R.G. “Stress-Strain data for vulcanized rubber under various types of deformation” *Trans. Faraday Soc.,* 40 (1944) 59-70

(93) Aklonis, J.J; MacKnight, W.J. Introduction to Polymer Viscoelasticity Second Edition, 1983, John Wiley and Sons, New York

(94) Zehnder AT (2012) Fracture Mechanics. Springer: New York

Appendix 1. *Supporting Material for Chapter 2*

Appendix 1.1. Alternative treatment for van der Waals attraction

If δ_c is small and the van der Waals (vdW) attractions become negligible long before the end of the adhesive zone, then the vdW stress can be taken into account by a linear bending moment boundary condition. To show this, consider the limit as $\delta_c \to 0$ then the material on which vdW attractions act will be in an unrelaxed state. Therefore, the material infinitely close to the adhesive zone tip can be treated as elastic with modulus E_o and the "J-integral" [25, 27] can be applied along a closed path Γ enclosing the adhesive zone tip to obtain a moment boundary condition. For quasi-static crack propagation in a linear elastic solid, the J-integral has been shown to be independent of path Γ and equal to the work of adhesion which is the energy required to advance a unit area of crack [26]. If the path Γ is chosen to be infinitely close to the adhesive zone tip then there is no contribution from the chains and the work of adhesion will be from vdW attractions only (denoted by W_{vdW}). A J-integral formulation for adhesion of a Bernoulli Euler beam to a substrate has been presented by Glassmaker and Hui [26]. Several small adjustments can be made to this result to apply it to our case. First, we do not consider large beam deflections therefore $2d\psi/ds = d^2\delta/dx^2$ where ψ is the angle between the beam's deformed neutral axis and undeformed neutral axis and s is an arc length parameter. Second we consider the strain energy from two beams. Finally we consider beams of width D rather than of unit width. With these three modifications the following relationship can be obtained from the results of Glassmaker and Hui [26]

$$\frac{d^2\delta}{dx^2}(0) = 2\sqrt{\frac{W_{vdW}D}{E_o I}}\,. \qquad \text{(A1.1)}$$

Since the material is unrelaxed at the adhesive zone tip we can also write

$$M(0) = \frac{E_o I}{2}\frac{d^2\delta}{dx^2}(0) = \sqrt{W_{vdW}DE_o I}\,. \qquad \text{(A1.2)}$$

Finally, in normalized form (see normalization in the main text, Eq. (2.5)) the moment boundary condition is

$M^*(0)=\frac{d^2\delta^*}{dx^{*2}}(0)=\sqrt{2W^*_{vdW}}$.	(A1.3)

Note that if the vdW attractions are explicitly considered in the adhesive stress then there is no work needed in opening the adhesive zone tip. In this case it would follow from Eq. (A1.3) that the moment and curvature at the adhesive zone tip are both zero.

Appendix 1.2. Impact of Numerical criteria on *L** and *G**

Numerical criteria to define the crack tip can be introduced based on adhesive stress or bond density. When the adhesive stress is dominated by polymer chains, criteria based on bond density and adhesive stress are very similar ($f^* \approx \Sigma_b^* F^*$).However, when both vdW attractions and polymer chains contribute to f^*, the adhesive stress can have a local minimum (data not shown) and care must be taken to ensure that the chosen criteria will not predict an incorrect crack tip around this minimum. In addition, when the adhesive zone is dominated by vdW attractions the criteria based on bond density requires a second condition to ensure that the crack opening displacement (COD) $\delta^*(L^*)$ is sufficiently large for the work done by the vdW attractions to approach W^*_{vdW}.

In the main text, the criteria used to determine the effective adhesive zone length has been specified as: $\delta^*(L^*)>4.605\delta_c^*$ and ($\Sigma_b^*(L^*)<0.0000001$ or $d^2\Sigma_b^*/dx^{*2}(L^*)>0$). The first condition requires a sufficient COD so that the work done by vdW attractions is >99% of W_{vdW}. The second condition pertains to requiring the chain density to be negligible outside the adhesive zone. The condition $d^2\Sigma_b^*/dx^{*2}(L^*)>0$ serves as an escape because at high speed the step size given by the adaptive step size control [24] will approach 0 near L^* and the numerical program would not be able to terminate the calculation under such conditions.

To evaluate the impact of changing the criteria we compared elastic DCB results generated from the seven criteria shown in Table A1.1 Note that Criteria 7 was adopted in the main text. Results for L^* are shown in Figure A1.1a) for a range of V^*/γ_τ. It is clear from Figure A1.1a) that at low speed the adhesive zone length is highly dependent on the criteria used. For this reason we

have not presented results for L^* in the main text (instead a brief discussion is given in Appendix 1.4). Although the adhesive zone length changes considerably depending on the criteria used, the adhesive fracture energy, shown in Figure A1.1b), does not. The difference between the adhesive fracture energy calculated using different criteria is negligible. Therefore as long as the tolerance is sufficiently small to ensure there will be no more contribution to G_{ad}^* past L^* any criteria can be used. It should be noted that criteria based on bond density was shown to be computationally more effective than criteria based on adhesive stress.

Table A1.1: Different L criteria evaluated*

Criteria #	Criteria
1	$\delta^*\left(L^*\right) > 4.605\delta_c^*$ and $f^*\left(L^*\right) < 0.01$
2	$\delta^*\left(L^*\right) > 4.605\delta_c^*$ and $f^*\left(L^*\right) < 0.001$
3	$\delta^*\left(L^*\right) > 4.605\delta_c^*$ and $f^*\left(L^*\right) < 0.0005$
4	$\delta^*\left(L^*\right) > 4.605\delta_c^*$ and $\Sigma_b^*\left(L^*\right) < 0.0001$
5	$\delta^*\left(L^*\right) > 4.605\delta_c^*$ and $\Sigma_b^*\left(L^*\right) < 0.00001$
6	$\delta^*\left(L^*\right) > 4.605\delta_c^*$ and $\Sigma_b^*\left(L^*\right) < 0.000001$
7	$\delta^*\left(L^*\right) > 4.605\delta_c^*$ and ($\Sigma_b^*\left(L^*\right) < 0.0000001$ or $d^2\Sigma_b^* / dx^{*2}\left(L^*\right) > 0$)

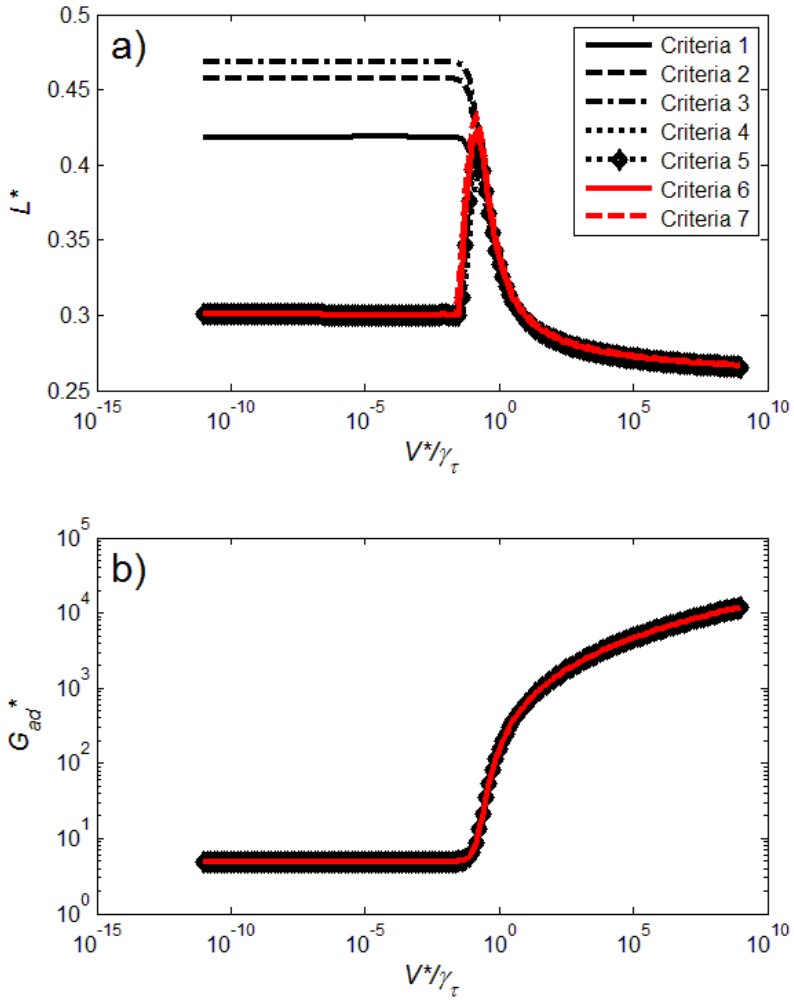

Figure A1.1: Plots for a) adhesive zone length, L^* and b) adhesive fracture energy G_{ad}^* obtained by varying V^*/γ_τ while holding the other governing parameters fixed at $U^* = 2850$, $\gamma_E = 1$, $\gamma_L = 0.0022222$, $\delta_c^* = 0.02$ and $W_{vdW}^* = 5$. Each curve in these figures represents a different criterion as indicated in the legend and Table A.

Appendix 1.3. Strain Energy Correction for Fracture Energy

Consider the work needed to be done by the applied moment M_∞ to advance a unit area of the crack. We have used a translating coordinate system to make the problem steady within the adhesive zone. However, M_∞ is applied outside of the adhesive zone (according to the definition of adhesive zone in the main text). A strain energy correction needs to be introduced in the evaluation of energy release rate, since the fracture energy was evaluated at a fixed point x_M in the translating coordinate system, and this point would translate with the adhesive zone tip as the crack propagates in a steady-state manner. This scenario can be thought of as if the moment M_∞ is applied at x_M and translates with the adhesive zone tip. During this process, the strain energy stored in the beam segment on the right of x_M would be released. Therefore, the work by the applied moment M_∞ at a fixed location x_M (in the translating coordinate system) to advance a unit area of crack consists of three parts

$$W = G_{ad} + G_{vis} + G_{se} \tag{A1.4}$$

where W is the work to advance a unit area of crack and G_{se} is the increase in strain energy per unit crack advancement due to the translation of x_M. We will formulate a correction to remove G_{se} from the fracture energy. The total work W can be evaluated from the work of the applied moment on the two beams in the DCB or

$$WD = M_\infty \delta''(x_M). \tag{A1.5}$$

We define an effective Young's modulus at position x_M outside of the adhesive zone so that

$$M_\infty = \frac{E(x_M) I \delta''(x_M)}{2}. \tag{A1.6}$$

For the viscoelastic model used $E(x_M)$ will be in the range $E_\infty < E(x_M) < E_o$. Consider the change in strain energy at x_M for an elastic DCB with modulus $E(x_M)$. The portion of strain energy that would be released from an elastic beam due to the translation of the applied load is given by

$$G_{se} = \frac{1}{D}\frac{dU_{se}}{dx}\bigg|_{x_M} = \frac{M_\infty^2}{DE(x_M)I} = \frac{W}{2}, \tag{A1.7}$$

where dU_{se} is the elastic strain energy of the two beam segments (one on each beam) each of length dx, and Eqs. (A1.5) and (A1.6) have been used. Even though the beam is viscoelastic, we have

calculated dU_{se} assuming that locally at x_M the beam is elastic with an effective modulus of $E(x_M)$. To isolate the energy release rate contributions from adhesion and viscous dissipation, we subtract G_{se} and define the energy release rate as follows

$$G = W - G_{se} = \frac{W}{2} = G_{ad} + G_{vis}. \quad \text{(A1.8)}$$

Here G can be directly evaluated from

$$G = \frac{M_\infty \delta''(x_M)}{2D}. \quad \text{(A1.9)}$$

As long as the moment is applied in a region where the beams are fully relaxed ($E = E_\infty$), the results can be made sufficiently close to the case where the moment were to be applied at infinity and

$$M_\infty = \frac{E_\infty I \delta''(\infty)}{2}. \quad \text{(A1.10)}$$

It then follows that

$$G(\infty) = \frac{M_\infty^2}{E_\infty ID}. \quad \text{(A1.11)}$$

Appendix 1.4. Results and Discussion on the Effective Adhesive Zone length

Here we present numerical results for the adhesive zone length L^* and discuss how it depends on the crack propagation speed and chain rupture kinetics for both elastic and viscoelastic beams. For all the results in this section, the criterion used to determine L^* is criteria 7 from Appendix 1.2.

First, consider the simplest case of an elastic beam where there is no bulk dissipation. In Figure A1.2a) the adhesive zone length L^* is plotted against V^*/γ_τ. At slow rates of crack propagation the adhesive zone length remains fixed. Once a critical speed is reached the adhesive zone length sharply increases. However, with further increases in speed the adhesive zone length reaches a maximum and begins to decrease. Ultimately the adhesive zone length asymptotically approaches a constant value (0.26 in this case, details discussed in Appendix 1.7) as V^* tends to infinity.

To understand the L^* behavior in Figure A1.2a) it is important to recognize that the adhesive zone could be controlled by either the vdW attractions or by the polymer chains. Typically at small V^*/γ_τ the vdW attractions control L^* whereas at higher speed the polymer chains control L^*. The transition to polymer-chain dominated regime occurs when there is sufficient remaining polymer chains as the COD reaches the critical vdW opening. The critical vdW opening is a constant dependent on δ_c^* and it must be reached before the remaining work that can be done by vdW attractions (on the interface beyond the critical vdW opening) becomes negligible.

Kinetic polymer chain scission causes two competing effects which impact the adhesive zone length. Firstly increasing V^*/γ_τ results in less time for chains to break as the crack propagates and hence the chains can survive longer along the adhesive zone, which tends to increase the adhesive zone length. Secondly, the accompanied survival of chains to larger openings results in larger adhesive stress. It will be discussed later that larger integral of the adhesive stress $S^*(0)=\int_{L^*}^{0} f^* dx^*$ causes the crack opening to increase more rapidly with respect to position, which tends to decrease the adhesive zone length. The first effect can be seen in Figure A1.2b) where COD is plotted against V^*/γ_τ. For the second effect consider that the shear force at the adhesive zone tip,

$S^*(0) = \int_{L^*}^{0} f^* dx^*$, provides a representation of the integral contribution of the adhesive stress in the adhesive zone. $S^*(0)$ is plotted against V^*/γ_τ in Figure A1.2c). $S^*(0)$ is dominated by vdW attractions for slow crack propagation, and decreases (increases in magnitude) due to the prolonged survival of polymer chains at larger V^*/γ_τ. The shear force distribution within the adhesive zone is a negative, monotonic increasing function; therefore as $S^*(0)$ increases its magnitude with V^*/γ_τ, the shear force over the entire adhesive zone becomes larger in magnitude as well. From Eq. (8) in the main text the increased shear force magnitude at larger V^*/γ_τ will cause δ^* to increase more rapidly with x^*. Accelerated increase of δ^* with respect to x^* will tend to decrease the adhesive zone length by either causing the vdW critical opening to be reached sooner and by increasing the extension of polymer chains which accelerates their rupture.

The competition between survival of polymer chains to larger openings and accelerated increase in δ^* result in the non-monotonic L^* behavior observed in Figure A1.2a). The former effect dominates at lower V^*/γ_τ and increases L^*, while the latter effect dominates at higher V^*/γ_τ and causes L^* to decrease. As crack propagation speed tends to infinity the two effects come into balance and the adhesive zone length approaches a constant value (0.26 in the present case).

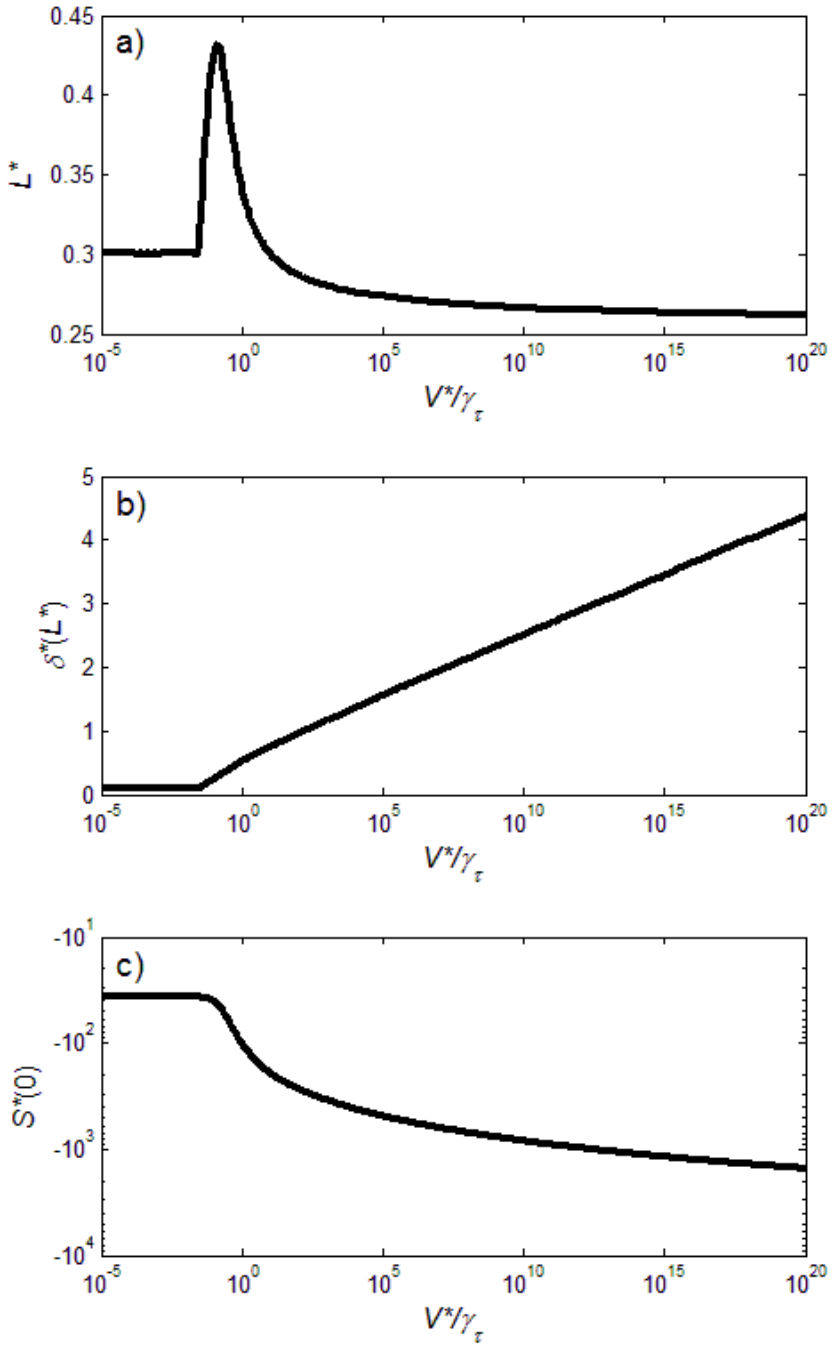

Figure A1.2: Plots for the a) adhesive zone length L* *b) COD* δ*(L*) *c) reaction shear* S*(0) *obtained by varying* V^*/γ_τ *while holding the other governing parameters fixed at* $U^* = 2850$, $\gamma_E = 1$, $\gamma_L = 0.0022222$, $\delta_c^* = 0.02$ *and* $W_{vdW}^* = 5$.

The adhesive zone length, COD and reaction shear force are shown for a viscoelastic DCB (γ_E = 0.01) in Figure A1.3. The main difference here is that the x-axes are now V^* rather than V^*/γ_τ, and each curve represents a different value of γ_τ. As discussed in the main text the behavior of the kinetic chain rupture equation (Eq. (2.6) in the main text) is determined by V^*/γ_τ. Therefore when results primarily determined by this equation, such as COD, are plotted on V^* axis the results for different values of γ_τ will be shifted horizontally; i.e. γ_τ acts as a speed shift. The adhesive zone length results shown in Figure A1.3a) are very similar to those shown in Figure A1.2a) for an elastic DCB but with the speed shift discussed above, as the local maxima all occur at roughly the same V^*/γ_τ. In addition to the behavior described for the elastic beam there is also a superimposed increase in L^* from about $V^* = 10^{-4}$ to 1, and the local maxima can occur before or after this increase. This increase in L^* is caused by effective stiffening of the DCB as the material will be less relaxed at higher rates of crack propagation. Since the unrelaxed material has a higher flexural rigidity, it resists opening and results in a larger L^* as seen in Figure A1.3a). This is the same reason why if we compare the five curves in Figure A1.3a), when the local maximum in L^* occurs at a higher V^*, the peak value is larger. The elastic case shown in Figure A1.2 was solved using the unrelaxed modulus so in the high speed limit the results in Figure A1.2a) and Figure A1.3a) both converge to the same limit (0.26). The COD results, shown in Figure A1.3b), also display the same behavior as what was seen in Figure A1.2a), only shifted horizontally for each γ_τ. Finally the reaction shear force, shown in Figure A1.3c), is also similar to Figure A1.2c), but overall the magnitude of the reaction shear force in Figure A1.2c) is lower for small V^*/γ_τ due to the relaxed material.

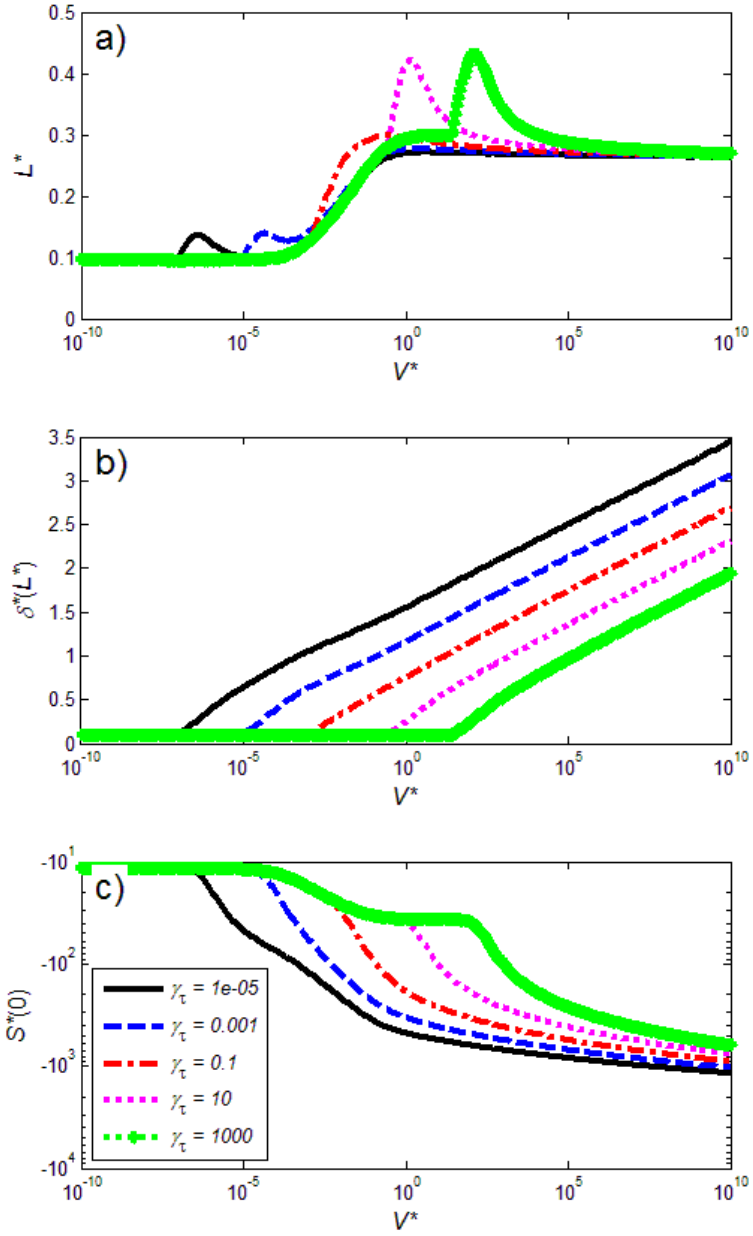

Figure A1.3: Plots for the a) adhesive zone length L^* *b) COD* $\delta^*(L^*)$ *and c) reaction shear* $S^*(0)$ *obtained by varying* V^* *while holding the other governing parameters fixed at* $U^* = 2850$, $\gamma_E = 0.01$, $\gamma_L = 0.0022222$, $\delta_c^* = 0.02$ *and* $W_{vdW}^* = 5$. *Each curve in these figures represents a different* γ_τ *as indicated in the legend.*

Appendix 1.5. Dependence of Fracture Energy on x_M^*

In Eq. (A1.5) we defined the location where the moment M_∞^* is applied, x_M^*. A different choice of x_M^* represents a different beam length. In this section results for G^* and G_{vis}^* are presented for x_M^* = 0.5, 1, 2, 100 and infinity, respectively in Figure A1.5, Figure A1.6, Figure A1.7, Figure A1.8 and Figure A1.9. Since x_M^* is outside of the adhesive zone, G_{ad}^*, presented in Figure A1.4, is insensitive to x_M^*. As G^* is the sum of G_{vis}^* and G_{ad}^*, only the G_{vis}^* results will be discussed; however results for G^* are provided for reference. In the main text G_{vis}^* was described to be negligible in both the low and high speed limits and have a peak value between these two limits. From Figure A1.5, Figure A1.6, Figure A1.7, Figure A1.8 and Figure A1.9, it can be seen that as x_M^* is increased the peak dissipation occurs at larger V^*. For x_M^* at infinity there is no noticeable peak in Figure A1.9b) since it would occur at infinite V^*. In the main text, it has been explained that as crack propagation speed is increased, there is less time for the bulk material to relax; this leads to an increase in the effective modulus at each point within the beam, which is what causes the non-monotonic dependence of G_{vis}^* on V^* for a finite sized beams. Similarly, the peak in G_{vis}^* shifts to higher V^* for longer beams because for larger x_M^* faster crack propagation is needed to see the same level of increase in the effective modulus throughout the beam. Comparing Figure A1.5, Figure A1.6, Figure A1.7 and Figure A1.8 also shows that at a given V^* where G_{vis}^* is not negligible, G_{vis}^* will increase as x_M^* is increased due to the extra dissipation from the additional length of beam.

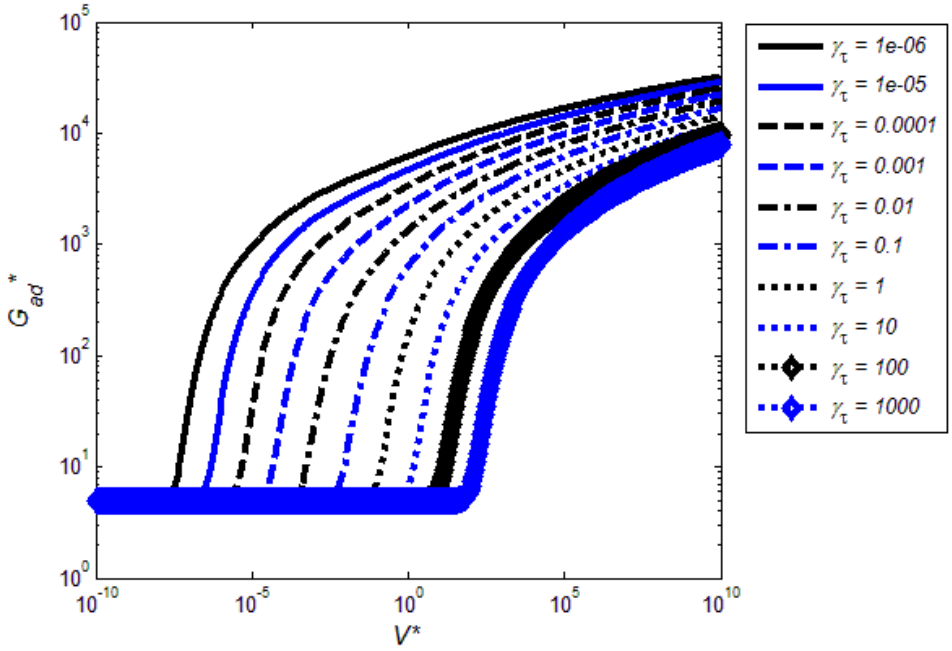

Figure A1.4: Plots for the adhesive fracture energy G_{ad}^* obtained by varying V^* while holding the other governing parameters fixed at $U^* = 2850$, $\gamma_E = 0.01$, $\gamma_L = 0.0022222$, $\delta_c^* = 0.02$ and $W_{vdW}^* = 5$. Each curve in these figures represents a different γ_τ as indicated in the legend.

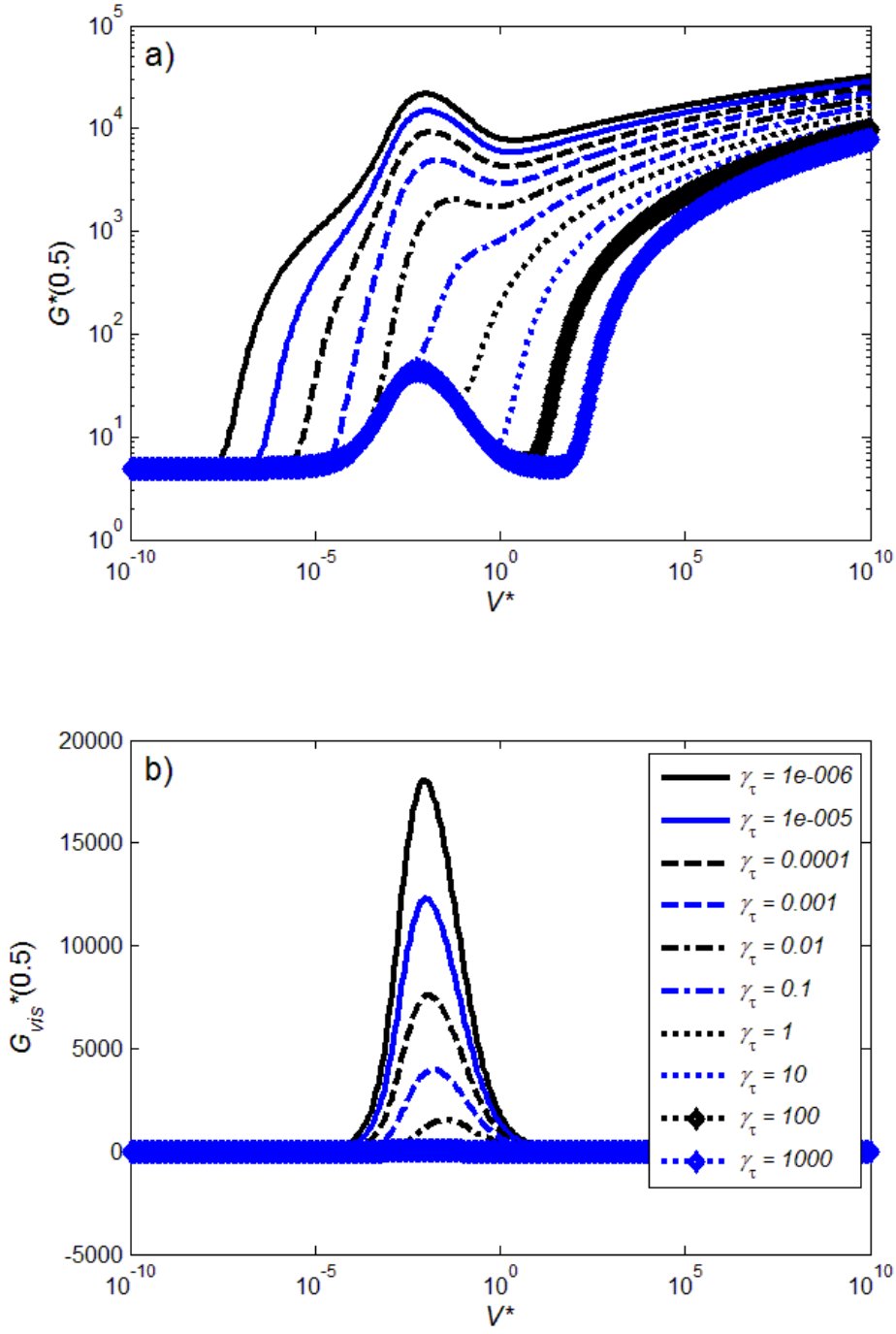

Figure A1.5: Plots for a) fracture energy $G^*(0.5)$ and b) viscous dissipation $G_{vis}^*(0.5)$ obtained by varying V^* while holding the other governing parameters fixed at $U^* = 2850$, $\gamma_E = 0.01$, $\gamma_L = 0.0022222$, $\delta_c^* = 0.02$ and $W_{vdW}^* = 5$. Each curve in these figures represents a different γ_τ as indicated in the legend.

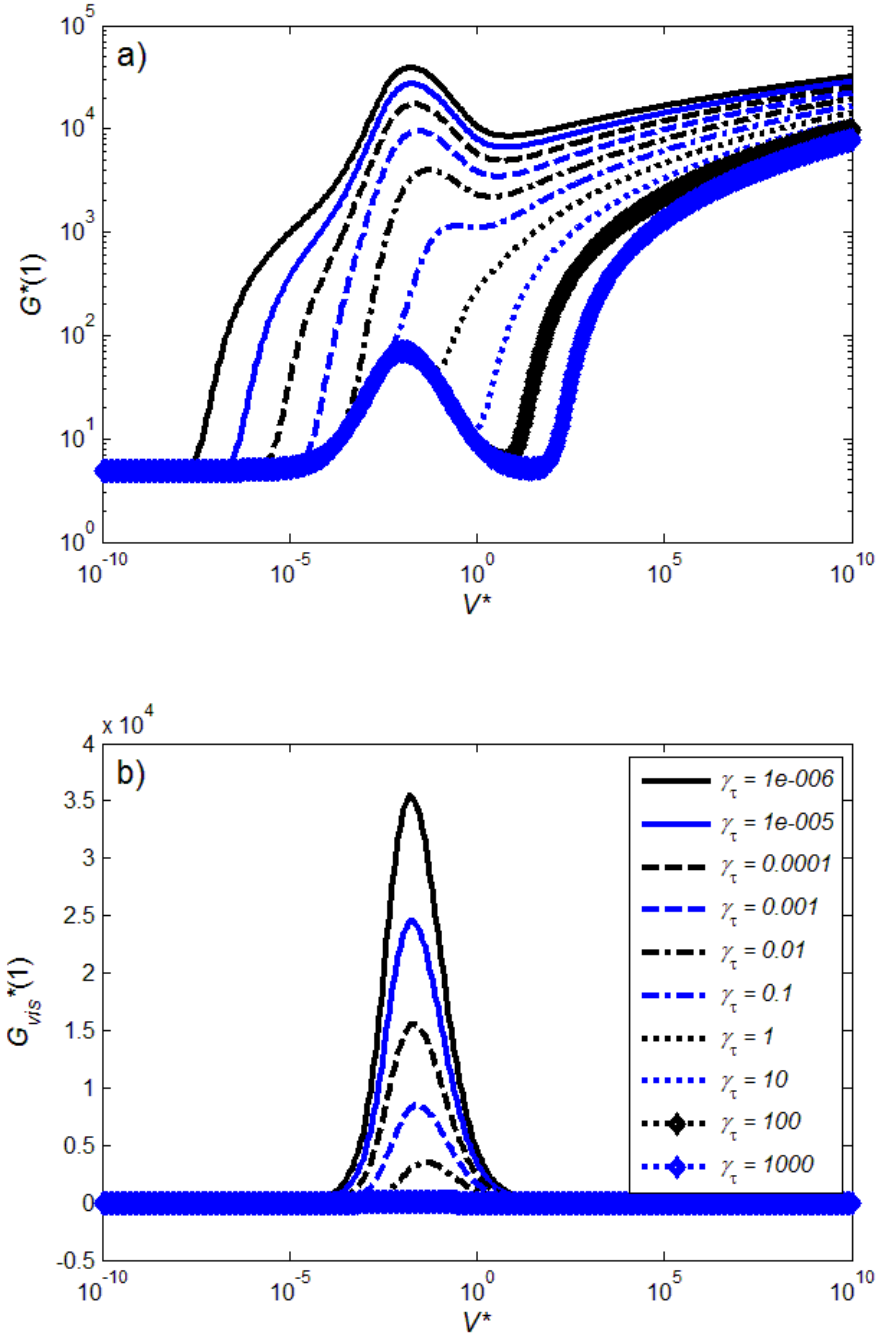

Figure A1.6: Plots for a) fracture energy $G^*(1)$ and b) viscous dissipation $G_{vis}^*(1)$ obtained by varying V^* while holding the other governing parameters fixed at $U^* = 2850$, $\gamma_E = 0.01$, $\gamma_L = 0.0022222$, $\delta_c^* = 0.02$ and $W_{vdW}^* = 5$. Each curve in these figures represents a different γ_τ as indicated in the legend.

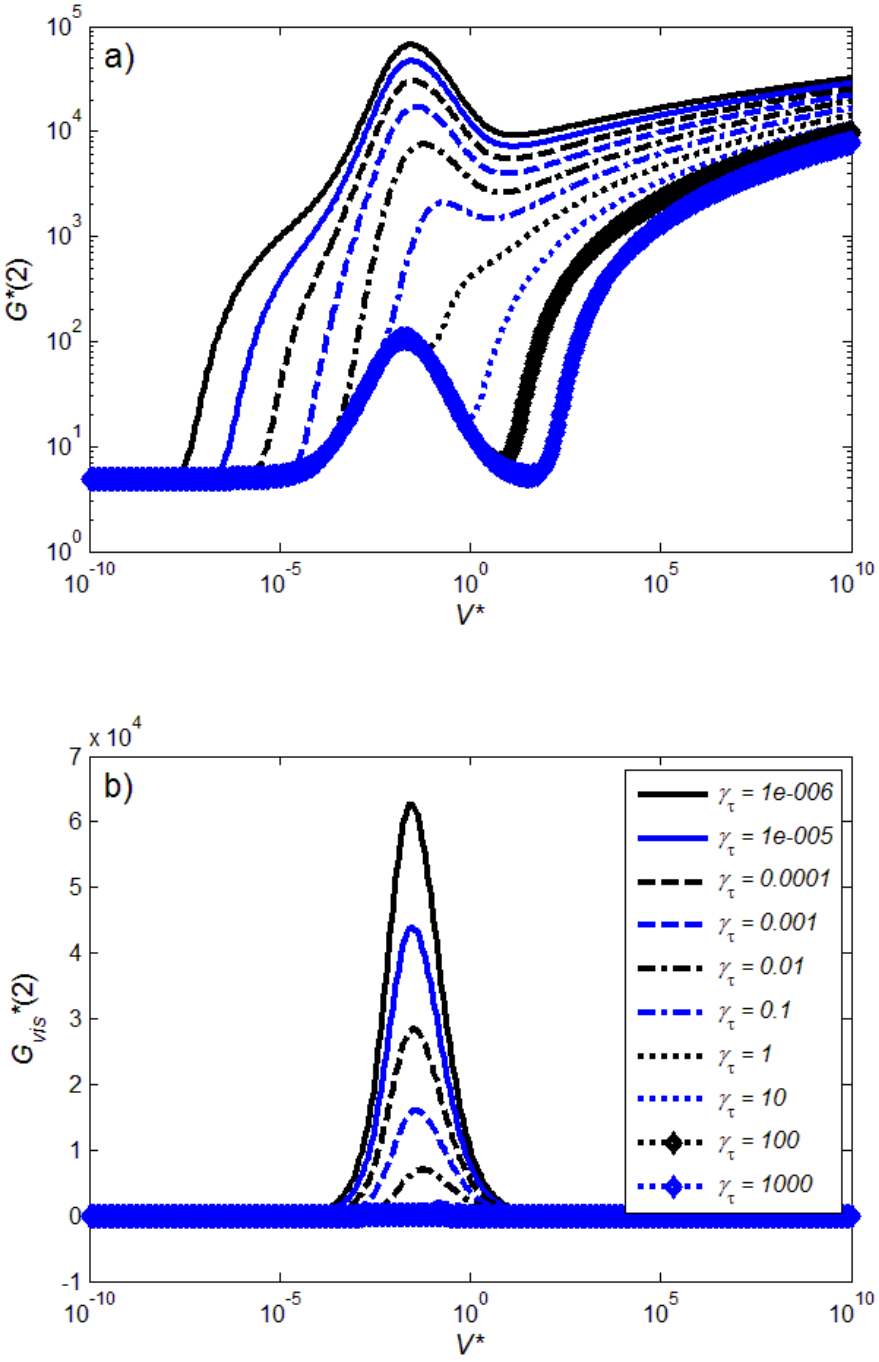

Figure A1.7: Plots for a) fracture energy $G^*(2)$ and b) viscous dissipation $G_{vis}^*(2)$ obtained by varying V^* while holding the other governing parameters fixed at $U^* = 2850$, $\gamma_E = 0.01$, $\gamma_L = 0.0022222$, $\delta_c^* = 0.02$ and $W_{vdW}^* = 5$. Each curve in these figures represents a different γ_τ as indicated in the legend.

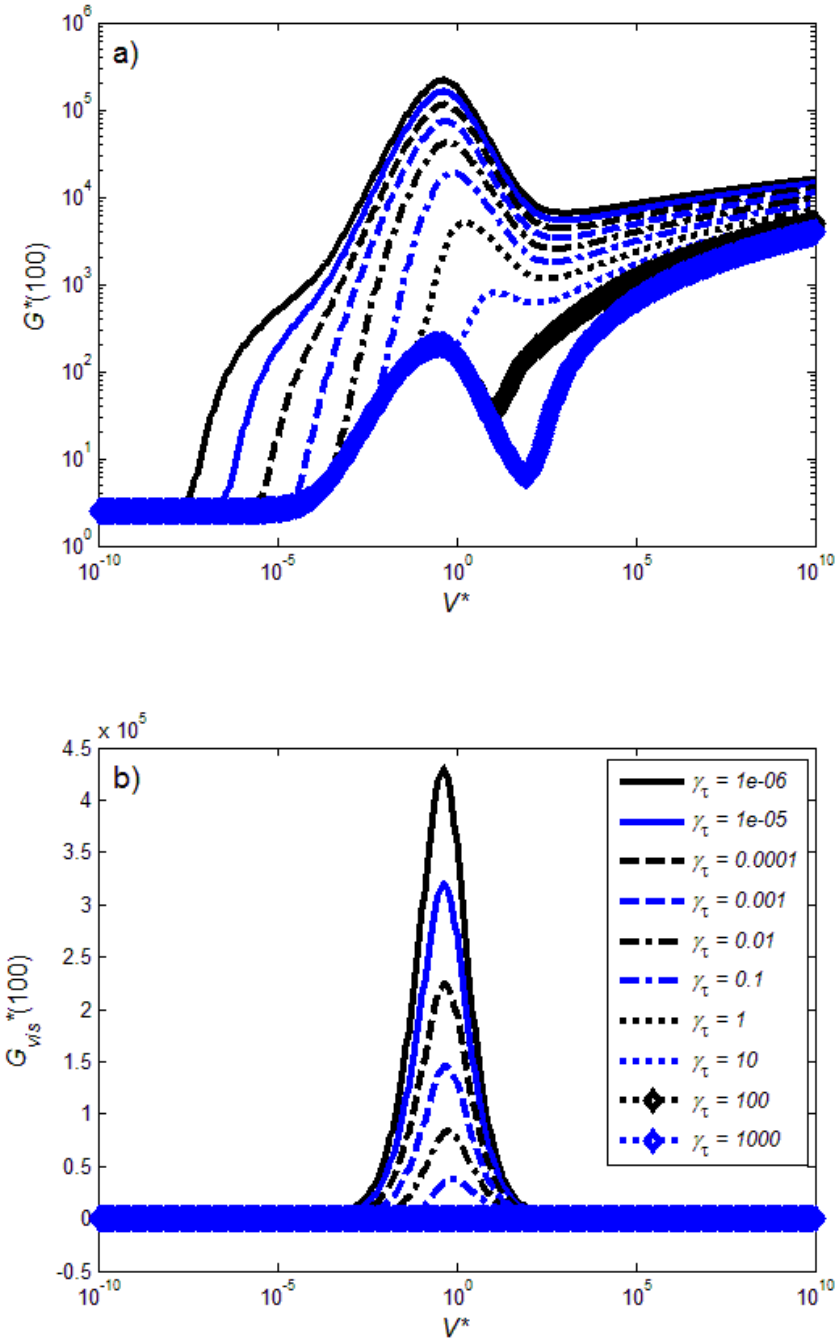

Figure A1.8: Plots for a) fracture energy $G^*(100)$ and b) viscous dissipation $G_{vis}^*(100)$ obtained by varying V^* while holding the other governing parameters fixed at $U^* = 2850$, $\gamma_E = 0.01$, $\gamma_L = 0.0022222$, $\delta_c^* = 0.02$ and $W_{vdW}^* = 5$. Each curve in these figures represents a different γ_τ as indicated in the legend.

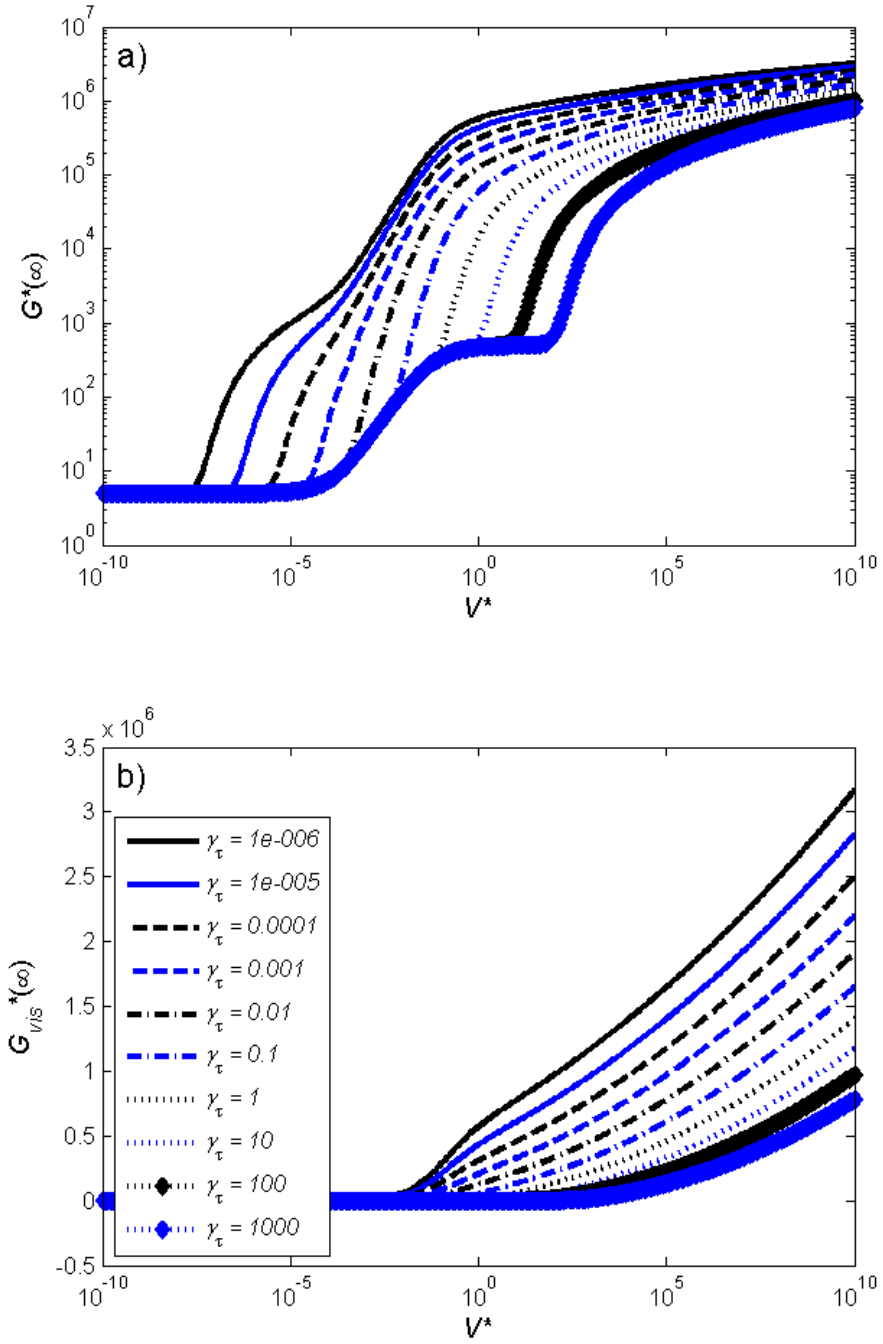

Figure A1.9: Plots for a) fracture energy $G^*(\infty)$ and b) viscous dissipation $G_{vis}^*(\infty)$ obtained by varying V^* while holding the other governing parameters fixed at $U^* = 2850$, $\gamma_E = 0.01$, $\gamma_L = 0.0022222$, $\delta_c^* = 0.02$ and $W_{vdW}^* = 5$. Each curve in these figures represents a different γ_τ as indicated in the legend.

Appendix 1.6. Effect of vdW Decay Length

In light of the vdW critical opening criteria from Appendix 1.2, the use of smaller values of δ_c^* can reduce the size of the adhesive zone. In addition the "$\delta_c^* = 0$" treatment (Appendix 1.1) replaces the nonlinear vdW attraction with non-zero but linear moment boundary condition; therefore this approach can simplify the calculation if it can predict acceptable fracture energies when compared with the explicit vdW adhesive stress model. Below we discuss the effect of this vdW decay length.

Results for a viscoelastic beam with $\gamma_E = 0.01$ and $\gamma_\tau = 0.001$ are shown in Figure. A1.10. In Figure. A1.10a) the COD $\delta^*(L^*)$ is plotted against crack propagation speed V^*. Since at low speed the COD is controlled by the critical vdW opening, we see different low speed plateau values of the COD for $\delta_c^* = 0.02$ and 0.2. The curve corresponding to $\delta_c^* = 0$, when a moment boundary condition was used (see Appendix 1.1), behaves differently at low speed. For $\delta_c^* = 0$ all vdW attractions are taken into account in the boundary condition so the adhesive zone will always be controlled by chains, which means that there will be no low speed plateau. At high speed all of the results collapse onto a single curve, indicating that fracture is governed by the chains and is insensitive to the vdW decay length. The fracture energy is plotted against crack propagation speed in Figure. A1.10b) and similarly the results collapse at high speeds. This observation agrees with a well-known result that the solutions of fracture problems are insensitive to the form of the interaction potentials provided that the maximum stress and the work of adhesion are chosen to be approximately the same for these potentials [1]. At high speed the maximum stress is determined by the chains and any of the vdW treatments will give the same work of adhesion. Finally the effective modulus, plotted against V^* in Figure. A1.10c), appears to be independent of δ_c^*.

However at low speed the value of G^* associated with $\delta_c^* = 0$ is several orders of magnitude larger than the other two and is not equal to the vdW adhesion energy. The reason for this discrepancy is that the moment boundary condition presented in section S1 is based on the condition that the length over which vdW attractions are important must be negligible compared to the adhesive zone length. At low speed the adhesive zone length is very small so this condition is not satisfied. The much higher G^* value for $\delta_c^* = 0$ at low speed is caused by an increase in

viscous dissipation and we will briefly explain it. In this case for slow crack propagation, the adhesive stress (only contributed by the chains) is negligible and therefore $f^* = S^* = 0$ and the moment is constant given by Eq. (A1.3) everywhere. At the adhesive zone tip the curvature is given by Eq. (A1.3), however immediately after the adhesive zone tip the material instantly relaxes and since the moment is constant the curvature increases to $d^2\delta^* / dx^{*2} = \sqrt{2W^*_{vdW}} / \gamma_E$. The work needed to create this large increase in curvature brings the low speed G^* value to (using Eq. (A1.9))

$$G^*\left(V^* \to 0, \delta_c^* \to 0\right) = \frac{W^*_{vdW}}{\gamma_E}. \qquad \text{(A1.12)}$$

We have used $W^*_{vdW} = 5$ and $\gamma_E = 0.01$ for which Eq.(A1.12) predicts $G^* = 500$, in agreement with the $V^* \to 0$ limit for $\delta_c^* = 0$ in Figure. A1.10b). However, it should be emphasized that since the $\delta_c^* = 0$ treatment violates its own assumption, this result is invalid and does not explain any physical phenomenon. Rather it is an interpretation of the numerical behavior observed in Figure. A1.10b).

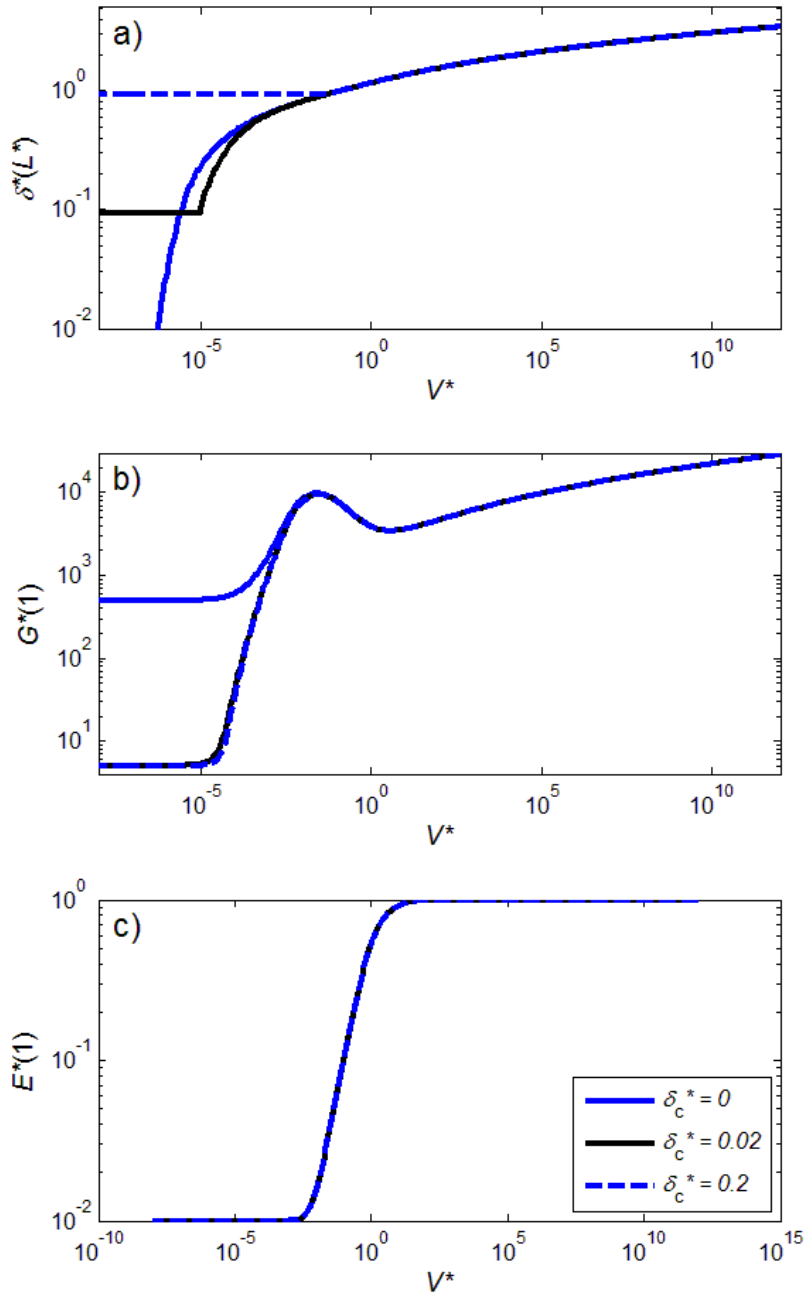

Figure. A1.10: Plots for (a) COD $\delta^*(L^*)$, (b) fracture energy $G^*(1)$ and (c) effective Young's Modulus $E^*(1)$ obtained by varying V^* while holding the other governing parameters fixed at $U^* = 2850$, $\gamma_E = 0.01$, $\gamma_L = 0.0022222$, $\gamma_\tau = 0.001$ and $W_{vdW}^* = 5$. Each curve in these figures represents a different δ_c^* as indicated in the legend.

Appendix 1.7. Analytical Solution for fast crack propagation speed

For fast crack propagation speeds we point out two observations. First within the adhesive zone the beam was completely unrelaxed or $E^* = 1$ and can be treated as elastic. Second the bond density distribution approached a reverse step (as shown in Figure 2.3a) of the main text) i.e.

$$\Sigma_b^*\left(x^*\right)=\begin{cases}1, & x^* < L^*,\\ 0, & x^* \geq L^*.\end{cases} \tag{A1.13}$$

Based on these two observations the governing equation inside the adhesive zone becomes linear:

$$\frac{d^4\delta^*}{dx^{*4}} = -f^* = -2U^*\delta^*. \tag{A1.14}$$

The corresponding boundary conditions are

$$\delta^*(0)=0,\ \frac{d\delta^*}{dx^*}(0)=0,\ M^*(0)=\frac{d^2\delta^*}{dx^{*2}}(0)=\sqrt{2W_{vdW}^*}\ , \tag{A1.15}$$

$$M^*\left(L^*\right)=\frac{d^2\delta^*}{dx^{*2}}\left(L^*\right)=M_\infty^*, \tag{A1.16}$$

$$S^*(L^*)=-\frac{d^3\delta^*}{dx^{*3}}(L^*)=0, \tag{A1.17}$$

where the vdW attractions have been represented using the moment boundary condition as presented in section S1. The general solution to Eq. (2.11) is

$$\delta^*\left(x^*\right)=\cosh\left(\alpha x^*\right)\left(c_1\cos\left(\alpha x^*\right)+c_2\sin\left(\alpha x^*\right)\right)+\sinh\left(\alpha x^*\right)\left(c_3\cos\left(\alpha x^*\right)+c_4\sin\left(\alpha x^*\right)\right), \tag{S1.18}$$

where $\alpha=\sqrt[4]{U^*/2}$. Applying boundary conditions (A1.15)-(A1.16) gives $c_1=0$, $c_2=-c_3$, $c_4=\sqrt{W_{ad}^*/U^*}=\beta^2$, and $\alpha^2\left[c_2\left(\sinh\left(\alpha L^*\right)\cos\left(\alpha L^*\right)+\cosh\left(\alpha L^*\right)\sin\left(\alpha L^*\right)\right)+\beta^2\cosh\left(\alpha x^*\right)\cos\left(\alpha x^*\right)\right]=M_\infty^*$. Therefore, the crack opening is given by

$$\delta^*\left(x^*\right)=c_2\left(\cosh\left(\alpha x^*\right)\sin\left(\alpha x^*\right)-\sinh\left(\alpha x^*\right)\cos\left(\alpha x^*\right)\right)+\beta^2\sinh\left(\alpha x^*\right)\sin\left(\alpha x^*\right), \tag{A1.19}$$

where c_2 can be determined from

$$c_2 = \frac{M_\infty^* - \alpha^2\beta^2 \cosh(\alpha x^*)\cos(\alpha x^*)}{\alpha^2\left(\sinh(\alpha L^*)\cos(\alpha L^*) + \cosh(\alpha L^*)\sin(\alpha L^*)\right)}. \quad \text{(A1.20)}$$

Applying the final boundary condition, Eq. (A1.17), gives the following eigenvalue equation

$$2c_2 \cosh(\alpha L^*)\cos(\alpha L^*) + \beta^2\left(\sinh(\alpha x^*)\cos(\alpha x^*) - \cosh(\alpha x^*)\sin(\alpha x^*)\right) = 0, \quad \text{(A1.21)}$$

which can be used to solve for L^*. In most cases we will have $U^* >> W_{ad}^*$, since it takes less energy to overcome vdW attractions than to break covalent bonds, so that $\beta << 1$ and Eq. (A1.21) can be simplified to give

$$2c_2 \cosh(\alpha L^*)\cos(\alpha L^*) \approx 0. \quad \text{(A1.22)}$$

Since only a trivial solution will result if $c_2 = 0$ and hyperbolic cosine is always positive this condition can only be satisfied if $\cos(\alpha L^*) = 0$. Furthermore, the shape of the crack should not be oscillatory, therefore only the first eigenvalue ($\alpha L^* = \pi/2$) is physical. From this eigenvalue the adhesive zone length can be determined as

$$L_{RS}^* = \frac{\pi}{\sqrt[4]{8U^*}}, \quad \text{(A1.23)}$$

where the subscript RS indicates that this is the adhesive zone length associated with a reverse-step bond density distribution. This result can be compared with the adhesive zone length results shown in Figure Aa), Figure A1.2a), and Figure A1.3a) where it has been seen that at high speed, L^* asymptotes to about 0.26; for U^* =2850, $L_{RS}^* = 0.2557$ which is in good agreement.

Finally, based on the above results, the adhesive fracture energy at very high crack speed can be directly evaluated as follows

$$\left(G_{ad}^*\right)_{RS} = \int_0^\infty f^* d\delta^* \approx \int_0^{\delta^*(L^*)} 2U^*\delta^* d\delta^* + W_{vdW}^* = U^*\delta^*\left(L^*\right)^2 + W_{vdW}^*. \quad \text{(A1.24)}$$

Based on the discussion from Appendix 1.2, in general L^* and therefore $\delta^*(L^*)$ can depend on the criteria used in the definition of L^*. In principle this behavior may impact our ability to use Eq. (2.19) to validate our model, as was done in the main paper (Figure. 2.2b)). Fortunately at high

speed L^* is insensitive to the numerical criteria (see Figure A1.1a). In fact when G_{ad}^* vs. $\delta^*\left(L^*\right)$ is plotted on a log-log scale, as was done in the main text, we see our results become linear with the slope of 2 and approach Eq. (2.19) at high $\delta^*\left(L^*\right)$, which also corresponds to high speed.

Appendix 1.8. Adhesive Stress for Viscoelastic DCB

In the main text we utilized the COD, bond density and adhesive stress distributions to aid the discussion of elastic beams. In this section we present distributions for a viscoelastic beam with $\gamma_E = 0.01$, $\gamma_\tau = 1$, and several different crack propagation speeds. The normalized bond density is plotted against position in Figure. A1.11a). Like the elastic case, for small V^*/γ_τ the bond density experiences gradual decrease from the adhesive zone tip; while for large V^*/γ_τ it first remains at one and drops off drastically near the end of the adhesive zone. The distribution of adhesive stress is shown in Figure. A1.11b). At the adhesive zone tip the normalized adhesive stress has a value of 250 which corresponds to the maximum vdW stress (W^*_{vdW}/δ^*_c). Moving away from the adhesive zone tip, the vdW stress decays while the tension in the polymer chains starts taking effect. For $V^*/\gamma_\tau = 0.01$ the adhesive stress from polymer chains is negligible but in all other cases this adhesive stress persists longer than the vdW attractions and results in a larger adhesive zone. In addition, large values of V^*/γ_τ lead to peaks in f^*, which result from the increase in adhesive stress due to chain extension coupled with the rapid scission of chains shown in Figure. A1.11a). In general higher values of V^*/γ_τ result in higher peaks in f^* and a steeper decline in f^* after the peak.

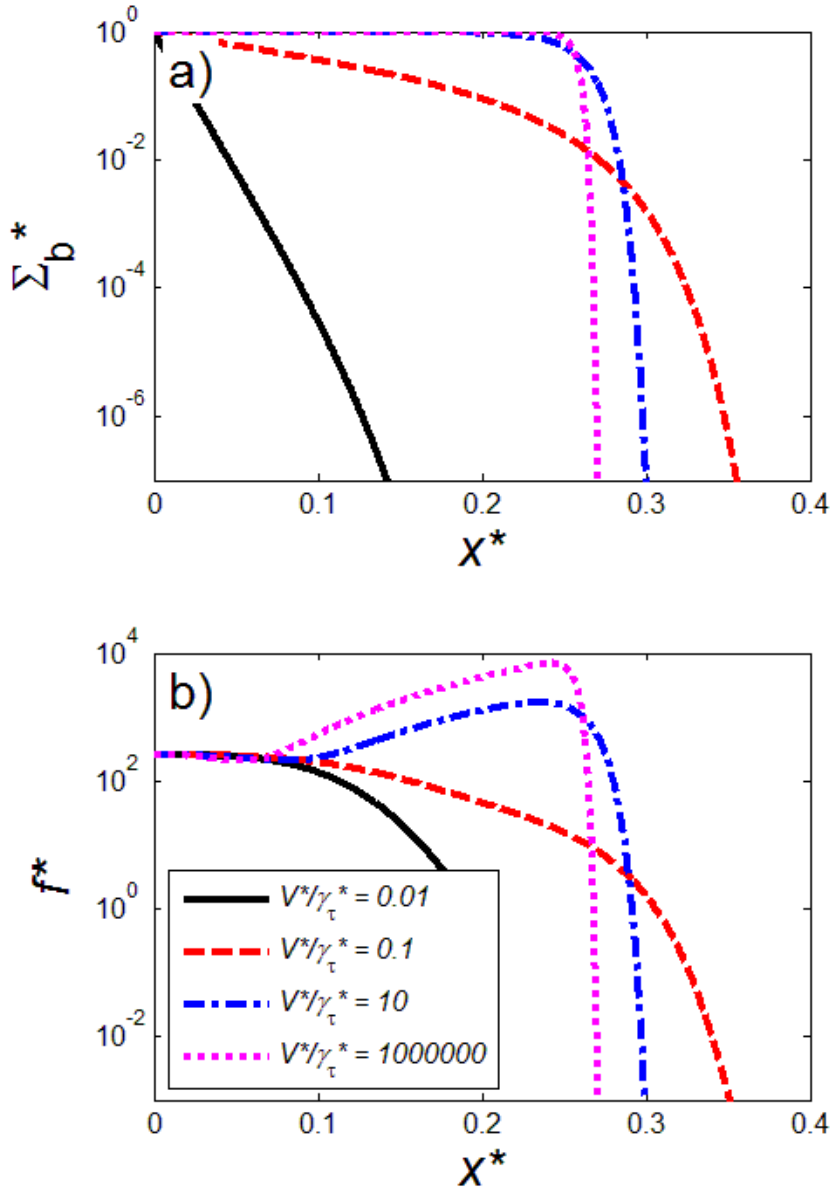

Figure. A1.11: Plots for a) bond density, Σ_b^*, and b) adhesive stress f within the adhesive zone. In each figure each curve represents a different value of V^*/γ_τ. Results were obtained while holding the following governing parameters fixed at $U^* = 2850$, $\gamma_E = 0.01$, $\gamma_L = 0.0022222$, $\gamma_\tau = 1$, $W_{vdW}^* = 5$ and $\delta_c = 0.02$.*

Appendix 1.9. Length of Dissipative Zone

In Appendix 1.5 the fracture energies G^* and $G_{vis}{}^*$ were evaluated at different positions $x_M{}^*$ outside the adhesive zone and were shown to be sensitive to the choice of $x_M{}^*$. This is because at $x_M{}^*$ the beam may not have fully relaxed. In light of this observation it is of interest to define a dissipative zone length L_∞^* so that beyond L_∞^* the viscous dissipation becomes negligible. In the main text a solution was presented for the curvature outside of the adhesive zone (Eq. (2.16) in main text). Dividing M_∞^* by this expression gives the effective modulus as a function of position, which after simplifying and rearranging gives the position in terms of the effective modulus

$$x^* = L^* + \frac{V^*}{\gamma_E}\ln\left(\frac{1-\gamma_E/E^*\left(L^*\right)}{1-\gamma_E/E^*\left(x^*\right)}\right), \tag{A1.25}$$

where $E^*(\infty)=\gamma_E$ and $E^*\left(L^*\right)$ is obtained from the solution within the adhesive zone. The length of the dissipation zone L_∞^* is defined so that

$$E^*\left(L_\infty^*\right)=\frac{\gamma_E}{(1-\varepsilon_L)}, \tag{A1.26}$$

where ε_L is a tolerance which was chosen to be 0.001 in the following calculations. Eq. (A1.26) requires that the effective modulus has relaxed to the infinite-time modulus within some tolerance. By substituting Eq. (A1.26) into Eq. (A1.25) we obtain

$$L_\infty^* = L^* + \frac{V^*}{\gamma_E}\left(\ln\left(1-\gamma_E/E^*\left(L^*\right)\right)-\ln\left(\varepsilon_L\right)\right). \tag{A1.27}$$

Results for the ratio L_∞^*/L^* are shown in Figure. A1.12. This ratio stays at 1 for slow crack propagation speed which implies that the DCB has relaxed to within the tolerance of Eq. (A1.26) at the crack tip. At higher speeds the DCB will not become fully relaxed until some distance past the crack tip. This distance increases as crack propagation speed is increased. At high speeds the dissipative zone can be several orders of magnitude larger than the adhesive zone length. Note that these results are sensitive to the tolerance chosen. If a smaller tolerance ε_L is used then the magnitude of L_∞^* with increase however the qualitative behavior will remain the same.

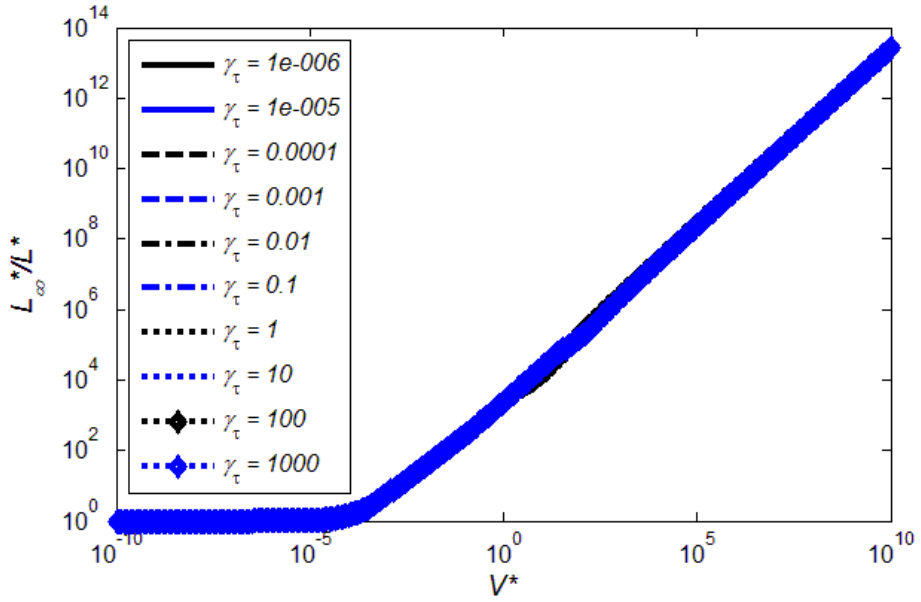

Figure. A1.12: Plots for the ratio of dissipative zone length to adhesive zone length L_∞^* / L^* *obtained by varying* V^* *while holding the other governing parameters fixed at* $U^* = 2850$, $\gamma_E = 0.01$, $\gamma_L = 0.0022222$, $\delta_c^* = 0.02$ *and* $W_{vdW}^* = 5$. *Each curve in these figures represents a different* γ_τ *as indicated in the legend.*

Appendix 1.10. Model Validation Using Constant Adhesive Stress

Another model has been previously presented in the literature [15] which studied constant speed crack propagation in a viscoelastic DCB but did not consider chain rupture kinetics. Instead this model assumed constant stress within the adhesive zone, which can be easily implemented into our model. In addition, an analytical solution can be found for the energy release rate in this case. Therefore, examining this case can be a useful check to make sure that our numerical code is running correctly. To do so we must first adjust the model in [15] to use our normalization and to have crack propagation driven by an applied moment rather than an applied force. For a constant adhesive stress σ_c the beam governing equations can be rewritten as follows

$\frac{dS^*}{dx^*} = \sigma_c ,$	(A1.28)
$\frac{dM^*}{dx^*} = -S^* ,$	(A1.29)
$M^* - V^* S^* = \gamma_E \frac{d^2\delta^*}{dx^{*2}} + V^* \frac{d^3\delta^*}{dx^{*3}} .$	(A1.30)

These equations are accompanied by boundary conditions at the adhesive zone tip:

$\delta^*(0) = 0 , \ \frac{d\delta^*}{dx^*}(0) = 0 , \ \frac{d^2\delta^*}{dx^{*2}}(0) = 0 , \ M^*(0) = 0 .$	(A1.31)

In addition, the crack tip, and hence length of the adhesive zone is defined using a critical COD,

$\delta^*(L^*) = \delta_c^* .$	(A1.32)

When crack propagation is driven by a moment applied outside of the adhesive zone the shear force at the crack tip must be zero, i.e.,

$S^*(L^*) = 0 .$	(A1.33)

Integrating Eqs. (A1.28) and (A1.29) yields

$S^* = S_o^* + \sigma_c x^* .$	(A1.34)

$$M^* = M_o^* - S_o^* x^* - \frac{\sigma_c}{2} x^{*2}. \qquad \text{(A1.35)}$$

Applying the last boundary condition in Eq. (A1.31) and Eq. (A1.33) leads to $M_o^* = 0$ and $S_o^* = -\sigma_c L^*$. Introducing Eqs. (A1.34) and (A1.35) into Eq. (A1.30) gives

$$-\left[S_o^* + \left(\frac{S_o^*}{V^*} + \sigma_c \right) x^* + \frac{\sigma_c}{2V^*} x^{*2} \right] = \frac{d^2}{dx^{*2}} \left(\frac{\gamma_E}{V^*} \delta^* + \frac{d\delta^*}{dx^*} \right). \qquad \text{(A1.36)}$$

Integrating Eq. (A1.36) twice gives

$$-\left[\frac{\sigma_c}{24V^*} x^{*4} + \left(\frac{S_o^*}{V^*} + \sigma_c \right) \frac{x^{*3}}{6} + S_o^* \frac{x^{*2}}{2} \right] + c_1 x^* + c_2 = \frac{\gamma_E}{V^*} \delta^* + \frac{d\delta^*}{dx^*}. \qquad \text{(A1.37)}$$

The first three boundary conditions in Eq. (A1.31) can be used to show that $c_1 = c_2 = 0$. Therefore solving the first order linear ordinary differential equation (Eq. (A1.37)) gives, after simplification and application of first boundary condition in Eq. (A1.31)

$$\delta^* = -\frac{\sigma_c}{\gamma_E} \frac{x^{*4}}{24} - \frac{V^*}{\gamma_E} \left(\frac{S_o^*}{V^*} + \sigma_c \left(1 - \frac{1}{\gamma_E} \right) \right) \frac{x^{*3}}{6}$$
$$- \frac{V^*}{\gamma_E} \left(S_o^* - \frac{V^*}{\gamma_E} \left[\frac{S_o^*}{V^*} + \sigma_c \left(1 - \frac{1}{\gamma_E} \right) \right] \right) \left(\frac{x^{*2}}{2} - \frac{V^*}{\gamma_E} x^* + \left(\frac{V^*}{\gamma_E} \right)^2 \left(1 - e^{-\frac{\gamma_E}{V^*} x^*} \right) \right). \qquad \text{(A1.38)}$$

Introducing Eq. (A1.32) and $S_o^* = -\sigma_c L^*$ into Eq. (A1.38) gives after simplification

$$\frac{\delta_c^*}{\sigma_c} = \frac{L^{*4}}{8\gamma_E} + \left(1 - \frac{1}{\gamma_E} \right) \left(\frac{V^*}{\gamma_E} \frac{L^{*3}}{3} - \left(\frac{V^*}{\gamma_E} \right)^2 \frac{L^{*2}}{2} - \left(\frac{V^*}{\gamma_E} \right)^3 L^* e^{-\frac{\gamma_E}{V^*} L^*} + \left(\frac{V^*}{\gamma_E} \right)^4 \left(1 - e^{-\frac{\gamma_E}{V^*} L^*} \right) \right). \qquad \text{(A1.39)}$$

This equation can be solved iteratively to obtain L^*. Afterwards, $G^*(1)$ can be evaluated using Eq. (2.15) in the main text, with $M_\infty^* = \sigma_c L^{*2}/2$ obtained from Eq. (A1.35) and the curvature is obtained by differentiating Eq. (A1.38).

We implemented the same model in our code by making $W_{vdW}^* = \sigma_c \delta_c^*$. As before, $W_{vdW}^* = 5$ and $\delta_c^* = 0.02$ so $\sigma_c = 250$. Thus the adhesive stress is constant $f^* = \sigma_c$ and since we specify V^* the applied moment is determined from the analysis. Finally $\gamma_E = 0.1$ was chosen and the result

from our code was compared against L^* solved from Eq. (A1.39) and $G^*(1)$ calculated based on it. The results for the adhesive zone length L^*, shown in Figure. A1.13a), and for $G^*(1)$, shown in Figure. A1.13b), are found to be in good agreement.

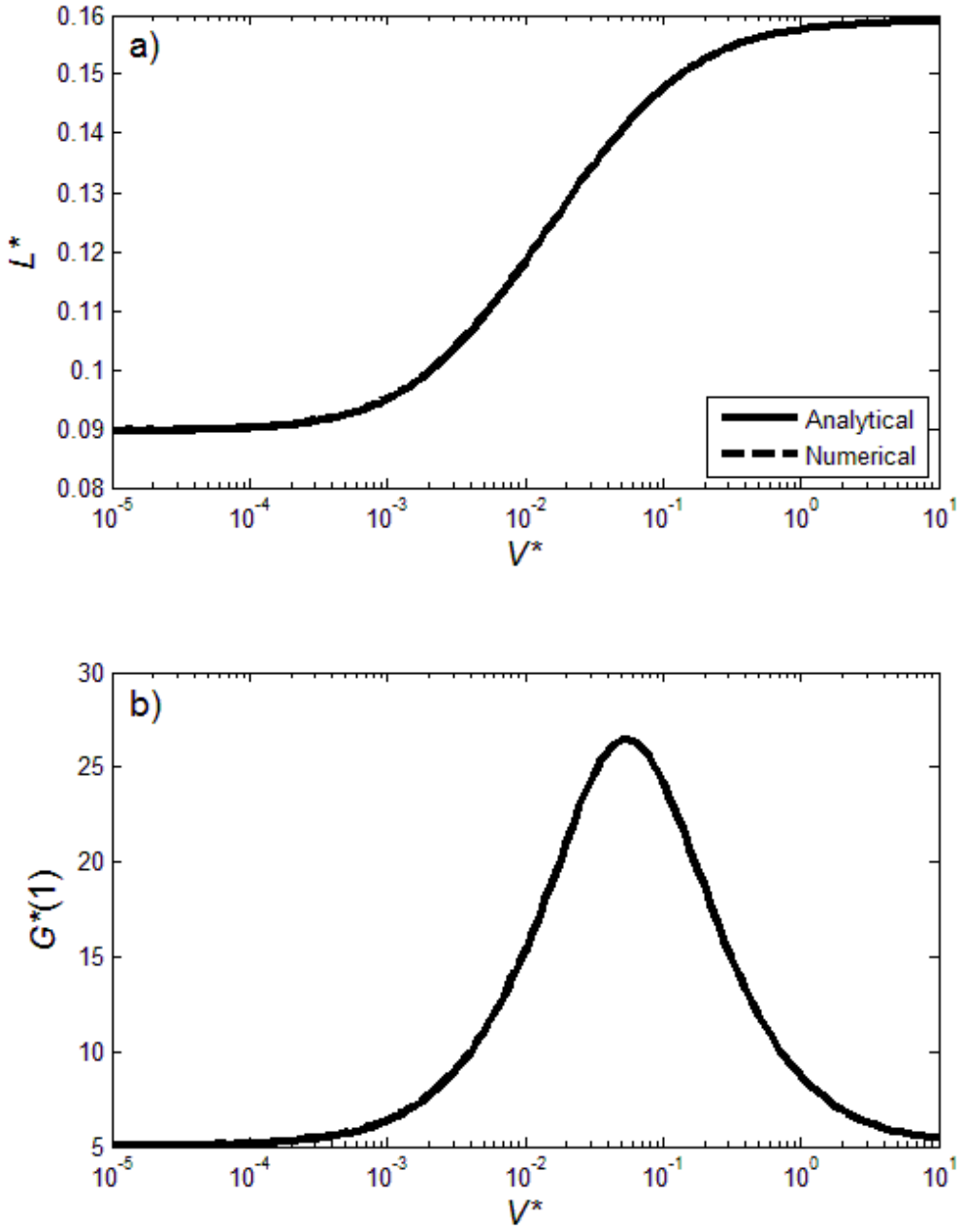

Figure. A1.13: a) Plots for a) adhesive zone length L^* *and b) fracture energy* $G^*(1)$ *obtained by varying* V^* *while holding the other governing parameters fixed at* $\gamma_E = 0.1$, $\delta_c^* = 0.02$ *and* $W_{vdW}^* = 5$. *The solid curve represents the result calculated using Eq. (A1.39) and the dashed line is calculated using our numerical code.*

Appendix 2. Supporting Material for Chapter 3

The equations governing the coupled response of the kinetic bond rupture equation, nonlinear chain model and a viscoelastic beam model are presented here. More details for the formulation can be found in references [6, 15].

Appendix 2.1. Non-dimensionalization

In dimensional form the governing equations have 18 parameters, which are needed to specify the geometry and properties of the beam, chains, and rate of fracture: V, n, τ_-, τ_+, λ, k_B, T, Σ_o, τ_o, E_o, E_∞, I, L_c, P, U, W_{vdW}, δ_c, and D. All these parameters are defined in the main text. To simplify the analysis we introduce the following nondimensionalization

$$\Sigma_b^* = \frac{\Sigma_b}{\Sigma_o},\ x^* = x\left(\frac{2k_BT\Sigma_oD}{E_oIL_c^2}\right)^{1/4},\ \delta^* = \frac{\delta}{L_c},\ F^* = \frac{FL_c}{k_BT},\ E_c^* = \frac{E_c}{k_BT},\ f^* = \frac{fL_c}{k_BT\Sigma_oD},$$

$$S^* = \frac{SL_c}{k_BT\Sigma_oD}\left(\frac{2k_BT\Sigma_oD}{E_oIL_c^2}\right)^{1/4},\quad M^* = M\left(\frac{2}{k_BT\Sigma_oDE_oI}\right)^{1/2},\quad V^* = \tau_oV\left(\frac{2k_BT\Sigma_oD}{E_oIL_c^2}\right)^{1/4},$$

$$U^* = \frac{U}{k_BT},\ \gamma_E = \frac{E_\infty}{E_o},\ \gamma_\tau = n\frac{\tau_o}{\tau_-},\ \gamma_L = \frac{\lambda}{L_c},\ n = \frac{L_c}{2P},\ K_{eq} = \frac{1}{n}\frac{\tau_-}{\tau_+} = \frac{\Sigma_{b0}^*}{1-\Sigma_{b0}^*},\ \delta_c^* = \frac{\delta_c}{L_c},$$

$$W_{vdW}^* = \frac{W_{vdW}}{k_BT\Sigma_o},\ G^* = \frac{G}{k_BT\Sigma_o},\ G_{ad}^* = \frac{G_{ad}}{k_BT\Sigma_o},\ G_{vis}^* = \frac{G_{vis}}{k_BT\Sigma_o}. \tag{A2.1}$$

The meanings of these variables are described in **Table A2.1**. The normalization reduces the number of governing parameters from 18 to 9 as given in Eq. (3.11) of the main text.

After normalization the chain kinetic equation, Eq. (3.4) in the main text, becomes

$$\frac{d\Sigma_b^*}{dx^*} = -\frac{\gamma_\tau}{V^*}\left(\Sigma_b^* e^{F^*\gamma_L} - \frac{\Sigma_{b0}^*}{1-\Sigma_{b0}^*}\left(1-\Sigma_b^*\right)e^{-E_c^*}\right), \tag{A2.2}$$

where the association rate constant has been written in terms of the initial fraction of bonded chains. Similarly, the polymer chain force-extension relationship, Eq. (3.6) in the main text, can be non-dimensionalized to

$$F^* = \begin{cases} 2n\left[\frac{1}{4}\left(1-\delta^*\right)^{-2} - \frac{1}{4} + \delta^*\right] & \delta^* \le 0.9 \\ 3000\left(U^* - 15n\right)\left(\delta^* - 0.9\right)^2 + 1002n\left(\delta^* - 0.9\right) + 51.3n & \delta^* > 0.9 \end{cases} \quad \text{(A2.3)}$$

Eq. (A2.3) is shown graphically in Figure 3.1 of the main text. This relationship can be integrated to give the energy required to bring two polymer chain segments into contact for bond reforming

$$E_c^* = \begin{cases} \frac{n}{2}\left(\delta^*\right)^2\left[\frac{3-2\delta^*}{1-\delta^*}\right] & \delta^* \le 0.9 \\ 2n\left\{2.43 + \left(\delta^* - 0.9\right)\left[500\left(\frac{U^*}{n} - 15\right)\left(\delta^* - 0.9\right)^2 + 250.5\left(\delta^* - 0.9\right) + 25.65\right]\right\} & \delta^* > 0.9 \end{cases} \quad \text{(A2.4)}$$

.

For the viscoelastic DCB, we will use the standard linear solid model as proposed in [15]. In this model the effective Young's modulus decays from an unrelaxed (short time) value, E_o, to a relaxed (infinite time) value E_∞ according to relaxation time τ_o. This model can be applied to relate the shear force (S), the moment (M) and the opening displacement (δ) in the viscoelastic DCB problem [6, 15], with the following result in the normalized form

$$M^* - V^* S^* = \gamma_E \frac{d^2\delta^*}{dx^{*2}} + V^* \frac{d^3\delta^*}{dx^{*3}}. \quad \text{(A2.5)}$$

The shear force and moment are related by the equilibrium condition

$$\frac{dM^*}{dx^*} = -S^*, \quad \text{(A2.6)}$$

and another equation can be written to relate the shear force to the distributed transverse load f [23],

$$\frac{dS^*}{dx^*} = f^* = \Sigma_b^* F^* + \frac{W_{vdW}^*}{\delta_c^*} e^{-\delta^*/\delta_c^*}. \quad \text{(A2.7)}$$

The right side of Eq. (A2.7) represents the transverse load acting on each beam in the adhesive zone, which has two components: $\Sigma_b^* F^*$ is the product of the density of chains and the tensile force in each chain i.e. the adhesive stress due to the chains, and $W_{vdW}^* e^{-\delta^*/\delta_c^*}/\delta_c^*$ is an approximation for the vdW attractions between the two beams.

Table A2.1. Description of Non-dimensional Parameters

Category	Parameter	Description of Normalized Parameter	Representative Values for Simulations[6]
Variables which change along beam	Σ_b^*	bond density	
	x^*	position	
	δ^*	opening, fractional extension	
	F^*	chain force	
	E_c^*	energy required to bring two polymer chain segments into contact for bond reforming	
	f^*	transverse load	
	S^*	shear force	
	M^*	bending moment	
Governing Parameters	V^*	crack propagation speed	10^{-10} to 10^{10}
	U^*	work needed to stretch a polymer chain to its contour length	2850
	γ_E	ratio of relaxed to unrelaxed Young's modulus	0.01,1 (elastic)
	γ_τ	ratio of relaxation times of bulk and bond dissociation	10^{-5} to 10^{3}
	γ_L	ratio of activation length to contour length	0.02222
	Σ_{b0}^*	Initial bond density	0.6-0.9
	δ_c^*	normalized vdW decay length	0.02
	W_{vdW}^*	vdW work of adhesion	5
Fracture Energies (Output)	G^*	fracture energy	
	G_{ad}^*	adhesive fracture energy	
	G_{vis}^*	viscous fracture energy	

Appendix 2.2. Boundary Conditions

In Section 2.1 we introduced an expression to calculate the initial bond density Σ_{b0}^* from the rate constants for the association and dissociation reactions. In the calculations, we will specify values for Σ_{b0}^*, which not only serves as a boundary condition, $\Sigma_b^*(0) = \Sigma_{b0}^*$, but also specifies the rate constant for the association reaction (in terms of the rate constant for dissociation) though $n\tau_+ / \tau_- = \left(1 - \Sigma_{b0}^*\right) / \Sigma_{b0}^*$.

All material ahead of the adhesive zone tip ($x < 0$) is undeformed and therefore, at the adhesive zone tip the slope and deflection of both beams will be zero i.e., $\delta^*(0) = d\delta^* / dx^*(0) = 0$. Furthermore for a steady state crack where the adhesive zone tip keeps moving, the modulus at the adhesive zone tip is equal to the instantaneous value, and the *J*-integral [94] from elasticity can be applied. For crack propagation in an elastic solid the *J*-integral is equal to the energy release rate, which is zero at the adhesive zone tip since all the adhesive attractions occur on the right of the adhesive zone tip. For a beam having zero *J*-integral at the adhesive zone tip implies that the curvature and moment must be zero [26, 28] or $M^*(0) = d^2\delta^* / dx^{*2}(0) = 0$.

As we move away from the adhesive zone tip in the direction of positive *x*, eventually the transverse load *f* must begin to decrease because: (1) the vdW attractions diminish with increased separation between the two beams and (2) the force from the polymer chains will also eventually decrease as more chains dissociate. We will define the crack tip as the position, $x^* = L^*$, where the transverse adhesive load, f^*, reduces below a sufficiently small tolerance or $f^*(L^*) \le \varepsilon_f^*$. Then since the externally applied load consists only of a moment, M_∞^*, it must be true that the shear force at the crack tip is zero, i.e. $S^*(L^*) = 0$. In our numerical analysis we will specify V^*, and evaluate the external applied load, M_∞^*, from $M_\infty^* = M^*\left(L^*\right)$.

Appendix 2.3. Numerical Methods

Eqs. (A2.2)-(A2.7) are solved using 4th order Runge-Kutta with adaptive step size control and a shooting method where $S^*(0)$ is guessed and a solution within the adhesive zone is calculated. If at the crack tip the shear force is not zero then a new guess for $S^*(0)$ is made until the crack tip criteria, $S^*(L^*) = 0$, is satisfied within a tolerance. The numerical solution is only obtained within the adhesive zone, outside which there is no load applied and analytical results for the beam

deformation can be easily obtained. It is important to note that the viscous dissipation will often be present over a much larger region than the adhesive zone. It follows that if we were to evaluate energies over a long beam, the behavior would be dominated by viscous dissipation and it may be difficult to distinguish the interesting features of the adhesive fracture energy. Since the primary objective of this paper is to implement an improved adhesive zone model we will evaluate fracture energies at $x^* = 1$, which is outside of the adhesive zone for all cases considered but on the same order of magnitude as the adhesive zone length.

For very small V^*/γ_τ, numerical solution of Eq. (A2.2) becomes extremely difficult due to round-off errors. However, in this case if we multiply both sides of the equation by V^*/γ_τ and consider the limit as $V^*/\gamma_\tau \to 0$ we obtain a simplified expression

$$\Sigma_b^*\left(1-\Sigma_{b0}^*\right)e^{F^*\gamma_L} - \Sigma_{b0}^*\left(1-\Sigma_b^*\right)e^{-E_c^*} = 0, \qquad \text{(A2.8)}$$

which can be used to determine the density of polymer chains Σ_b^*. The physical interpretation of this equation is that the crack propagates so slowly that bond association and dissociation can exist in dynamic equilibrium. This nonlinear algebraic equation must still be solved numerically to find the bond density as a function of the separation.

In the calculations presented in this work, Σ_b^* was solved from Eq. (A2.2) for $V^*/\gamma_\tau \geq 0.001$, and from Eq. (A2.8) for $V^*/\gamma_\tau < 0.001$. The COD and adhesive fracture energy obtained using this "hybrid" approach are shown in Figure: A2.1, along with results obtained by solving Eq. (A2.2) alone (curves labeled with "Rate Equation"), and those obtained from Eq. (A2.8) alone (curves labeled with "Equilibrium"). The equilibrium solution represents a horizontal line. The hybrid solution is identical to the Rate Equation solution above roughly $V^*/\gamma_\tau = 0.001$, below which it transitions to the Equilibrium solution. Below this point numerical solution of the Rate Equation becomes difficult and time consuming; however as can be seen in Figure: A2.1 the equilibrium equation produces acceptable results for these low speeds.

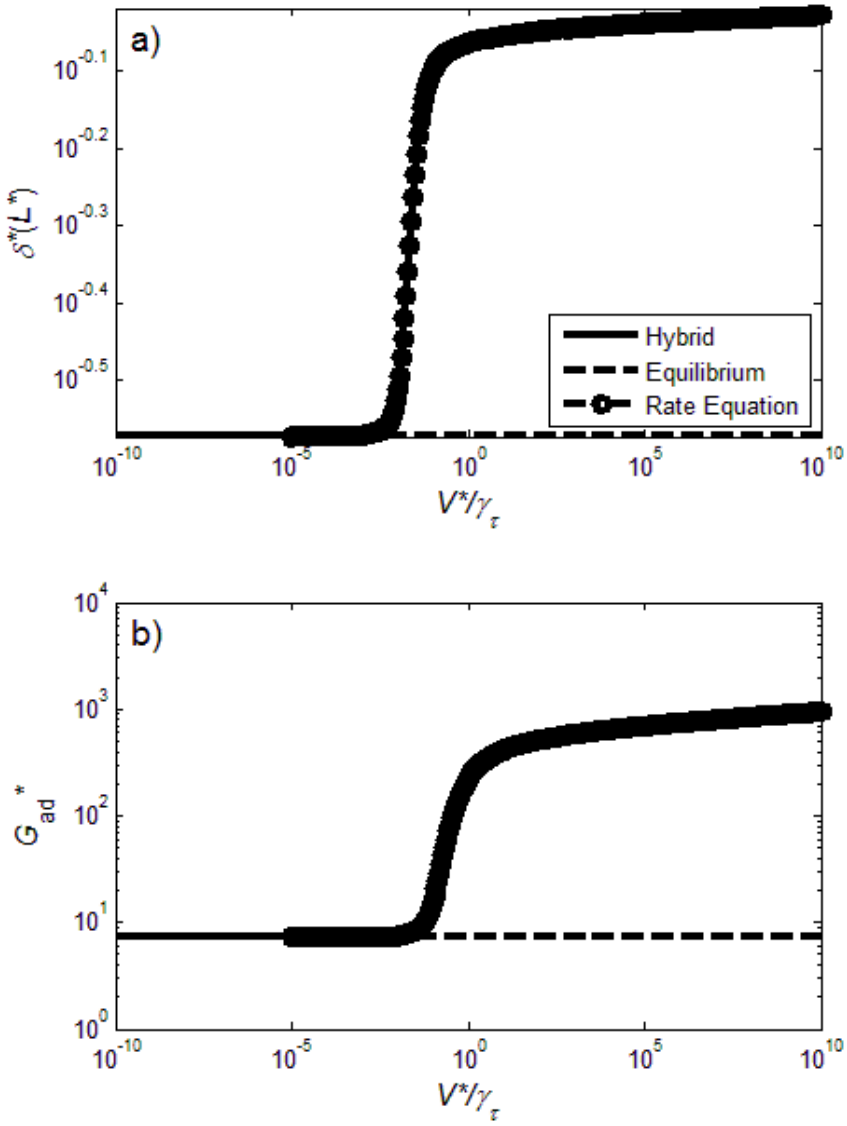

Figure: A2.1 Plots for **a** crack opening displacement, $\delta^*(L^*)$, and **b** adhesive fracture energy, G_{ad}^*, obtained by varying V^*/γ_τ while holding the other governing parameters fixed at $U^* = 2850$, $\gamma_E = 1$ (i.e. elastic beams), γ_L=0.0022222, $\Sigma_{b0}^* = 0.9$, $n = 150$, $\delta_c^* = 0.02$ and $W_{vdW}^* = 5$. Each curve in these figures represents a different approach used to solve for the chain density: "Hybrid" means solved from Eq. (A2.2) for $V^*/\gamma_\tau \geq 0.001$, and from Eq. (A2.8) for $V^*/\gamma_\tau < 0.001$; "Equilibrium" means solved from Eq. (A2.8); "Rate Equation" means solved from Eq. (A2.2).

Appendix 3. Supporting Material for Chapter 4

Appendix 3.1. Stress and Dissipation

When evaluating the rate of work care must be taken to choose the correct work-conjugate deformation rate for the chosen stress tensor [40]. For Eq. (4.4) in the main text,

$$\dot{W} = \dot{U} + \dot{D}_{\text{int}} = \underline{\mathbf{P}} : \dot{\underline{\mathbf{F}}} = J\underline{\boldsymbol{\sigma}}\underline{\mathbf{F}}^{-T} : \dot{\underline{\mathbf{F}}} = J\underline{\boldsymbol{\sigma}} : \dot{\underline{\mathbf{F}}}\underline{\mathbf{F}}^{-1} = J\underline{\boldsymbol{\sigma}} : \underline{\mathbf{L}} = J\underline{\boldsymbol{\sigma}} : \underline{\mathbf{D}} \tag{A3.1}$$

where W, U, D_{int}, $\underline{\mathbf{F}}$, $J = \det(\underline{\mathbf{F}})$, $\underline{\mathbf{L}}$, $\underline{\mathbf{D}} = \left(\underline{\mathbf{L}} + \underline{\mathbf{L}}^{T}\right)/2$, $\underline{\boldsymbol{\sigma}}$, $\underline{\mathbf{P}} = J\underline{\boldsymbol{\sigma}}\underline{\mathbf{F}}^{-T}$ are respectively the work, strain energy, dissipation, deformation gradient tensor, its determinant, velocity gradient tensor, symmetric part of velocity gradient tensor, Cauchy stress, and 1st Piola-Kirchhoff stress. Here the overhead dot indicates differentiation with respect to time, and in component form $\underline{\mathbf{A}} : \underline{\mathbf{B}} = \sum_{i=1}^{3}\sum_{j=1}^{3} A_{ij}B_{ij}$. Because $\underline{\boldsymbol{\sigma}}$ is symmetric $\underline{\boldsymbol{\sigma}} : \underline{\mathbf{L}} = \underline{\boldsymbol{\sigma}} : \underline{\mathbf{D}}$. $\dot{U}$ can be evaluated by taking the appropriate derivatives of Eq. (4.2) in the main text as follows

$$\dot{U} = \left(\sum_{i=1}^{M} b_i \frac{\partial U_{o,i}(\underline{\mathbf{B}})}{\partial \underline{\mathbf{B}}} - p\frac{J}{2}\underline{\mathbf{B}}^{-1}\right) : \dot{\underline{\mathbf{B}}} + \sum_{i=1}^{M} \dot{b}_i U_{o,i}(\underline{\mathbf{B}}) = \left(\sum_{i=1}^{M} b_i \frac{\partial U_{o,i}(\underline{\mathbf{B}})}{\partial \underline{\mathbf{B}}} - p\frac{J}{2}\underline{\mathbf{B}}^{-1}\right) : \left(\underline{\mathbf{L}}\underline{\mathbf{B}} + \underline{\mathbf{B}}\underline{\mathbf{L}}^{\mathbf{T}}\right) + \sum_{i=1}^{M} \dot{b}_i U_{o,i}(\underline{\mathbf{B}}) \tag{A3.2}$$

where $\underline{\mathbf{B}} = \underline{\mathbf{B}}^{\mathbf{T}} = \underline{\mathbf{F}}\underline{\mathbf{F}}^{\mathbf{T}}$ and $\dot{\underline{\mathbf{B}}} = \underline{\mathbf{L}}\underline{\mathbf{B}} + \underline{\mathbf{B}}\underline{\mathbf{L}}^{\mathbf{T}}$. Further manipulations of Eq. (A3.2) gives

$$\begin{aligned}\dot{U} &= \left(\sum_{i=1}^{M} b_i \frac{\partial U_{o,i}(\underline{\mathbf{B}})}{\partial \underline{\mathbf{B}}}\underline{\mathbf{B}} - p\frac{J}{2}\underline{\mathbf{I}}\right) : \left(\underline{\mathbf{L}} + \underline{\mathbf{L}}^{\mathbf{T}}\right) + \sum_{i=1}^{M} \dot{b}_i U_{o,i}(\underline{\mathbf{B}}) = \left(\sum_{i=1}^{M} \underline{\mathbf{B}} b_i \frac{\partial U_{o,i}(\underline{\mathbf{B}})}{\partial \underline{\mathbf{B}}} - p\frac{J}{2}\underline{\mathbf{I}}\right) : \left(\underline{\mathbf{L}} + \underline{\mathbf{L}}^{\mathbf{T}}\right) + \sum_{i=1}^{M} \dot{b}_i U_{o,i}(\underline{\mathbf{B}}) \\ &= \left(\sum_{i=1}^{M} 2b_i \frac{\partial U_{o,i}(\underline{\mathbf{B}})}{\partial \underline{\mathbf{B}}}\underline{\mathbf{B}} - p\underline{\mathbf{I}}\right) : \underline{D} + \sum_{i=1}^{M} \dot{b}_i U_{o,i}(\underline{\mathbf{B}}) = \left(\sum_{i=1}^{M} 2\underline{\mathbf{B}} b_i \frac{\partial U_{o.i}(\underline{\mathbf{B}})}{\partial \underline{\mathbf{B}}} - p\underline{\mathbf{I}}\right) : \underline{D} + \sum_{i=1}^{M} \dot{b}_i U_{o,i}(\underline{\mathbf{B}}),\end{aligned} \tag{A3.3}$$

where $\underline{\mathbf{I}}$ is the 2nd order identity tensor and $J = 1$ for an incompressible material has been used in the last step. Note that the last two expressions in Eq. (A3.3) are equivalent (owing to the symmetry of $\underline{\mathbf{B}}$). Comparing Eq. (A3.3) with Eq. (A3.1) two equivalent expressions for the stress can be extracted

$$\underline{\boldsymbol{\sigma}} = \sum_{i=1}^{M} 2b_i \frac{\partial U_{o,i}(\underline{\mathbf{B}})}{\partial \underline{\mathbf{B}}}\underline{\mathbf{B}} - p\underline{\mathbf{I}} = \sum_{i=1}^{M} 2\underline{\mathbf{B}} b_i \frac{\partial U_{o,i}(\underline{\mathbf{B}})}{\partial \underline{\mathbf{B}}} - p\underline{\mathbf{I}}. \tag{A3.4}$$

Similarly from comparing Eq. (A3.3) with Eq. (A3.1) the dissipation can be identified as

$$\dot{D}_{\text{int}} = -\sum_{i=1}^{M} \dot{b}_i U_{o,i}(\underline{\mathbf{B}}). \tag{A3.5}$$

Note that the second law of thermodynamics is satisfied since $\dot{b}_i \le 0$ and $U_{o,i} \ge 0$.

Many hyperelastic models only depend on the 1st invariant of $\underline{\mathbf{B}}$, I_1, in which case

$$\frac{\partial U_{o,i}(I_1)}{\partial \underline{\mathbf{B}}} = \frac{\partial U_{o,i}(I_1)}{\partial I_1}\frac{\partial I_1}{\partial \underline{\mathbf{B}}} = \frac{\partial U_{o,i}(I_1)}{\partial I_1}\underline{\mathbf{I}}. \tag{A3.6}$$

For the Arruda-Boyce model (Eq. (4.8) in main text) we can evaluate

$$\frac{\partial U_{o,i}}{\partial I_1} = \frac{N_o k_B T}{6}\left(\frac{I_1(\underline{\mathbf{B}})}{3n_i}\right)^{-1/2}\beta_i. \tag{A3.7}$$

Appendix 3.2. Stress in uniaxial extension

For uniaxial extension the deformation gradient is given by

$$\underline{\mathbf{F}} = \lambda \underline{\mathbf{e}}_1 \otimes \underline{\mathbf{E}}_1 + \lambda_t \underline{\mathbf{e}}_2 \otimes \underline{\mathbf{E}}_2 + \lambda_t \underline{\mathbf{e}}_3 \otimes \underline{\mathbf{E}}_3 \tag{A3.8}$$

where λ is the stretch, λ_t is the transverse stretch, $\underline{\mathbf{e}}_i$ are bases in the deformed configuration and $\underline{\mathbf{E}}_i$ are bases in the reference configuration. Note that the tensor product $\otimes$ is defined so that $(\underline{\mathbf{a}} \otimes \underline{\mathbf{b}})\underline{\mathbf{c}} = \underline{\mathbf{a}}(\underline{\mathbf{b}} \cdot \underline{\mathbf{c}})$ and $(\underline{\mathbf{a}} \otimes \underline{\mathbf{b}})(\underline{\mathbf{c}} \otimes \underline{\mathbf{d}}) = (\underline{\mathbf{b}} \cdot \underline{\mathbf{c}})(\underline{\mathbf{a}} \otimes \underline{\mathbf{d}})$. If the elastomer is incompressible then its volume does not change during the deformation or $J = \det(\underline{\mathbf{F}}) = \lambda\lambda_t\lambda_t = 1$ which requires that $\lambda_t = \lambda^{-1/2}$. Knowing this and Eq. (4.10) in the main text we can evaluate various tensors which describe the deformation

$$\begin{aligned}
&\underline{\mathbf{F}} = \lambda \underline{\mathbf{e}}_1 \otimes \underline{\mathbf{E}}_1 + \lambda^{-1/2} \underline{\mathbf{e}}_2 \otimes \underline{\mathbf{E}}_2 + \lambda^{-1/2} \underline{\mathbf{e}}_3 \otimes \underline{\mathbf{E}}_3 \\
&\underline{\mathbf{F}}^{-1} = \lambda^{-1} \underline{\mathbf{E}}_1 \otimes \underline{\mathbf{e}}_1 + \lambda^{1/2} \underline{\mathbf{E}}_2 \otimes \underline{\mathbf{e}}_2 + \lambda^{1/2} \underline{\mathbf{E}}_3 \otimes \underline{\mathbf{e}}_3 \\
&\underline{\mathbf{F}}^{-\mathbf{T}} = \lambda^{-1} \underline{\mathbf{e}}_1 \otimes \underline{\mathbf{E}}_1 + \lambda^{1/2} \underline{\mathbf{e}}_2 \otimes \underline{\mathbf{E}}_2 + \lambda^{1/2} \underline{\mathbf{e}}_3 \otimes \underline{\mathbf{E}}_3 \\
&\underline{\mathbf{B}} = \lambda^2 \underline{\mathbf{e}}_1 \otimes \underline{\mathbf{e}}_1 + \lambda^{-1} \underline{\mathbf{e}}_2 \otimes \underline{\mathbf{e}}_2 + \lambda^{-1} \underline{\mathbf{e}}_3 \otimes \underline{\mathbf{e}}_3 \\
&\dot{\underline{\mathbf{F}}} = R\left[\underline{\mathbf{e}}_1 \otimes \underline{\mathbf{E}}_1 - 0.5\lambda^{-3/2}(\underline{\mathbf{e}}_2 \otimes \underline{\mathbf{E}}_2 + \underline{\mathbf{e}}_3 \otimes \underline{\mathbf{E}}_3)\right] \\
&\underline{\mathbf{L}} = \dot{\underline{\mathbf{F}}}\underline{\mathbf{F}}^{-1} = \frac{R}{\lambda}\left[\underline{\mathbf{e}}_1 \otimes \underline{\mathbf{e}}_1 - (\underline{\mathbf{e}}_2 \otimes \underline{\mathbf{e}}_2 + \underline{\mathbf{e}}_3 \otimes \underline{\mathbf{e}}_3)\right] = \underline{\mathbf{D}}
\end{aligned} \tag{A3.9}$$

With these quantities we can evaluate the stress using Eqs. (A3.4), (A3.6), (A3.7) and (4.12)

$$\underline{\boldsymbol{\sigma}} = \sum_{i=1}^{M} 2b_i \frac{\partial U_{o,i}}{\partial I_1}\left[\lambda^2 - \lambda^{-1}\right]\underline{\mathbf{e}}_1 \otimes \underline{\mathbf{e}}_1$$

$$\underline{\mathbf{P}} = \sum_{i=1}^{M} 2b_i \frac{\partial U_{o,i}}{\partial I_1}\lambda^{-1}\left[\lambda^2 - \lambda^{-1}\right]\underline{\mathbf{e}}_1 \otimes \underline{\mathbf{E}}_1 \qquad \text{(A3.10)}$$

Finally, the internal rate of work can be determined to be

$$\dot{W} = \underline{\mathbf{P}} : \dot{\underline{\mathbf{F}}} = J\underline{\boldsymbol{\sigma}} : \underline{\mathbf{D}} = \sum_{i=1}^{M} 2b_i \frac{\partial U_{o,i}}{\partial I_1}\left[\lambda^2 - \lambda^{-1}\right]\frac{R}{\lambda} \qquad \text{(A3.11)}$$

Appendix 3.3. Modifying Model to Consider Prestretch

In the main text we have used our model to fit the experimental data for cyclic loading of the triple network (TN) elastomer described in Ducrot et al. [4]. In this type of elastomer the first network is swollen which adds significant prestretch to the first network. Because chain fractional extension plays an important role on the tensile force and hence the scission kinetics, we will modify the model to account for prestretch. In Table S2 of the Supporting Material of Ducrot et al. [4] the change in thickness of the final $EA_{0.5}EAEA$ sample relative to the original network is 2.5. If we assume that transverse dimensions change by the same ratio we can calculate the volume change of the material $J_s = (2.5)^3 = 15.625$. Assume that the total deformation gradient can be decomposed into two parts (i) isotropic swelling, $\underline{\mathbf{F}}_s = (J_s)^{1/3}\underline{\mathbf{I}}$, of the first network to create the TN elastomer and (ii) deformation gradient for uniaxial extension of the TN, $\underline{\mathbf{F}}_m$, described by Eq. (A3.9). Hence the total deformation gradient is given by

$$\underline{\mathbf{F}} = \underline{\mathbf{F}}_s\underline{\mathbf{F}}_m = (J_s)^{1/3}\left(\lambda\underline{\mathbf{e}}_1 \otimes \underline{\mathbf{E}}_1 + \lambda^{-1/2}\underline{\mathbf{e}}_2 \otimes \underline{\mathbf{E}}_2 + \lambda^{-1/2}\underline{\mathbf{e}}_3 \otimes \underline{\mathbf{E}}_3\right), \qquad \text{(A3.12)}$$

and $\underline{\mathbf{B}} = (J_s)^{2/3}\underline{\mathbf{B}}_m$ where $\underline{\mathbf{B}}_m$ is given in Eq. (A3.9). The first invariant of $\underline{\mathbf{B}}$ is then

$$I_1 = (J_s)^{2/3}\left(\lambda^2 + 2/\lambda\right). \qquad \text{(A3.13)}$$

The total $\underline{\mathbf{B}}$ and I_1 are used in Eq. (A3.4) and (A3.7) to evaluate the stress. To fit the experimental data we have neglected the 2nd and 3rd networks and any coupled effects, and attempted to find a chain length distribution, shown in Figure A3.1, which provides a good fit.

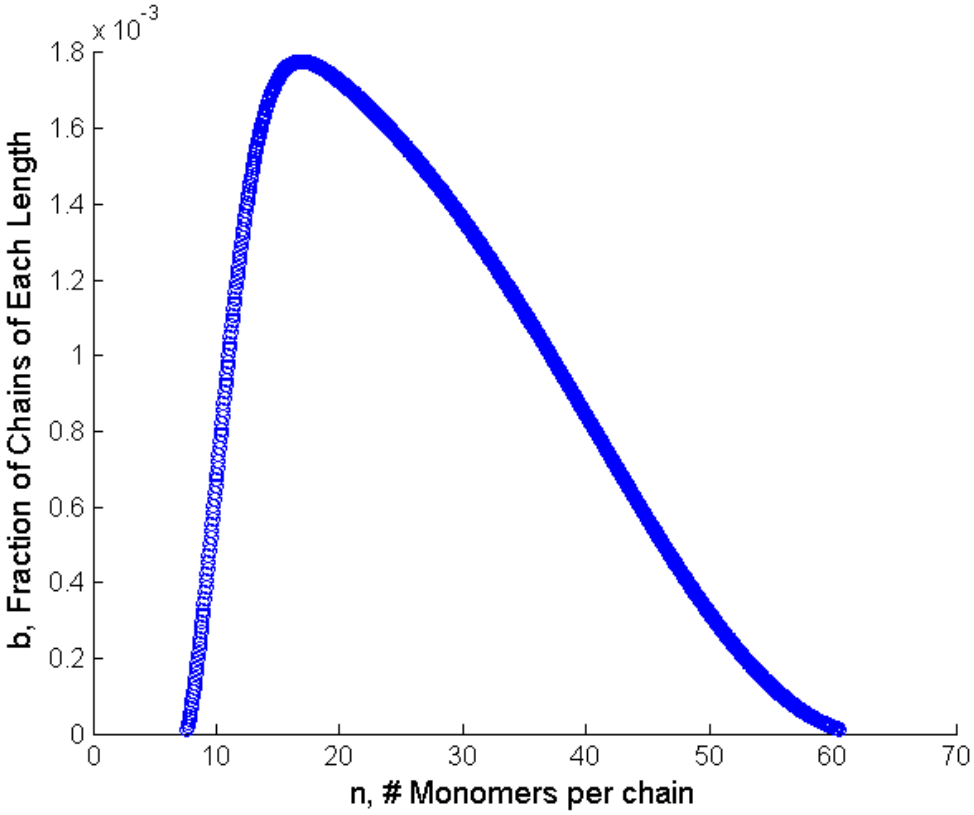

Figure A3.1: Chain length distribution used to fit TN elastomer. Based on the distribution given in Eq. (A3.14) with $a_o = 25$, $a_f = 1000$, $n_o = 6.5$, $n_f = 63$. A is set to normalize the distribution so $b_t = 1$.

To provide a good fit to the experimental data we used another distribution which as an exponential increase, followed by a possible plateau and then an exponential decrease as follows:

$$f(n) = \begin{cases} A\left(1 - e^{-\frac{(n-n_o)^2}{a_o}} - e^{-\frac{(n-n_f)^2}{a_f}}\right) & n_o < n < n_f \\ 0 & otherwise \end{cases}. \qquad \text{(A3.14)}$$

Appendix 3.4. Shifted Maxwell-Boltzmann Distribution

The original Maxwell-Boltzmann distribution $f(n)$ has zero probability for $n \leq 0$ and is fully specified if the mean value $\bar{n}$ is known. However, for a polymer chain it is unphysical to have the number of Kuhn segments ≤ 1. Thus it is beneficial to introduce a second parameter $n_o \geq 1$ which can be used to shift the distribution so that zero probability occurs at a different value. The following is the resulting probability distribution

$$f(n) = \begin{cases} \dfrac{32}{\pi^2} \dfrac{(n-n_o)^2}{(\bar{n}-n_o)^3} e^{-\frac{4}{\pi}\left(\frac{n-n_o}{\bar{n}-n_o}\right)^2} & n > n_o \\ 0 & n \leq n_o \end{cases} . \qquad \text{(A3.15)}$$

In this work when n_o is not specified its value should be taken to be 1.

Appendix 4. *Supporting Material for Chapter 5*

Appendix 4.1. Stress and Dissipation

The stress and dissipation associated with Eq. (5.13) can be derived by using the second law of thermodynamics. If we introduce a Lagrange multiplier into the strain energy function, we can rewrite Eq. (5.13) as follows

$$U_N = \sum_{i=1}^{N} \phi^i U_N^i\left(\underline{\mathbf{B}}_N^i\right) - p(J-1), \tag{A4.1}$$

where $p(J-1)=0$ since this formulation will be restricted to an incompressible MNE ($J=1$).

Consider the balance of power per unit volume

$$\dot{W} = \dot{U}_N + \dot{D}_{\text{int}} = \underline{\mathbf{P}} : \dot{\underline{\mathbf{F}}} = J\underline{\boldsymbol{\sigma}}\underline{\mathbf{F}}^{-T} : \dot{\underline{\mathbf{F}}} = J\underline{\boldsymbol{\sigma}} : \dot{\underline{\mathbf{F}}}\underline{\mathbf{F}}^{-1} = J\underline{\boldsymbol{\sigma}} : \underline{\mathbf{L}} = J\underline{\boldsymbol{\sigma}} : \underline{\mathbf{D}} \tag{A4.2}$$

where W, U_N, D_{int}, $\underline{\mathbf{F}}$, $J=\det(\underline{\mathbf{F}})$, $\underline{\mathbf{L}}$, $\underline{\mathbf{D}}=\left(\underline{\mathbf{L}}+\underline{\mathbf{L}}^T\right)/2$, $\underline{\boldsymbol{\sigma}}$, $\underline{\mathbf{P}}=J\underline{\boldsymbol{\sigma}}\underline{\mathbf{F}}^{-T}$ are respectively the work, strain energy, dissipation, deformation gradient tensor, its determinant, velocity gradient tensor, symmetric part of velocity gradient tensor, Cauchy stress, and 1st Piola-Kirchhoff stress. Here the overhead dot indicates differentiation with respect to time, and in component form $\underline{\mathbf{A}} : \underline{\mathbf{B}} = \sum_{i=1}^{3}\sum_{j=1}^{3} A_{ij}B_{ij}$. Because $\underline{\boldsymbol{\sigma}}$ is symmetric $\underline{\boldsymbol{\sigma}} : \underline{\mathbf{L}} = \underline{\boldsymbol{\sigma}} : \underline{\mathbf{D}}$. $\dot{U}$ can be evaluated by taking the appropriate derivatives of Eq. (S1) as follows

$$\dot{U}_N = \left(\sum_{i=1}^{N} \phi^i \frac{\partial U_N^i\left(\underline{\mathbf{B}}_N^i\right)}{\partial \underline{\mathbf{B}}} - p\frac{\partial J}{\partial \underline{\mathbf{B}}}\right) : \dot{\underline{\mathbf{B}}} + \phi^1 \mu \int_1^{\infty} f\left(N_K\right)\dot{b}\left(r_{\max}^*, N_K\right) N_K E_{ch}^*\left(r^*\right) dN_K . \tag{A4.3}$$

Using $\partial J / \partial \underline{\mathbf{B}} = \partial\sqrt{I_3(\underline{\mathbf{B}})} / \partial \underline{\mathbf{B}} = J\underline{\mathbf{B}}^{-1}/2$, $\dot{\underline{\mathbf{B}}} = \underline{\mathbf{L}}\underline{\mathbf{B}} + \underline{\mathbf{B}}\underline{\mathbf{L}}^{\mathbf{T}}$, Eq. (5.8) in the main text, and denoting $\dot{D}_{\text{int}} = -\phi^1 \mu \int_1^{\infty} f\left(N_K\right)\dot{b}\left(r_{\max}^*, N_K\right) N_K E_{ch}^*\left(r^*\right) dN_K$ this can be rewritten as

$$\dot{U}_N = \left(\sum_{i=1}^{N} \phi^i \left(J_{s(N-1)}^i\right)^{2/3} \frac{\partial U_N^i\left(\underline{\mathbf{B}}_N^i\right)}{\partial \underline{\mathbf{B}}_N^i} - p\frac{J}{2}\underline{\mathbf{B}}^{-1}\right) : \left(\underline{\mathbf{L}}\underline{\mathbf{B}} + \underline{\mathbf{B}}\underline{\mathbf{L}}^{\mathbf{T}}\right) - \dot{D}_{\text{int}} \tag{A4.4}$$

Further manipulations of Eq. (A4.4) gives

$$\dot{U}_N + \dot{D}_{\text{int}} = \left(\sum_{i=1}^{N} \phi^i \frac{\partial U_N^i\left(\underline{\mathbf{B}}_N^i\right)}{\partial \underline{\mathbf{B}}_N^i} \left(J_{s(N-1)}^i\right)^{2/3} \underline{\mathbf{B}} - p\frac{J}{2}\underline{\mathbf{I}} \right) : \left(\underline{\mathbf{L}} + \underline{\mathbf{L}}^{\mathrm{T}}\right) = \left(\sum_{i=1}^{N} \phi^i \left(J_{s(N-1)}^i\right)^{2/3} \underline{\mathbf{B}} \frac{\partial U_N^i\left(\underline{\mathbf{B}}_N^i\right)}{\partial \underline{\mathbf{B}}_N^i} - p\frac{J}{2}\underline{\mathbf{I}} \right) : \left(\underline{\mathbf{L}} + \underline{\mathbf{L}}^{\mathrm{T}}\right)$$

$$\dot{U}_N + \dot{D}_{\text{int}} = \left(\sum_{i=1}^{N} \phi^i 2 \frac{\partial U_N^i\left(\underline{\mathbf{B}}_N^i\right)}{\partial \underline{\mathbf{B}}_N^i} \underline{\mathbf{B}}_N^i - pJ\underline{\mathbf{I}} \right) : \underline{\mathbf{D}} = \left(\sum_{i=1}^{N} \phi^i 2 \underline{\mathbf{B}}_N^i \frac{\partial U_N^i\left(\underline{\mathbf{B}}_N^i\right)}{\partial \underline{\mathbf{B}}_N^i} - pJ\underline{\mathbf{I}} \right) : \underline{\mathbf{D}}, \quad \text{(A4.5)}$$

where $\underline{\mathbf{I}}$ is the 2nd order identity tensor. Note that the last two expressions in Eq. (A4.5) are equivalent (owing to the symmetry of $\underline{\mathbf{B}}$). Comparing Eq. (A4.5) with Eq. (A4.2) two equivalent expressions for the stress can be extracted

$$\underline{\boldsymbol{\sigma}} = \sum_{i=1}^{N} \phi^i \frac{2}{J} \frac{\partial U_N^i\left(\underline{\mathbf{B}}_N^i\right)}{\partial \underline{\mathbf{B}}_N^i} \underline{\mathbf{B}}_N^i - p\underline{\mathbf{I}} = \sum_{i=1}^{N} \phi^i \frac{2}{J} \underline{\mathbf{B}}_N^i \frac{\partial U_N^i\left(\underline{\mathbf{B}}_N^i\right)}{\partial \underline{\mathbf{B}}_N^i} - p\underline{\mathbf{I}}. \quad \text{(A4.6)}$$

Similarly, from comparing Eq. (A4.5) with Eq. (A4.2) the dissipation can be identified as

$$\dot{D}_{\text{int}} = -\phi^1 \mu \int_1^{\infty} f\left(N_K\right) \dot{b}\left(r_{\max}^*, N_K\right) N_K E_{ch}^*\left(r^*\right) dN_K. \quad \text{(A4.7)}$$

Note that the second law of thermodynamics is satisfied since $\dot{b}\left(r_{\max}^*, N_K\right) \le 0$ and all the other quantities in the equation are non-negative.

Many hyperelastic models only depend on the 1st invariant of $\underline{\mathbf{B}}$, I_1, in which case

$$\frac{\partial U_N^i\left(I_1\left(\underline{\mathbf{B}}_N^i\right)\right)}{\partial \underline{\mathbf{B}}_N^i} = \frac{\partial U_N^i\left(I_1\left(\underline{\mathbf{B}}_N^i\right)\right)}{\partial I_1\left(\underline{\mathbf{B}}_N^i\right)} \frac{\partial I_1\left(\underline{\mathbf{B}}_N^i\right)}{\partial \underline{\mathbf{B}}_N^i} = \frac{\partial U_N^i\left(I_1\left(\underline{\mathbf{B}}_N^i\right)\right)}{\partial I_1\left(\underline{\mathbf{B}}_N^i\right)} \underline{\mathbf{I}}. \quad \text{(A4.8)}$$

For this case we can also define the initial Young's and shear modulus for the material. Introducing Eq. (S8) into Eq. (S6), and setting $J = 1$ gives

$$\underline{\boldsymbol{\sigma}} = \sum_{i=1}^{N} \phi^i 2 \frac{\partial U_N^i\left(I_1\left(\underline{\mathbf{B}}_N^i\right)\right)}{\partial I_1\left(\underline{\mathbf{B}}_N^i\right)} \left(J_{s(N-1)}^i\right)^{2/3} \underline{\mathbf{B}} - p\underline{\mathbf{I}} = \sum_{i=1}^{N} \phi^i 2 \frac{\partial U_N^i\left(I_1\left(\underline{\mathbf{B}}_N^i\right)\right)}{\partial I_1\left(\underline{\mathbf{B}}\right)} \underline{\mathbf{B}} - p\underline{\mathbf{I}}. \quad \text{(A4.9)}$$

Where Eq. Eq. (5.8) from the main text, $\underline{\mathbf{B}}_N^i = \left(J_{s(N-1)}^i\right)^{2/3} \underline{\mathbf{B}}$, has been used. The initial shear modulus, G_o^N, is defined for consistency with linear elasticity when $I_1\left(\underline{\mathbf{B}}\right) = 3$, therefore $I_1\left(\underline{\mathbf{B}}_N^i\right) = 3\left(J_{s(N-1)}^i\right)^{2/3}$ and

$$G_o^N = \frac{E_o^N}{3} = \sum_{i=1}^{N} \phi^i 2\left(J_{s(N-1)}^i\right)^{2/3} \frac{\partial U_N^i\left(3\left(J_{s(N-1)}^i\right)^{2/3}\right)}{\partial I_1\left(\underline{\mathbf{B}}_N^i\right)} = \sum_{i=1}^{N} \phi^i 2 \frac{\partial U_N^i\left(3\left(J_{s(N-1)}^i\right)^{2/3}\right)}{\partial I_1\left(\underline{\mathbf{B}}\right)}, \quad \text{(A4.10)}$$

where the initial Young's modulus is $E_o^N = 3G_o^N$ due to incompressibility.

Appendix 4.2. Damage Evolution

The damage evolution functions derivation is to be reported in a separate paper [74] where Weibull distributions where found to provide a reasonable fit for large deformation rates. The functions given are as follows

$$\frac{db}{dr^*_{\max}} = \frac{c_1}{c_2}\left(\frac{F_{cr}-F}{c_2}\right)^{c_1-1}\exp\left(-\left(\frac{F_{cr}-F}{c_2}\right)^{c_1}\right), \quad \text{(A4.11)}$$

$$b = 1-\exp\left(-\left(\frac{F_{cr}-F}{c_2}\right)^{c_1}\right). \quad \text{(A4.12)}$$

Note that Eq. (S11) represents the Weibull probability distribution function while Eq. (S12) represents the Weibull cumulative distribution function. The constants F_{cr}, c_1, and c_2 depend on the material, the chain length and the chain extension rate. For the MNE with photophore in the rate-independent regime $F_{cr} = 1.99nN$ and

$$c_1 = 0.000174N_K^2 - 0.0138N_K + 1.2436, \quad \text{(A4.13)}$$

$$c_2 = -0.03019N_K^2 - 2.9816N_K + 22.314. \quad \text{(A4.14)}$$

For the MNE without photophore in the rate independent regime $F_{cr} = 3.47nN$ and

$$c_1 = -0.00034N_K^2 + 0.053178N_K + 0.6822, \quad \text{(A4.15)}$$

$$c_2 = -0.29114N_K^2 + 33.01N_K + 4.8072. \quad \text{(A4.16)}$$

Appendix 4.3. Numerical Methods

The following method is used to evaluate the integration with respect to N_K in Eqs. (5.16), (5.19), and (5.29) in the main text. The integration of the product of the probability density function, $f(N_K)$, and an arbitrary function $g(r^*, N_K)$ is evaluated by dividing the range of chain lengths into *M* bins and evaluating the following summation

$$\int_1^{\infty} f(N_K)g(r^*, N_K)dN_K \approx \sum_{m=1}^{M} \Delta F_m g(r_m^*, \overline{N}_{K,m}), \quad \text{(A4.17)}$$

where

$$\Delta F_m = 0.5(f(N_{K,m+1}) + f(N_{K,m}))(N_{K,m+1} - N_{K,m}), \quad \text{(A4.18)}$$

and $\overline{N}_{K,m}$ is the average Kuhn length for chains in bin *m* defined as

$$\overline{N}_{K,m} = 0.5(N_{K,m+1} + N_{K,m}). \quad \text{(A4.19)}$$

Here $N_{K,m+1}$, and $N_{K,m}$ are the chain lengths at the endpoints of bin *m*.

Appendix 4.4. Repeatability

In determining fitting parameters to provide the best fit of the model to the experimental data, results were used from numerous experiments. To examine how much the parameters may vary between different samples with a similar MNE structure, we did a comparison of 3 data sets of DN elastomers and 3 datasets of TN elastomers. In each case the crosslink density is the same and the network is swollen with approximately the same monomer/solvent ratio. The results are shown in Figure A4.1. Here the yellow curves correspond to the data presented in Figure 5.9 (DN3/TN3). The red curves correspond to data from Fig 2. C of Ducrot et al [4] (DND2C/TND2C). The red curves correspond to the MNE with photophore from Figure 5.5 (DNP/TNP). Due to the presence of photophores it is expected that the blue curves would behave slightly differently. However, the variability between the red and yellow curves suggests possible variation in the prestretch and/or the chain length distribution between samples. Nevertheless, in each measurement the initial shear modulus is relatively constant.

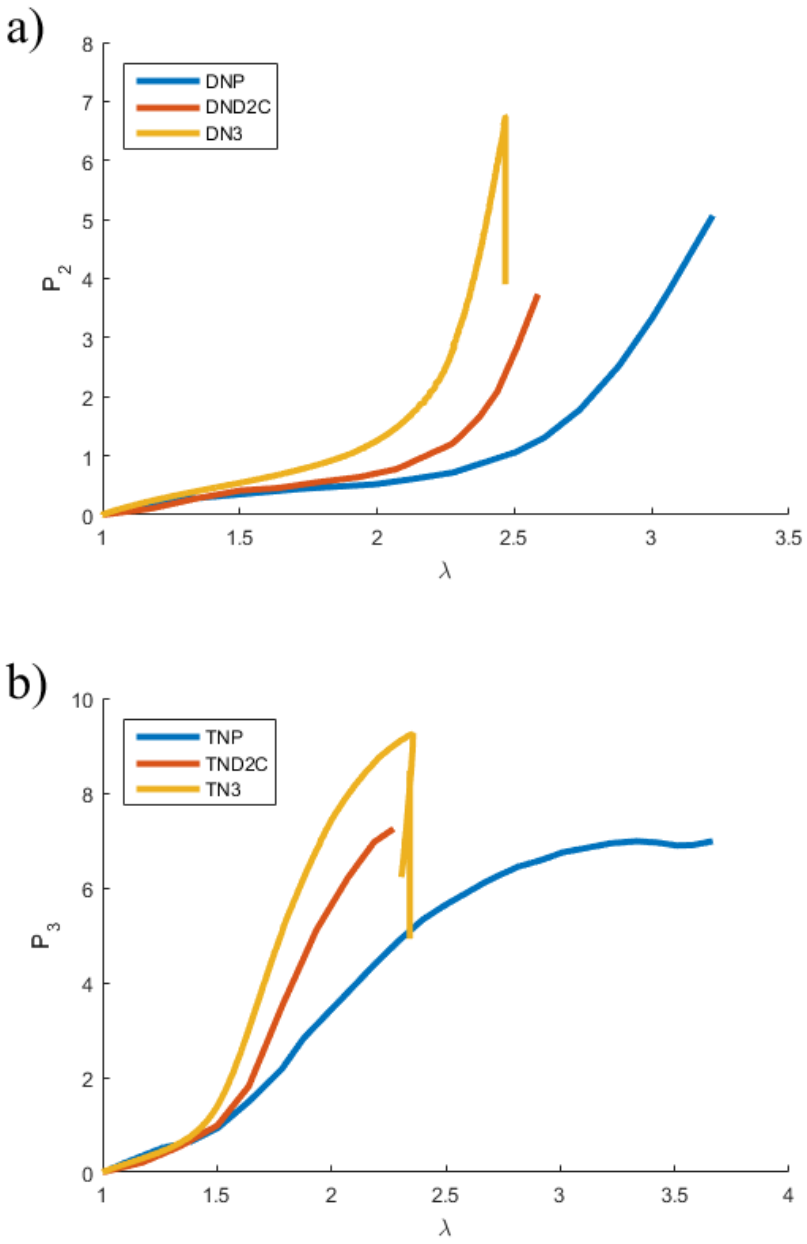

Figure A4.1: Engineering Stress plotted against stretch for 3 MNEs. a) DN elastomers b) TN elastomers. The yellow curves correspond to the data presented in Figure 5.9 (DN3: EAe1.45(1.68)EA/TN3: EAe1.45(2.55)EA). The red curves correspond to data from Fig 2. C of Ducrot et al [4] (DND2C: EAe1.45(1.71)EA/TND2C: EAe1.45(2.71)EA). The blue curves correspond to the MNE with photophore from Figure 5.5 (DNP: EAe1.45(1.48)EA/TNP: EAe1.45(2.72)EA).

Appendix 5. *Supporting Material for Chapter 6*

Appendix 5.1. Alternative Entropic Chain Energies

In the literature, there are numerous models which present the entropic energy of a polymer chain which would be used in place of Eqs. (6.1) and (6.6). For example, for a Gaussian chain the energy and force are given by the following expressions [93]

$E_{ent} = \frac{3}{2} k_B T N_K \left(r^*\right)^2,$	(A5.1)
$F = 3\frac{k_B T}{A} r^*.$	(A5.2)

A second common model in from the literature which can be used in place of Eq. (6.1) and (6.6) is the Arruda-Boyce model [9] which is based on Langevin statistics. In this model the entropic energy of a polymer chain is given by

$E_{ent} = k_B T N_K \left(r^* \beta + \ln\left(\frac{\beta}{\sinh \beta} \right) \right),$	(A5.3)

where $\beta = L^{-1}\left(r^*\right)$. The chain force is given by

$F = \frac{k_B T}{A} \beta .$	(A5.4)

Appendix 5.2. Chain Force Curve Fit

To facilitate the implementation of the model in higher level numerical simulations (e.g., finite element), it is desirable to obtain curve fits for some of the quantities which are calculated by the model. In Figure 6.4a) in the main text we can see that $r_o^* \approx r^*$ for $r_o^* < 0.9$ hence reasonable accuracy can be obtained if bond deformation is neglected for this portion of the extension; hence we fit a polynomial function to the numerical data for the force extension relationship:

$$F^*\left(r_o^*\right)=\frac{F\left(r_o^*\right)A_o}{k_BT}=\begin{cases}2\left(\frac{1}{4}\left(1-r_o^*\right)^{-2}-\frac{1}{4}+r_o^*\right) & r_o^*\le 0.9\\ \frac{513}{10}+1002\left(r_o^*-0.9\right)+\sum_{i=1}^{2}c_i\left(r_o^*-0.9\right)^{i+1} & r_o^*>0.9\end{cases}, \quad \text{(A5.5)}$$

The expression for $r_o^*<0.9$ is directly adopted from the entropic chain model (Eq. (6.1) in the main text) and c_i's for $r_o^*>0.9$ are fitting constants that depend on the polymer. It was found that a third order polynomial provide a good fit to the data, this means that there are two unknown coefficients since the first two terms of Eq. (A5.5) do not involve undetermined constants because they were used to match the force and slope at $r_o^*=0.9$. An example of the fit (PEA) is shown in Figure A5.1 The curve fit constants used in generating Figure A5.1, as well as for the remainder of the polymers from Table 6.2, are presented in Table A 5.1.

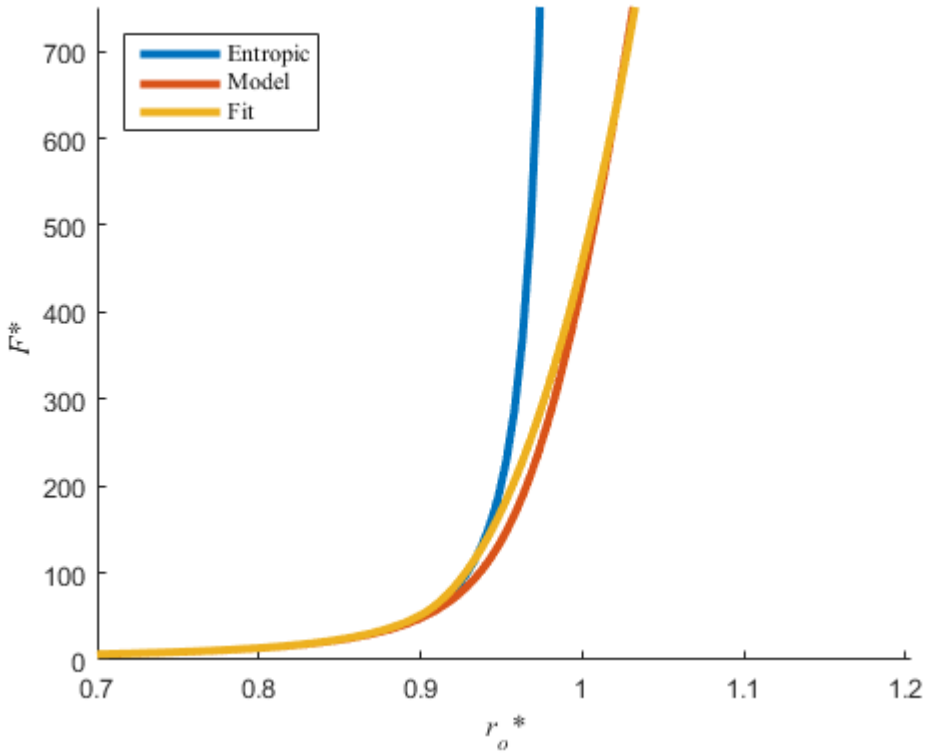

Figure A5.1: Comparison of the purely entropic chain force Eq. (6.1), with the chain force predicted by the model presented in this work and the polynomial curve fit for this force. The parameters used in generating these graphs are for PEA (Table 6.2) and C-C bond (Table 6.1)

Table A 5.1: Polymer force curve fit constants

Polymer	c_1	c_2
Poly(dimethyl siloxane) (PDMS)	2359.9	197560
Polypropylene (PP)	14715	31514
Polyethylene (PE)	19261	38669
Poly(methyl methacrylate) (PMMA)	23633	46307
Atactic Polystyrene (PS)	24895	49595
Poly(methyl acrylate) (PMA)	20601	38346
Poly(ethyl acrylate) (PEA)	25516	49636

Appendix 5.3. Rate of Chain Extension Under Uniaxial Loading

Eqs. (6.24) and (6.27) are rate equations and to solve for the surviving chain fraction integrations need to be done with respect to time. On the other hand, it is usually desired to establish the relationship between force and chain extension r_o^*. Therefore, it is more convenient to write db/dt as

$$\frac{db}{dt} = \frac{db}{dr_o^*}\frac{dr_o^*}{dt}, \tag{A5.6}$$

which would enable integration with respect to r_o^* rather than time. Consider now a polymeric network under uniaxial extension at a constant rate. The rate of chain extension is not the same as the rate of loading on the bulk polymer. In fact, following the "8-chain" [9], dr_o^*/dt can be evaluated as follows

$$\frac{dr_o^*}{dt} = \frac{d}{dt}\sqrt{\frac{I_1}{3N_K}} = \frac{\dot{I}_1}{2\sqrt{3N_K I_1}} = \frac{\left(\lambda - /\lambda^2\right)\dot{\lambda}}{\sqrt{3N_K\left(\lambda^2 + 2/\lambda\right)}}, \tag{A5.7}$$

Where $I_1 = \lambda^2 + 2/\lambda$ is the first invariant of the Left-Cauchy Green deformation tensor, and λ is the uniaxial extension stretch. Eq. (A5.7) is plotted against λ in Figure A5.2 where it can be seen that although the stretch rate of the material is constant the rate of chain extension is not constant. However, the rate of chain extension does asymptotically approach a constant value.

Using Eq. (A5.7), we can solve Eqs. (6.24) and (6.27) using Runge-Kutta with adaptive stepsize control [24] to obtain the surviving chain fraction b for a given stretch rate $\dot{\lambda}$.

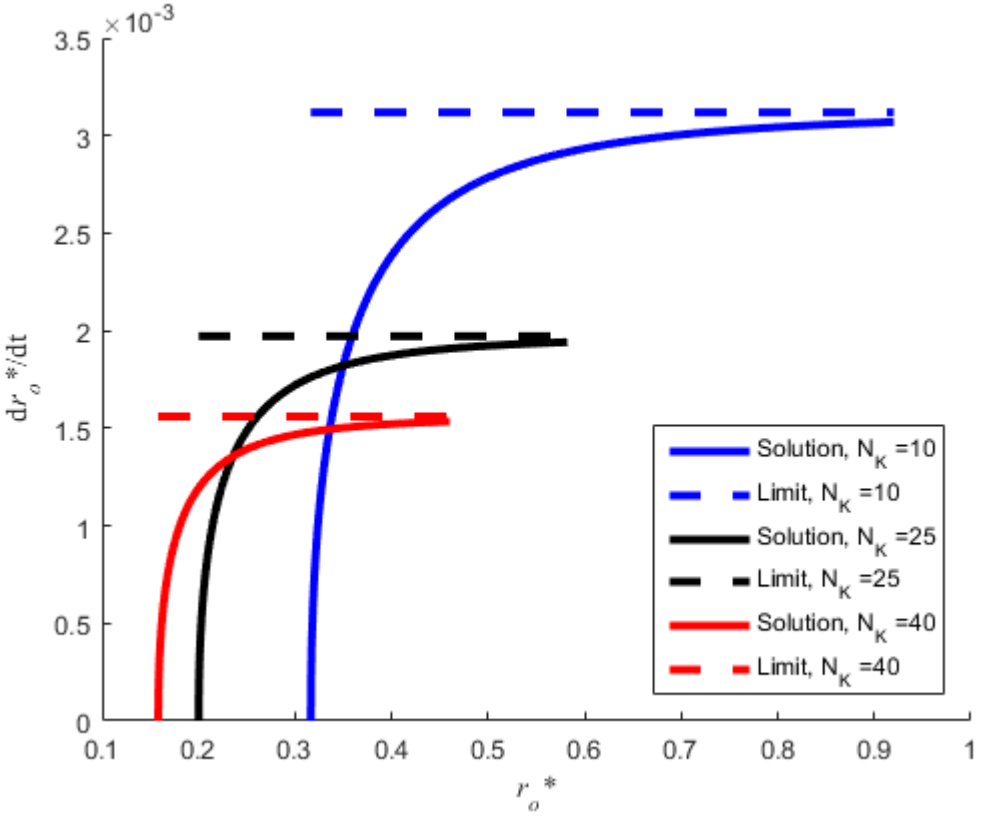

Figure A5.2: Rate of increase in chain fractional extension during constant speed uniaxial extension. $\dot{\lambda} = 0.0171 s^{-1}$

.

Appendix 5.4. Surviving Chain Fraction Curve Fit

If it is needed to solve Eq. (6.24) at many points in a material, it can become very computationally expensive, therefore it is desirable to have a reasonably accurate curve fit to approximate the soliton. The surviving chain fractions at each chain force is shown in Figure A5.3 for $\dot{\lambda} = 0.0171 s^{-1}$. At forces corresponding to fractional extensions less than 0.9 the rate of scission is negligible. With further increasing in force the surviving chain fraction smoothly decrease to zero. The shape of Figure A5.3 somewhat resembles a Weibull distribution, so this distribution is made the base function for fitting the numerical results. The fitting is broken up into several steps. First $F_{str} = f_{crit}$ is evaluated from Eq. (6.23) then the maximum chain force,

$F_{\max}$, is evaluated from Eqs. (6.1), (6.8), (6.10)-(6.12). Then the surviving chain fraction is defined to be the following Weibull cumulative distribution function

$b = 1 - \exp\left(-\left(\frac{F_{\max} - F}{c_2} \right)^{c_1} \right).$	(A5.8)

The constants $F_{\max}$, c_1, and c_2 depend on the material, temperature, the chain length and the chain extension rate. For PEA at 298K, $\dot{\lambda} = 0.0171 s^{-1}$, $F_{cr} = 3.47nN$ and

$c_1 = -0.00034N_K^2 + 0.053178N_K + 0.6822.$	(A5.9)
$c_2 = -0.29114N_K^2 + 33.01N_K + 4.8072.$	(A5.10)

For PEA with photophores at 298K, $\dot{\lambda} = 0.0171 s^{-1}$, $F_{cr} = 1.99nN$ and

$c_1 = 0.000174N_K^2 - 0.0138N_K + 1.2436.$	(A5.11)
$c_2 = -0.03019N_K^2 - 2.9816N_K + 22.314.$	(A5.12)

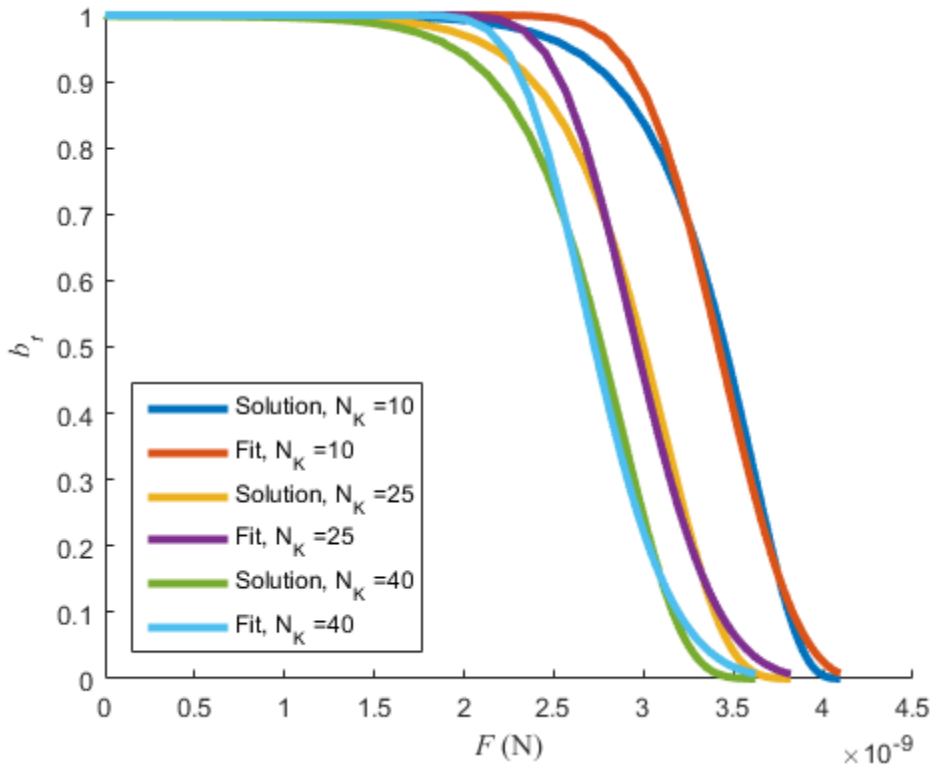

Figure A5.3: Rate of change of surviving chain fraction with respect to time at each fractional extension for two different chain lengths and the associated curve fits. The parameters used in generating these graphs are for PEA (Table 6.2), C-C bond (Table 6.1), Temperature T = 298 K, *stretch rate* $\dot{\lambda} = 0.0171 s^{-1}$ $k_o = 5\times10^{-9}$, $\Delta G^{\ddagger} = 40\times10^{-21} J$, *and* $x^{\ddagger} = 0.021\times10^{-9} m$.

Appendix 5.5. Comparison of Different Polymers

Because this chain model is based upon physical parameters, it can not only explain the behavior of existing material but also be used to make predictions in material design. For example, let us consider polymers made of the monomers listed in Table 6.2 and the hypothetical scenario where the polymerization leads to the same molecular weight, $M_{ch} = 10000 g/mol$, for all the chains. The effective force for each polymer is shown in Figure A5.4a). The curves are somewhat similar since all have C-C backbone bonds with similar θ_o and l_o (Table 6.3). At a given extension PP has the highest force, followed by PE and PMA because these polymers have lower Kuhn lengths (A_o Table 6.2) which causes larger entropic chain forces Eq. (6.1). To interpret the

differences in break force seen in Figure a) there is a trend where polymers with larger forces break relatively lower extensions. However, there is a secondary effect which influences the break force when $M_{ch} = 10000 g/mol$ is held constant each polymer will have different numbers of Kuhn segments and backbone bonds as shown in Table A 5.2. More backbone bonds provides more possible break locations and increase the rate of scission (Eq. (6.24)) which results in lower break forces.

Table A 5.2: Calculated parameters for polymers with $M_{ch} = 10000 g/mol$

Polymer	N_K	n_b	υ_{ch} (m^{-3}) ($x10^{25}$)	$\upsilon_{ch} k_B T$ (MPa)
Polypropylene (PP)	55.56	470.56	4.76	0.20
Polyethylene (PE)	66.67	713.33	4.72	0.19
Poly(methyl methacrylate) (PMMA)	15.27	199.69	6.81	0.28
Atactic Polystyrene (PS)	13.89	192.08	5.84	0.24
Poly(methyl acrylate) (PMA)	20.22	232.31	7.35	0.30
Poly(ethyl acrylate) (PEA)	14.08	199.69	6.81	0.28

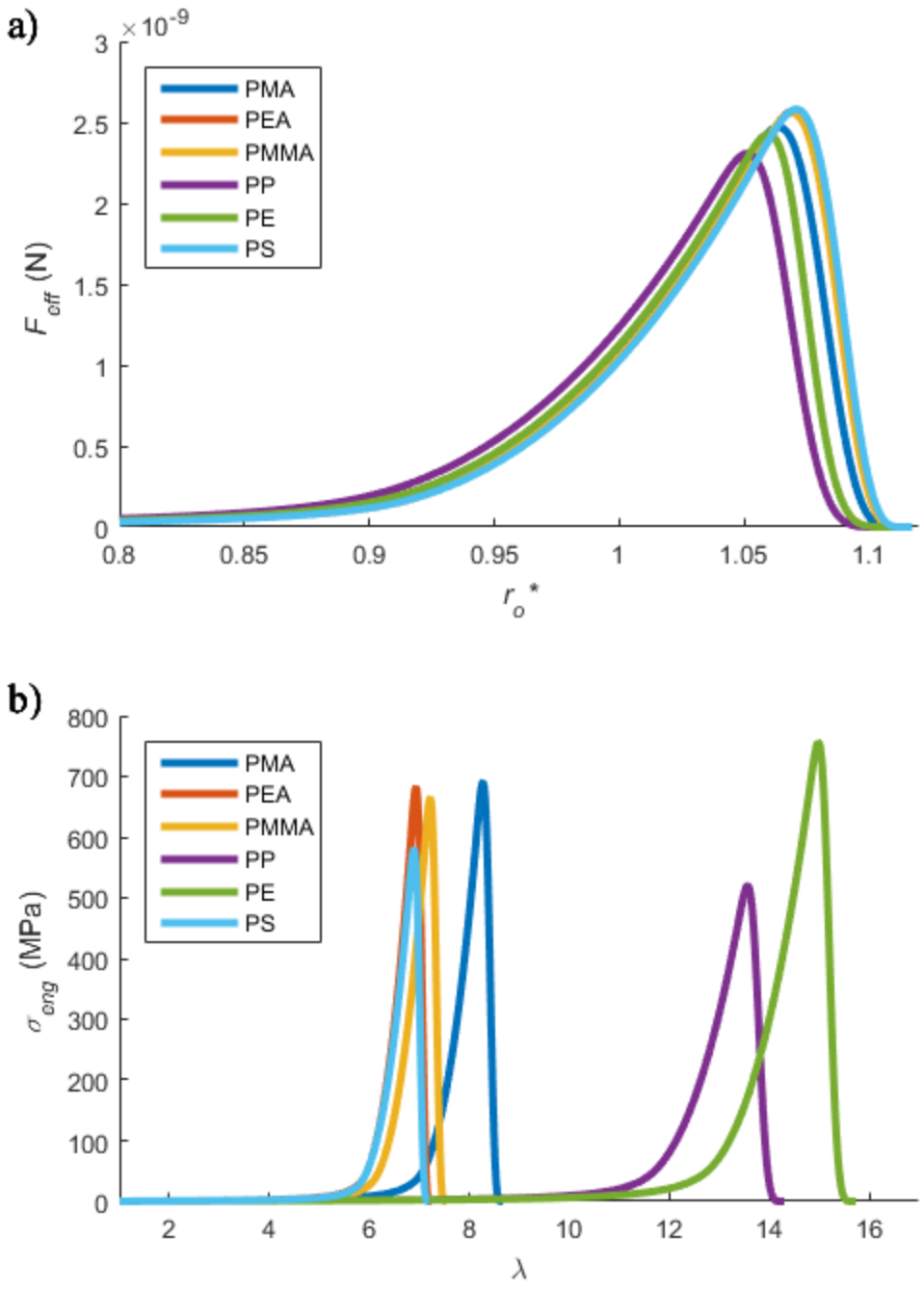

Figure A5.4: a) Effective forces vs fractional extension. b) Engineering stress σ_{eng} *vs stretch* □. *Comparison for 6 polymers where the molecular weight of the polymer chain,* $M_{ch} = 10000 g/mol$, *has been held constant.*

It is desirable to understand how the properties of each polymer chain can translate into mechanical properties of the material. Assuming the molecular weight of a polymer chain M_{ch} and the density of the material ρ are known the volumetric density of chains can be calculated from [50]

$$\upsilon_{ch} = \frac{\rho}{M_{ch}} N_{av}, \quad \text{(A5.13)}$$

where N_{av} is Avogadro's number. For a uniaxial extension deformation, the engineering stress can be evaluated from [5]

$$\sigma_{eng} = \frac{\upsilon_{ch} k_B T}{3} \frac{F^*_{eff}}{r^*_o} \left(\lambda - \frac{1}{\lambda^2} \right), \quad \text{(A5.14)}$$

If we fix $M_{ch} = 10000 g/mol$ we can evaluate $N_K = M_{ch}/M_K$, υ_{ch} and σ_{eng} for each of the 8 example polymers and the result is shown in Figure A5.4b). Note that since the chain molecular weight is held fixed the chains pf polymers with lower Kuhn segment molecular weight M_K (Table 6.2) are comprised of more Kuhn segments (Table A 5.2). Due to the "8-chain" assumption $r^*_o = \sqrt{I_1/3N_K}$ for a given stretch and hence I_1 these chains will have smaller r^*_o. Therefore, chains with larger N_K, such as PE, experience the upturn in force, and therefore stress, at larger stretch in Figure A5.4b). In addition polymers with higher densities result in higher volumetric densities of chains, υ_{ch} (Table), which along with the break forces shown in Figure A5.4a), fractional extension and stretch, scales the stress magnitude (Eq. (A5.14)). For example comparing PEA and PS which show nearly identical behavior in Figure A5.4a), PEA has larger stress because υ_{ch} is larger.

Note that the magnitude of the stress in Figure A5.4b) is much larger than anything that would be seen experimentally for these materials; it is important to understand that the results in Figure A5.4b) are an idealization for comparison between polymers. In reality polymers are polydisperse, meaning that, while there may be an average chain molecular weight, the chains which make up the material have a distribution of lengths. This implies that at a given stretch only a fraction of the total chains in the material would be at an extension which results in large forces; this also leads to a stress-stretch curve with progressive damage (more ductile), than the brittle failure shown in Figure A5.4b). Secondly, this idealization assumes that the deformation and

scission are homogenous. In reality, small imperfection in samples result in stress concentrations, localized damage, proportion of cracks and failure at much lower stretches compared with Figure A5.4b). Thirdly, it is assumed that the network is in a rubbery state where chains do not interfere each other and respond to macroscopic strain independently which is not true at room temperature for all of the polymers presented in Figure A5.4b); for example, PE has a glassy state a room temperature where chain mobility is severely reduced. Fourthly, stress induced crystallization at large stretches is also not considered either.

Appendix 5.6. Active Chain Curve Fit

If chain force extension relationship from Figure 6.10b) needs to be at many points in a material, it can become very computationally expensive, therefore it is desirable to have a reasonably accurate curve fit to approximate the soliton. This is accomplished by using a piecewise fit as follows

$$F^*\left(r_o^*\right)=\frac{F\left(r_o^*\right)A_o}{k_BT}=\begin{cases}2\left(\frac{1}{4}\left(1-r_o^*\right)^{-2}-\frac{1}{4}+r_o^*\right) & r_o^*\le 0.9\\ F_1^*\left(r_o^*\right) & F_R^*>F_1^*>F_2^* \quad r_o^*>0.9\\ F_R^*\left(r_o^*\right) & F_1^*>F_R^*>F_2^* \quad r_o^*>0.9\\ F_2^*\left(r_o^*\right) & F_1^*>F_2^*>F_R^* \quad r_o^*>0.9\end{cases}, \tag{A5.15}$$

where the force acting on the 100% unreacted chain is given by

$$F_1^*\left(r_o^*\right)=\frac{F\left(r_o^*\right)A_o}{k_BT}=\frac{513}{10}+1002\left(r_o^*-0.9\right)+2386\left(r_o^*-0.9\right)^2+11058\left(r_o^*-0.9\right)^3, \tag{A5.16}$$

the force acting on the 100% reacted chain is given by

$$F_2^*\left(r_o^*\right)=\frac{F\left(r_o^*\right)A_o}{k_BT}=\frac{513}{10}+1002\frac{l_{1o}}{l_{2o}}\left(r_o^*\frac{l_{1o}}{l_{2o}}-0.9\right)+960\left(r_o^*\frac{l_{1o}}{l_{2o}}-0.9\right)^2+22491\left(r_o^*\frac{l_{1o}}{l_{2o}}-0.9\right)^3, \tag{A5.17}$$

and the force for the reacting portion of the force-extension relationship is given by

$$F_R^*\left(r_o^*\right)=\frac{F\left(r_o^*\right)A_o}{k_BT}=-26724+75617r_o^*-71076r_o^{*2}+22351r_o^{*3}. \tag{A5.18}$$

The piecewise fit from Eq. (A5.15), as well as the components, are compared with the corresponding model solutions in Figure A5.5. In evaluating the curves in Figure 6.11, Eq. (A5.15), and (A5.16) were used in conjunction with the damage function Eq. (A5.8) where

$F_{max} = 2.6449nN$, $c_1 = 27.216$, and $c_2 = 1.312$; note that this surviving chain fraction function was prescribed.

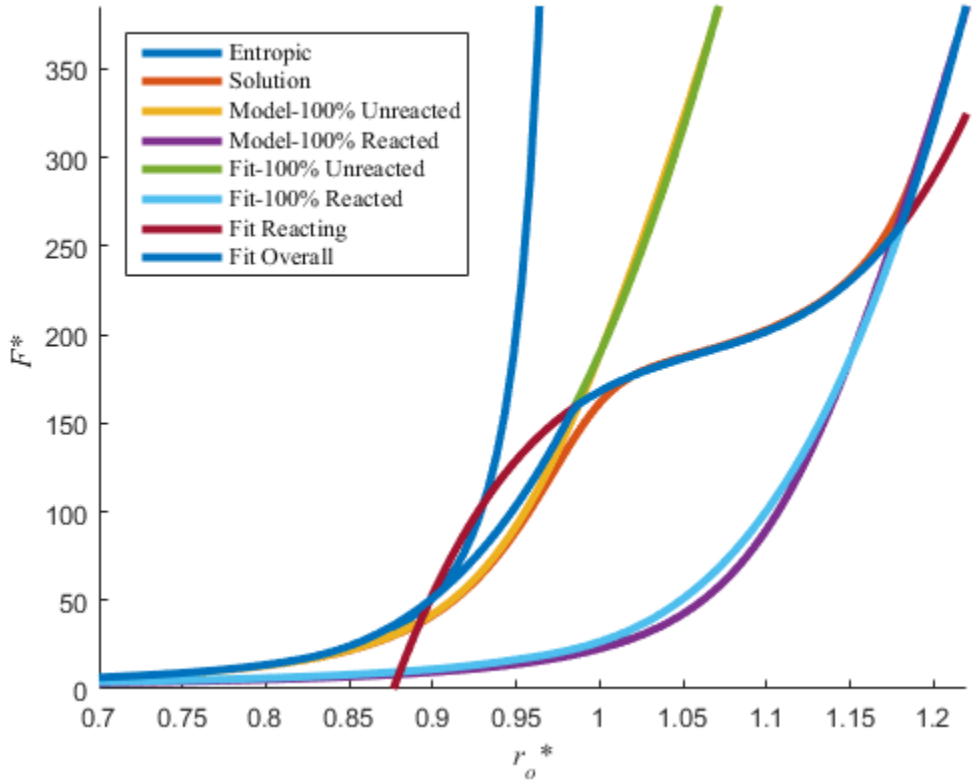

Figure A5.5: Comparison of the purely entropic chain force Eq. (6.1), with the chain force predicted by the model presented in this work, and the special cases for 100% reacted and 100% unreacted solutions. Also shown are the curve fits to represent !00% unreacted, reacting, and 100% reacted portion of the force-extension curve. The overall fit is a piecewise continuous curve that is made up of these three fits and the entropic model.